Geochemical, Paleoclimate, and Thermodynamic Insights into Lithium Enrichment and Extraction in Western U.S. Volcano-Sedimentary Deposits

by

Catherine Anne Gagnon

B.S., The Pennsylvania State University: State College, PA, 2020

M.Sc., Brown University: Providence, RI, 2022

A dissertation submitted in partial fulfillment of the requirements for the degree of Doctor of Philosophy in the Department of Earth, Environmental, and Planetary Sciences at Brown University

Providence Rhode Island, USA

February 2026

This dissertation by Catherine A. Gagnon is accepted in its present form by the Department of Earth, Environmental, and Planetary Sciences as satisfying the dissertation requirement for the degree of Doctor of Philosophy.

Date_____ _____

Dr. Daniel E. Ibarra, Advisor

Recommended to the Graduate Council

Date_____ _____

Dr. Colleen Dalton, Reader

Date_____ _____

Dr. James Russell, Reader

Date_____ _____

Dr. Greg Hirth, Reader

Date_____ _____

Dr. Michael Whittaker, Reader

Approved by the Graduate Council

Date_____ _____

David Lindstrom, Dean of the Graduate School

Curriculum Vitae

Catherine Anne Gagnon
(LinkedIn/ResearchGate)

EDUCATION

May 2026 **(Anticipated) PhD Earth, Environmental, and Planetary Sciences**, Brown University, RI
Thesis: *Geochemical, Paleoclimate, and Thermodynamic Insights into Lithium Enrichment and Extraction in Western U.S. Volcano-Sedimentary Deposits* (Advisor: Daniel E. Ibarra)

May 2022 **MS Earth Environmental, and Planetary Sciences**, Brown University, RI
Thesis: *Paleoclimate controls on lithium enrichment in Great Basin Pliocene–Pleistocene lacustrine clays* (Advisor: Daniel E. Ibarra)

Nov 2021 **Sheridan Teaching Certificate I,** The Harriet W. Sheridan Center for Teaching and Learning, Brown University, RI

May 2020 **B.S. Geoscience (hydrogeology concentration)**, Penn State University, PA
Thesis: *Hydrologic and landscape evolution near a Neolithic Village in Dalmatia, Croatia* (Advisors: Katherine H. Freeman and Sarah Ivory)

Sept 2016 **B.S. Geoscience (declared)**, West Chester University, PA

RESEARCH/TEACHING INTERESTS

(1) Earth resources and their related sustainability, societal, and geopolitical considerations
(2) Earth system engineering and modern climate change
(3) Environmental geochemistry and hydrogeology
(4) Field geology and mapping

INTERNSHIPS

2024-2025 **DOE SCGSR Intern**, Lawrence Berkeley National Laboratory, CA
- Investigating energetics governing Li enrichment in smectite deposits in collaboration with NETL, Jindalee Lithium, and Oregon State University
- Analyzed samples by X-ray diffraction, scanning electron microscopy and energy dispersive spectroscopy, laser induced breakdown spectroscopy, and nano isothermal titration calorimetry

2023 **LNC Exploration Intern**, Lithium Nevada Corporation, Reno, NV
- Collected field samples and analyzed the geochemistry of various Li ore deposits
- Analyzed geospatial data using Geographic Information Systems (GIS)

2017-2018 **South Pole Ice Core Lab Assistant**, Penn State University, PA
- Responsible for preparing South Pole Ice Core samples for trace gas analysis and operating a semi-automated vacuum/gas chromatograph system for paleoclimate data collection, supervised by Dr. Todd Sowers.

AWARDS AND FELLOWSHIPS

2025 **Jeanne E. Harris Chrysalis Scholarship**, Association for Women Geoscientists, $1500

2024-2025 **DOE SCGSR award,** Department of Energy, *"Investigating geochemical and thermodynamic mechanisms governing lithium mineralization in volcano-sedimentary ore deposits"* (working with Michael Whittaker, Lawrence Berkeley National Laboratory), ~$15,000 + travel and analytical expenses.

2021 **Continental Scientific Drilling Division Student Research Grant**, Geological Society of America, *"Stable isotope-based Pliocene to present hydroclimate reconstruction from Clayton Valley, NV"*, $2,400 + $500 for Conference Travel.

2023 **IBES Graduate Research, Training, and Travel Award, Institute at Brown for Environment and Society,** *"Hydroclimate in the southwestern Great Basin: Implications for economically viable lithium accumulation in lake clay deposits"*, $5,000.

2021 **IBES Graduate Research, Training, and Travel Award**, Institute at Brown for Environment and Society, *"Pliocene to present hydroclimate reconstructions from the Great Basin"*, $4,991. §

2019 **Julie and Trem Smith Family Undergraduate Scholarship,** Penn State University
2019 **Timothy and Cindie Mullen Scholarship in Geosciences**, Penn State University
2019 **AWG Field Camp Award**, Association for Women Geoscientists, $500

SHORT COURSES

2025 **North American Workshop on Critical Minerals**, Jackson School of Geosciences, UT Austin
2023 **SYBILLA Clay X-ray Diffractometry Short Course**, CMS Annual Meeting, Austin, TX
2021 **IsoCamp Mass Spectrometry Short Course,** Center for Stable Isotopes, University of New Mexico, NM
2018 **Geology of the Marcellus Shale Field Course (EARTH 109)**, Penn State University, PA
2019 **Penn State Summer Field Camp (GEOSC 472)**, 6 weeks, Penn State University, PA 2016
2020 **Field Geology (ESS 201),** West Chester University, PA

PUBLICATIONS (*undergraduate mentee)

Z Sharp, J Wostbrock, A Gargano, V Hare, J Johnson, T Cerling, P Banerjee, C Peshek, C Knutson, L Hartzell, E Cano, E Stiles, KR Bassett, K Holland, MH Dowd, J Sae-Lim, T Dominguez, D Bryant, E Di Marcantonio, J Wainwright, M Horsford, P Botte, **CA Gagnon**, PJ Rudall, J Ehleringer, (in review), Extreme triple oxygen isotope fractionation in *Equisetum*, Proceedings of the National Academy of Sciences, 122(44) https://doi.org/10.1073/pnas.250745512

W Dong, R Yan, **CA Gagnon**, DA Khaladj, M Getenet, ML Whittaker, (submitted), Multistep incongruent dissolution controls lithium extraction from hectorite

C Emproto, TR Benson, **CA Gagnon**, W Baek, DE Ibarra, AC Simon, 2025, Clay Chemistry of the Thacker Pass Deposit, Nevada: Implications for the Formation of High-grade Volcano-sedimentary Lithium Resources, *Economic Geology*, 120, (5): 1047–1070, https://doi.org/10.5382/econgeo.5155

CA Gagnon, KL Butler, K Robertson, C Emproto, P Gans, R Eden, DE Ibarra, TR Benson, *In Press*, Volcano-sedimentary lithium occurrences in Barstow, CA and their related formation mechanisms determined by stable isotope analyses of carbonates and clays, *Economic Geology*, 120, (5), 1261-1285, https://doi.org/10.5382/econgeo.5174

S Miller*, CW Kinsley, **CA Gagnon**, WD Sharp, JL Oster, DE Ibarra, *In revision*, Carbonate Clumped Isotopes Record Variable Carbonate Formation Depth in Response to Fluctuating Last Interglacial Lake Hydrology at Owens Lake, California, *Geochemistry, Geophysics, Geosystems*

CA Gagnon, R Havel, J Chen, G Piccione, DE Ibarra, 2025, Determination of KGa-1b and SHCa-1 Δ'17O and δ18O via laser fluorination of lithium fluoride clay pellets, *Rapid Communications in Mass Spectrometry,* 39 (11), e10021. https://doi.org/10.1002/rcm.10021

MJ Custado, **CA Gagnon**, B Belanger, N Sekhon, J Bernstein-Schalet, CW Kinsley, WD Sharp, JL Oster, DE Ibarra, 2025, Constraining the Modern Hydrological Balance of Bear Lake, Utah-Idaho: Insights from Stable Isotopes (^{18}O and ^{2}H), *Water Resources Research*, *61*(4), https://doi.org/10.1029/2024WR038264

T Bhattacharya, PR Brennan, DE Ibarra, **CA Gagnon**, KL Butler, A Terrazas, S Miller, LA Munk, DF Boutt, R Feng, SN Bullinger, L Weisbeck, 2024, Pleistocene shifts in Great Basin hydroclimate seasonality govern the formation of lithium-rich paleolake deposits, *Quaternary Science Reviews*, 108747. https://doi.org/10.1016/j.quascirev.2024.108747

CA Gagnon, K Butler, E Gaviria*, A Terrazas, A Gao*, T Bhattacharya, DF Boutt, LA Munk, and DE Ibarra, 2023, Paleoclimate controls on lithium enrichment in Great Basin Pliocene-Pleistocene lacustrine clays, *Geological Society of America Bulletin*, 135, no. 11-12: 3201-3212. https://doi.org/10.1130/B36572.1

CONFERENCE ABSTRACTS (*undergraduate mentee)

I Rangel, A Cawood, K Butler, Z Sickmann, M Blake, B Swanson, D Ibarra, **CA Gagnon**, LA Munk, D Boutt, D Ferrill, K Smart, 2025, Revised tectonic framework for the Clayton Valley, NV volcano-sedimentary lithium deposits, 272-3 GSA Connects 2025.

A Cawood, D Ferrill, I Rangel-Landeros, K Butler, Z Sickmann, B Madigan, D Ibarra, B Swanson, L Munk, D Boutt, L Stockli, D Stockli, **CA Gagnon**, 2025, Geochemical Constraints on Lithium Transport in Fault and Fracture Systems, 19-10 GSA Connects 2025.

CA Gagnon, Butler KL, Robertson K, Emproto C, Gans, P, Eden R, Ibarra DE, Benson, TR, 2025, Utilizing stable isotopes to identify the formation processes responsible for lithium enrichment in clay deposits of the Western United States, AIPEA International Clay Conference, 2025

S Miller*, **CA Gagnon,** C Kinsley, BK Belanger, CY Chen, W Sharp, JL Oster, DE Ibarra, 2023, Identifying drivers of hydroclimate change during Marine Isotope Stage 5 in Owens Valley CA using carbonate clumped isotopes. PP43F-1735, AGU 2023.

DE Ibarra, **CA Gagnon**, R Havel, J Chen, G Piccione, ER Nigro, EB Hodgin, CP Chamberlain, 2024, Triple Oxygen Isotope Standardization of Low Temperature Silicate and Oxide Standards. V23A-3315, AGU Fall Meeting.

DE Ibarra, **CA Gagnon**, R Havel, J Chen, G Piccione, ER Nigro, EB Hodgin, CP Chamberlain, 2024, Triple Oxygen Isotope Standardization of Low Temperature Silicate and Oxide Standards. 9th International Clumped Isotope Workshop.

DE Ibarra, S Miller, CW Kinsley, **CA Gagnon**, W Sharp, JL Oster, 2024, Investigating late Pleistocene stable isotope systematics of lakes in the western United States using carbonate clumped isotopes: an example from Owens Valley, CA. 9th International Clumped Isotope Workshop.

DE Ibarra, S Miller*, MJ Custado, CW Kinsley, BK Belanger, N Sekhon, **CA Gagnon**, W Sharp, JL Oster, 2024, INVESTIGATING LATE PLEISTOCENE STABLE ISOTOPE SYSTEMATICS OF LAKES IN THE WESTERN UNITED STATES. AMQUA 2024.

DE Ibarra, S Miller, MJ Custado, CW Kinsley, BK Belanger, N Sekhon, **CA Gagnon**, W Sharp, JL Oster, 2024, INVESTIGATING LATE PLEISTOCENE STABLE ISOTOPE SYSTEMATICS OF LAKES IN THE WESTERN UNITED STATES. 135-8, GSA Connects 2024.

MJ Custado, **CA Gagnon**, B Belanger, N Sekhon, J Bernstaein-Schalet, CW Kinsley, WD Sharp, JL Oster, DE Ibarra, 2024, Insights into the hydrological balance of Bear Lake (Utah-Idaho) through stable water isotope analysis. 162-5, GSA Connects 2024.

T Bobik, J Chen, XJ Du, **CA Gagnon**, WV Ribeiro, JKC Rugenstein, Y Gao, **DE Ibarra**, 2023, Filling in the gaps: paleosols as regional recorders of east Asian hydroclimate response to the Cretaceous-Paleogene. PP21E1342, AGU 2023.

CA Gagnon, KL Butler, K Robertson, DE Ibarra, TR Benson, 2023, Investigating lithium enrichment mechanisms within the Barstow Formation using stable isotopes of lacustrine carbonates, clays, and cherts. 74-2, GSA Connects 2023.

CA Gagnon, C Emproto, TR Benson, LA Munk, DE Ibarra, Investigating Lithium-Rich Clays: What Formation Mechanisms are Responsible For Producing Economically Viable Sedimentary-Volcanic Li Deposits?, conference talk, presented at 2023 Forum on the Geology of Industrial Minerals/ Clay Mineral Society Annual Meeting, Austin, Texas, 21-23 May.

MJG Custado, S Miller*, N Chang*, M Prausnitz-Weinbaum, **CA Gagnon**, B Belanger, C de Wet, CW Kinsley, WD Sharp, JL Oster, DE Ibarra, 2023, Hydrological balance in the Bear Lake Watershed, Utah and Idaho using major-ion and stable isotope analysis. 6-5, 2023 GSA Rocky Mountain Regional Meeting.

P Brennan, T Bhattacharya, DE Ibarra, EM Jorgensen, **CA Gagnon**, LA Munk, DF Boutt, KL Butler, 2022, Leaf Wax Isotope Records of Paleohydrology in the Western US from the Pliocene to present, PP42D-1144, AGU Fall Meeting, 2022.

CR Emproto, TR Benson, DE Ibarra, **CA Gagnon**, AC Simon, 2022, STABLE ISOTOPES FOR TRACKING ORE FORMATION AT THE THACKER PASS SEDIMENT-HOSTED LITHIUM DEPOSIT, NEVADA, USA, 224-10, GSA Annual Meeting 2022.

JL Oster, C de Wet, DE Ibarra, WD Sharp, C Kinsley, B Belanger, **CA Gagnon**, 2022, PATTERNS AND DRIVERS OF HYDROCLIMATE VARIABILITY ACROSS WESTERN NORTH AMERICA DURING THE LAST INTERGLACIAL, 179-2, GSA Annual Meeting 2022.

KL Butler, LA Munk, **CA Gagnon**, DF Boutt, BJ Moran, SV McKnight, KW Huntington, DE Ibarra, 2022, ~200 KYR PALEOCLIMATE RECORD FROM SALAR DE ATACAMA BASIN-MARGIN CARBONATES: IMPLICATIONS FOR LITHIUM ACCUMULATION IN THE WORLD'S LARGEST PRODUCING LITHIUM BRINE DEPOSIT, 224-3, GSA Annual Meeting 2022.

CA Gagnon, S Miller*, KL Butler, DF Boutt, LA Munk, DE Ibarra, 2022, CLIMATE VS. HYDROTHERMAL CONTROLS ON LITHIUM ENRICHMENT IN LACUSTRINE CLAYS: A CASE STUDY FROM CLAYTON VALLEY, NEVADA, 224-12, GSA 2022.

DE Ibarra, LA Munk, **CA Gagnon**, N Chang, J Jenckes, B Moran, D Boutt, C Emproto, T Benson, 2022, TRIPLE OXYGEN AND CARBONATE CLUMPED ISOTOPES OF MIOCENE CALDERA LAKE SEDIMENTS AND IMPLICATIONS FOR CALDERA LAKE LITHIUM ACCUMULATION, 224-8, GSA Annual Meeting 2022

CA Gagnon, KL Butler, E Gaviria*, A Terrazas, A Gao*, T Bhattacharya, DF Boutt, LA Munk, DE Ibarra, 2022, A LONG-LIVED LACUSTRINE PLIO-PLEISTOCENE HYDROCLIMATE RECORD FROM CLAYTON VALLEY, NEVADA, AMQUA 2022.

EC Gaviria, **CA Gagnon**, S Dee, DE Ibarra, 2022, Modeling seasonal and interannual climate variability in modern precipitation pathways across western North America using air parcel trajectories. Abstract S65, 2022 American Meteorological Society Annual Meeting

CA Gagnon, K Butler, E Gaviria*, T Bhattacharya, DF Boutt, LA Munk, and DE Ibarra Long-lived Pliocene to present lacustrine hydroclimate record from Clayton Valley, NV, Abstract (PP23B-03) presented at 2021 AGU Fall Meeting, 13-17 Dec.

CA Gagnon, KL Butler, EC Gaviria, T Bhattacharya, DF Boutt, LA Munk, DE Ibarra, 2021, Long-lived Pliocene to present lacustrine hydroclimate record from Clayton Valley, NV. Poster presented at the 2021 Graduate Climate Conference

CA Gagnon, KL Butler, EC Gaviria, T Bhattacharya, DF Boutt, LA Munk, DE Ibarra, 2021, Long-lived Pliocene to present lacustrine hydroclimate record from Clayton Valley, NV. Abstract PP23B-03, 2021 AGU Fall Meeting. (Abstract)

EC Gaviria, **C Gagnon**, DE Ibarra, 2021, Modeling seasonal and interannual climate variability in modern precipitation pathways across western North America using air parcel trajectories. Presentation at the 2021 Leadership Alliance National Symposium.

TEACHING

2025 **New England Field Geology (EEPS 1250)**, graduate TA, Brown University, RI

- Assisted students with field mapping projects, digitizing maps in GIS
- Grading and providing feedback/help on assignment design and completion

2023 **Understanding Earth and Environmental Processes (EEPS 0220)**, graduate TA, Brown University, RI

- Coordination of labs and field trips for large introductory course on geology and earth processes
- Grading and providing feedback/help on assignment design and completion

2023 **BELL: Eastern Sierras (CEES 0945)**, co-instructor, Brown University, RI

- Designed and co-led 11-day pre-college course at the Sierra Nevada Aquatic Research Laboratory
- Taught on concepts in environmental studies, geology, and leadership, with a mission of developing socially responsible leaders
- Instructor Score: 4.95/5

2023 **The Global Water Cycle (EEPS 1310)**, graduate TA, Brown University, RI

- Grading and providing feedback on written materials
- Gave occasional lectures

2022 **Earth: Evolution of a Habitable Planet (EEPS 0240)**, graduate TA, Brown University, RI

- Coordination of undergraduate teaching assistants through large introductory course
- Developed mini lectures for hands on lab activities

2019 **Natural Disasters: Hollywood versus Reality (EARTH 101)**, undergraduate TA, Penn State University, PA

- Facilitated class discussions and helped students with in-class exercises

COMMUNITY ENGAGEMENT

2020-2022 **DEEPS STEP Volunteer**, Brown University, RI

- Designing and implementing 3rd and 4th grade science curriculum (line graphs, weather, energy, seasons, scientific process, and more) into providence public schools

2021-2022 **Geoclub President**, Brown University, RI

- Organized social and fundraiser events for Brown graduate students

2021-2022 **DEEPS Mental Health Maintenance,** Brown University, RI

- Organizing and leading a mental health in academia discussion group that promotes healthy work-life balance

2019 **The Discovery Space Museum Intern**, NSF *In Search of Earth's Secrets* exhibit, State College, PA

- Engaged in community outreach education of JOIDES Resolution, training volunteers on the various hands-on activities and helping with the set up/break down of the exhibit

2018-2019 **Children's Science Museum Activities Host**, The Discovery Space, State College, PA

- Led and helped design science activities for kids' birthday parties and events at a non-profit science center. Kid- friendly science lessons included circuits/building a robot, states of matter, chemical reactions, dinosaurs/fossils, and space/constructing a simple rocket.

2017 **Project ASTRO**, West Chester University, PA

- Revised old and designed new astronomy activities to be implemented more easily into the PA public schools' k-12 curriculum

STUDENT MENTORING

Brook Wagenheim (Brown), undergraduate researcher, 2023-2024.

- Fall 2023 SPRINT|UTRA
- Processed Li ore samples, performed clay separations, and pressed clay pellets for isotope analysis

Shaw Miller (Brown), undergraduate researcher, 2022-2024.

- Summer 2022 SPRINT | UTRA
- DOE SULI program to work at the Molecular and Nanogeochemistry group at Lawrence Berkeley National Lab.
- Nominated for and awarded 2023 Sarah LaMendola Undergraduate Research Award for Senior Thesis work, $1,000.
- Senior thesis: *Identifying drivers of hydroclimate change during MIS 5 in Owens Valley, California using carbonate clumped isotopes*

Madelyn Stewart (Yale University), IBES Leadership Alliance REU, summer 2022

- REU Project: *Emulating ICESat-2 Laser Altimetry to Measure Sea Ice Concentration*
- Goldwater Scholar, 2023

Phoebe Karkos (Hampshire College), IBES Leadership Alliance REU, summer 2022

- REU Project: *The downy woodpecker's "whinny" call and its role in communication*

Jahred Rosa-Sullivan (UCLA), IBES Leadership Alliance REU, summer 2022

- REU Project: *Men, Meat, and 'Merica: Attitudes Towards Climate Politics When Affirming or Denying Traditional Consumption Practices*
- Current master's student at University Virginia

Grace Kowalski (Purdue University) IBES Leadership Alliance REU, summer 2022

- REU Project: *Accuracy of Narragansett Bay Tides in the Ocean State Ocean Model*
- Current PhD student at Johns Hopkins

Maya Gong, (Haverford College) IBES Leadership Alliance REU undergraduate researcher, summer 2022

- REU Project: *Modeling River Runoff Using Precipitation Data in Narragansett Bay*
- Current graduate student at University of Washington

Natalie Chang, Brown, undergraduate researcher, summer 2022

- Summer 2022 SPRINT | UTRA
- Oxygen isotopes of various carbonates

Annabelle Gao, Brown, undergraduate researcher, DEEPS, Fall 2021 to Summer 2023.

- Caltech WAVE Program, summer 2022

- Processed, weighed, and analyzed oxygen isotopes of lacustrine carbonates from western US sites
- Senior Award for Excellence in Research, Academics and Service, Brown University
- Current PhD student at Boston University.

Elizabeth Gaviria (Rice University), DEEPS Leadership Alliance REU and Remote Undergraduate Researcher, Summer 2021 to Spring 2022.

- Senior Project: *Modeling Seasonal and Interannual Climate Variability in Modern Precipitation Pathways Across Western North America.*

Acknowledgements

It was a truly remarkable adventure pursuing scientific questions related to some of my generation's most pressing issues as a part of my PhD. This dissertation showcases many years of mentorship, collaboration, and support from an extraordinary community of people and institutions.

First and foremost, I am deeply grateful to Dr. Daniel E. Ibarra, my advisor, for his guidance, unwavering encouragement, and patience throughout every stage of my graduate research experience. His infectious passion, curiosity, and generosity as a scientist have not only shaped the way I think about Earth systems but also how I connect with peers and the greater scientific community. He is a role model for mentorship.

I am also thankful to my committee members Dr. James Russell, Dr. Greg Hirth, Dr. Colleen Dalton, and Dr. Michael Whittaker. They have provided invaluable expertise, feedback, and support throughout my graduate journey that has strengthened my scientific breadth and toolbox.

Finally, I owe my deepest thanks to my family and friends for their constant love and grounding presence. To Kyle Sousa, for his patience, humor, and unwavering belief in me; to my parents, for encouraging my curiosity and independence; and to the countless people that have dared to asking me, "What rock is this?" — thank you. This work is as much yours as it is mine.

Table of Contents

List of Figures

List of Tables

CHAPTER 1

Introduction

Catherine A. Gagnon

Department of Earth, Environmental, and Planetary Science

Institute at Brown for Environment and Society

Brown University

Providence, RI

Lithium has become a highly sought after necessity for the global energy transition, since it is a critical component in rechargeable batteries for electric vehicles and grid-scale energy storage (Bussar et al., 2016; Connolly et al., 2016; Breyer et al., 2018; Bogdanov et al., 2019; Greim et al., 2020). The expected growth in demand has increased efforts to identify more efficient and sustainable methods for extracting lithium from new and diverse geologic environments (Benson et al., 2023; Putzolu et al., 2025). Additionally, there have been more recent efforts to "on-shore" or increase the domestic supply chain of lithium in the United States for the purposes of national energy security (USGS, 2023; IEA, 2021; IEA, 2024).

Conventional lithium production from spodumene pegmatites and salar brines, through high-temperature roasting or solar evaporation respectively, currently dominates global supply (e.g., Nandihalli et al., 2024; Zhao, 2023). However, these deposits are geographically limited, and water or energy intensive (Roy et al., 2024). In contrast, sediment-hosted and volcano-sedimentary lithium deposits, composed primarily of smectite and illite, represent a potentially vast but underexploited resource in the western United States (Castor and Henry, 2020; Benson et al., 2023; Putzolu et al., 2025). In these systems, lithium is structurally bound within the silicate lattice requiring chemical leaching for recovery (Xie et al., 2024). Despite their promise, the fundamental mechanisms responsible for lithium enrichment in volcano-sedimentary systems are not well constrained and require more investigation to guide exploration efforts and resource estimates. Additionally, the chemistry between these sedimentary systems is highly variable (Crocker, 1987; Putzolu et al., 2025) and requires in-depth characterization and knowledge of fundamental reaction chemistry to optimize processing methods by deposit type (Xie et al., 2024). Understanding these processes demands an integrated approach across spatial and temporal scales: the paleoclimatic

and hydrologic evolution of closed-basin sedimentary systems, the geochemical and isotopic fingerprints of authigenic clays, and the thermodynamic mechanisms that control lithium release.

In this dissertation, the studies I present aim to better understand the distribution, formation mechanisms, and extraction thermodynamics of lithium clays from several volcano-sedimentary lithium deposits in the western United States. Specifically, studies were conducted in three different geologic basins: (1) Clayton Valley, NV which represents a closed Plio-pleistocene extensional basin with an active Li brine and claystone resource, (2) Barstow, CA which contains periodically closed-basin Li-rich lacustrine strata from the Miocene-Pliocene, and (3) the McDermitt, Caldera, NV-OR which hosts a Li mudstone deposit in the north eastern region of a Miocene collapsed caldera. The projects discussed in this body of work contribute new data to quantify lithium distribution and hydroclimate variability in these basins and constrain thermodynamics governing acid leaching extractions of hectorite. Part of conducting this work resulted in the novel method development of measuring triple oxygen isotopes of silicate clays by laser fluorination and the establishment, for the first time, of two clay silicate standards for triple oxygen isotope analysis.

The goal of the study presented in chapter 2, published in 2023 in *Geological Society of American Bulletin* (Gagnon et al., 2023), was to (1) produce a record of hydroclimate change for Clayton Valley, NV utilizing drill cores described in Coffey et al. (2021), and (2) investigate whether sedimentological or climatological variability contrived with lithium abundance. The study presents a new carbonate-based isotope record from Clayton Valley, integrating Li concentration data, age modeling, and back-trajectory storm track analyses to evaluate paleoclimate control on Li accumulation. It applies stable-isotope and elemental analyses from the Clayton Valley core EXP2 to quantify the relationship between hydroclimate evolution and Li

accumulation. This case study establishes the foundation for the subsequent chapters and ongoing work led by our collaborators and other investigators (Benson et al., 2023; Bhattacharya et al., 2024; Munk et al., 2025; Putzolu et al., 2025; Emproto et al., 2025; Darin et al., 2025) by linking lithium enrichment directly to climate-driven geochemical processes within closed-basin lacustrine systems.

The goal of chapter 3 was to establish a reliable methodology for measuring triple oxygen isotopes ($\Delta'^{17}O$ and $\delta^{18}O$) of silicate clays, like Li-smectite, via laser fluorination. This study resulted in two newly established clay isotopic standards (KGa-1b, a kaolinite, and SHCa-1, a hectorite) from the Clay Mineral society for $\Delta'^{17}O$ and $\delta^{18}O$. Stable oxygen isotopes of clays provide quantitative tools for reconstructing paleoclimate and mineral formation temperatures in addition to carbonate. This newly established method, published in 2025 in *Rapid Communications in Mass Spectrometry* (Gagnon et al., 2025a), was applied in chapter 4 to explore the processes contributing to Li enrichment at Barstow and has contributed to other hydrous mineral analyses in the oxygen isotope lab at Brown University (e.g., Havel et al., 2025).

The goal of the study presented in chapter 4 was to (1) Characterize the elemental and mineralogical variance of Li mudstones in Barstow, CA (2) provide hydroclimate context for sedimentary units of the Barstow Formation (3) and investigate the link between geochemical and environmental variability and lithium abundance. Chapter 4 includes elemental, mineralogical, and isotopic datasets ($\delta^{18}O$, δD, $\delta^{13}C$, Δ^{47}) to reconstruct the conditions of authigenic clay and carbonate formation. This study, published in 2025 in *Economic Geology* (Gagnon et al., 2025b), resulted in a lithium enrichment conceptual model for the Barstow Basin, which integrates mechanisms described in chapter 2 with other mechanisms related to hydrothermal activity as observed in other deposits such as Thacker Pass (e.g., Benson et al., 2023; Emproto et al., 2025).

Chapter 5 builds on a related study I am a co-author on, Dong et al. (submitted) and aims to (1) characterize the elemental and mineralogical variability of the McDermitt deposit and (2) experimentally quantify the enthalpy (ΔH), entropy (ΔS), and Gibbs free energy (ΔG) associated with proton-exchange and dissolution reactions in clays from the McDermitt deposit. While understanding formation processes constrains the natural concentration of Li, optimizing its extraction requires quantifying the energetics of clay–acid reactions. In smectite and illite, Li^+ occupies interlayer and structural sites and its release depends on acid strength, ionic substitution, and clay surface energy (Roy et al., 2024). Chapter 5 applies isothermal titration calorimetry (ITC) to quantify the thermodynamics of proton-exchange and dissolution reactions in natural (McDermitt) and reference hectorite clay (SHCa-1). These measurements provide direct insight into the reaction favorability and mechanism, offering a predictive basis for improving extraction efficiency while minimizing environmental impact.

Together, all studies add to the growing understanding of how lithium becomes enriched and extracted within volcano-sedimentary systems. Comparing sites across the Great Basin—from the long-lived lacustrine sequences of Clayton Valley, Nevada, to the exposed volcano-sedimentary deposits of Barstow, California—reveal how fluctuations in hydroclimate, diagenesis, hydrothermal activity, and basin hydrology control lithium distribution in authigenic clays. The conceptual models described within chapters 1 and 3 capture the main features of V-S lithium deposits and can be used to assist exploration efforts identifying and assessing new deposits.

Despite our growing understanding of the factors that go into creating V-S lithium deposits, there are still some challenges to finding and developing these resources. Outside of the Great Basin, there are other similar geologic systems that contain comparable lithium clay deposits in terms of overall lithium abundance and grade. However, not all geologic settings matching those

of known V-S deposits contain economic sources of lithium, making them difficult to locate initially. In some cases, like in Owens Valley, CA and Fish Lake Valley, CA, the bulk lithium concentrations from mudstones are at most, a few hundred ppm lithium. Even more, when lithium is present abundantly within a particular V-S deposit the grade can be extremely variable geospatially. To achieve reliable resource estimates, optimize geochemical processing procedures, and target high grade areas, each individual deposit requires extensive geochemical and mineralogical assay data, surveying, coring, and detailed stratigraphic basin modeling. Future research to address these potentially cost-prohibited challenges will come in the form of innovative techniques to acquire geospatial assay data rapidly. For example, Corrado et al. (2025) demonstrated the use of hyperspectral analysis to map potential Li prospective zones within the McDermitt caldera, defining potential mineralogical-hyperspectral vectors to be used for exploration of undiscovered volcano-sedimentary Li mineralization.

Another aspect of this work that prompts further research is understanding the fundamental molecular interactions and natural chemical conditions that lead to lithium being incorporated into the structural component of clays. There are a handful of places on Earth today that share the same features of the ancient environments that we know accumulated lithium smectite, but none have been shown to form authigenic Li-bearing smectite that we can study directly. Deep Springs Lake, CA was found to have authigenic clays and carbonates, however they were exclusively magnesium smectite (Hobbs et al., 2024). East African rift lakes match the conceptual model for where Li-clays may form as well, but there is no mention of authigenic lithium-bearing clays within the literature currently. Instead of observing a modern system, kinetic and thermodynamic experiments on existing clay samples may provide constraints on the conditions required for lithium clay formation in near surface environments. The ITC experiments in this dissertation are

an attempt to ground the basin scale conceptual models for lithium clay formation by constraining the energetics related to their formation/breakdown at the molecular level. Although the experiments yielded only partial breakdown of the clay lattice, they at least provide the first quantitative framework for assessing the favorability of leaching reactions commonly used in hectorite ore processing. Continuing these efforts to constrain formation energies for various types of Li-bearing clay would enhance our fundamental understanding of clay chemistry and consequently enable for the optimization of ore processing of this complex and novel emerging resource.

References

Benson, T.R., Coble, M.A., and Dilles, J.H., 2023, Hydrothermal enrichment of lithium in intracaldera illite-bearing claystones: Science Advances, v. 9, no. 35, p. 1-10. eadh8183.

Bogdanov, D., Farfan, J., Sadovskaia, K., Aghahosseini, A., Child, M., Gulagi, A., Oyewo, A.S., de Souza Noel Simas Barbosa, L., and Breyer, C., 2019, Radical transformation pathway towards sustainable electricity via evolutionary steps: Nature communications, v. 10, no. 1, p. 1–16.

Breyer, C., Bogdanov, D., Aghahosseini, A., Gulagi, A., Child, M., Oyewo, A.S., Farfan, J., Sadovskaia, K., and Vainikka, P., 2018, Solar photovoltaics demand for the global energy transition in the power sector: Progress in Photovoltaics: Research and Applications, v. 26, no. 8, p. 505–523.

Bussar, C., Stöcker, P., Cai, Z., Moraes Jr, L., Magnor, D., Wiernes, P., van Bracht, N., Moser, A., and Sauer, D.U., 2016, Large-scale integration of renewable energies and impact on storage demand in a European renewable power system of 2050—Sensitivity study: Journal of Energy Storage, v. 6, p. 1–10.

Castor, S.B., and Henry, C.D., 2020, Lithium-rich claystone in the McDermitt Caldera, Nevada, USA: Geologic, mineralogical, and geochemical characteristics and possible origin: Minerals, v. 10, no. 1, p. 68.

Connolly, D., Lund, H., and Mathiesen, B.V., 2016, Smart Energy Europe: The technical and economic impact of one potential 100% renewable energy scenario for the European Union: Renewable and Sustainable Energy Reviews, v. 60, p. 1634–1653.

Corrado, F., Putzolu, F., Armstrong, R.N., Mondillo, N., Chirico, R., Casarotto, B., Massironi, M., Fuller, D., Ball, R. and Herrington, R.J., 2025. Application of satellite and proximal hyperspectral sensing to target lithium mineralization in volcano-sedimentary deposits: A case study from the McDermitt caldera, USA. *Remote Sensing of Environment*, *323*, p.114724.

Greim, P., Solomon, A.A., and Breyer, C., 2020, Assessment of lithium criticality in the global energy transition and addressing policy gaps in transportation: Nature communications, v. 11, no. 1, p. 4570.

Hobbs, F.W., Fang, Y., Lebrun, N., Yang, Y. and Xu, H., 2024. Co-precipitation of primary dolomite and Mg-rich clays in Deep Springs Lake, California. *Sedimentology*, *71*(4), pp.1363-1383.

Putzolu, F., Armstrong, R.N., Benson, T.R., Boutt, D.F., Butler, K.L., Dolgopolova, A., Herrington, R.J., Ibarra, D.E. and Munk, L.A., 2025. Volcano-sedimentary deposits: Overview of an emerging type of lithium resource. *Economic Geology*, *120*(3), pp.541-573.

IEA, 2021, The Role of Critical Minerals in Clean Energy Transitions, International Energy Agency, Paris. www.iea.org/reports/the-role-of-critical-minerals-in-clean-energy-transitions.

U.S. Geological Survey, 2024, Mineral commodity summaries 2024. https://pubs.usgs.gov/periodicals/mcs2024/mcs2024.pdf

International Energy Agency. *Lithium – Analysis*. Paris: IEA, 2024.

Nandihalli, N., Chouhan, R.K., Kuchi, R. and Hlova, I.Z., 2024. Aspects of spodumene lithium extraction techniques. *Sustainability*, *16*(19), p.8513.

Zhao, H., Wang, Y. and Cheng, H., 2023. Recent advances in lithium extraction from lithium-bearing clay minerals. *Hydrometallurgy*, *217*, p.106025.

Roy, V., Paranthaman, M.P. and Zhao, F., 2024. Lithium from clay: Assessing the environmental impacts of extraction. *Sustainable Production and Consumption*, *52*, pp.324-332.

Xie, R., Zhao, Z., Tong, X., Xie, X., Song, Q. and Fan, P., 2024. Review of the research on the development and utilization of clay-type lithium resources. *Particuology*, *87*, pp.46-53.

L. Crocker, R.H. Lien, Lithium and its Recovery from Low-grade Nevada Clays, United States Bureau of Mines (1987)

CHAPTER 2

Paleoclimate controls on lithium enrichment in Great Basin Pliocene–Pleistocene lacustrine clays

Catherine A. Gagnon1,2, Kristina L. Butler1,3, Elizabeth Gaviria1,4, Alexa Terrazas5, Annabelle Gao1,Tripti Bhattacharya6, David F. Boutt7, Lee Ann Munk8, and Daniel E. Ibarra1,2

1 Department of Earth, Environmental and Planetary Science
2 Institute at Brown for Environment and Society
Brown University
Providence, Rhode Island, 02912

3 Department of Geological Sciences
Jackson School of Geosciences
University of Texas at Austin
Austin, Texas,78712

4 Department of Earth, Environmental and Planetary Sciences
Rice University
Houston, Texas,77005

5 Department of Atmospheric and Ocean Sciences
University of California, Los Angeles, California 90095, USA

6 Department of Earth Sciences
Syracuse University
Syracuse, New York, 12344

7 Department of Geosciences
University of Massachusetts–Amherst
Amherst, Massachusetts, 01003

8 Department of Geological Sciences
University of Alaska–Anchorage
Anchorage, Alaska, 99508

Abstract

Terminal lakes are important archives of continental hydroclimate and in some cases contain important economic resources. Here, we present an ~2.9 m.y. lacustrine carbonate carbon and oxygen stable isotope record from a Great Basin continental drill core. We paired these measurements with bulk lithium concentrations to reveal a relationship between past climate and lithium enrichment in authigenic lacustrine clays. Further, we explored the possible effects of changing seasonality on the isotope record through the use of paired air mass trajectories and modern isotope data. Our findings show the evolution of the basin's moisture balance over million-year time scales, which we attribute to variations in precipitation seasonality as well as fluctuations in the amount of evaporation associated with changes in atmospheric moisture convergence and divergence. We found a positive correlation between the oxygen isotope values of the lake carbonate and the bulk sediment lithium concentrations, which we argue is indicative of evapoconcentration of the lake environment and subsequent enrichment of the authigenic clays. Our results suggest a link between past hydroclimate changes and the formation of lithium-rich authigenic clays feeding high lithium concentrations in this modern brine aquifer system.

Introduction

Evidence from the relatively recent geologic past suggests that the Great Basin region of the western United States experienced enhanced moisture convergence in both warmer and colder climates compared to modern conditions (Matsubara and Howard, 2009; Salzmann et al., 2011; Pound et al., 2014; Ibarra et al., 2014, 2018; Lee et al., 2021; Fu et al., 2022). For example, the Last Glacial Maximum (LGM) was a vastly different climate state, with global sea level 140 m lower and global mean annual temperatures ~6 °C cooler than present (Clark et al., 2009; Annan

and Hargreaves, 2013; Lora and Ibarra, 2019). During that time, the Great Basin sustained many pluvial lakes, the maximum extents of which represent a balance between precipitation and evaporative demand and suggest a much wetter environment (Mifflin and Wheat, 1979; Reheis, 1999a, 1999b; Orme, 2008; Kurth et al., 2011; Godsey et al., 2011; Munroe and Laabs, 2013; Ibarra et al., 2014; Reheis et al., 2014; Oster and Ibarra, 2018; Santi et al., 2020). A metric for evaluating the moisture balance of these pluvial lakes is precipitation minus evaporation (P − E), associated with regional atmospheric convergence (e.g., Lora and Ibarra, 2019), which we will use hereafter when referring to moisture balance. Similarly, the mid- Pliocene (defined as ca. 3.3–2.9 Ma for climate model simulations) experienced wetter-than-modern conditions in the southwestern United States (Pound et al., 2014; Ibarra et al., 2018; Fu et al., 2022). However, and in contrast to the LGM, a combination of proxies and modeling efforts suggested the late Pliocene global mean annual temperature was around 3.5 °C warmer than today and had atmospheric CO2 levels greater than pre-industrial values (Ravelo et al., 2004; Dowsett and Caballero Gill, 2010; Burke et al., 2018; Haywood et al., 2020). Numerous hypotheses have been invoked to explain the wet conditions in the mid-Pliocene. Some have proposed that weaker atmospheric circulation in response to the different ocean-surface temperature patterns of the Pliocene reduced meridional and zonal temperature gradients (Molnar and Cane, 2002; Burls and Fedorov, 2017). Another recent hypothesis argued for more enhanced convergent monsoonal circulation developing over the late boreal summer due to increased sea-surface temperature (SST) in the Pliocene (Fu et al., 2022). Last, strengthened southwesterly moisture delivery could have resulted in greater wintertime precipitation that fed the southwest U.S. lakes (Ibarra et al., 2018).

Lake basins in the Great Basin are important archives of climate, and, in some cases, they also host significant economic resources (e.g., Davis et al., 1986; Munk et al., 2011; Bradley et al.,

2013; Castor and Henry, 2020). Clayton Valley, Nevada, is a long-lived Pliocene–Pleistocene lake basin and is also the location of the largest lithium brine resource in North America (Coffey et al., 2021). The availability of lithium is critical for the transition to renewable energy and electric vehicles because it is an important component of modern battery technology (e.g., Munk et al., 2016; Manthiram, 2017). In this study, deep sediment cores from Clayton Valley provided the opportunity to explore the intersection between Pliocene–Pleistocene hydroclimate change and the formation of this important resource. Additionally, the similarity between the climate state of the late Pliocene and today (Burke et al., 2018; Haywood et al., 2020), with minimal changes in continental configuration, orography, and paleogeography, makes this lake basin an excellent study area in which to investigate how regional hydroclimate in the southwestern United States might evolve in the future. In this study, we addressed the following two key questions: (1) How did the hydroclimate of Clayton Valley vary during the late Pliocene and Pleistocene? (2) What role did climate play in the formation of lithium-rich clays in the Clayton Valley basin?

To answer these questions, we obtained a new carbonate-based stable isotope hydroclimate record for Clayton Valley, a terminal basin in the Great Basin of the western United States, and demonstrated through additional geochronology (cf. Coffey et al., 2021) that this basin contains lake deposits from the late Pliocene to late Pleistocene. We measured stable carbon and oxygen isotopes of carbonates from a previously described sediment core (EXP2) and expanded on the sedimentologic interpretations of Coffey et al. (2021) to include thin section analysis and chemical weathering indices of alteration (CIA) based on bulk elemental analyses, as well as additional higher-resolution bulk lithium concentration measurements. Further, to provide a clear picture of the modern hydroclimate dynamics, we also included air mass back-trajectory and analyses of precipitation for Clayton Valley using the Hybrid Single-Particle Lagrangian Integrated Trajectory

model (HYSPLIT; Stein et al., 2015; Warner, 2018). We compared these trajectories with nearby modern precipitation isotope data. Our results demonstrated that the long-term late Pliocene to late Pleistocene hydroclimate evolution from wet deep-lake conditions to increasingly desiccated and punctuated pluvial lake conditions greatly influenced lithium accumulation in this lacustrine clay deposit, which is the primary source of lithium to the modern brine aquifer system (Coffey et al., 2021).

Setting

Clayton Valley is a topographically closed half-graben basin in Esmeralda County, Nevada, along the western margin of the Basin and Range Province, ~130 km (80 miles) to the northwest of Death Valley (M in Fig. 1). Fish Lake Valley neighbors Clayton Valley to the west. Basement fault blocks of late Neoproterozoic to Ordovician, North American western passive-margin, metamorphosed siliciclastic and carbonate units bound the basin on all sides. Surficial deposits consist of Tertiary volcanic and sedimentary rocks. During the late Paleozoic and Mesozoic, the region underwent shortening and low-grade metamorphism. Since ca. 16 Ma, the area has undergone continuous extension (Coffey et al., 2021; Oldow et al., 2009; Burrus, 2013). Clayton Valley lies at the northernmost extent of the North American monsoon (e.g., Ray et al., 2007; Means, 2013; Bhattacharya et al., 2017). The average annual precipitation is 13 cm (Munk and Chamberlain, 2011), which is delivered in the summer months by the North American monsoon and in the winter months by westerlies. The valley floor playa spans 100 km2 at an elevation of 1298 m. The entire topographic watershed for Clayton Valley is 1437 km2 (Coffey et al., 2021). Recent groundwater flow modeling has shown a potential contribution from surrounding basins up to 12,610 km2 (Brooks et al., 2014; Underdown et al., 2017). Despite the large influence of

interbasin flow (Fig. 1), the groundwater from all surrounding basins terminates in Clayton Valley (Rush, 1968; Coffey et al., 2021). Water outflow is therefore limited to playa evaporation and evapotranspiration in the lowland areas of the valley where there is a shallow groundwater table (Corenthal et al., 2016).

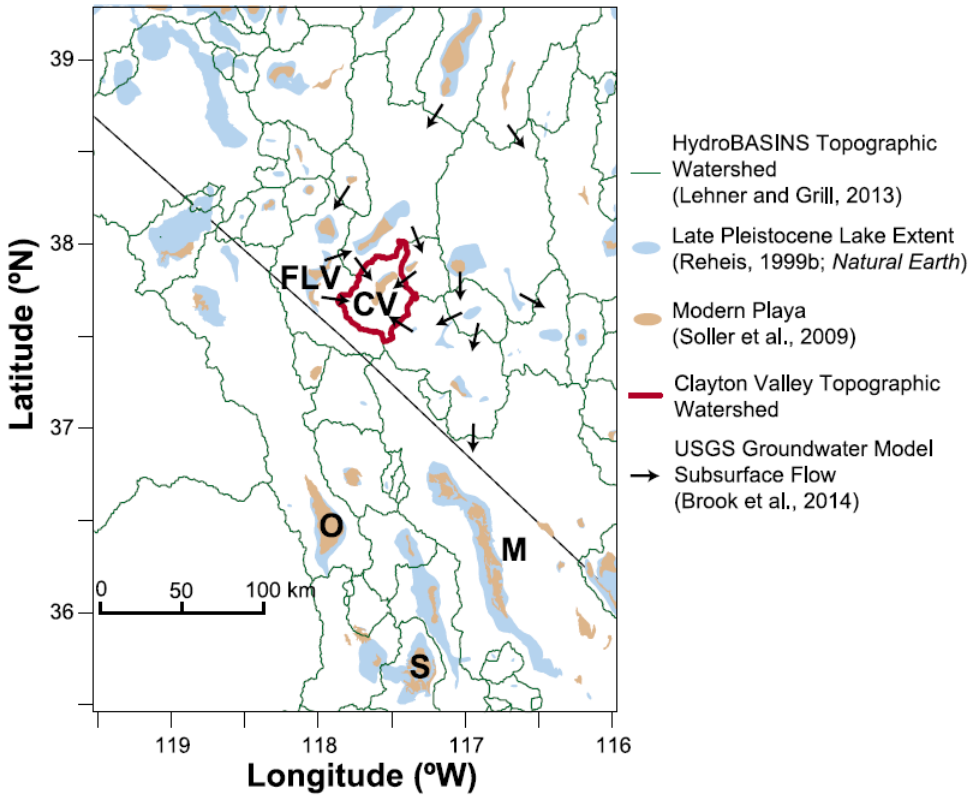

Figure 1. Map of Clayton Valley (CV), Fish Lake Valley (FLV), Lake Manly (M), Searles Lake (S), and Owens Valley (O) with watershed boundaries, late Pleistocene lake extents, and modern playas. Note that the groundwater flow vectors (Brook et al., 2014) surrounding the study site terminate in the Clayton Valley basin. USGS—U.S. Geological Survey.

Materials and Methods

Core EXP2

The EXP2 core was one of five cores drilled in the Clayton Valley basin between June 2017 and November 2017 by the Albemarle Corporation. The 990.6-m-long (3250-ft-long) core was

photographed and logged to the nearest tenth of a foot (~3 cm), with depths herein converted to meters.

From top to bottom, we summarize the major lithologic units (Fig. 2) after Coffey et al. (2021). The upper clastic unit spans 0–228.6 m depth. The dominant sedimentology from 0 to 45.7 m consists of sands and gravels with interbedded clays, which transition to clays with thin infrequent sand interlayers from 45.7 to 228.6 m. The lower clastic unit spans 228.6–405.4 m, and it primarily consists of brown and green clay with sparse interlayers of volcanic ash and silty clay. The clastic and salt unit is composed of thick layers of halite as much as 6.1 m thick with thin layers of clay from 405.4 to 535.0 m. The clastic and ash unit is next in succession from 535.0 to 896.7 m depth. This unit consists of green clay and thin volcanic ash layers with silt near the base of the unit. The remainder of the core below 897.7 m is angular gravel composed primarily of clasts of siltstone derived from the fault block mountains on the east side of the basin; this gravel unit overlies a Tertiary crystal lithic tuff that is also exposed on the east side of Clayton Valley on Angel Island.

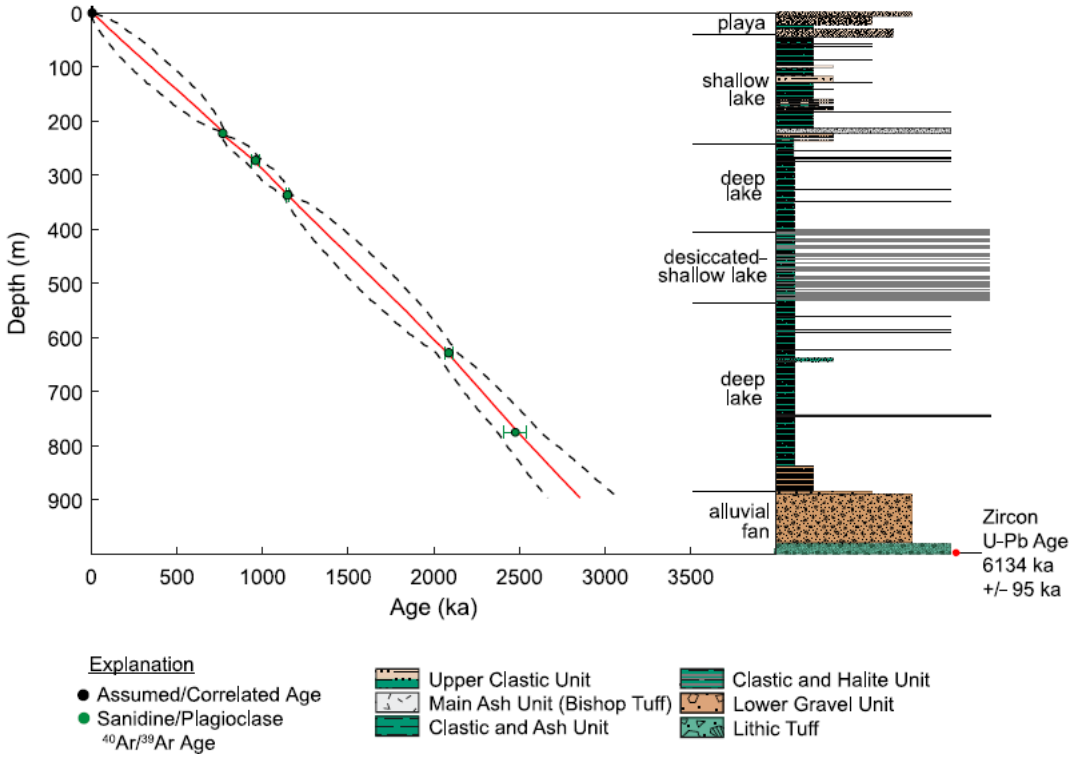

Figure 2. Age model for Clayton Valley EXP2 core alongside a stratigraphic column detailing the major lithologic units modified from Coffey et al. (2021). Light-gray units in the stratigraphic column are halite beds, while thin black units are ashes.

Fish Lake Valley Outcrop Samples

Fish Lake Valley outcrop samples were collected in the summer 2021 field season (Table S61) and measured for stable isotopes for comparison with the Clayton Valley record that we generated. We visited the southeast playa and rimrock sections (Reheis et al., 1991, their figs. 2 and 4) as well as the northeast 179-EP section (see Reheis et al., 1993, their fig. 7). We attributed depths/heights to the outcrop samples relative to the boundaries of units described by Reheis et al. (1991, 1993). We then used a combination of previously dated ashes (Knott et al., 2018, 2019) and previously correlated magnetostratigraphy (Sarna-Wojcicki et al., 2005, their fig. 15), following Mix et al. (2019), to assign ages (Tables S5 and S6). All reported age-depth relationships in the

playa and badlands sections are estimations of contact points along the major lithologic units in the stratigraphic column.

Whole-Rock Elemental Analyses and Lithium Concentrations

As in Coffey et al. (2021), whole-rock samples were analyzed by SGS Environmental Services for whole-rock geochemistry by X-ray fluorescence (XRF) and for lithium concentrations by inductively coupled plasma–optical emission spectrometry (ICP-OES). Briefly, ~1 g aliquots of crushed and pulverized samples were formed into a homogeneous glass disk by fusion with a lithium tetraborate/lithium metaborate mixture and then analyzed by wavelength dispersion XRF (WD-XRF). All reporting limits were less than or equal to 0.01%. Calibration checks were performed daily. SGS methods conformed to the ISO/IEC 17025 (2017) requirements. Lithium concentrations in solid samples were obtained by ICP-OES by SGS. A 0.1 g aliquot of crushed and pulverized sample was fused using Na2O2 and digested in HCl, and Li concentrations were analyzed on an Agilent ICP-OES.

Dating Methods

In previous work, Coffey et al. (2021) dated six ashes from the EXP cores using 40Ar/39Ar methods on sanidine. In this work, we present two additional 40Ar/39Ar ages and one zircon U-Pb age to refine the age model for EXP2. For the new 40Ar/39Ar ages at 336.35 m and 774.8 m, sanidine and plagioclase (respectively) were isolated from the tephras via magnetic and density sorting techniques, and their composition was verified using a variable-pressure scanning electron microscope. Separates were wrapped in aluminum foil, placed in 2.5 cm aluminum disks, and irradiated along with the 1.1864 Ma Alder Creek sanidine standard (Jicha et al., 2016) at the Oregon State University TRIGA reactor in the Cadmium-Line In-Core Irradiation Tube (CLICIT). Single-crystal fusion experiments were performed with a 50 W CO2 laser in the WiscAr laboratory

at the University of Wisconsin–Madison. Gas was analyzed using a Noblesse multicollector mass spectrometer and the procedures in Jicha et al. (2016). Weighted mean ages were calculated using the decay constants of Min et al. (2000) and are reported with analytical uncertainties at the 95% confidence level. The atmospheric argon value used was that of Lee et al. (2006). Weighted mean average and relative probability plots are included in Figure 3.

One volcanic ash sample (EXP2_3277) was collected from the EXP2 drill core for zircon U-Pb crystallization age determination at a depth of 998.8 m. Zircon grains were isolated by traditional physical and chemical mineral separation methods, including crushing, grinding, and hydraulic, heavy-liquid, and magnetic separation. Zircon grains were then poured onto double-sided tape on epoxy resin mounts, and 33 inclusion-free zircons were selected for U-Pb analysis by laser ablation–inductively coupled plasma–mass spectrometry (LA-ICP-MS) at the University of Texas at Austin. Mounts were transferred to a large-volume Helex sample cell and analyzed by a magnetic sector, single-collector Thermo Scientific Element2 High-Resolution ICP-MS with an attached Photon Machine Analyte G.2 excimer laser-ablation system. Data reduction was performed in the Iolite software (Paton et al., 2011). A weighted mean average age (6.134 ± 0.095 Ma) was calculated from the unimodal youngest population of 16 zircon ages, resulting in a mean square of weighted deviates (MSWD) of 0.78. Ages with discordance >30% were excluded from the age calculation as well as ages clearly defining older age populations (i.e., inherited zircons). Weight mean average plots and Wetherill concordia were constructed using IsoplotR (Fig. 3; Vermeesch, 2018). See Table S3 for zircon U-Pb analytical results.

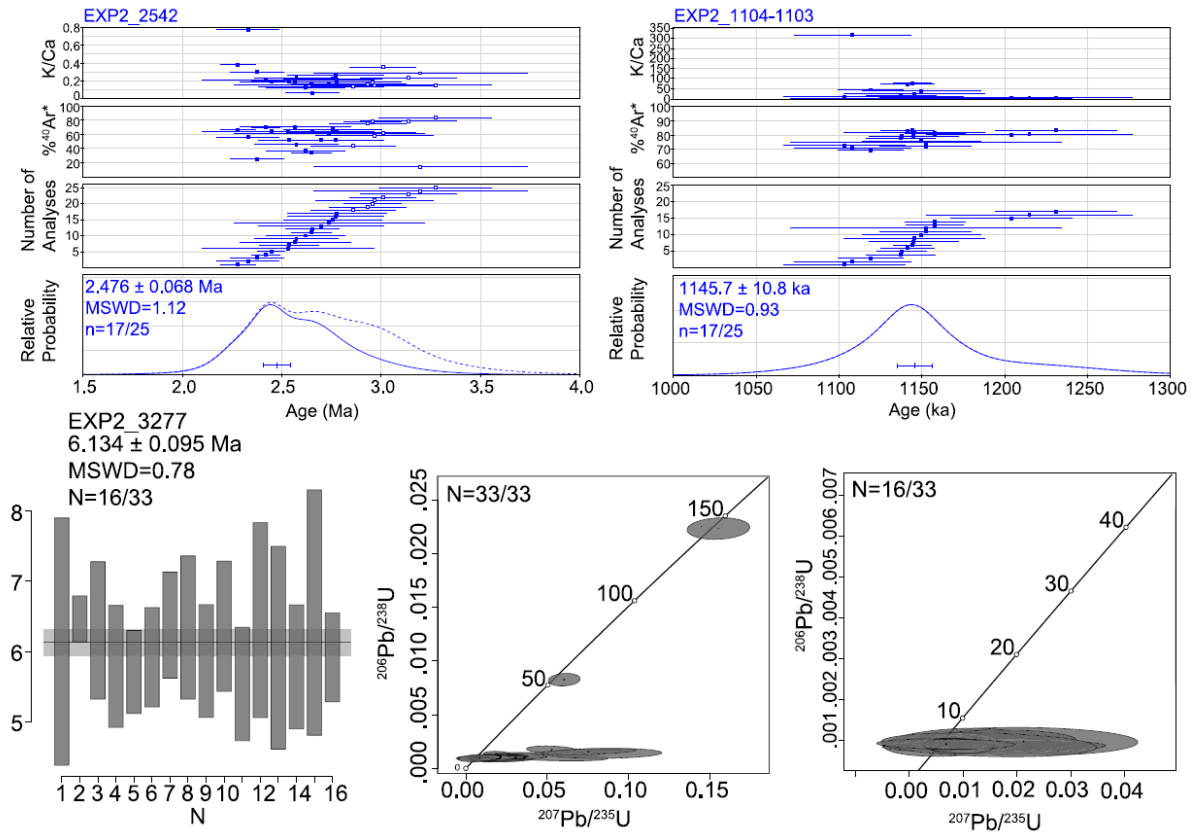

Figure 3. Age calculation from volcanic ashes. From top right to bottom left: 40Ar-39Ar results for samples EXP2_1104–1103 and EXP2_2542 showing KCa, % 40Ar, number of analyses, and relative probability by age, including those analyses that were used in the age calculation; weighted mean average age calculation for sample EXP2_3277; and U-Pb results shown as concordia plots. MSWD—mean square of weighted deviates.

Thin Sections

Thin section billets were cut and made into oriented standard-sized 30-µm-thick sections using a 600 mesh grit by Quality Thin Sections (Tucson, Arizona). No stains were applied. Thin sections were imaged using a Zeiss Axio M2M microscope (Fig. 4) and an optical microscope to assess the degree of alteration of lake carbonates.

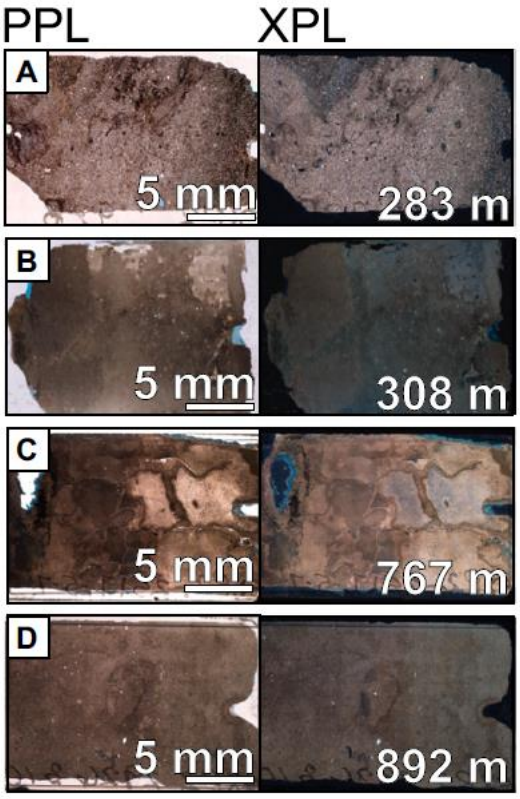

Figure 4. Photomicrographs of select lacustrine carbonate intervals from the EXP2 core in plane-polarized light (PPL) and cross-polarized light (XPL) showing rare mixed clastic-carbonate intervals (A, D) and micritic texture with limited porosity (B–D). Scale bar (5 mm) is displayed on PPL image, and core depth in meters is displayed on XPL image.

Age-Depth Model

The hydroclimate interpretation for Clayton Valley relied significantly on the time evolution of oxygen and carbon isotopes along with the sedimentology of the core. We constructed a *rbacon* (Blaauw and Christen, 2011) age-depth model (Fig. 2) and assigned mean ages to all samples based on the five 40Ar/39Ar ages that spanned the stable isotope data set (Table S1). We chose to not include the U-Pb age in the model because the sample depth was so far beneath the lacustrine sequence where all our stable isotope measurements were made. We modeled the top of the core to be Holocene in age, 5 ± 5 ka. Since our isotope record did not extend into the alluvial-fan deposits, we chose to cut off our age model at the interface between these coarse deposits and

the silt deposits to avoid extrapolating over major changes in lithology. We used the "slump" command in *rbacon* to account for geologically instantaneous deposition of the Bishop Tuff and other ash layers. Additionally, in the Supplemental Material, we present the age model using the "slump" command in *rbacon* for each of the halite deposits, which we believe were deposited more rapidly than the overlying and underlying fine clays.

Stable Isotope Analyses

In total, 285 carbonate samples from EXP2 were measured for δ18O and δ13C. The stable isotope measurements were made on one of three instruments: Thermo Finnigan MAT 252 with a Kiel III at Brown University, Thermo Finnigan MAT 253 + with a Kiel IV at Brown University, or a Thermo Finnigan Deltaplus XL with a gas bench at Stanford University (Table S2), with replication across laboratories and mass spectrometers. Carbonate stable isotope values are reported using standard δ notation relative to the Vienna Peedee belemnite (VPDB) standard.

The samples that were analyzed at Brown University were first dried overnight at 60 °C and then homogenized via mortar and pestle. Of the sample, 500 µg aliquots were weighed out and reacted with 70 °C phosphoric acid using a Thermo Finnigan Kiel III or Kiel IV carbonate device. This measured weight was based on a typical 10% sample carbonate content and the required 50 µg of CaCO3 for the desired range of measurement voltage (3–6 V). The evolved CO_2 was measured on either a Thermo Finnigan MAT 252 gas-ratio mass spectrometer or Thermo Finnigan MAT 253+ (Table S2). External precision (1σ) of oxygen and carbon isotope data was <0.1‰, based upon repeated measurements of two internal laboratory standards, BYM63150 and Carrara63150, calibrated against NBS 18, NBS 19, and IAEA 603.

The samples that were analyzed at Stanford University in 2018 were homogenized via mortar and pestle. Stable carbon and oxygen isotope values of carbonates were obtained at the

Stable Isotope Biogeochemistry Laboratory, Stanford University, using a Thermo Finnigan GasBench and measured on a Finnigan MAT Delta + XL mass spectrometer using a Thermo Finnigan ConFlo III unit. Approximately 300 µg aliquots of sample powder were weighed into sealed vials that were flushed with helium gas and reacted with ~0.25 mL of phosphoric acid (H3PO4) for 1 h at 72 °C. External precision (1σ) of oxygen and carbon isotope data was <0.1‰, based upon repeated measurements of two internal laboratory standards calibrated against NBS 18, NBS 19, and LSVEC.

We calculated a running correlation coefficient (*R*) for the entire δ18O and δ13C record using the *movcorr* function in MATLAB. This function calculates a running *R* value for a moving window of data points. For our record, we used a 5 point moving window and plotted the resulting *R* value in Figure 5.

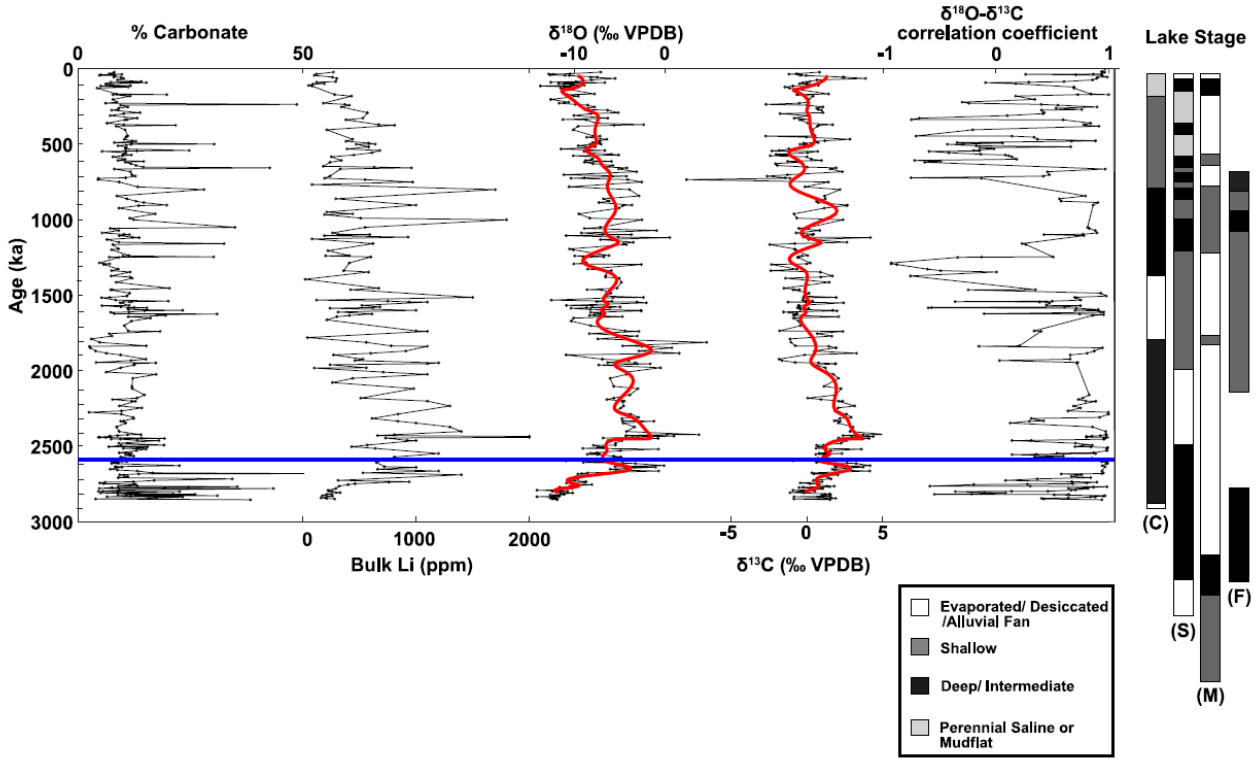

Figure 5. Time series from the Clayton Valley EXP2 core. From left to right: percent carbonate; bulk sediment lithium concentrations (ppm); carbonate δ 18O (‰, Vienna

Peedee belemnite [VPDB]); carbonate δ13C (‰, VPDB); running correlation coefficient between oxygen and carbon isotopes with a moving window of 10 data points; lake stage for Clayton Valley (C) compared to neighboring valleys (S—Searles Lake, M—Lake Manly, F—Fish Lake Valley), adapted after Knott et al. (2019). Solid red lines are a low-pass filtered curve on the carbonate δ18O and δ13C records. Blue horizontal line marks the Pliocene-Pleistocene boundary (2588 ka).

Precipitation Back-Trajectory Analyses

To understand the influence of seasonality and moisture source on our oxygen isotope record, we modeled the moisture source trajectories entering Clayton Valley and paired these with modern water oxygen isotopes. Back-trajectories were generated using the desktop version of the Hybrid Single-Particle Lagrangian Integrated Trajectory (HYSPLIT) model and the North American Regional Reanalysis (NARR) as the HYSPLIT meteorological input. We tracked air parcels backward for 72 h every 24 h at 1500 m above ground level to gauge the precipitation sources for each of the study sites. Daily 72 h back-trajectories began at the end of the day and were generated for every day between 1979 and 2019, which covered the extent of the NARR climate record.

In order to filter trajectories by precipitation events, we used weather station data in the Global Historical Climatology Network-Daily (GHCN-D) database, keeping both geographic location and elevation as close as possible. The station record from Silver Peak, Nevada (within Clayton Valley), recorded historic snow and rain events throughout 1979–2019, both of which were considered in our precipitation analyses. For each site, trajectories were matched with the corresponding day in the meteorological record and filtered based on whether there was any rain or snow for that day. Days that were missing both a rain and snow record were not included in the analyses. The resulting precipitation trajectories were then filtered by summer (April–September) and winter (October–March) half-year months.

Once the precipitation-carrying trajectories were filtered, a cluster analysis was completed for each site's summer and winter trajectories using HYSPLIT's built-in clustering program. The number of clusters in each analysis was determined by the change in total spatial variance (TSV) curve generated as clusters were combined. The point at which the fewest number of clusters had a change in TSV less than ~15% was selected for the analysis. The trajectories in each cluster were then averaged and plotted on a map with a topographic overlay. Finally, we weighted the cluster means by total precipitation delivered. The thicknesses of the lines on Figure 6 are scaled to this weighting.

A similar set of HYSPLIT analyses (without clustering) was conducted for weekly precipitation samples from the NV00 site at Red Rock Canyon (36.13483°N, 115.422°W, 1137 m) from the United States Networks for Isotopes in Precipitation (USNIP) network (Welker, 2012), the closest site to Clayton Valley. Figure 6A shows daily trajectories for all days with precipitation colored by the oxygen isotope value of the weekly aggregated rainfall. This station recorded data spanning May 1989 to December 1994, with 29 total weeks of isotope data.

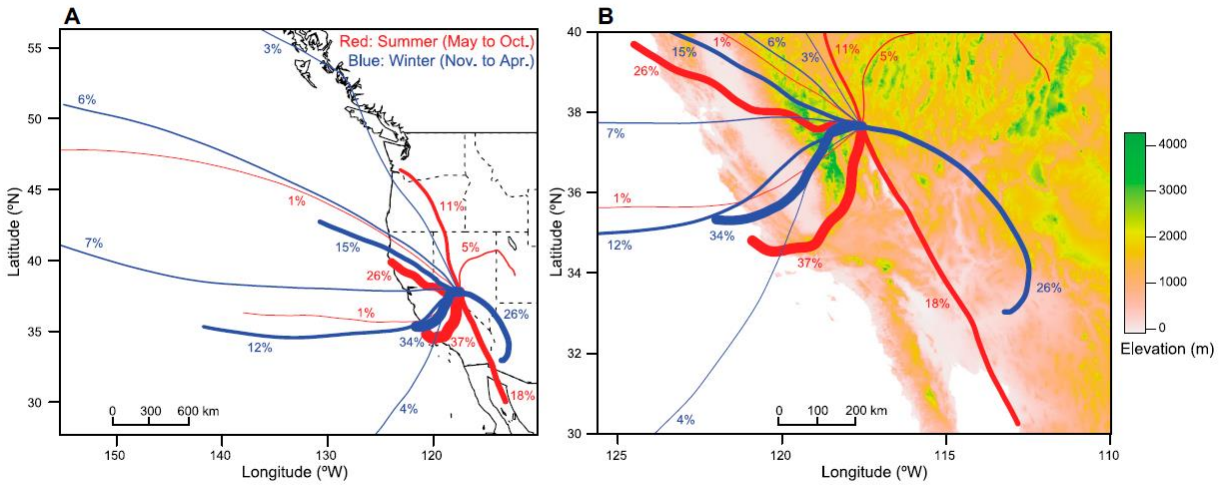

Figure 6. (A) Average winter (blue) and summer (red) 3 d air mass back-trajectories for Clayton Valley weighted by precipitation. (B) Same as A but zoomed in with elevation contoured.

Results and Discussion

New Ash Ages

In previous work, Coffey et al. (2021) dated six ashes from the EXP cores using 40Ar/39Ar methods on sanidine. In this work, we present two additional 40Ar/39Ar ages and one zircon U-Pb age to refine the age model for EXP2. Sample EXP2_1103–1104 was collected at 336.35 m depth. A weighted mean average age of 1145.7 ± 10.8 ka (MSWD = 0.93) was calculated from 17 of 25 dated sanidine crystals (Fig. 3). Sample EXP2_2542 was collected at 774.8 m depth. A weighted mean average age of 2.476 ± 0.068 Ma (MSWD = 1.12) was calculated from 17 of 25 dated plagioclase crystals (Fig. 3). We present a new U-Pb zircon age from an ash at 998.8 m depth in the EXP2 core, sample EXP2_3277. The youngest coherent population of 16 of the 33 dated zircons was selected to calculate a weighted mean average age of 6.134 ± 0.095 Ma (Fig. 3). The remaining 16 zircon ages defined older age populations (interpreted to be inherited zircon crystals) or were filtered out with our discordance filters (see the Materials and Methods section). We note here that the U-Pb age matches a K-Ar age on a rhyolite flow that is well exposed in the Silver Peak range to the east (Robinson et al., 1988).

Age-Depth Model

The age-depth model for EXP2 is relatively linear, with a larger uncertainty near the base of the lacustrine sequence (Fig. 2). The model only extends to the top of the alluvial-fan deposits (~896.7 m), since we had very little age control into these coarser units. We suspected some change in sedimentation rate across this boundary and therefore did not feel justified in extrapolating the above sedimentation rate into the base of the core. All lacustrine samples were assigned mean *rbacon* ages (Table S2). The bottommost silt/clay deposits overlying the basal alluvial-fan deposits

were modeled to be 2900 ka, while the topmost sample was ca. 20 ka. This age for the bottom of the lacustrine sequence makes sense, considering that there are thick, slightly older tephra deposits in Fish Lake Valley that do not appear in EXP2 (Reheis, 1991, 1992; Reheis et al., 1993; Sarna-Wojcicki et al., 2005).

We suspect that the halite deposits were laid down at a faster rate than the clay deposits in a drying environment, which would shift the ages below the halite section but above the ashes dated below the halite section to be slightly younger. To get a minimum age estimate on our samples due to varied sedimentation rate, we explored the effects of modeling the halite beds as slumps. We found that the bottommost silt/clay deposits became 2850 ka with the added slumps, which is within error of the model run used to assign ages.

Depositional System in Clayton Valley

The stratigraphic succession of the EXP2 core is typical of an underfilled to balance-filled lake in an extensional basin setting (e.g., Carroll and Bohacs, 1999; Ingersoll, 2019). Assuming no hiatuses, the sedimentation rate appears to be relatively linear throughout, with the possibility of some variance toward the bottom of the core, where we have little age control and clays transition to coarser-grained material.

Based on the sedimentology, we describe the depositional system. Starting ca. 2900 ka, Clayton Valley episodically held a deep lake, which is evident from the thick green laminated lacustrine muds that persisted intermittently until the late Pleistocene, with the youngest lacustrine muds deposited ca. 20 ka. The base of the record begins at 2900 ka as a deep lake. Thick halite beds abruptly punctuate the lacustrine deposits in the interval between 1750 and 1380 ka. These halite beds likely represent rapid changes in the moisture balance for the Clayton Valley area. We interpret this period of time to be a perennial saline/mudflat environment. This change in the

moisture budget is also supported by a notable decrease in the degree of weathering, which persists until increasing again around 800 ka (Fig. S2). Around 780 ka, the record transitions from a deep lake to a shallow lake environment. Circa 60 ka, the sediments coarsen upward in the section, signifying a gradual transition from a long-standing lake to a more arid playa environment, consistent with no significant LGM lake above the playa being present in this basin (Reheis, 1999a). The uppermost coarse-grained sediments in EXP2 are more difficult to interpret, due to the poor core recovery, so it is unclear when the playa lake became permanently desiccated; we infer this transition to have occurred ca. 23 ka, which corresponds to the youngest carbonate sample recovered. Further, in the neighboring valley to the west, Fish Lake Valley, there is no evidence for a large LGM (ca. 21 ka) lake. Pluvial Lake Rennie existed in Fish Lake Valley from 2.0 Ma until after 0.77 Ma, when Lake Rennie was either contiguous with or overflowed into a lake to the north in Columbus Salt Marsh. Subsequently, Lake Rennie was dry or maintained very low levels from 0.5 Ma to the present (Reheis et al., 1993; Kurth et al., 2011).

Stable Isotope Results

The δ18O values range from −14.1‰ to +4.6‰ (Fig. 5). The δ13C values range from −8.0‰ to +5.4‰ (Fig. 5; Table S2). The running correlation coefficient between δ13C and δ18O shows a strong positive correlation for much of the time series, confirming the interpretation that the basin was closed and terminal throughout its existence (Li and Ku, 1997; Leng and Marshall, 2004). The running standard deviation of δ18O from 2 Ma to 20 ka increases by a factor of 2 relative to the pre–2 Ma samples (Fig. S2). This is likely related to the onset of Northern Hemisphere glaciation and the intensification of glacial-interglacial cycles during the Pleistocene. There is also a gradual positive shift of ∼10‰ in the oxygen isotopes from the base of the core to

around 2 Ma (Fig. 5). From 2 Ma to ca. 20 ka, there is a long-term decreasing trend in the oxygen isotopes of ~10‰.

There are three hypotheses that may explain the long-term trend we observe from the late Pliocene to present. First, Quaternary uplift in the White Mountains and Sierra Nevada and subsequent blocking of winter moisture derived from the west of Clayton Valley could have led to further depletion of source δ18O via orographic effects (Lechler and Galewsky, 2013; Mix et al., 2019; Hildreth et al., 2022). Second, changes in precipitation seasonality from summer precipitation to winter precipitation could have driven source water δ18O toward progressively depleted values. For example, this would entail the addition of moisture from a more northerly source during colder glacial periods rather than the central Pacific Ocean (Oster et al., 2020; discussed further below). Both changes in orographic rainout due to topographic changes or changes in seasonality would primarily influence the light end members in the observed oxygen isotope time series. Last, a gradual decrease in temperature through the Pleistocene and subsequent reduction in the effective evaporation could also have led to a more depleted lake-water composition (i.e., more overall P – E). This effect would influence the declining average and the range in the observed oxygen isotope time series. Because of the evaporative nature of lacustrine carbonate oxygen isotope records, we cannot necessarily rule out any of these scenarios with existing data. However, as described in the next section, data from adjacent basins with differential evaporation suggest that further orographic rainout can be ruled out (first scenario above associated with Quaternary uplift of the White Mountains and Sierra Nevada). Further, we can rule out an additional alternate scenario where changes in carbonate formation temperature (i.e., lake-water temperature) influenced our observations. Long-term cooling (third scenario) would cause an increase, not a decrease, in the carbonate δ18O values toward the present because of a larger

fractionation factor between lake water and carbonate at decreasing temperatures (Kim and O'Neil, 1997).

Comparison to Regional Records

There are multiple records of pluvial lakes in the region surrounding Clayton Valley ranging in age from the late Pliocene to the late Pleistocene. These records indicate a different regional moisture balance for this area of the Great Basin relative to today. The lake stages shown on Figure 5, adapted from Knott et al. (2019), show the interpreted lake stages for Clayton Valley and nearby lakes. Pluvial lakes in Death Valley (Lake Manly; Lowenstein et al., 1999; Forester et al., 2005; Knott et al., 2018), to the south in Searles Valley (Smith, 1983; Jannik et al., 1991; Knott et al., 2018), and in Eureka Valley (Lake Andrei) began to form ca. 3.5–3.4 Ma in the late Pliocene during the cooler, wetter, glacial climate of marine isotope stage MG5 (Knott et al., 2019). The Death Valley lake persisted until ca. 3.30 Ma, while the Searles lake persisted through the start of Northern Hemisphere glaciation until ca. 2.5 Ma. Lake Andrei was very short-lived, existing for only around 400,000 yr (Knott et. al, 2019). Evidence from Fish Lake Valley suggests a lake existed from ca. 3.4 to 2.8 Ma (Reheis et al., 1993, 2002; Knott et al., 2018). Lakes in these areas also existed intermittently during the Pleistocene. Pluvial lakes in Death Valley formed again ca. 1.98–1.78 Ma, 1.3–1.0 Ma, and ca. 0.6 Ma, while Searles Lake existed from ca. 2 Ma to the late Pleistocene. Fish Lake Valley episodically sustained a lake in the middle Pleistocene ca. 2.2–0.7 Ma. A lake was also present in Owens Valley ca. 0.8 Ma to the late Pleistocene (Smith et al., 1997) and also ca. 2.6–2.0 Ma, as recorded in the Waucobi lake beds (Sarna-Wojcicki et al., 2005; DeMasi, 2013).

Modern back-trajectory analyses for Clayton Valley show the area receiving different sources of water vapor depending on the season (Fig. 3). Winter parcels have a more northwesterly

origin, tend to originate from more distant sources, and usually pass over the southern Sierra Nevada and White Mountains. Summer trajectories originate from southerly areas, such as the Gulf of California, and divert around the high relief to the west. Modern meteoric water δ18O is also shown to have different compositions depending on the season (Fig. 7).

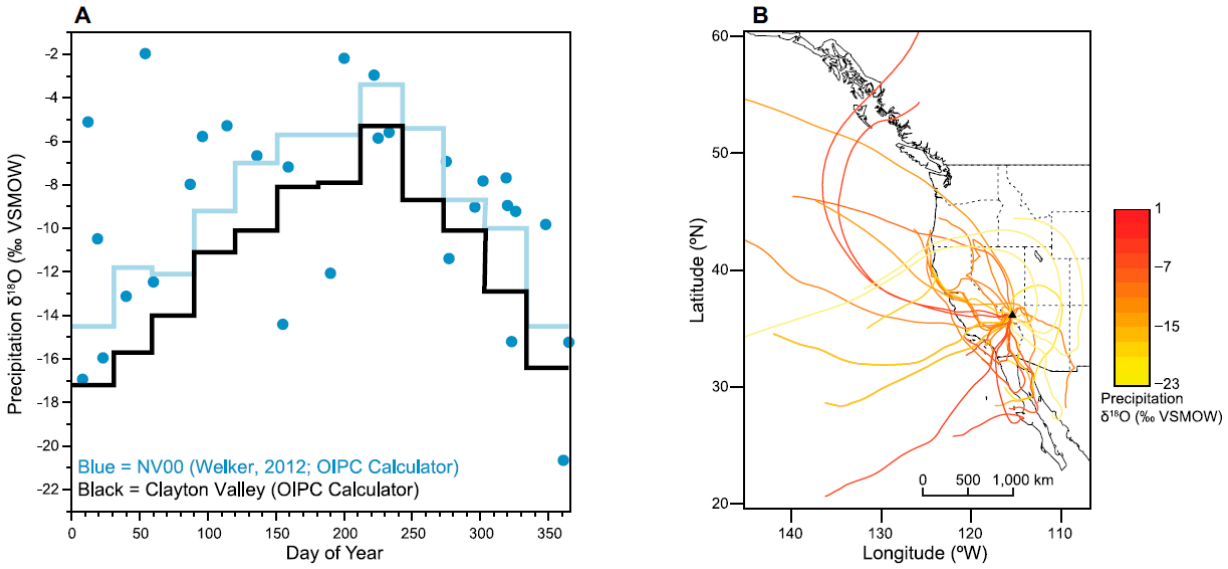

Figure 7. (A) Measured (dots) vs. calculated (solid lines) precipitation δ18O (‰, Vienna standard mean ocean water [VSMOW]) throughout the year for Clayton Valley (black) and Las Vegas, Nevada (light blue). Calculations were made using the Oxygen Isotope Precipitation Calculator (OIPC; Welker, 2000; Bowen and Revenaugh, 2003; Bowen, 2022). (B) Annual average 3 d air mass back-trajectories for Las Vegas weighted by precipitation. Colors indicate modern precipitation isotope values (Welker, 2012) recorded in Las Vegas, Nevada.

We interpret the lightest δ18O values at a given time slice in our record to represent meteoric water values (e.g., Rowley and Currie, 2006; Caves et al., 2017). Different seasonal source signals could impact the source water composition of the lake in Clayton Valley, directly impacting the light δ18O end member of our record. Therefore, we argue that the majority of the variance in the isotope record for Clayton Valley was controlled by changes in seasonality and subsequent evaporative enrichment. Specifically, through the latest Pliocene, there are more

summertime precipitation events characterized by high δ18O values, likely related to an enhancement of the convergent monsoonal circulation (Bhattacharya et al., 2022). Through the Pleistocene, we observe a very gradual decrease in light δ18O end-member values, which we attribute to the weakening of monsoonal circulation and strengthened southwesterly moisture delivery of wintertime precipitation. Our interpretation of the light δ18O end member is subject to uncertainty because it is difficult to disentangle changes in the meteoric water composition relative to changes in evaporation. As such, future work analyzing the leaf wax δD from Clayton Valley may help to isolate the meteoric signal.

Stable isotope evidence from the neighboring Fish Lake Valley (Figs. 1 and 8) demonstrates a different water balance than Clayton Valley, which complicates our interpretation that source changes are responsible for the long-term trends in δ18O. If both records were dominated by source changes, the δ18O would have a consistent slight offset between them, since they are geographically proximal. Further, lake stage transitions between basins were asynchronous as well, suggesting a different water balance between basins. We explored the possibility that these asynchronous changes in lake stage could have been linked to uplift in the White Mountains and Sierra Nevada west of Fish Lake Valley. Blocking of westerly moisture (Mix et al., 2019) could potentially have led to Fish Lake Valley drying prior to Clayton Valley (Reheis et al., 1993), which is why a shallow lake is observed for Clayton Valley after Fish Lake Valley desiccated (by ca. 0.6 Ma). In this case, we would expect to see progressively more depletion in oxygen isotopes as moisture moved eastward encountering subsequent orographic rainout, into Fish Lake Valley and then into Clayton Valley. The oxygen isotope record generated for Fish Lake Valley (this study; Mix et al., 2019) discredits this hypothesis, as the lightest end-member values of δ18O in Fish Lake Valley are more depleted than those in Clayton Valley (Fig. 8). Further, ca. 0.7–0.6 Ma

coincides with the integration of Fish Lake Valley and the Columbus Salt Marsh (Reheis et al., 1993), which suggests that changes in basin hydrology—not climate or tectonics—may have been responsible for asynchronous changes in lake stage between the neighboring valleys.

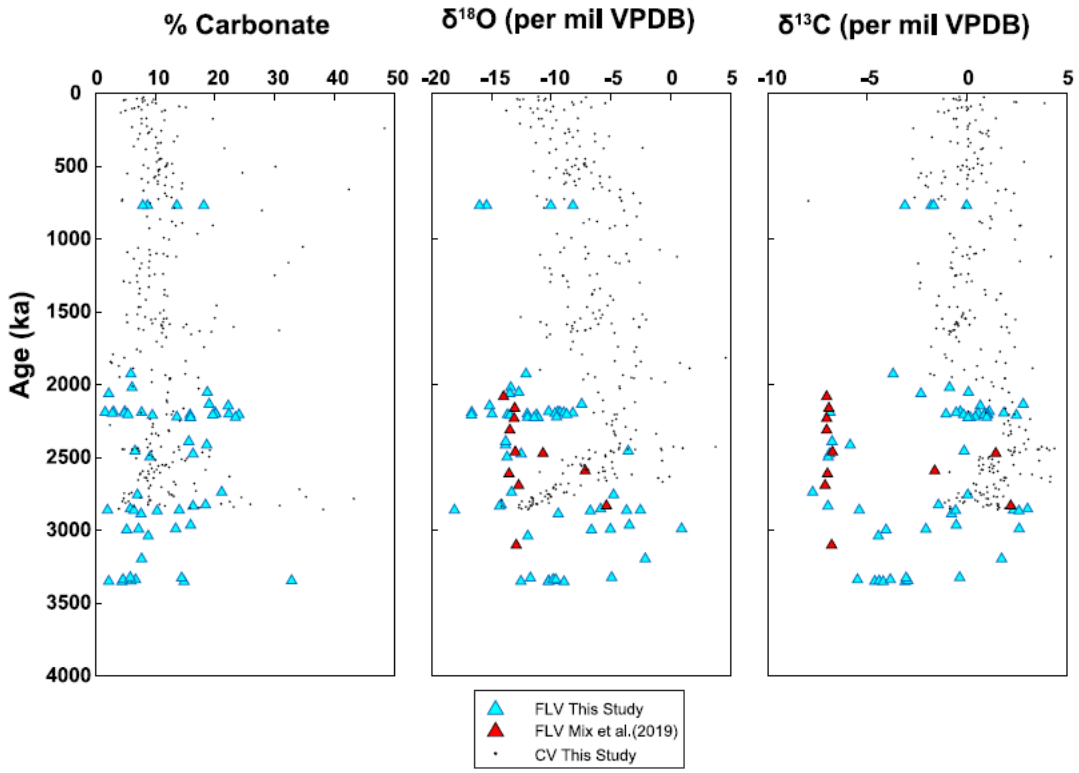

Figure 8. Stable isotopes of Clayton Valley carbonates (CV; black) compared to neighboring Fish Lake Valley (FLV). Fish Lake Valley samples from this study (in blue) were collected in the summer of 2021. Red samples were taken from Mix et al. (2019). VPDB—Vienna Peedee belemnite.

Hydroclimate Controls on Lithium Enrichment

The lithium concentrations in the clays are one to two orders of magnitude greater than those of the average continental crust (Fig. 5), 35 ± 11 ppm (Teng et al., 2004). There is no statistically significant correlation between lithium and sediment age. However, there is a distinct positive logarithmic correlation ($R2$ = 0.56) between the paired measurements of lithium concentrations and carbonate δ18O (Fig. 9A).

We drew from Coffey et al. (2021) for the conceptual model for lithium brine development in basins like Clayton Valley. Geothermal fluids rich in lithium interact with the basin sediment. For example, results from Araoka et al. (2014) indicate that the lithium concentrated in playas in Nevada was supplied mainly through high-temperature water-rock interaction associated with local geothermal activity and not directly by low-temperature weathering of surface materials. However, over long periods of time, water-rock interaction in the Clayton Valley aquifer allows lithium and other solutes to accumulate in pore spaces. These high-solute pore waters over time move from high-pressure (deeper) to lower-pressure (shallower) zones in the aquifer as part of the brine-forming process. Basin clays can form with or adsorb lithium until groundwater liberates the lithium into the shallow subsurface waters. The lithium then becomes concentrated in the shallow subsurface brines through evapoconcentration. The findings of this study bear on the initial lithium enrichment of the basin sediments and link them to the hydroclimate evolution of the basin and lake system over the Pliocene–Pleistocene.

We argue that our new observations showing a covariance between the authigenic carbonate $\delta^{18}O$ in the lacustrine clays and the bulk lithium concentrations (Fig. 9) are related to the degree of evapoconcentration of the lake during authigenic clay and carbonate precipitation in the lake water. Variations in the past surface area to volume ratio of the lake could have had an impact on the degree of effective evapoconcentration of the lake water. For example, early in the record (ca. 2.9 to ca. 1.8 ka), as indicated by the CIA values and sedimentology (Fig. S2), P – E was relatively large, the lake was deep, and the surface area to volume ratio of the lake was likely smaller. This deep lake persisted until the onset of halite deposition. The climate then transitioned ca. 1.8 ka to a lower P – E value, the lake became smaller, and it was frequently desiccated. Due to the higher surface area to volume ratio of the shallower lake, there was highly effective evapo-

ration that concentrated lithium in the lake. We propose that the lithium was then incorporated into the structure and adsorbed onto the surfaces of the authigenic clays precipitating in the lake water. Additionally, a survey of brine samples (Fig. 9B) from the basin demonstrated a similar logarithmic relationship between water δ18O and brine lithium concentrations (this study; Coffey et al., 2021) compared to the geologic EXP2 samples shown in Figure 9A.

We infer that evaporation played a dominant role in the concentration of lithium in both the brine and clay deposits; however, ongoing work will better clarify the lithium mass balance of the basin. While surface weathering of volcanic rocks may have contributed lithium to the lake, these fluxes were likely small across the topographic watershed. We speculate that a combination of groundwater with long transport pathways draining from neighboring landscapes (Brooks et al., 2014; Underdown et al., 2017), surface weathering, and hot springs in the north, west, and south parts of the basin (deposits observed by Coffey et al., 2021) contributed lithium into the lake in Clayton Valley. Very high lithium concentrations (thousands of parts per million) are reported in lacustrine clay deposits recently explored in the Tonopah basin (Loveday and Turner, 2020) to the northeast of Clayton Valley. This region is hydraulically up gradient of Clayton Valley; therefore, we hypothesize that some of the lithium was transported by interbasin groundwaters (e.g., Corenthal et al., 2016).

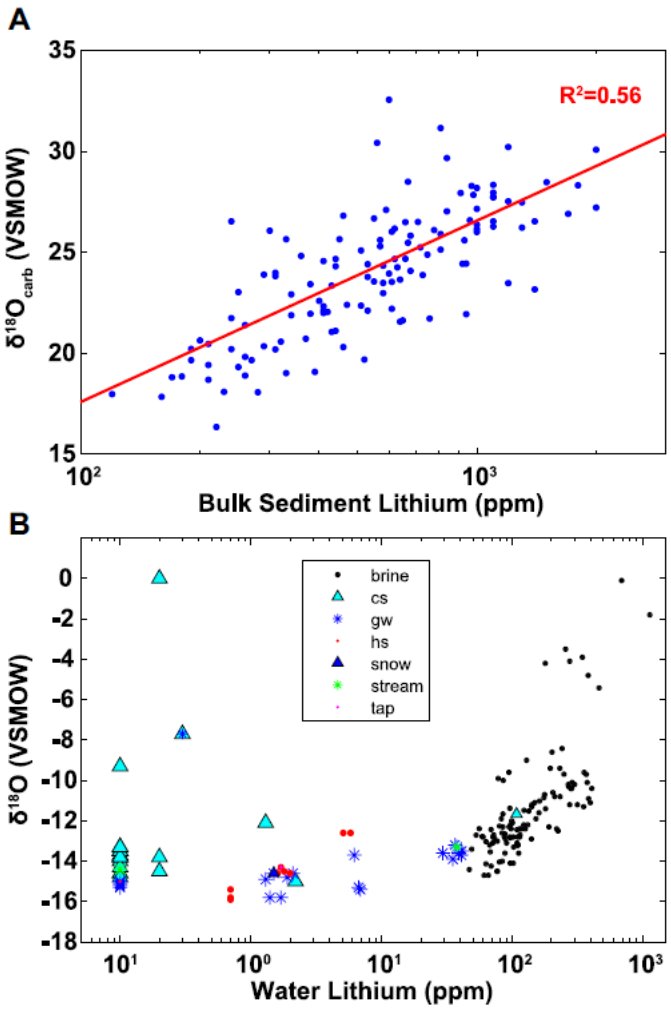

Figure 9. (A) Bulk sediment lithium concentrations (ppm) for EXP2 samples paired with carbonate oxygen isotope values (‰, Vienna standard mean ocean water [VSMOW]). Red line is a logarithmic fit with an R2 value of 0.56. (B) Lithium (ppm) and oxygen isotope values (‰, VSMOW) of natural water samples taken around Clayton Valley, where cs—cold spring water, hs—hot spring water, and gw—groundwater.

Primary versus Secondary Mineralization

Did the lithium become incorporated into the clays after deposition due to geothermal interactions, or did the clays incorporate the lithium during initial genesis in the lake water (Kunasz and Hummer, 1974; Davis, 1981; Morissette, 2012; Coffey et al., 2021)? Our paleoclimate and lithium-enrichment conceptual model interpretations rely on the assumption that most of the bulk

sediment carbonates and clays are primary authigenic minerals. We based this assumption on: (1) qualitative analysis of thin section images, and (2) prior X-ray diffraction work conducted by Morissette (2012) and Coffey et al. (2021).

Four thin sections taken at 283 m, 308 m, 767 m, and 892 m (Fig. 4) support our assumption that the carbonate minerals within the sediments are primarily authigenic. The carbonate minerals within all four thin sections have a homogeneous micritic texture within an even beige to gray-green clay matrix. There appear to be no dissolution features, rimming cements, or stylolitic features present in any of the images, which are all features that would likely be present if the sediments had experienced significant postdepositional alteration. The 308 m and 767 m thin sections have some lighter-beige features due to uneven sample thickness on the thin section mount (Figs. 4B and 4C). Further sedimentologic work is currently ongoing.

Previous mineralogic work suggests the clay minerals also may be authigenic. Substantial lithium deposits tend to be found within three different clay mineral types—smectite, illite, and montmorillonite (Morissette, 2012; Castor and Henry, 2020; Li et al., 2021; Coffey et al., 2021). Coffey et al. (2021) claimed that the bulk sediments could be hectorite, which contains lithium in the octahedral layer of trioctahedral smectite in place of Mg or more loosely held in the interlayer sites. Hectorite is thought to form in several ways: (1) precipitation in alkaline lake deposits (Starkey, 1982; Calvo et al., 1995); (2) alteration of volcanic glass under hydrothermal and low temperatures; and (3) incorporation of lithium into preexisting smectite (Starkey, 1982; Kloprogge et al., 1999; Coffey et al., 2021). We argue that mechanism 1 was the dominant mechanism for lithium enrichment at this site based on prior interpretations and thin section work presented in this study. Locally, where volcanic ash was deposited into the lake, there was likely some alteration of the ash to release solutes including lithium, but this would introduce lithium to the lake at

punctuated times, and the alteration would be confined to areas near the ash layers. Davis (1981) hypothesized that the hectorite was precipitated from lake waters or pore fluids during early burial diagenesis in the Clayton Valley basin. The case for authigenic hectorite is further supported by the leach experiments performed by Coffey et al. (2021), which indicated that a large fraction of the lithium is contained in more difficult-to-dissolve silicate structures rather than on the more-exchangeable interlayer surfaces of the clays. Ongoing work will shed light on the conditions for clay and carbonate formation—whether authigenic precipitation or hydrothermal alteration of existing smectites—and ultimately refine our understanding of the lithium-brine system in Clayton Valley as a whole.

Based on the evidence above and the covariance between δ18O and lithium concentrations (Fig. 9A), we infer that the bulk of lithium enrichment occurred at the time of clay mineralization in equilibrium with the lake water, and not postdepositionally. Future work analyzing the oxygen, hydrogen, and lithium isotopes of clay fractions from EXP2 may demonstrate this link more concretely.

Conclusion

In this work, we (1) presented a 2.9 m.y. Great Basin paleoclimate record and (2) investigated the mechanisms behind the enrichment of lithium in clays. The lacustrine carbonate isotope record for Clayton Valley revealed a rich continuous history of hydroclimate spanning the last ∼2.9 m.y. We argue that although the lake sustained high overall isotope values due to evaporative enrichment, million-year scale variations were driven by changes in the seasonality of precipitation being transported to the basin as well as changes in P − E. Specifically, we argue that the late Pliocene to early Pleistocene saw enhanced convergent monsoonal circulation, and,

through the middle to late Pleistocene, strengthened southwesterly moisture delivery could have resulted in greater wintertime precipitation. In addition to the climate record, we found a covariance between carbonate oxygen isotopes and paired bulk lithium concentrations. We attribute this covariance to the effects of evapoconcentration prior to authigenic clay precipitation in the lake water. This finding suggests that climate may play a key role in the concentration of lithium in authigenic lacustrine clays in terminal basins containing pluvial lake systems. Understanding the climate-driven or other mechanisms responsible for the formation of lithium-rich clay and brine deposits will assist in future economic exploration efforts.

Acknowledgements

This work was partially supported by National Science Foundation (NSF) / Geological Society of America (GSA) Graduate Student Geoscience grant 13087-21 to C.A. Gagnon, which was funded by NSF grant 1949901, and funding from the Miller Institute at the University of California, Berkeley to D.E. Ibarra. T. Bhattacharya was supported by NSF P2C2 grant OCE-1903148. D.E. Ibarra and C. Gagnon were partially supported by P2C2 grant AGS-2102901. We greatly appreciate the Albemarle Corporation for providing access to Clayton Valley drill cores. We would like to thank Steven Clemens for assistance with the carbonate stable isotope measurements; Brian Jicha for Ar/Ar analyses; Hari Mix and Michele Bezanson for help with field work; and Sylvia Dee and Jim Russell for discussions and assistance with HYSPLIT analyses.

References

Annan, J.D., and Hargreaves, J.C., 2013, A new global reconstruction of temperature changes at the Last Glacial Maximum: Climate of the Past, v. 9, p. 367–376, https://doi .org /10 .5194 /cp-9-367-2013.

Araoka, D., Kawahata, H., Takagi, T., Watanabe, Y., Nishimura, K., and Nishio, Y., 2014, Lithium and strontium isotopic systematics in playas in Nevada, USA: Constraints on the origin of

lithium: Mineralium Deposita, v. 49, p. 371–379, https://doi .org /10 .1007 /s00126-013-0495-y.

Bhattacharya, T., Tierney, J.E., and DiNezio, P., 2017, Glacial reduction of the North American monsoon via surface cooling and atmospheric ventilation: Geophysical Research Letters, v. 44, p. 5113–5122, https://doi .org /10 .1002 /2017GL073632.

Bhattacharya, T., Feng, R., Tierney, J., Rubbelke, C., Burls, N.J., Knapp, S., and Fu, M.J., 2022, Expansion and intensification of the North American monsoon during the Pliocene: American Geophysical Union Advances, v. 3, no. 6, https://doi .org /10 .1029 /2022AV000757.

Blaauw, M., and Christen, J.A., 2011, Flexible paleoclimate age-depth models using an autoregressive gamma process: Bayesian Analysis, v. 6, no. 3, p. 457–474, https://doi .org /10 .1214 /ba /1339616472.

Bowen, G.J., 2022, The Online Isotopes in Precipitation Calculator, Version 3.1: http://www .waterisotopes .org (January 2022).

Bowen, G.J., and Revenaugh, J., 2003, Interpolating the isotopic composition of modern meteoric precipitation: Water Resources Research, v. 39, no. 10, 1299, https://doi .org /10 .1029 /2003WR002086.

Bradley, D.C., Munk, L., Jochens, H., Hynek, S., and Labay, K., 2013, A Preliminary Deposit Model for Lithium Brines: U.S. Geological Survey Open-File Report 2013-1006, 6 p., https://doi .org /10 .3133 /ofr20131006.

Brooks, L.E., Masbruch, M.D., Sweetkind, D.S., and Buto, S.G., 2014, Steady-State Numerical Groundwater Flow Model of the Great Basin Carbonate and Alluvial Aquifer System: U.S. Geological Survey Scientific Investigations Report 2014-5213, 124 p., https://doi .org /10 .3133 /sir20145213.

Burke, K.D., Williams, J.W., Chandler, M.A., Haywood, A.M., Lunt, D.J., and Otto-Bliesner, B.L., 2018, Pliocene and Eocene provide best analogs for near-future climates: Proceedings of the National Academy of Sciences of the United States of America, v. 115, p. 13,288–13,293, https://doi .org /10 .1073 /pnas .1809600115.

Burls, N.J., and Fedorov, A.V., 2017, Wetter subtropics in a warmer world: Contrasting past and future hydrological cycles: Proceedings of the National Academy of Sciences of the United States of America, v. 114, p. 12,888–12,893, https://doi .org /10 .1073 /pnas .1703421114.

Burrus, J.B., 2013, Structural and Stratigraphic Evolution of the Weepah Hills Area, NV: Transition from Basin-and- Range Extension to Miocene Core Complex Formation [M.S. thesis]: Austin, Texas, University of Texas at Austin, 104 p.

Calvo, J.P., Blanc-Valleron, M.M., Rodrígues-Arandía, J.P., Rouchy, J.M., and Sanz, M.E., 1995, Authigenic clay minerals in continental evaporitic environments, *in* Thiry, M., and Simon-Coinçon, R., eds., Palaeoweathering, Palaeosurfaces and Related Continental Deposits: New York, Wiley, p. 129–151, https://doi .org /10 .1002 /9781444304190 .ch5.

Carroll, A.R., and Bohacs, K.M., 1999, Stratigraphic classification of ancient lakes: Balancing tectonic and climatic controls: Geology, v. 27, p. 99–102, https://doi .org /10 .1130 /0091-7613(1999)027<0099:SCOALB>2 .3.CO;2.

Castor, S.B., and Henry, C.D., 2020, Lithium-rich claystone in the McDermitt caldera, Nevada, USA: Geologic, mineralogical, and geochemical characteristics and possible origin: Minerals (Basel), v. 10, p. 68, https://doi .org /10 .3390 /min10010068.

Caves, J.K., Ritch, A.J., Ibarra, D.E., Chamberlain, C.P., Bayshashov, B.U., Zhamangara, A., Sjostrom, D.J., Mix, H.T., and Winnick, M.J., 2017, Late Miocene uplift of the Tian Shan and Altai and reorganization of Central Asia climate: GSA Today, v. 27, no. 2, p. 20–26, https://doi .org /10 .1130 /GSATG305A .1.

Clark, P.U., Dyke, A.S., Shakun, J.D., Carlson, A.E., Clark, J., Wohlfarth, B., Mitrovica, J.X., Hostetler, S.W., and McCabe, A.M., 2009, The Last Glacial Maximum: Science, v. 325, p. 710–714, https://doi .org /10 .1126 /science .1172873.

Coffey, D.M., Munk, L.A., Ibarra, D.E., Butler, K.L., Boutt, D.F., and Jenckes, J., 2021, Lithium storage and release from lacustrine sediments: Implications for lithium enrichment and sustainability in continental brines: Geochemistry, Geophysics, Geosystems, v. 22, https://doi .org /10 .1029 /2021GC009916.

Corenthal, L.G., Boutt, D.F., Hynek, S.A., and Munk, L.A., 2016, Regional groundwater flow and accumulation of a massive evaporite deposit at the margin of the Chilean Altiplano: Geophysical Research Letters, v. 43, no. 15, p. 8017–8025, https://doi .org /10 .1002 /2016GL070076.

Davis, J.R., 1981, Late Cenozoic Geology of Clayton Valley, Nevada, and the Genesis of a Lithium-Enriched Brine [Ph.D. dissertation]: Austin, Texas, University of Texas Austin, 283 p.

Davis, J.R., Friedman, I., and Gleason, J.D., 1986, Origin of the lithium-rich brine, Clayton Valley, Nevada, *in* Peterman, Z.E., and Schnabel, D.C., eds., Shorter Contributions to Isotope Research: U.S. Geological Survey Bulletin 1622, p. 131–138, https://doi .org /10 .3133 /b1622.

De Masi, C.L., 2013, Ancient Sedimentary Fill of the Waucobi Lake Beds as an Archive of Owens Valley, California, Tectonics and Climate [M.S. thesis]: Long Beach, California, California State University, Long Beach, 93 p.

Dowsett, H.J., and Caballero Gill, R.P., 2010, Pliocene climate: Stratigraphy, v. 7, p. 106–110.

Forester, R.M., Lowenstein, T.K., and Spencer, R.J., 2005, An ostracode based paleolimnologic and paleohydrologic history of Death Valley: 200 to 0 ka: Geological Society of America Bulletin, v. 117, p. 1379–1386, https://doi .org /10 .1130 /B25637 .1.

Fu, M., Cane, M.A., Molnar, P., and Tziperman, E., 2022, Warmer Pliocene upwelling site SST leads to wetter subtropical coastal areas: A positive feedback on SST: Paleoceanography and Paleoclimatology, v. 37, https://doi .org /10 .1029 /2021PA004357.

Godsey, H.S., Oviatt, C.G., Miller, D.M., and Chan, M.A., 2011, Stratigraphy and chronology of offshore to nearshore deposits associated with the Provo shoreline, Pleistocene Lake

Bonneville, Utah: Palaeogeography, Palaeoclimatology, Palaeoecology, v. 310, p. 442–450, https://doi .org /10 .1016 /j .palaeo .2011 .08 .005.

Haywood, A.M., et al., 2020, The Pliocene Model Intercomparison Project Phase 2: Large-scale climate features and climate sensitivity: Climate of the Past, v. 16, p. 2095–2123, https://doi .org /10 .5194 /cp-16-2095-2020.

Hildreth, W., Fierstein, J., Phillips, F.M., and Calvert, A., 2022, Trachyandesite of Kennedy Table, its vent complex, and post–9.3 Ma uplift of the central Sierra Nevada: Geological Society of America Bulletin, v. 134, no. 5–6, p. 1143–1159, https://doi .org /10 .1130 /B36125 .1.

Ibarra, D.E., Egger, A.E., Weaver, K.L., Harris, C.R., and Maher, K., 2014, Rise and fall of late Pleistocene pluvial lakes in response to reduced evaporation and precipitation: Evidence from Lake Surprise, California: Geological Society of America Bulletin, v. 126, p. 1387–1415, https://doi .org /10 .1130 /B31014 .1.

Ibarra, D.E., Oster, J.L., Winnick, M.J., Caves Rugenstein, J.K., Byrne, M.P., and Chamberlain, C.P., 2018, Warm and cold wet states in the western United States during the Pliocene–Pleistocene: Geology, v. 46, p. 355–358, https://doi .org /10 .1130 /G39962 .1.

Ingersoll, R.V., 2019, Subduction-related sedimentary basins of the U.S. Cordillera, *in* Miall, A., ed., The Sedimentary Basins of the United States and Canada: Amsterdam, Netherlands, Elsevier, p. 477–510, https://doi .org /10 .1016 /B978-0-444-63895-3 .00011-5.

IOfS, ISO, 2017, ISO/IEC 17025 General requirements for the competence of testing and calibration laboratories (ISO manual): ABNT, https://www .iso .org /publication /PUB100424 .html.

Jannik, N.O., Phillips, F.M., Smith, G.I., and Elmore, D., 1991, A 36Cl chronology of lacustrine sedimentation in the Pleistocene Owens River system: Geological Society of America Bulletin, v. 103, p. 1146–1159, https://doi .org /10 .1130 /0016-7606(1991)103<1146: ACCOLS>2 .3.CO;2.

Jicha, B.R., Singer, B.S., and Sobol, P., 2016, Re-evaluation of the ages of 40Ar/39Ar sanidine standards and supereruptions in the western US using a Noblesse multi-collector mass spectrometer: Chemical Geology, v. 431, p. 54–66, https://doi .org /10 .1016 /j .chemgeo .2016 .03 .024.

Kim, S.T., and O'Neil, J.R., 1997, Equilibrium and nonequilibrium oxygen isotope effects in synthetic carbonates: Geochimica et Cosmochimica Acta, v. 61, p. 3461–3475, https://doi .org /10 .1016 /S0016-7037(97)00169-5.

Kloprogge, J.T., Komarneni, S., and Amonette, J.E., 1999, Synthesis of smectite clay minerals: A critical review: Clays and Clay Minerals, v. 47, no. 5, p. 529–554, https://doi .org /10 .1346 /CCMN .1999 .0470501.

Knott, J.R., et al., 2018, Late Neogene–Quaternary tephrochronology, stratigraphy, and paleoclimate of Death Valley, California, USA: Geological Society of America Bulletin, v. 130, p. 1231–1255, https://doi .org /10 .1130 /B31690 .1.

Knott, J.R., Wan, E., Deino, A.L., Casteel, M., Reheis, M.C., Phillips, F.M., Walkup, L., McCarty, K., Manoukian, D.N., and Nunez, E., 2019, Lake Andrei: A Pliocene pluvial lake in Eureka

Valley, eastern California, *in* Starratt, S., and Rosen, M.R., eds., From Saline to Freshwater: The Diversity of Western Lakes in Space and Time: Geological Society of America Special Paper 536, p. 125–142, https://doi .org /10 .1130 /2018 .2536(08).

Kunasz, I.A., and Hummer, D.G., 1974, Lithium occurrence in the brines of Clayton Valley, Esmeralda County, Nevada, *in* Coogan, A.G., ed., Proceedings of the Fourth Symposium on Salt: Cleveland, Ohio, Northern Ohio Geological Society, v. 166, p. 57–78, https://doi .org /10 .1093 /mnras /166 .1.57.

Kurth, G., Phillips, F.M., Reheis, M.C., Redwine, J.L., and Paces, J.B., 2011, Cosmogenic nuclide and uranium-series dating of old, high shorelines in the western Great Basin, USA: Geological Society of America Bulletin, v. 123, p. 744–768, https://doi .org /10 .1130 /B30010 .1.

Lechler, A.R., and Galewsky, J., 2013, Refining paleoaltimetry reconstructions of the Sierra Nevada, California, using air parcel trajectories: Geology, v. 41, no. 2, p. 259–262, https://doi .org /10 .1130 /G33553 .1.

Lee, J.Y., Marti, K., Severinghaus, J.P., Kawamura, K., Yoo, H.S., Lee, J.B., and Kim, J.S., 2006, A redetermination of the isotopic abundances of atmospheric Ar: Geochimica et Cosmochimica Acta, v. 70, no. 17, p. 4507–4512, https://doi .org /10 .1016 /j .gca .2006 .06 .1563.

Lee, J.-Y., et al., 2021, Future global climate: Scenario-based projections and near-term information, *in* Masson-Delmotte, V., et al., eds., Climate Change 2021: The Physical Science Basis, Contribution of Working Group I to the Sixth Assessment Report of the Intergovernmental Panel on Climate Change: Cambridge, UK, Cambridge University Press, p. 553–672.

Lehner, B., and Grill, G., 2013, Global river hydrography and network routing: Baseline data and new approaches to study the world's large river systems: Hydrological Processes, v. 27, p. 2171–2186, https://doi .org /10 .1002 /hyp .9740.

Leng, M.J., and Marshall, J.D., 2004, Palaeoclimate interpretation of stable isotope data from lake sediment archives: Quaternary Science Reviews, v. 23, p. 811–831, https://doi .org /10 .1016 /j .quascirev .2003 .06 .012.

Li, C., Li, Z., Wu, T., Luo, Y., Zhao, J., Li, X., Yang, W., and Chen, X., 2021, Metallogenic characteristics and formation mechanism of Naomugeng clay-type lithium deposit in central inner Mongolia, China: Minerals (Basel), v. 11, no. 3, https://doi .org /10 .3390 /min11030238.

Li, H.C., and Ku, T.L., 1997, δ13C–δ18C covariance as a paleohydrological indicator for closed-basin lakes: Palaeogeography, Palaeoclimatology, Palaeoecology, v. 133, p. 69–80, https://doi .org /10 .1016 /S0031 -0182(96)00153-8.

Lora, J.M., and Ibarra, D.E., 2019, The North American hydrologic cycle through the last deglaciation: Quaternary Science Reviews, v. 226, https://doi .org /10 .1016 /j .quascirev .2019 .105991.

Loveday, D., and Turner, A., 2020, NI43–101 American Lithium TLC Lithium Property, Nevada, USA: Edmonton, Alberta, Canada, Stantec Consulting Ltd., Technical Report for American Lithium Corporation, 105 p.

Lowenstein, T.K., Li, J., Brown, C., Roberts, S.M., Ku, T.L., Luo, S., and Yang, W., 1999, 200 ky paleoclimate record from Death Valley salt core: Geology, v. 27, p. 3–6, https://doi .org /10 .1130 /0091-7613(1999)027<0003:KYPRFD>2 .3.CO;2.

Manthiram, A., 2017, An outlook on lithium ion battery technology: ACS Central Science, v. 3, no. 10, p. 1063–1069, https://doi .org /10 .1021 /acscentsci .7b00288.

Matsubara, Y., and Howard, A.D., 2009, A spatially explicit model of runoff, evaporation, and lake extent: Application to modern and late Pleistocene lakes in the Great Basin region, western United States: Water Resources Research, v. 45, https://doi .org /10 .1029 /2007WR005953.

Means, J.D., 2013, GPS precipitable water as a diagnostic of the North American monsoon in California and Nevada: Journal of Climate, v. 26, p. 1432–1444, https://doi .org /10 .1175 /JCLI-D-12-00185 .1.

Mifflin, M.D., and Wheat, M.M., 1979, Pluvial Lakes and Estimated Pluvial Climates of Nevada: Nevada Bureau of Mines and Geology Bulletin 94, 57 p.

Min, K., Mundil, R., Renne, P.R., and Ludwig, K.R., 2000, A test for systematic errors in 40Ar/39Ar geochronology through comparison with U/Pb analysis of a 1.1-Ga rhyolite: Geochimica et Cosmochimica Acta, v. 64, no. 1, p. 73–98, https://doi .org /10 .1016 /S0016 -7037(99)00204-5.

Mix, H.T., Rugenstein, J.K.C., Reilly, S.P., Ritch, A.J., Winnick, M.J., Kukla, T., and Chamberlain, C.P., 2019, Atmospheric flow deflection in the late Cenozoic Sierra Nevada: Earth and Planetary Science Letters, v. 518, p. 76–85, https://doi .org /10 .1016 /j .epsl .2019 .04 .050.

Molnar, P., and Cane, M.A., 2002, El Niño's tropical climate and teleconnections as a blueprint for pre–Ice Age climates: Paleoceanography, v. 17, no. 2, p. 11-1–11-11, https://doi .org /10 .1029 /2001PA000663.

Morissette, C.L., 2012, The Impact of Geological Environment on the Lithium Concentration and Structural Composition of Hectorite Clays: Reno, Nevada, University of Nevada, Reno, 259 p.

Munk, L., and Chamberlain, C.P., 2011, Final Technical Report: G10AP00056—Lithium Brine Resources: A Predictive Exploration Model: U.S. Geological Survey, 16 p., https://www .usgs .gov /media /files /mrerp-report -g10ap00056.

Munk, L., Jennings, M., Bradley, D., Hynek, S., Godfrey, L., and Jochens, H., 2011, Geochemistry of lithium-rich brines in Clayton Valley, Nevada, USA, *in* Barra, F., Reich, M., Campos, Eduardo, and Tornos, F., eds., Proceedings of the 11th Society for Geology Applied to Mineral Deposits Biennial Meeting, Antofagasta, Chile: Antofagasta, Chile, Ediciones Universidad Católica del Norte, p. 26–29, https://e-sga .org /nc /publications /sga-biennial-meetings-abstract-volumes /2011-antofagasta/.

Munk, L.A., Hynek, S.A., Bradley, D., Boutt, D., Labay, K., and Jochens, H., 2016, Lithium brines: A global perspective: Reviews in Economic Geology, v. 18, p. 339–365, https://doi .org /10 .5382 /Rev .18 .14.

Munroe, J.S., and Laabs, B.J., 2013, Latest Pleistocene history of pluvial Lake Franklin, northeastern Nevada, USA: Geological Society of America Bulletin, v. 125, p. 322–342, https://doi .org /10 .1130 /B30696 .1.

Oldow, J.S., Elias, E.A., Ferranti, L., McClelland, W.C., McIntosh, W.C., and Cashman, P.H., 2009, Late Miocene to Pliocene synextensional deposition in fault-bounded basins within the upper plate of the western Silver Peak–Lone Mountain extensional complex, west-central Nevada, *in* Oldow, J.S., and Cashman, P.H., eds., Late Cenozoic Structure and Evolution of the Great Basin–Sierra Nevada Transition: Geological Society of America Special Paper 47, p. 275–312, https://doi .org /10 .1130 /2009 .2447(14).

Orme, A.R., 2008, Pleistocene pluvial lakes of the American West: A short history of research, *in* Grapes, R.H., Oldroyd, D., and Grigelis, A., eds., History of Geomorphology and Quaternary Geology: Geological Society, London, Special Publication 301, p. 51–78, https://doi .org /10 .1144 /SP301 .4.

Oster, J.L., and Ibarra, D.E., 2018, Glacial Hydroclimate of Western North America: Insights from Proxy-Model Comparison and Implications for Lake Bonneville: Utah Geological Survey Miscellaneous Publication 170, 8 p.

Oster, J.L., Weisman, I.E., and Sharp, W.D., 2020, Multi-proxy stalagmite records from northern California reveal dynamic patterns of regional hydroclimate over the last glacial cycle: Quaternary Science Reviews, v. 241, https://doi .org /10 .1016 /j .quascirev .2020 .106411.

Paton, C., Hellstrom, J., Paul, B., Woodhead, J., and Hergt, J., 2011, Iolite: Freeware for the visualisation and processing of mass spectrometric data: Journal of Analytical Atomic Spectrometry, v. 26, p. 2508–2518, https://doi .org /10 .1039 /C1JA10172B.

Pound, M.J., Tindall, J., Pickering, S.J., Haywood, A.M., Dowsett, H.J., and Salzmann, U., 2014, Late Pliocene lakes and soils: A global data set for the analysis of climate feedbacks in a warmer world: Climate of the Past, v. 10, p. 167–180, https://doi .org /10 .5194 /cp-10 -167-2014.

Ravelo, A.C., Andreasen, D.H., Lyle, M., Olivarez Lyle, A., and Wara, M.W., 2004, Regional climate shifts caused by gradual global cooling in the Pliocene Epoch: Nature, v. 429, p. 263–267, https://doi .org /10 .1038 /nature02567.

Ray, A.J., Garfin, G.M., Wilder, M., Vásquez-León, M., Lenart, M., and Comrie, A.C., 2007, Applications of monsoon research: Opportunities to inform decision making and reduce regional vulnerability: Journal of Climate, v. 20, p. 1608–1627, https://doi .org /10 .1175 /JCLI4098 .1.

Reheis, M.C., 1992, Geologic Map of Late Cenozoic Deposits and Faults in Parts of the Soldier Pass and Magruder Mountain 15′ Quadrangles, Inyo and Mono Counties, California, and Esmeralda County, Nevada: U.S. Geological Survey Miscellaneous Investigations Series Map I-2268, scale 1:24,000, https://doi .org /10 .3133 /i2268.

Reheis, M.C., 1999a, Highest pluvial-lake shorelines and Pleistocene climate of the western Great Basin: Quaternary Research, v. 52, p. 196–205, https://doi .org /10 .1006 /qres .1999 .2064.

Reheis, M.C., 1999b, Extent of Pleistocene Lakes in the Western Great Basin: U.S. Geological Survey Miscellaneous Field Studies Map MF-2323, scale 1:800,000, 1 sheet, https://doi .org /10 .3133 /mf2323.

Reheis, M.C., Sarna-Wojcicki, A.M., Burbank, D.M., and Meyer, C.E., 1991, The late Cenozoic section at Willow Wash, west-central California—a tephrochronologic rosetta stone: Late Cenozoic stratigraphy and tectonics of Fish Lake Valley, Nevada and California: U.S. Geological Survey Open-File Report (United States), v. 91, no. 290, p. 46–66.

Reheis, M.C., Slate, J.L., Sarna-Wojcicki, A.M., and Meyer, C.E., 1993, A late Pliocene to middle Pleistocene pluvial lake in Fish Lake Valley, Nevada and California: Geological Society of America Bulletin, v. 105, p. 953–967, https://doi .org /10 .1130 /0016-7606(1993)105<0953:ALPTMP>2 .3.CO;2.

Reheis, M.C., Sarna-Wojcicki, A.M., Reynolds, R.L., Repenning, C.A., and Mifflen, M.D., 2002, Pliocene to middle Pleistocene lakes in the western Great Basin: Ages and connections, *in* Hershler, R., Currey, D., and Madsen, D., eds., Great Basin Aquatic Systems History: Smithsonian Contributions to the Earth Sciences 33, p. 53–108, https://doi .org /10 .5479 /si .00810274 .33 .1.

Reheis, M.C., Adams, K.D., Oviatt, C.G., and Bacon, S.N., 2014, Pluvial lakes in the Great Basin of the western United States—a view from the outcrop: Quaternary Science Reviews, v. 97, p. 33–57, https://doi .org /10 .1016 /j .quascirev .2014 .04 .012.

Robinson, P.T., McKee, E.H., and Moiola, R.J., 1988, Cenozoic volcanism and sedimentation, Silver Peak region, western Nevada and adjacent California, *in* Coats, R.R., Hay, R.L., and Anderson, C.A., eds., Studies in Volcanology: Geological Society of America Memoir 116, p. 577–611, https://doi .org /10 .1130 /MEM116-p577.

Rowley, D.B., and Currie, B.S., 2006, Palaeoaltimetry of the late Eocene to Miocene Lunpola basin, central Tibet: Nature, v. 439, p. 677–681, https://doi .org /10 .1038 /nature04506.

Rush, F.E., 1968, Water-Resources Appraisal of Clayton Valley–Stonewall Flat Area, Nevada and California: Carson City, Nevada, State of Nevada Department of Conservation and Natural Resources, 54 p.

Salzmann, U., Williams, M., Haywood, A.M., Johnson, A.L., Kender, S., and Zalasiewicz, J., 2011, Climate and environment of a Pliocene warm world: Palaeogeography, Palaeoclimatology, Palaeoecology, v. 309, p. 1–8, https://doi .org /10 .1016 /j .palaeo .2011 .05 .044.

Santi, L.M., Arnold, A.J., Ibarra, D.E., Whicker, C.A., Mering, J.A., Lomarda, R.B., Lora, J.M., and Tripati, A., 2020, Clumped isotope constraints on changes in latest Pleistocene hydroclimate in the northwestern Great Basin: Lake Surprise, California: Geological Society of America Bulletin, v. 132, p. 2669–2683, https://doi .org /10 .1130 /B35484 .1.

Sarna-Wojcicki, A.M., Reheis, M.C., Pringle, M.S., Fleck, R.J., Burbank, D., Meyer, C.E., Slate, J.L., Wan, E., Budahn, J.R., Troxel, B., and Walker, J.P., 2005, Tephra Layers of Blind Spring Valley and Related Upper Pliocene and Pleistocene Tephra Layers, California,

Nevada, and Utah—Isotopic Ages, Correlation, and Magnetostratigraphy: U.S. Geological Survey Professional Paper 1701, 63 p., https://doi .org /10 .3133 /pp1701.

Smith, G.I., 1983, Core KM-3, a Surface-To-Bedrock Record of Late Cenozoic Sedimentation in Searles Valley, California: U.S. Geological Survey Professional Paper 1256, 24 p., https://doi .org /10 .3133 /pp1256.

Smith, G.I., Bishchoff, J.L., and Bradbury, J.P., 1997, Synthesis of the paleoclimatic record from Owens Lake core OL-92, *in* Smith, G.I., and Bishchoff, J.L., eds., An 800,000-Year Paleoclimatic Record from Core OL-92: Geological Society of America Special Paper 317, p. 143–160, https://doi .org /10 .1130 /0-8137-2317-5 .143.

Soller, D.R., Reheis, M.C., Garrity, C.P., and Van Sistine, D.R., 2009, Map database for surficial materials in the conterminous United States: U.S. Geological Survey Data Series 425, scale 1:5,000,000, https://pubs .usgs .gov /ds /425/.

Starkey, H.C., 1982, The Role of Clays in Fixing Lithium: U.S. Geological Survey Bulletin 1278-F, 8 p., https://pubs .usgs .gov /bul /1278f /report .pdf.

Stein, A.F., Draxler, R.R., Rolph, G.D., Stunder, B.J., Cohen, M.D., and Ngan, F., 2015, NOAA's HYSPLIT atmospheric transport and dispersion modeling system: Bulletin of the American Meteorological Society, v. 96, p. 2059–2077, https://doi .org /10 .1175 /BAMS-D-14-00110 .1.

Teng, F.Z., McDonough, W.F., Rudnick, R.L., Dalpé, C., Tomascak, P.B., Chappell, B.W., and Gao, S., 2004, Lithium isotopic composition and concentration of the upper continental crust: Geochimica et Cosmochimica Acta, v. 68, p. 4167–4178, https://doi .org /10 .1016 /j .gca .2004 .03 .031.

Underdown, C.G., Boutt, D.F., Hynek, S.A., and Munk, L.A., 2017, Evaluating hydrologic transience in watershed delineation, numerical modeling and solute transport in the Great Basin, Clayton Valley, Nevada: New Orleans, Louisiana, American Geophysical Union, Fall Meeting supplement, abstract H53O-08.

Vermeesch, P., 2018, IsoplotR: A free and open toolbox for geochronology: Geoscience Frontiers, v. 9, no. 5, p. 1479–1493, https://doi .org /10 .1016 /j .gsf .2018 .04 .001.

Warner, M.S., 2018, Introduction to PySPLIT: A Python toolkit for NOAA ARL's HYSPLIT model: Computing in Science & Engineering, v. 20, p. 47–62, https://doi .org /10 .1109 /MCSE .2017 .3301549.

Welker, J.M., 2000, Isotopic (δ18O) characteristics of weekly precipitation collected across the USA: An initial analysis with application to water source studies: Hydrological Processes, v. 14, p. 1449–1464, https://doi .org /10 .1002 /1099-1085(20000615)14:8<1449:: AID-HYP993>3 .0.CO;2-7.

Welker, J.M., 2012, ENSO effects on δ18O, δ2H and d-excess values in precipitation across the U.S. using a high-density, long-term network (USNIP): Rapid Communications in Mass Spectrometry, v. 26, p. 1893–1898, https://doi .org /10 .1002 /rcm .6298.

Chapter 2 Supplementary Material

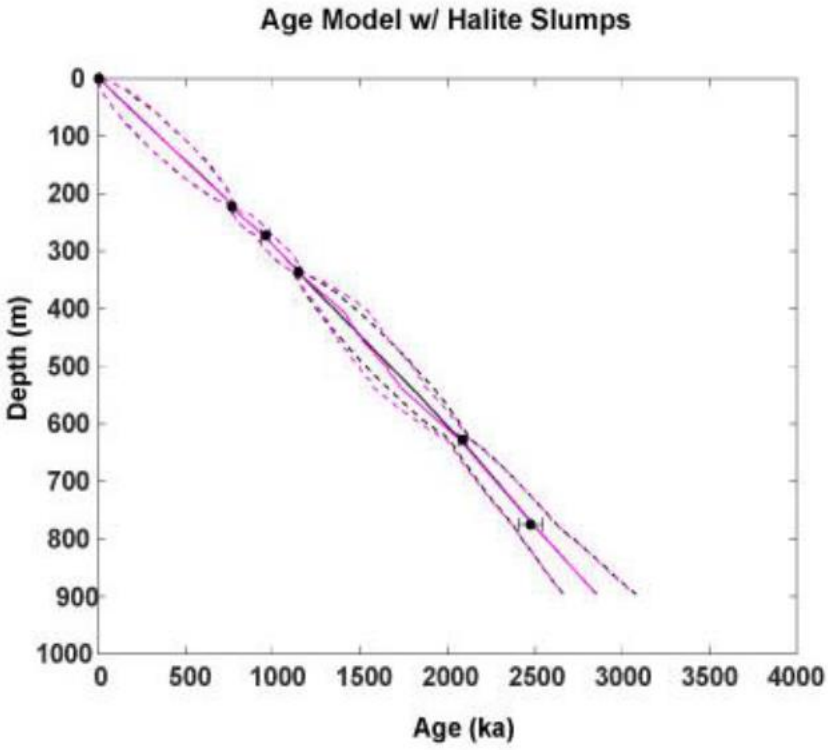

Figure S1. Bacon age-depth model using ash slumps only (black) and added halite slumps (magenta). Age control points are the same as Fig 1.

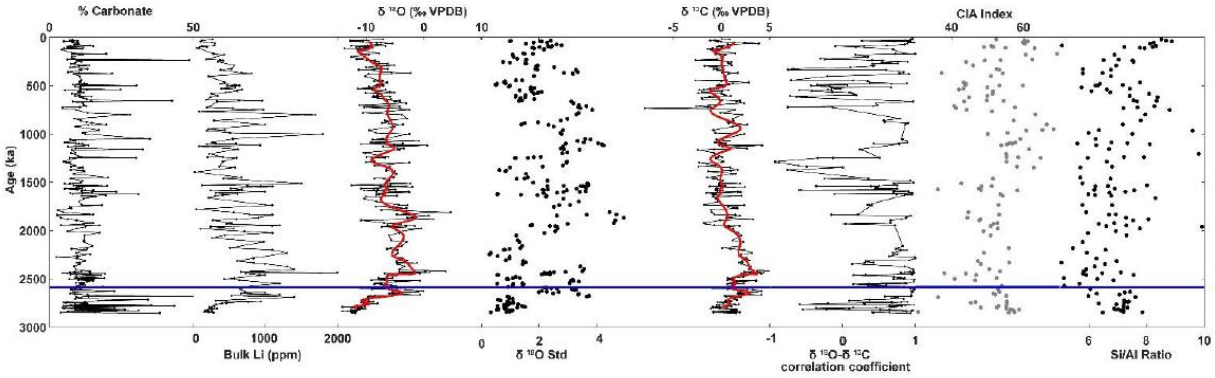

Figure S2. Full time series from Clayton Valley EXP2. From left to right: percent carbonate; bulk sediment lithium concentrations (ppm); carbonate $\delta^{18}O$ (‰ VPDB); 5 point running carbonate $\delta^{18}O$ standard deviation; carbonate $\delta^{13}C$ (‰ VPDB); correlation coefficient between oxygen and carbon isotopes with a moving window of 10 data points; chemical index

of alteration; and Si/Al ratio. Solid red lines are a low pass filtered curve on the carbonate $\delta^{18}O$ and $\delta^{13}C$ records.

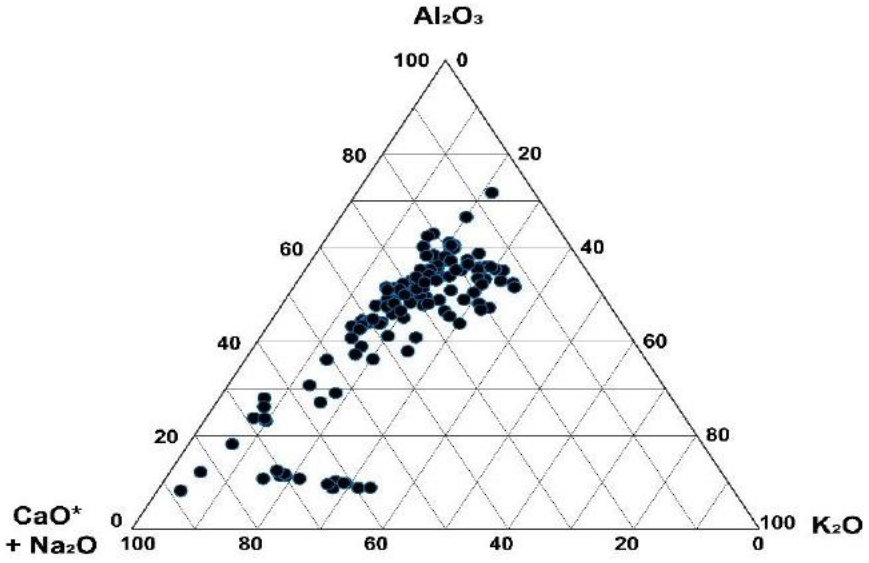

Figure S3. Ternary diagram for all clay samples with available data, showing the relative mole fractions of CaO+Na2O, K2O, and Al2O3.

Weathering Indices

The results of the CIA calculations are summarized in Figure S2 and shown in the time series in Figure S3. There does not appear to be a distinction between the lithologies in terms of the CIA values, with most plotting close to the Ca/Na and Al endmembers. There are, however, distinct shifts in the CIA value time series (Figure S3). From the base of the core, the CIA values stay below 40 until they reach the top of the halite beds where they then increase their weathered CIA value to ~60. The weathering indices stay high until the base of the thick ash at ~750 ka where they drop to below 40. From the base of the ash to the top of the core the CIA values then increase gradually. We also plot Si/Al on Figure S3, which shows similar trends.

CHAPTER 3

Determination of KGa-1b and SHCa-1 $\Delta'^{17}O$ and $\delta^{18}O$ via Laser Fluorination of Lithium Fluoride Clay Pellets

Catherine A. Gagnon[1,2], Riley Havel[1], Jiquan Chen[1,3], Gavin Piccione[1,2], Daniel E. Ibarra[1,2]

1 Department of Earth, Environmental and Planetary Science
2 Institute at Brown for Environment and Society
Brown University
Providence, Rhode Island, 02912

3 School of Earth Sciences and Resources
China University of Geosciences (Beijing)
Beijing, China

Abstract

Rationale: Stable oxygen isotope measurements in silicate clays, such as smectite and kaolinite, provide crucial information for understanding Earth's climate history and environmental changes. Despite a growing interest in the oxygen isotope analysis of silicate clays and clay-rich sediments, there lacks a consensus on the preparation and standardization of clay mineral samples. To improve the accuracy and interlaboratory comparisons of clay isotope measurements, especially those involving laser fluorination techniques, newly established kaolinite and smectite oxygen isotope standards are much needed.

*Methods***:** We employed conventional nickel bomb fluorination combined with dual-inlet isotope ratio mass spectrometry to establish precise δ18O and Δ′17O values for leached clay reference materials KGa-1b and SHCa-1, a kaolinite and a hectorite/smectite, respectively. We further measured leached KGa-1b and SHCa-1 pressed into pellets with a lithium fluoride as a binding agent for the laser fluorination method, allowing us to test the reproducibility between methods and utilize a standard laser chamber drift correction scheme.

Results: The laser fluorination technique yielded highly precise and reproducible δ18O and Δ′17O measurements for the KGa-1b and SHCa-1, aligning with bomb values of δ18O. This confirms the method's reliability and comparability to conventional isotope measurement techniques while also stressing the importance of proper sample preparation and laser chamber drift corrections.

Conclusions: This study demonstrates that laser fluorination is an effective method for accurately measuring the stable oxygen isotope composition of silicate clays or clay-rich sediments when corrected with known silicate clay standards. These methods offer a valuable methodology

for future research and applications that will significantly improve our understanding of past climate and environmental conditions.

1. Introduction

The stable oxygen isotope ratio ($\delta^{18}O$) of geological materials has been used to understand Earth's system processes for decades [1-3]. Applications include reconstructing climatological changes in temperature [4-6], regional water balance [7-10], global ice [11, 12], and the determination of ore formation conditions [13-18]. Silicate clays like smectite or kaolinite are particularly useful for understanding regional weathering processes and water balance since these processes are closely tied to their formation in soils and fluvio-lacustrine settings [19-32]. Further, the oxygen isotope composition of clay weathering products may be combined with modern hydrosphere mass–balance equations to infer past ocean water composition [32]. Despite their demonstrated usefulness in paleoclimate and environmental studies, the methodology for analyzing $\delta^{18}O$ silicate clay has lagged that of more commonly measured sample types, like marine carbonates. For example, measuring the $\delta^{18}O$ value of carbonates has become increasingly more automated through the use of peripheral sample preparation devices since the first measurements were made by hand on a vacuum line in the 1950s and 1960s [33-35].

The first measurements of $\delta^{18}O$ on clay minerals were made in 1963 [36] using previously established mineral fluorination techniques [37]. This method involves using either fluorine or an interhalogen fluoride (BrF_5, or ClF_3) to oxidize the clay minerals in nickel rod bombs to O_2 gas, which was then quantitatively converted to CO_2 using heated graphite rods [1, 3, 19, 21, 22, 27, 28, 30, 38-41]. The carbon dioxide was then purified using liquid nitrogen traps and hot mercury, which removed any residual bromine or fluorine prior to measurement on a mass spectrometer. More recent mass spectrometry methods eliminated the need for conversion

of O_2 to CO_2 and instead measured the evolved O_2 gas directly following purification [16, 23, 25, 29, 31, 42-45].

Since the 1990s, laser fluorination has also been used on silicate materials in lieu of nickel reaction tubes (referred throughout as Ni bombs), which allows for smaller sample volume, faster and more complete reactions, and the elimination of hygroscopic contaminant NiF_2 buildup [46]. Laser fluorination is generally reserved for in situ materials, ore chips, or individual large sample grains, as unconsolidated clay and silt-sized particles often containing highly reactive, hydrous minerals (e.g., phyllosilicates) are subject to dispersion within the laser chamber, partial fluorinations, and vaporization, leading to lower sample yield and the depletion of $\delta^{18}O$ values [46-50]. To accurately determine $\delta^{18}O$ of fine-grained materials by laser, homogenized powders are now mixed with a LiF binder and pressed into a pellet prior to loading into the sample holder [23, 25, 26, 42, 45, 49, 51]. The LiF binder physically reduces sample dispersion upon heating, allowing for a more rapid, high-temperature reaction reducing the risk of partial fluorinations and vaporization. Reported $\delta^{18}O$ precision among the various fluorination methods for clay minerals is around 0.2‰ for minerals that do not contain molecular water, such as kaolinite [25, 35], and between 0.2‰ and 0.4‰ for clay minerals with interlayer water, such as smectite [29, 35, 45]. In most cases, the reported precision for a given clay sample was determined from the repeat analysis of quartz or garnet standards, not concurrent measurement of clay standards. Only in a few cases were in-house clays, kaolinite or smectite, analyzed alongside quartz or garnet standards for data quality assurance [23, 29, 31, 45].

Recent technological advancements have allowed for the precise measurement of mass-dependent variations of triple oxygen isotopes (^{16}O, ^{17}O, and ^{18}O) in silicate materials using the laser methods described above [46, 49, 52-56]. Small deviations of $\delta'^{18}O$ and $\delta'^{17}O$ from a mass-

dependent reference relationship ($\Delta'^{17}O$) [55, 57] provide additional context for the interpretation of $\delta^{18}O$ values by constraining isotope effects of kinetic fractionation and other confounding processes that follow different mass law from the typical reference relationship [52, 58]. Despite its applicability to terrestrial paleoclimate reconstructions, there are currently no studies that have precisely determined the triple oxygen isotope value for pure silicate clay minerals, including widely distributed kaolinite and smectite mineral standards. The closest materials to pure silicate clays analyzed for $\Delta'^{17}O$ include < 4 μm river sediment collected from major world rivers [32], borehole shales [59], and mixed illite-smectite clay separates from hydrothermally altered mudstones [60].

In the following, we determine the $\Delta'^{17}O$ value for two internationally distributed clay mineral standards (KGa-1b and SHCa-1) and one in-house clay (C-6) using laser fluorination of 1:1 LiF-clay pressed pellets. We aim to demonstrate that the determination of $\Delta'^{17}O$ by LiF-clay pellet laser fluorination can achieve similar precision to other commonly measured silicate materials. Secondly, we test the reproducibility of previously reported $\delta^{18}O$ values for KGa-1b [61] and SHCa-1 [62] by both laser and bomb fluorination techniques. Lastly, we show that applying a laser chamber drift correction using KGa-1b leads to better precision of unknown clay samples than corrections commonly made using other silicate standards.

2. Isotope Notation

Oxygen isotope ratios for $^{17}O/^{16}O$ and $^{18}O/^{16}O$ are reported in standard δ-notation [63] relative to VSMOW-SLAP scale. We also report linearized $\delta^{18}O$ and $\delta^{17}O$ values to account for curvature when making comparisons [64], which are defined as

$$\delta'^{x}O = 1000\ln(\delta^{x}O/1000 + 1)$$

where ^{x}O refers to ^{17}O or ^{18}O. Using the δ′ notation, the mass-dependent fractionation between two phases can be written as $1000\ln\alpha_{a\text{-}b} = \delta'^{x}O_a - \delta'^{x}O_b$ and deviations in $\delta'^{17}O$ from a reference slope can be expressed as $\Delta'^{17}O$:

$$\Delta'^{17}O = \delta'^{17}O - \lambda_{RL} \times \delta'^{18}O + \gamma$$

where λ_{RL} is the reference slope and γ is the y-intercept (for this study $\gamma = 0$). In this work, we adopt a λ_{RL} value of 0.528 consistent with other reported standards within the triple oxygen literature and geological community [43, 52, 54, 65-67].

3. Methods

3.1 Clay Standards

Kga-1b is a well-crystallized natural kaolinite obtained from the Source Clays Repository of The Clay Minerals Society (CMS). A large aliquot (> 100 g) was obtained from C. Page Chamberlain (Stanford University) for this work from bulk material distributed by The Clay Minerals Society. KGa-1b contains 96% kaolinite and trace dickite (3% anatase, 1% crandallite + quartz) [68]. KGa-1b is used to replace the exhausted supply of KGa-1 because of near identical x-ray diffraction (XRD) patterns and only slight mineralogical and chemical differences including higher order crystal phases in KGa-1b [68-71]. Although there are no published $\delta^{18}O$ values for KGa-1b, Chapligin et al. [61] report a value of 21.5‰ (VSMOW) for KGa-1 analyzed at the University of Western Ontario. Evidence indicates that, once formed, diagenetic clay minerals may preserve their original isotopic composition, unless subjected to dissolution–reprecipitation reactions [72]. We therefore use the reported KGa-1 $\delta^{18}O$ value for KGa-1b (Table 1) as a point of interlaboratory comparison.

SHCa-1 is a natural hectorite from the Red Mountain Andesite formation in San Bernardino County, CA. As with Kga-1b, an aliquot (> 100 g) was obtained from Page Chamberlain. This

standard was also obtained from the Source Clays Repository. SHCa-1 contains approximately 50% smectite, 43% calcite, 3% dolomite, 3% quartz, and 1% other [68]. Reported $\delta^{18}O$ values for SHCa-1 range from 21.2‰ to 24.1‰ (VSMOW) depending on what pretreatments were used [62] (Table 1).

C-6 is an Mg-rich pedogenic clay collected from the Uinta alpine zone, which consists of a smectite dominated mixture of kaolinite, illite, and smectite [75] obtained from Jeffrey Munroe. We chose to establish C-6 as an in-house standard because of its low $\delta^{18}O$ value, which falls within the range of natural clay samples from continental settings commonly measured at Brown University [16, 60].

In addition to clay standards, known quartz, olivine, garnet, chert, and diatom/diatomite standards [43, 53, 54, 76, 77] were also measured during the analysis period (Table 1). The non-pellet standards were used to (1) determine the long-term reference tank $\Delta'^{17}O$ value and (2) monitor the precision and accuracy of the corrected clay $\Delta'^{17}O$ values (details below).

Table 1. Silicate reference materials

Standard material	Mineralogy	Isotope analysis pretreatments	$\delta^{17}O$ (‰ VSMOW-SLAP)	$\delta^{18}O$ (‰ VSMOW-SLAP)	$\Delta'^{17}O$ (‰ VSMOW-SLAP) $\lambda = 0.528$	References
KRS	Garnet	None	−13.34 ± 0.11	−24.95 ± 0.21	−0.091 ± 0.003	Miller et al. [73]; Sharp and Wostbrock [53][a]; Ibarra et al. [43]
SCO	Olivine	None	2.75 ± 0.08	5.32 ± 0.16	−0.052 ± 0.014	Sharp and Wostbrock [53][a]; Ibarra et al. [43]
UWG-2	Garnet	None	2.94	5.70 ± 0.01	−0.064	Wostbrock et al. [55][a]; Sharp and Wostbrock [53]; Tanaka and Nakamura [74]; Ibarra et al. [43]
NBS-28	Quartz	None	4.991	9.57	−0.050	Sharp and Wostbrock [53][a]; Ibarra et al. [43]
SKFS	Chert	None	17.57 ± 0.13	33.81 ± 0.26	−0.137 ± 0.004	Sharp and Wostbrock [53][a]; Ibarra et al. [43]
PS1772-8	Opal A	None		41.54 ± 1.63	−0.179 ± 0.007	Ibarra et al. [43][a]
UCD-DFS	Opal-CT	None		29.857 ± 1.13	−0.215 ± 0.016	Ibarra et al. [43][a]
KGa-1	Similar to KGa-1b; less crystalline	None		21.5		Chipera and Bish [68]; Mermut and Cano [70]; Sakharov et al. [71]; Chapligin et al. [61][a]
KGa-1b	~96% kaolinite and trace dickite [3% anatase, 1% crandallite + quartz (?)]; slightly higher crystallinity than KGa-1	K-acetate		21.69 ± 0.45		Pruett and Webb [69]; Chipera and Bish [68]; Mermut and Cano [70]; Sakharov et al. [71]; Longstaffe Lab, personal communication[a]
SHCa-1	~50% smectite [43% calcite, 3% dolomite, 3% quartz, 1% other]	H_2O_2, Na-acetate		21.4		Chipera and Bish [68]; Fagan and Longstaffe [62][a]
C-6	Smectite-rich paleosol clay	H_2O_2 $(NaPO_3)_6$				Munroe et al. [71]

Note: Description of silicate standard materials used in this study including mineralogy. Accepted oxygen isotope values are reported when known. References include major contributions towards the characterization of the standard material.
[a]Source for accepted $\delta^{18}O$ and/or $\Delta'^{17}O$ values.

3.2 Sample Preparation

Powdered clay standards were first reacted with a 1 M potassium acetate-acetic acid buffer solution (pH = 5) to remove any carbonate phases. Samples were then triple rinsed with Milli-Q water and re-homogenized via ceramic mortar and pestle. To prevent clay particles from dispersing in the laser chamber during analysis, ~3 mg of each sample was then mixed with LiF (1:1 ratio by weight) and pressed into pellets [16, 23, 25, 26, 42, 45, 49, 51]. A custom pellet die set with a 2-cm-tall chute 0.24 cm in diameter was used to form 0.24-cm pellets, which were loaded into 0.3-cm-wide slots in the laser chamber sample holder (Figure 1). A combination of 9–11 pellets and

1–3 non-pellet standards were loaded into sample holder at a time. The loaded sample holder was placed within the laser chamber and dried under vacuum using a molecular turbo pump for 12+ h, reaching typical backgrounds in the 1×10^{-6} mbar range. All samples within the laser chamber were analyzed within an 8- to 14-h window the following day.

3.3 Fluorination Methods

The oxygen isotope ratios of the clays pellets were measured via laser fluorination at Brown University Oxygen Isotope Fluorination Lab. At the beginning of each analysis day, the samples were exposed to three 3- to 5-min preflourinations under vacuum with BrF_5 to liberate impurities from the samples and fluorination line. The O_2 gas was liberated from the samples by reaction with BrF_5 in a 3–5:1 stoichiometric excess while being heated using a 50 W CO_2 infrared laser as described in detail [16, 43, 44, 60]. Briefly, the O_2 gas was passed through a liquid N_2 trap, a NaCl trap, a second liquid N_2 trap, and then sorbed on to a zeolite trap at liquid N_2 temperature. After evacuating remaining non-condensables, the O_2 gas was then passed through a molecular sieve gas chromatography column [43, 55, 78] to another chilled zeolite using a He carrier gas before being introduced to the sample side bellow of the mass spectrometer after evacuating the He carrier gas.

When analyzing via the conventional Ni bombs, roughly 3 mg of leached sample powder was added to the nickel bombs. The bombs were then heated to 200°C for 2 h under vacuum afterwards pre-fluorinated 3× for 5 min to remove any surficial contaminants [43, 79]. BrF_5 at an ~5:1 stoichiometric excess was then added to each reaction vessel and heated to 600°C for 16 h. Once the bomb samples are reacted with BrF_5, the analytical procedure is identical to that of the laser samples. All clay isotopic ratios are reported with respect to Vienna standard mean ocean water (VSMOW) based on corrections described below.

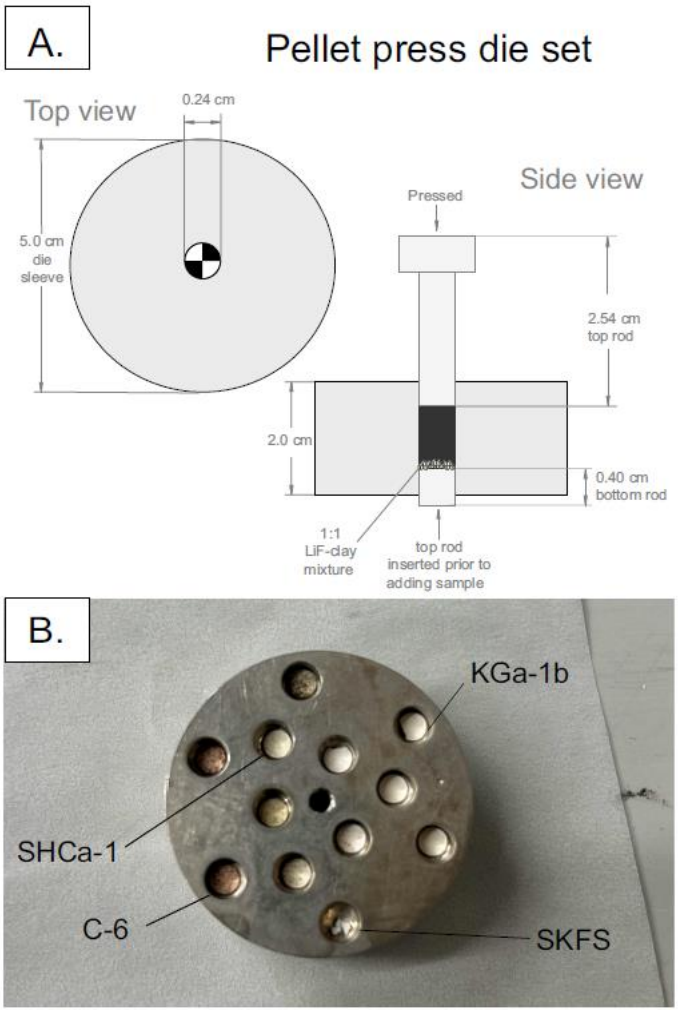

Figure 1. (A) Die set used to form clay pellets and (B) laser chamber sample holder containing 11 prepared pellets and 1 non-pellet standard typical of one daily analysis period.

3.4 IRMS Methods

Following laser fluorination and purification, sample O_2 was analyzed on a dual inlet MAT 253 + isotope ratio mass spectrometer. An initial argon background check was performed on each bellow to screen for leaks introduced during the sample reaction and purification steps. Samples that maintained low Ar backgrounds (< 3000 mV on a ~1×10^{13} Ω resistor) were then measured 2–3 times with an integration time of 26 s with 10 iterations per analysis and against the same

O_2 reference gas. Samples were run at an intensity of 5 V on mass of 32, corresponding to a pressure of ~25 mbar in the bellows and ~1×10^{-7} mbar in the source.

3.5 Drift Corrections ($\delta^{18}O$)

There is an observable drift in the measured isotope values of clays analyzed in the laser chamber [25, 42]. This drift is likely attributed to the liberation of excess contaminants and interstitial waters throughout the course of the run and/or the partial reaction of clays during subsequent reactions. At least 3 KGa-1b pellets were measured in each chamber in the beginning, middle, and end of the analysis day and used to make daily $\delta^{18}O$ drift corrections. The difference between the measured KGa-1b and the internal bomb-determined KGa-1 $\delta^{18}O$ value (21.459‰; Table S1) was plotted against the daily run order, and the resulting linear trend (typical R^2 of 0.25–0.91; Table S1) applied to the other clay samples within the laser chamber. Identical corrections were made using an externally determined value for KGa-1 for comparison (Table S2).

Typically, the KGa-1 $\delta^{18}O$ value becomes more positive after applying the correction. The average magnitude of the correction is 0.88‰. This correction was only performed on the clay samples run by laser fluorination. Samples run via conventional Ni bomb fluorination are corrected via a daily offset [43, 44].

3.6 Reference Gas Corrections ($\Delta'^{17}O$)

Because there are currently no reported $\Delta'^{17}O$ values for the clay standards, the $\Delta'^{17}O$ corrections for KGa-1b, SHCa-1, and C-6 are made against known non-clay standards measured alongside the clays [16, 32, 59]. To reserve space for like-material standards and allow for higher sample throughput, we tested using the long-term determined laboratory reference tank $\Delta'^{17}O$ value as a means for making sample chamber corrections and compare the results with the conventional non-clay standard correction method. The assumption is that fractionation in bulk

composition ($\delta^{18}O$ values) follows a mass law of ~0.528, as previously assumed in comparable work [54]. Further, this assumption is made to address a practical need for sample throughput because triple oxygen isotope measurements take ~1–1.5 h per sample.

The reference tank calibration to the VSMOW-SLAP scale was achieved by analyzing five known silicate standards by laser over several years (March 2022 to April 2024; Table S3). The calibration to the VSMOW-SLAP scale also involves the determination of the compression scale factor, which is unique for each mass-spectrometer and reflects its deviation from perfect linearity of slope of 1.00 across a wide range of δ values [80]. Repeat analysis of silicate standards over time has allowed for the determination of the compression factor of the Brown University MAT 253+ and the transformation of its measurements to the VSMOW-SLAP scale. The results with an r^2 value of 0.9993 for $\delta'^{18}O$ and 0.9993 for $\delta'^{17}O$, respectively, with slopes of 1.0019 and 1.0017, respectively, cover a range of 60‰ in $\delta^{18}O$ and via the intercept values provide the calibrated $\delta'^{18}O$ and $\delta'^{17}O$ values and thus the $\Delta'^{17}O$ of the Brown University MAT 253+ reference gas (Figure 2; $\delta'^{18}O = -10.0296$; $\delta'^{17}O = -5.2560$; $\Delta'^{17}O = +0.00396‰$).

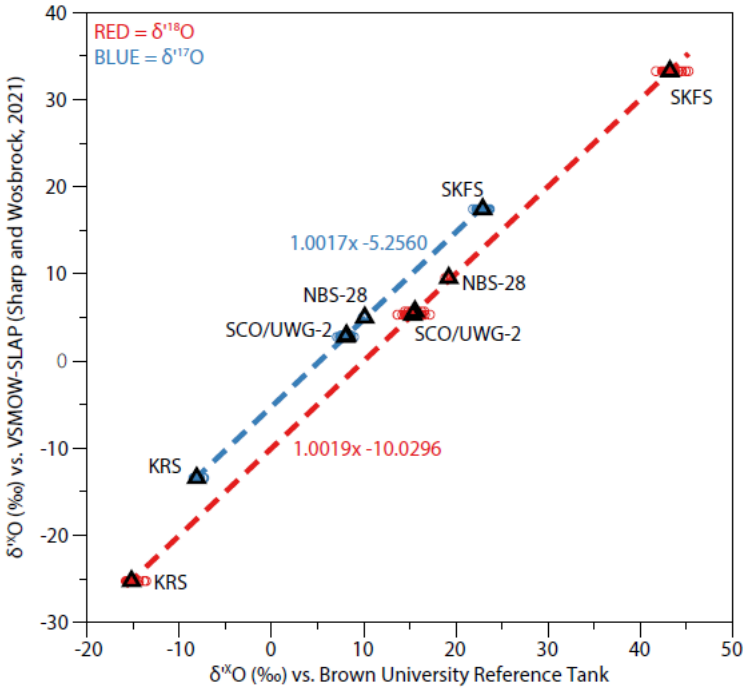

Figure 2. Measured isotope values versus the Brown University reference tank against the known standard values in VSMOW-SLAP for both δ′18O (red) and δ′17O (blue) (Table S3). Known values are taken from the multi-laboratory average given in Sharp and Wostbrock [53] (their table 1).

4. Results

In the following, we report and compare the values obtained using multiple correction schemes. For clarity, we define them here. Correcting via "daily offset" pertains to samples that have been corrected to the average daily offset of the non-clay silicate standards run in that day's laser chamber or bomb set (Table S5). This is the traditional method of standard correction. Correcting via "the known reference tank value" corresponds to isotope values that were corrected using the previously established known value for the reference tank (see above section).

4.1 KGa-1b

The laser KGa-1b $\delta^{18}O$ values corrected via daily offset from non-clay standards have a value of 19.787‰ (±1.000 [1σ]; ±0.158 [1SE]; $n = 40$) (Table 2; Table S1), whereas the

conventional Ni bomb value corrected via daily offset is 21.459 (±0.771 [1σ]; ±0.257 [1SE]; $n = 9$) (Table S4). In addition to the laser-produced clay $\delta^{18}O$ values being generally lower than bomb-produced clay $\delta^{18}O$ values, laser-produced clay $\delta^{18}O$ values experienced on average a 0.996‰ magnitude drift between the first and last sample analyzed each day.

The drift-corrected laser fluorination $\delta^{18}O$ value for KGa-1b is 21.478‰ (±0.267 [1σ]; ±0.042 [1SE]; $n = 40$) (Figure 1 and Table S1) when made using the reference tank value and 21.427‰ (±0.948 [1σ]; ±0.03 [1SE]; $n = 40$) when corrected via non-clay chamber standards. The laser fluorination-based $\Delta'^{17}O$ value for KGa-1b is −0.074 (±0.014 [1σ]; ±0.002 [1SE]; $n = 40$) when the correction is made using the known reference tank value (Figure 3 and Table S1). The laser fluorination-based $\Delta'^{17}O$ value is nearly identical to the mean conventional Ni bomb $\Delta'^{17}O$ value, which is −0.073 (±0.014 [1σ]; ±0.005 [1SE]; $n = 9$) and corrected by non-clay bomb standards (Table S4). When corrected using the non-clay chamber standards, the drift-corrected laser fluorination-based $\Delta'^{17}O$ value for KGa-1b is −0.067 (±0.017 [1σ]; ±0.003 [1SE]; $n = 40$) (Table S1).

Table 2. Resulting silicate $\delta^{18}O$ and $\Delta'^{17}O$ values by method (this study).

	Reaction method[a]	Drift correction method[b]	$\delta^{18}O$ (‰ VSMOW-SLAP)	$\delta^{18}O$ 1(σ)	$\delta^{18}O$ 1SE	$\Delta'17O$ (‰ VSMOW-SLAP) λ = 0.528	$\Delta'^{17}O$ 1(σ)	$\Delta'^{17}O$ 1SE	n
Silicate clay samples									
KGa-1b	Bomb	N/A	21.4590	0.7710	0.2570	−0.0647	0.0146	0.0049	9
	Laser	Internal	21.4783	0.2666	0.0422	−0.0735	0.0144	0.0023	40
	Laser	external	21.5173	0.2640	0.0417	−0.0735	0.0144	0.0023	40
SHCa-1	Bomb	N/A	22.0420	0.8289	0.3384	−0.1005	0.0136	0.0045	6
	Laser	Internal	21.7686	0.7534	0.2271	−0.1222	0.0078	0.0023	11
	Laser	External	21.8079	0.7527	0.2269	−0.1222	0.0078	0.0023	11
C-6	Laser	Internal	13.5765	1.1408	0.2767	−0.1056	0.0131	0.0032	17
	Laser	External	13.6161	1.1401	0.2765	−0.1056	0.0131	0.0032	17
Primary non-clay standards									
SCO	Laser		6.5510	2.1824	1.2600	−0.0644	0.0195	0.0112	3
SKFS	Laser		32.7423	1.6644	0.4805	−0.1270	0.0091	0.0026	12
	Bomb		33.2770	0.8566	0.2709	−0.1159	0.0186	0.0059	10
UCD-DFS	Bomb		29.2265	0.9307	0.2943	−0.1880	0.0302	0.0095	10
PS-diatom	Bomb		43.5293	0.5190	0.2997	−0.1897	0.0058	0.0033	3
NBS-28	Bomb		10.0010	0.2903	0.1298	−0.0574	0.0034	0.0015	5
Recommended silicate clay values for future normalization									
KGa-1b			21.4590		0.2570	−0.0735		0.0023	
SHCa-1			22.0420		0.3384	−0.1222		0.0023	

Note: Isotope results summary of all silicate materials analyzed in this study including new silicate clay standards and non-silicate clay primary standards measured. Recommended $\delta^{18}O$ and $\Delta'^{17}O$ values for future normalization using Kga-1b and SHCa-1 standards are included at the bottom of the table.
[a]Refers to BrF_5 fluorination via laser chamber or BrF_5 fluorination via heated Ni-bomb.
[b]Refers to the drift correction made on clay samples analyzed via laser fluorination. Internal corrections refer to drift corrections made using the bomb-determined value for KGa-1b (this study; 21.459‰). External corrections refer to drift corrections made using a value of KGa-1 provided by Longstaffe Lab (21.69‰).

4.2 SHCa-1

The mean drift–corrected laser fluorination $\delta^{18}O$ value for SHCa-1 is 21.769‰ (±0.753 [1σ]; ±0.227 [1SE]; $n = 11$) when corrected against the reference tank value (Figure 3) and 21.784‰ (±1.102 [1σ]; ±0.348 [1SE]; $n = 11$) when corrected by non-clay chamber standards (Table S1). The conventional Ni bomb value corrected via daily standard offsets is 22.042‰ (±0.830 [1σ]; ±0.338 [1SE]; $n = 5$) (Table 2 and Table S4). The mean laser fluorination-based $\Delta'^{17}O$ value for SHCa-1 is −0.1162‰ (±0.0073 [1σ]; ±0.0023 [1SE]; $n = 11$) when corrected daily against non-clay chamber standards and −0.1222‰ (±0.0078 [1σ]; ±0.0023 [1SE]; $n = 11$) when corrected against the long-term reference tank value (Table S1). The mean conventional Ni bomb

$\Delta'^{17}O$ value is −0.1083‰ (±0.016 [1σ]; ±0.007 [1SE]; $n = 5$) when corrected via chamber standards and −0.1005‰ (±0.014 [1σ]; ±0.006 [1SE]; $n = 5$) when corrected using the reference tank value (Table S4). The bomb-determined $\Delta'^{17}O$ and $\delta^{18}O$ values for SHCa-1 are higher than the laser-determined values.

4.3 C-6

The mean drift–corrected laser fluorination $\delta^{18}O$ value for the unknown C-6 is 13.577‰ (±1.141 [1σ]; ±0.277 [1SE]; $n = 17$) when corrected against the reference tank value (Figure 3 and Table 2) and 13.261‰ (±1.360 [1σ]; ±0.330 [1SE]; $n = 17$) when corrected using non-clay chamber standards (Table S1). The mean laser fluorination-based $\Delta'^{17}O$ value for C-6 is −0.1056 (±0.0131 [1σ]; ±0.0032 [1SE]; $n = 17$) when corrected using the tank value and −0.0993 (±0.0155 [1σ]; ±0.0038 [1SE]; $n = 17$) when corrected using non-clay chamber standards. No C-6 samples were analyzed via bomb.

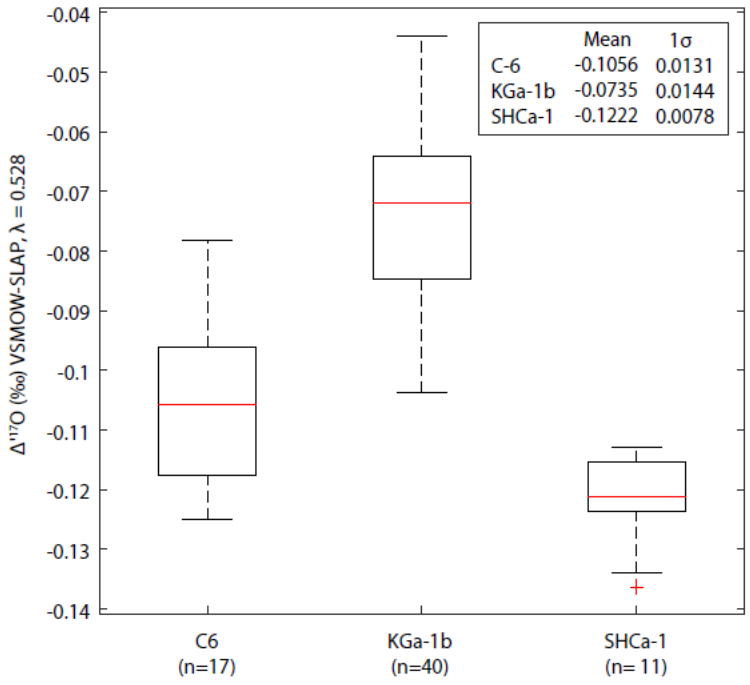

Figure 3. Reference tank–corrected $\Delta'^{17}O$ values measured by laser for C-6, KGa-1b, and SHCa-1 shown using box and whisker plots.

5. Discussion

5.1 New Standards for Clay-Rich Geologic Materials

KGa-1b, SHCa-1, and C-6 are ideal standards for assessing the quality of $\Delta'^{17}O$ and $\delta^{18}O$ data generated from clay-rich geological materials because of similar mineralogy, grain size, and consequently reactivity. Further, when plotted in $\Delta'^{17}O$–$\delta^{18}O$ space, the isotopic composition of KGa-1b, SHCa-1, and C-6 falls within the same field as clay-rich shales [59], mixed illite and smectite clays from hydrothermally altered mudstones [60], and mixed clays from rivers around the world [32] (Figure 4). This is particularly useful considering most clay materials plotted in a region ($\delta'^{18}O = 3.24‰$–$19.96‰$ and $\Delta'^{17}O = -0.17‰$ to $-0.06‰$) underrepresented by existing inter-laboratory silicate standards (Figure 4). As such, we propose that KGa-1b and SHCa-1, both widely distributed clay mineral materials, can be used by other groups and laboratories as either primary or secondary standards to allow for more direct interlaboratory comparisons between clay-rich sediments or clay separates. For example, if leaching protocols can be standardized for oxygen isotope analyses (beyond the scope of this work), like recent efforts by Kanik et al. for δD measurements, these two clay mineral standards appear suitable for use to ensure cross-laboratory intercalibration of $\Delta'^{17}O$–$\delta^{18}O$.

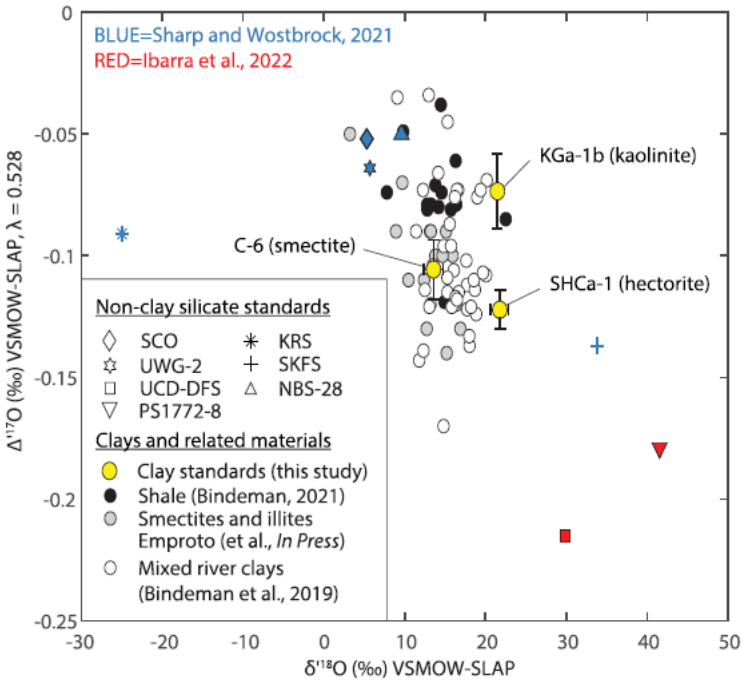

Figure 4. Comparison of newly established clay mineral standard values (this study, yellow) to well-established non-clay silicate standard values (blue and red) and clay-rich geological samples (black, gray, and white) plotted within the $\Delta'^{17}O$–$\delta^{18}O$ reference frame.

The drift-corrected laser fluorination $\delta^{18}O$ value for SHCa-1 is within 0.1‰ accuracy of values reported by Fagan and Longstaffe for sodium acetate–treated SHCa-1 samples analyzed by bomb. Our bomb-produced clay $\delta^{18}O$ value is slightly lower but accurate within 0.16‰ of the sodium acetate–treated SHCa-1 samples [62]. The incomplete fluorination of SHCa-1 with BrF_5 within the nickel bombs may account for the unexpected low bomb-produced clay $\delta^{18}O$ values. In this case, slow and low-temperature reactions can lead to the vaporization of SiO_2, which preferentially preserves Si–^{18}O bonds and results in lower O_2 yields and $\delta^{18}O$ values [49]. High-temperature reactions involving methanation prior to fluorination [81] are shown to generate more complete reactions in organic materials and could perhaps also curb these effects in analogous reactions. Alternatively, laser-produced clay $\delta^{18}O$ values are higher than bomb-produced clay $\delta^{18}O$ values due to the repeat exposure of the sample to BrF_5 and resulting passive fluorination over the

course of the analysis day. This phenomenon, only observed in very fine-grained hydrous phases, preferentially liberates ^{16}O, resulting in higher residual clay $\delta^{18}O$ values [49]. The effects of passive fluorination are likely higher for SHCa-1 compared to KGa-1b, considering hectorite has a higher capacity for structural waters than kaolinite via a higher specific surface area and thus may react more readily. Drift corrections based on KGa-1b may therefore underestimate these effects in smectites.

5.2 Proposed Method for the Laser Determination of $\Delta'^{17}O$ and $\delta^{18}O$ in Clay Materials

In this work, clay samples were standardized to the VSMOW-SLAP scale by adjusting them based on known 2–3 silicate standards analyzed in the same laser chamber on the same day. Additionally, internal clay standards were analyzed in the same chamber to account for any drift related to the clay materials. The combination of clay and non-clay standards restricts the number of unknown samples that can be feasibly run in each day. We instead propose that our newly determined bomb-produced clay $\delta^{18}O$ value for KGa-1b (21.459‰ ± 0.771 [1σ]) and laser-determined $\Delta'^{17}O$ value for Kga-1b (−0.0735‰ ± 0.0144 [1σ]) be used as a primary standard for the analysis of $\delta^{18}O$ and $\Delta'^{17}O$ of clay materials, which eliminates the need for additional non-clay standards (Table 2). Additionally, the bomb-produced $\delta^{18}O$ value of SHCa-1 (22.042‰ ± 0.3384 [1σ]) and the laser-determined $\Delta'^{17}O$ value for SHCa-1 (−0.1222‰ ± 0.0023 [1σ]) may be used as a standard when analyzing $\delta^{18}O$ and $\Delta'^{17}O$ of smectite-rich clay materials (Table 2).

Practical considerations for standardization of clay materials include necessary pretreatments, the number and type of samples, and standards to be analyzed per day (limited by the 60- to 90-min measurement on the IRMS) and whether the $\Delta'^{17}O$ value of a given lab's reference tank is precisely known. Aliquots of KGa-1b obtained from CMS should be leached prior to isotope analysis, to be consistent with established pretreatments necessary for clay mineral

separation. When analyzing via laser fluorination, no less than 3 KGa-1b pellets should be analyzed across the beginning, middle, and end of day. These standards should be used to apply a daily drift correction normalized to our accepted bomb value for KGa-1b. The laser chamber may then contain up to 9 additional samples or standards, which would typically equate to a 12- to 14-h analysis period. If the $\Delta'^{17}O$ of the dual inlet reference tank is precisely known, up to 9 remaining sample slots may be filled with unknowns. Otherwise, we recommend analyzing an additional non-clay silicate standard in addition to KGa-1b when correcting $\Delta'^{17}O$ values.

6. Conclusion

Advancements in the stable oxygen isotope analysis of silicate clays, particularly kaolinite and smectite, have provided significant insights into paleoclimate and environmental studies. However, a consensus is lacking on the proper preparation and standardization of clay minerals, which are much more susceptible to isotopic drift from incomplete reactions and contamination than standard silicate materials. By employing a combination of LiF-clay pellet preparation and laser fluorination methods, this study demonstrates the capability to achieve high precision in $\delta^{18}O$ and $\Delta'^{17}O$ values for kaolinite and smectite, comparable to those of other silicate materials. The findings affirm that KGa-1b and SHCa-1 can serve as reliable standards for oxygen isotope analysis in clay-rich materials, promoting consistent interlaboratory calibration. Furthermore, the study underscores the importance of standardizing leaching protocols and correcting for procedural drifts to enhance the accuracy of clay isotope data.

Author Contributions

Catherine A. Gagnon: writing – original draft, methodology, formal analysis, data curation, conceptualization, investigation. Riley Havel: writing – review and editing, methodology, investigation, data curation. Jiquan Chen: writing – review and editing, investigation, methodology. Gavin Piccione: formal analysis, writing – review and editing, project administration, methodology. Daniel E. Ibarra: formal analysis, writing – review and editing, funding acquisition, supervision, resources, data curation, project administration, software, visualization, validation, methodology, conceptualization.

Acknowledgments

We thank Joe Orchardo and Steve Clemens for support in laboratory analyses, C. Page Chamberlain for providing the clay mineral standards and methodological discussions, and Cameron Meyers and Greg Hirth for help with pellet press methodology. We thank Fred Longstaffe for sharing internal standard values and Jeffrey Munroe for sharing the C-6 sample. Gagnon was partially supported by NSF AGS 2102901 to Ibarra; Piccione was partially supported by NSF EAR 2303484 to Ibarra; and Havel was supported by NSF GRFP (Grant No. 2040433).

References

O'Neil JR, Kharaka YK. Hydrogen and oxygen isotope exchange reactions between clay minerals and water. Geochim Cosmochim Acta. 1976;40(2):241-246.

Urey HC. The thermodynamic properties of isotopic substances. Journal of the Chemical Society (Resumed). 1947;(0):562-581. doi:10.1039/JR9470000562

Savin SM, Epstein S. The oyxgen and hydrogen isotope geochemistry of ocean sediments and shales. Geochim Cosmochim Acta. 1970;34(1):43-63.

Zachos J, Pagani M, Sloan L, Thomas E, Billups K. Trends, rhythms, and aberrations in global climate 65 Ma to present. Science (1979). 2001;292(5517):686-693.

Erez J, Luz B. Experimental paleotemperature equation for planktonic foraminifera. Geochim Cosmochim Acta. 1983;47(6):1025-1031.

Prentice ML, Matthews RK. Cenozoic ice-volume history: development of a composite oxygen isotope record. Geology. 1988;16(11):963-966.
Gat JR. Oxygen and hydrogen isotopes in the hydrologic cycle. Annu Rev Earth Planet Sci. 1996;24(1):225-262.
Dee S, Bailey A, Conroy JL, et al. Water isotopes, climate variability, and the hydrological cycle: recent advances and new frontiers. Environmental Research: Climate. 2023;2(2):022002.
Dansgaard W. Stable isotopes in precipitation. Tellus. 1964;16(4):436-468. doi:https://doi.org/10.1111/j.2153-3490.1964.tb00181.x
Konecky BL, McKay NP, Churakova (Sidorova) O V, et al. The Iso2k database: a global compilation of paleo-δ18O and δ2H records to aid understanding of Common Era climate. Earth Syst Sci Data. 2020;12(3):2261-2288. doi:10.5194/essd-12-2261-2020
Raymo ME, Lisiecki LE, Nisancioglu KH. Plio-Pleistocene ice volume, Antarctic climate, and the global δ18O record. Science (1979). 2006;313(5786):492-495.
Shakun JD, Lea DW, Lisiecki LE, Raymo ME. An 800-kyr record of global surface ocean δ18O and implications for ice volume-temperature coupling. Earth Planet Sci Lett. 2015;426:58-68. doi:https://doi.org/10.1016/j.epsl.2015.05.042
Pacey A, Wilkinson JJ, Boyce AJ, Millar IL. Magmatic Fluids Implicated in the Formation of Propylitic Alteration: Oxygen, Hydrogen, and Strontium Isotope Constraints from the Northparkes Porphyry Cu-Au District, New South Wales, Australia. Economic Geology. 2020;115(4):729-748. doi:10.5382/econgeo.4732
Huston DL, Trumbull RB, Beaudoin G, Ireland T. Light stable isotopes (H, B, C, O and S) in ore studies—methods, theory, applications and uncertainties. In: Isotopes in Economic Geology, Metallogenesis and Exploration. Springer; 2023:209-244.
Bindeman HN, Valley JW. Oxygen isotope study of the Long Valley magma system, California: Isotope thermometry and convection in large silicic magma bodies. Contributions to Mineralogy and Petrology. 2002;144(2):185-205. doi:10.1007/s00410-002-0371-8
Gagnon CA, Butler KL, Robertson K, et al. Economic Geology ¬VOLCANO-SEDIMENTARY LITHIUM OCCURRENCES IN BARSTOW, CA AND THEIR RELATED FORMATION MECHANISMS DETERMINED BY STABLE ISOTOPE ANALYSES OF CARBONATES AND CLAYS-Manuscript Draft-Manuscript Number: SEG-D-24-00096R1
Wagner T, Mlynarczyk MSJ, Williams-Jones AE, Boyce AJ. Stable Isotope Constraints on Ore Formation at the San Rafael Tin-Copper Deposit, Southeast Peru. Economic Geology. 2009;104(2):223-248. doi:10.2113/gsecongeo.104.2.223
Wilkinson JJ. Fluid inclusions in hydrothermal ore deposits. Lithos. 2001;55(1):229-272. doi:https://doi.org/10.1016/S0024-4937(00)00047-5
Gilg HA, Hall AM, Ebert K, Fallick AE. Cool kaolins in Finland. Palaeogeogr Palaeoclimatol Palaeoecol. 2013;392:454-462.
Gilg HA. D–H evidence for the timing of kaolinization in Northeast Bavaria, Germany. Chem Geol. 2000;170(1-4):5-18.

Mora G, Pratt LM. Isotopic evidence for cooler and drier conditions in the tropical Andes during the last glacial stage. Geology. 2001;29(6):519-522.
Rosenau NA, Tabor NJ. Oxygen and hydrogen isotope compositions of paleosol phyllosilicates: differential burial histories and determination of Middle–Late Pennsylvanian low-latitude terrestrial paleotemperatures. Palaeogeogr Palaeoclimatol Palaeoecol. 2013;392:382-397.
Mix HT, Chamberlain CP. Stable isotope records of hydrologic change and paleotemperature from smectite in Cenozoic western North America. Geochim Cosmochim Acta. 2014;141:532-546.
Hall AM, Gilg HA, Fallick AE, Merritt JW. Kaolins in gravels and saprolites in north-east Scotland: Evidence from stable H and O isotopes for Palaeocene–Miocene deep weathering. Palaeogeogr Palaeoclimatol Palaeoecol. 2015;424:6-16.
Mix HT, Ibarra DE, Mulch A, Graham SA, Chamberlain CP. A hot and high Eocene Sierra Nevada. Bulletin. 2016;128(3-4):531-542.
Gao Y, Gao Y, Ibarra DE, et al. Clay mineralogical evidence for mid-latitude terrestrial climate change from the latest Cretaceous through the earliest Paleogene in the Songliao Basin, NE China. Cretac Res. 2021;124:104827.
Stern LA, Chamberlain CP, Reynolds RC, Johnson GD. Oxygen isotope evidence of climate change from pedogenic clay minerals in the Himalayan molasse. Geochim Cosmochim Acta. 1997;61(4):731-744.
Vitali F, Longstaffe FJ, McCarthy PJ, Plint AG, Caldwell WGE. Stable isotopic investigation of clay minerals and pedogenesis in an interfluve paleosol from the Cenomanian Dunvegan Formation, NE British Columbia, Canada. Chem Geol. 2002;192(3-4):269-287.
Sjostrom DJ, Hren MT, Horton TW, Waldbauer JR, Chamberlain CP. Stable isotopic evidence for a pre–late Miocene elevation gradient in the Great Plains–Rocky Mountain region, USA. Published online 2006.
Feng W, Yapp CJ. 18O/16O and D/H ratios of pedogenic kaolinite in a North American Cenomanian laterite: Paleoclimatic implications. Geochim Cosmochim Acta. 2009;73(20):6249-6263.
Muttik N, Kirsimäe K, Vennemann TW. Stable isotope composition of smectite in suevites at the Ries crater, Germany: Implications for hydrous alteration of impactites. Earth Planet Sci Lett. 2010;299(1-2):190-195.
Bindeman IN, Bayon G, Palandri J. Triple oxygen isotope investigation of fine-grained sediments from major world's rivers: Insights into weathering processes and global fluxes into the hydrosphere. Earth Planet Sci Lett. 2019;528:115851.
Keith ML, Weber JN. Carbon and oxygen isotopic composition of selected limestones and fossils. Geochim Cosmochim Acta. 1964;28(10-11):1787-1816.
Degens ET, Epstein S. Oxygen and carbon isotope ratios in coexisting calcites and dolomites from recent and ancient sediments. Geochim Cosmochim Acta. 1964;28(1):23-44.
Epstein S, Buchsbaum R, Lowenstam H, Urey HC. Carbonate-water isotopic temperature scale. Geol Soc Am Bull. 1951;62(4):417-426.

Clayton RN, Mayeda TK. The use of bromine pentafluoride in the extraction of oxygen from oxides and silicates for isotopic analysis. Geochim Cosmochim Acta. 1963;27(1):43-52.
TAYLOR JR. HP, EPSTEIN S. Relationship Between O18/O16 Ratios in Coexisting Minerals of Igneous and Metamorphic Rocks: Part 1: Principles and Experimental Results. GSA Bulletin. 1962;73(4):461-480. doi:10.1130/0016-7606(1962)73[461:RBORIC]2.0.CO;2
Chamberlain CP, Poage MA, Craw D, Reynolds RC. Topographic development of the Southern Alps recorded by the isotopic composition of authigenic clay minerals, South Island, New Zealand. Chem Geol. 1999;155(3-4):279-294.
Girard JP, Freyssinet P, Chazot G. Unraveling climatic changes from intraprofile variation in oxygen and hydrogen isotopic composition of goethite and kaolinite in laterites: an integrated study from Yaou, French Guiana. Geochim Cosmochim Acta. 2000;64(3):409-426.
Tabor NJ, Montanez IP. Shifts in late Paleozoic atmospheric circulation over western equatorial Pangea: Insights from pedogenic mineral δ18O compositions. Geology. 2002;30(12):1127-1130.
Tabor NJ, Montañez IP. Oxygen and hydrogen isotope compositions of Permian pedogenic phyllosilicates: Development of modern surface domain arrays and implications for paleotemperature reconstructions. Palaeogeogr Palaeoclimatol Palaeoecol. 2005;223(1-2):127-146.
Pope EC, Bird DK, Arnórsson S. Evolution of low-18O Icelandic crust. Earth Planet Sci Lett. 2013;374:47-59.
Ibarra DE, Yanchilina AG, Lloyd MK, et al. Triple oxygen isotope systematics of diagenetic recrystallization of diatom opal-A to opal-CT to microquartz in deep sea sediments. Geochim Cosmochim Acta. 2022;320:304-323.
Ibarra DE, Dai J, Gao Y, et al. High-elevation Tibetan Plateau before India–Eurasia collision recorded by triple oxygen isotopes. Nat Geosci. 2023;16(9):810-815.
Kukla T, Ibarra DE, Rugenstein JKC, et al. High-Resolution Stable Isotope Paleotopography of the John Day Region, Oregon, United States. Front Earth Sci (Lausanne). 2021;9:635181.
Sharp ZD. A laser-based microanalytical method for the in situ determination of oxygen isotope ratios of silicates and oxides. Geochim Cosmochim Acta. 1990;54(5):1353-1357. doi:https://doi.org/10.1016/0016-7037(90)90160-M
Rowe MW, Clayton RN, Mayeda TK. Oxygen isotopes in separated components of CI and CM meteorites. Geochim Cosmochim Acta. 1994;58(23):5341-5347.
Fouillac AM, Girard JP. Laser oxygen isotope analysis of silicate/oxide grain separates: Evidence for a grain size effect? Chem Geol. 1996;130(1-2):31-54.
Kirschner DL, Sharp ZD. Oxygen isotope analyses of fine-grained minerals and rocks using the laser-extraction technique. Chem Geol. 1997;137(1-2):109-115.
Ghoshmaulik S, Bhattacharya SK, Roy P, Sarkar A. A simple cryogenic method for efficient analysis of triple oxygen isotopes in silicates. Rapid Communications in Mass Spectrometry. 2020;34(18):e8833.

Kukla T, Rugenstein JKC, Ibarra DE, Winnick MJ, Strömberg CAE, Chamberlain CP. Drier winters drove Cenozoic open habitat expansion in North America. AGU Advances. 2022;3(2):e2021AV000566.

Mix HT, Chamberlain CP. Stable isotope records of hydrologic change and paleotemperature from smectite in Cenozoic western North America. Geochim Cosmochim Acta. 2014;141:532-546.

Sharp ZD, Wostbrock JAG, Pack A. Mass-dependent triple oxygen isotope variations in terrestrial materials. Geochem Perspect Lett. 2018;7:27-31.

Sharp ZD, Wostbrock JAG. Standardization for the Triple Oxygen Isotope System: Waters, Silicates, Carbonates, Air, and Sulfates. Rev Mineral Geochem. 2021;86(1):179-196. doi:10.2138/rmg.2021.86.05

Wostbrock JAG, Cano EJ, Sharp ZD. An internally consistent triple oxygen isotope calibration of standards for silicates, carbonates and air relative to VSMOW2 and SLAP2. Chem Geol. 2020;533:119432. doi:https://doi.org/10.1016/j.chemgeo.2019.119432

Pack A, Herwartz D. The triple oxygen isotope composition of the Earth mantle and understanding ΔO17 variations in terrestrial rocks and minerals. Earth Planet Sci Lett. 2014;390:138-145.

Hofmann MEG, Pack A. Technique for high-precision analysis of triple oxygen isotope ratios in carbon dioxide. Anal Chem. 2010;82(11):4357-4361.

Luz B, Barkan E. Variations of 17O/16O and 18O/16O in meteoric waters. Geochim Cosmochim Acta. 2010;74(22):6276-6286.

Aron PG, Levin NE, Beverly EJ, et al. Triple oxygen isotopes in the water cycle. Chem Geol. 2021;565:120026.

Bindeman IN. Triple oxygen isotopes in evolving continental crust, granites, and clastic sediments. Rev Mineral Geochem. 2021;86(1):241-290.

Emproto C, Benson TR, Gagnon CA, Baek W, Ibarra DE, Simon AC. Clay Chemistry of the Thacker Pass Deposit, Nevada: Implications for the Formation of High-grade Volcano-sedimentary Lithium Resources. Economic Geology.

Chapligin B, Leng MJ, Webb E, et al. Inter-laboratory comparison of oxygen isotope compositions from biogenic silica. Geochim Cosmochim Acta. 2011;75(22):7242-7256.

Fagan R, Longstaffe F. The effects of laboratory pretreatments on the hydrogen-and oxygen-isotope compositions of clay minerals. In: Clays in and for the Environment. 33rd Annual Meeting of the Clay Minerals Society, Program and Abstracts . ; 1996:55.

McKinney CR, McCrea JM, Epstein S, Allen HA, Urey HC. Improvements in Mass Spectrometers for the Measurement of Small Differences in Isotope Abundance Ratios. Review of Scientific Instruments. 1950;21(8):724-730. doi:10.1063/1.1745698

Miller MF. Isotopic fractionation and the quantification of 17O anomalies in the oxygen three-isotope system: an appraisal and geochemical significance. Geochim Cosmochim Acta. 2002;66(11):1881-1889. doi:https://doi.org/10.1016/S0016-7037(02)00832-3

Meijer HAJ, Li WJ. The Use of Electrolysis for Accurate δ17O and δ18O Isotope Measurements in Water. Isotopes Environ Health Stud. 1998;34(4):349-369. doi:10.1080/10256019808234072

Passey BH, Hu H, Ji H, et al. Triple oxygen isotopes in biogenic and sedimentary carbonates. Geochim Cosmochim Acta. 2014;141:1-25. doi:https://doi.org/10.1016/j.gca.2014.06.006

Barkan E, Affek HP, Luz B, Bergel SJ, Voarintsoa NRG, Musan I. Calibration of δ17O and 17Oexcess values of three international standards: IAEA-603, NBS19 and NBS18. Rapid Communications in Mass Spectrometry. 2019;33(7):737-740. doi:https://doi.org/10.1002/rcm.8391

Wostbrock JAG, Cano EJ, Sharp ZD. An internally consistent triple oxygen isotope calibration of standards for silicates, carbonates and air relative to VSMOW2 and SLAP2. Chem Geol. 2020;533:119432. doi:https://doi.org/10.1016/j.chemgeo.2019.119432

Chipera SJ, Bish DL. Baseline Studies of the Clay Minerals Society Source Clays: Powder X-Ray Diffraction Analyses. Clays Clay Miner. 2001;49(5):398-409. doi:DOI: 10.1346/CCMN.2001.0490507

Pruett RJ, Webb HL. Sampling and Analysis of KGa-1B Well-Crystallized Kaolin Source Clay. Clays Clay Miner. 1993;41(4):514-519. doi:DOI: 10.1346/CCMN.1993.0410411

Mermut AR, Cano AF. Baseline Studies of the Clay Minerals Society Source Clays: Chemical Analyses of Major Elements. Clays Clay Miner. 2001;49(5):381-386. doi:DOI: 10.1346/CCMN.2001.0490504

Sakharov BA, Drits VA, McCarty DK, Walker GM. Modeling Powder X-ray Diffraction Patterns of the Clay Minerals Society Kaolinite Standards: KGa-1, KGa-1b, and KGa-2. Clays Clay Miner. 2016;64(3):314-333. doi:DOI: 10.1346/CCMN.2016.0640307

Morad S, Worden RH, Ketzer JM. Oxygen and Hydrogen Isotopic Composition of Diagenetic Clay Minerals in Sandstones: A Review of the Data and Controls. In: Clay Mineral Cements in Sandstones. ; 1999:63-91. doi:https://doi.org/10.1002/9781444304336.ch3

Munroe JS, Ryan PC, Proctor A. Pedogenic clay formation from allochthonous parent materials in a periglacial alpine critical zone. Catena (Amst). 2021;203:105324. doi:https://doi.org/10.1016/j.catena.2021.105324

Menicucci AJ, Matthews JA, Spero HJ. Oxygen isotope analyses of biogenic opal and quartz using a novel microfluorination technique. Rapid Communications in Mass Spectrometry. 2013;27(16):1873-1881. doi:https://doi.org/10.1002/rcm.6642

Piccione G, Blackburn T, Tulaczyk S, et al. Subglacial precipitates record Antarctic ice sheet response to late Pleistocene millennial climate cycles. Nat Commun. 2022;13(1):5428. doi:10.1038/s41467-022-33009-1

Ibarra DE, Dai J, Gao Y, et al. High-elevation Tibetan Plateau before India–Eurasia collision recorded by triple oxygen isotopes. Nat Geosci. 2023;16(9):810-815.

Yeung LY, Young ED, Schauble EA. Measurements of 18O18O and 17O18O in the atmosphere and the role of isotope-exchange reactions. Journal of Geophysical Research: Atmospheres. 2012;117(D18). doi:https://doi.org/10.1029/2012JD017992

Swann GEA, Leng MJ, Juschus O, Melles M, Brigham-Grette J, Sloane HJ. A combined oxygen and silicon diatom isotope record of Late Quaternary change in Lake El'gygytgyn, North East Siberia. Quat Sci Rev. 2010;29(5):774-786. doi:https://doi.org/10.1016/j.quascirev.2009.11.024

Shemesh A, Yam R, Assulin M, Elish E. The triple oxygen isotope signature of uranium oxides in the nuclear fuel cycle. Journal of Nuclear Materials. 2024;590:154889.

CHAPTER 4

Volcano-sedimentary lithium occurrences in Barstow, CA, and their related formation mechanisms determined by stable isotope analyses of carbonates and clays

Catherine A. Gagnon[1,2,†], Kristina L. Butler[3], Kevin Robertson[1], Christopher Emproto[4], Phil Gans[5], Ryan Eden[5], Daniel E. Ibarra[1,2], Thomas R. Benson[6,7]

[1]Department of Earth, Environmental, and Planetary Sciences
2Institute at Brown for Environment and Society
Brown University
Providence, RI

[3]Department of Sustainable Earth Systems Sciences
University of Texas
Dallas, TX

[4] Department of Earth and Environmental Science
University of Michigan
Ann Arbor, MI

[5] Department of Earth Science
University of California Santa Barbara
Santa Barbara, CA

[6] Lithium Americas (Argentina) Corporation
Vancouver, Canada

[7]Lamont-Doherty Earth Observatory
Columbia University
Palisades, NY

Abstract

The production of lithium (Li) from underexplored volcano-sedimentary Li deposits could increase the Li stockpile for the future, while diversifying the available sources of Li needed for the energy transition. Here, we investigate the occurrence, distribution, and potential enrichment mechanisms for recently discovered Li-rich mudstones within the Miocene Barstow Formation in the Mojave Desert of California. Bulk mudstone Li concentrations from the Barstow Formation range from 20 to 2,500 ppm, and the most enriched samples correspond to a greater proportion of smectite, relative to illite, chlorite, and kaolinite. The Li-enriched mudstones tend to contain analcime, calcite, dolomite, and feldspar. Bulk mudstone Li concentrations covary with the oxygen isotopic composition of the carbonate phases ($\delta^{18}O_{carb}$; 17–35‰ VSMOW). Smectite $\delta^{18}O$ values mirror paired carbonate trends and contain an evaporitic slope in $\delta^{18}O$-δD space, suggesting both minerals formed from the same evaporatively enriched evolving water reservoir. Calculated smectite formation temperatures range from 17–51°C and carbonate clumped isotope formation temperatures range from 15–50°C suggesting low temperature processes drive Li enrichment. The combined geochemical and stable isotope results suggest that between 19 Ma and 13 Ma, evaporation of ephemeral underfilled to perennial balance-filled lake waters led to the Li enrichment of pore waters and subsequent Li-smectite authigenesis. We speculate the primary source of Li to ancient lake/pore waters came from the weathering of ash falls to the lake and aqueous Li weathered from coeval felsic volcanic rocks in and around the Barstow basin. Evidence for Li-rich hydrothermal contributions to lake/pore waters is minor. Our study suggests that other deposits set in nearby extensional regimes may have had similar paleoenvironmental controls surrounding the formation of authigenic, Li-rich smectite.

Introduction

Lithium (Li) is recognized by major world governments as a critical mineral resource (USGS, 2023; IEA, 2021) because it is a necessary component of modern batteries vital to portable electronics and electric vehicles (Bussar et al., 2016; Connolly et al., 2016; Breyer et al., 2018; Bogdanov et al., 2019; Greim et al., 2020). The anticipated demand for Li in the coming years has led to enhanced efforts to explore the economic potential of extracting Li from non-traditional resource types such as volcano-sedimentary lithium deposits (Benson et al., 2023; Putzolu et al., *This Volume*). These deposits could supplement and diversify the global supply, enabling a more rapid attainment of global sustainability and emission reduction goals. However, a large challenge to exploration and extraction is the geochemical heterogeneity that exists both within a given deposits and between different deposits. Understanding the potential variability and extent of Li enrichment in various types of deposits requires both and geospatial abundance of assay data, but also an understanding of the formation conditions and mechanisms required for Li enrichment to take place (Putzolu et al., *This Volume*). In the following work, we characterize the Barstow Formation volcano-sedimentary Li deposit for the first time, and investigate potential sources, enrichment mechanisms, and mineralization conditions.

Volcano-sedimentary Li deposits

Volcano-sedimentary Li deposits are an example of a non-traditional potential Li resource found in semi-arid basins of the western United States, Mexico, and Serbia (Benson et al., 2023; Putzolu et al., *This Volume*; Darin et al., *This Volume*). We define volcano-sedimentary Li deposits as Li rich sedimentary rocks formed in hydrologically restricted lake basins within felsic magmatic provinces, which can include mixed volcanic and sedimentary strata and/or volcaniclastic strata (Benson et al., 2023; Putzolu et al, *This Volume*). The two largest resources of its kind are found within the McDermitt caldera in northern Nevada and Oregon, USA. The Thacker Pass Project

(TP) on the Nevada side of the caldera reports a Measured and Indicated resource estimate of 16.1 Mt lithium carbonate equivalent (LCE) (Putzolu et al., *This Volume*), while the McDermitt Lithium Project on the Oregon side has an Indicated mineral resource estimate of 11.1 Mt LCE (Jindalee Resources Limited. The TP deposit contains illite- and smectite-bearing claystones containing up to ~1 wt % Li on a whole-rock basis (Castor and Henry, 2020; Benson et al., 2023). Recently, Benson and others (2023), proposed that the high-grade deposits at TP were associated with high-temperature hydrothermal alteration of primary smectite-bearing sediments to illite, related to early magmatic resurgence of the caldera system. Though widely known, TP is an anomalous example of a volcano-sedimentary Li deposit in terms of its bulk ore Li concentrations and genesis.

More commonly, volcano-sedimentary Li deposits are located within extensional basins including those found in eastern Europe (e.g., Serbia and Turkey) and the Basin and Range province of the western United States. In these locations, they are generally characterized by lacustrine Mg-smectites and mixed illite-smectite with generally lower bulk ore concentrations of Li than smectite claystones at TP (Putzolu et al., *This Volume*). Dioctahedral Mg-smectite claystones within Clayton Valley (CV), an extensional basin in central Nevada, host bulk Li concentrations of up to 2,400 ppm (Morissette, 2012; Coffey et al., 2021; Gagnon et al., 2023). Similarly, at Rhyolite Ridge in Nevada, mixed illite-smectite clays make up the lacustrine units of the Cave Spring formation, where sediments are enriched by up to 2,620 ppm Li (Reynolds and Chafetz, 2020; Chafetz, 2023; Darin et al., *This Volume*). Reported values for the hectorite-rich Horse Spring Formation in southern Nevada average around 1,000 ppm Li, with some ore samples containing as much as 5,000 ppm Li (Brenner-Tourtelot and Glanzman, 1978). Hectorite clays with ~2,000 ppm Li occur in Hector, California, within a lacustrine basin in the Mojave block (Morissette, 2012). Volcano-sedimentary deposits in Arizona include the Big Sandy and Basin

deposits, with grades reaching a maximum of ~4,400 ppm in claystones of the Big Sandy Formation (Arizona Lithium, 2024; Thompson and others, *This Volume*).

Origin and enrichment of Li in volcano-sedimentary deposits

Various types of Li sources have been called upon as the origin for volcano-sedimentary Li. Weathering of the Rhyolite Ridge tuff (25-211 ppm) supplied Li to the Cave Spring and Esmeralda formations (Darin et al., this issue). The Hector deposit is thought to be sourced from alteration of dacitic ash and hot spring waters (Foshag and Woodford, 1936; Ames et al., 1958b). Additional sources of Li to volcano-sedimentary deposits include hydrothermal fluids derived from silicic magma bodies (Benson et al., 2023; Putzolu et al., *This Volume*, references therein). In the case of TP, these fluids deliver additional Li into existing smectites via faults around the caldera resurgent dome (Benson et al., 2023). At Rhyolite Ridge, additional hydrothermal sources are proposed sources of Li to the basin, however it has been noted that there is no correlation between Li concentrations in source rocks and proximity to basin bounding faults (Ogilvie, 2023). Alternatively, additional hydrothermal Li is indirectly transferred to smectites from hydrothermal fluids mixing with waters in the catchment. This scenario is likely the case for the deposit at Clayton Valley (CV) in Nevada, where playa sediments were found to have hydrothermal Li isotopic signatures (Araoka et al., 2014), despite additional evidence that lacustrine units preserve geochemical signatures consistent with evaporative lake conditions (Morissette, 2012; Coffey et al., 2021; Gagnon et al., 2023).

In addition to Li supply, ancient endorheic lake geochemical and hydrologic processes may have a substantial impact on the Li enrichment within a basin (Asher-Bolinder, 1991; Orris and Bliss, 1991). Processes that control the temperature and concentration of the ancient lake waters will impact authigenic lacustrine clay Li concentrations. Experiments have shown that increasing

the temperature and/or concentration of aqueous solutions will increase the concentration of structurally-bound Li in clays (Decarreau et al., 2012). Additionally, recent sequential leaching experiments performed on CV clay-rich bulk sediments suggest that up to 70% of Li is structurally bound in clay octahedral sites (Coffey et al., 2021) and work by Emproto et al. (*This Volume*) concludes that very minimal Li is contained in the interlayer of TP smectites and illites. In underfilled to balance-filled lake basins (Carroll and Bohacs, 1999) like CV, Li is concentrated through successive evaporation and ultimately sequestered in authigenic smectite (Gagnon et al., 2023). This process works most efficiently in shallow to ephemeral, alkaline, and saline lakes such as those abundant in the semi-arid basins of the western US. These lake conditions concentrate not only Li, but other ions (e.g., Mg^{+}, F^{-}) necessary for generating tri- and dioctahedral smectites (Asher-Bolinder, 1991; Emproto et al., *This Volume*).

Altogether, there are many characteristics of a basin that could impact the likelihood of it hosting an economic volcano-sedimentary Li resource. These include, but are not limited to, basin size and structural evolution, hydrothermal evolution, surrounding bedrock geology and volcanic inputs, paleoclimate, and whether the basin is balance-filled, underfilled, or open. To better characterize the geochemical variability and distribution of sedimentary Li resources beyond the exceptional and unique TP case, further research involving basin and Li enrichment processes in the more common, non-caldera settings is needed. Here, we investigate the occurrence, distribution, and potential enrichment mechanisms for Li-rich claystones within the Miocene Barstow Formation (BF) of the central Mojave Desert, California (Fig. 1).

Study Location

The focus of this study are the Li-rich mudstones of the Barstow Formation (19.5-13.0 Ma), located within the Mud Hills and Calico Mountains north of Barstow, CA (Fig 1). Barstow

is in the central Mojave Desert of California, which is found south of the Sierra Nevada and west of the Basin and Range province of the United States (Fig 1). The BF is exposed discontinuously across an area of ca. 5,600 km^2 in the central Mojave region (MacFadden et al., 1990; Eden et al., in review). Its thickness ranges from 370-730 m and increases to the northwest (Byers Jr, 1960; Dibblee Jr, 1994). This region sits within the tectonically active eastern California shear zone (ECSZ), bounded by the Garlock Fault and southern Sierra Nevada to the north, the Basin and Range to the east, and the San Andreas fault system to the west.

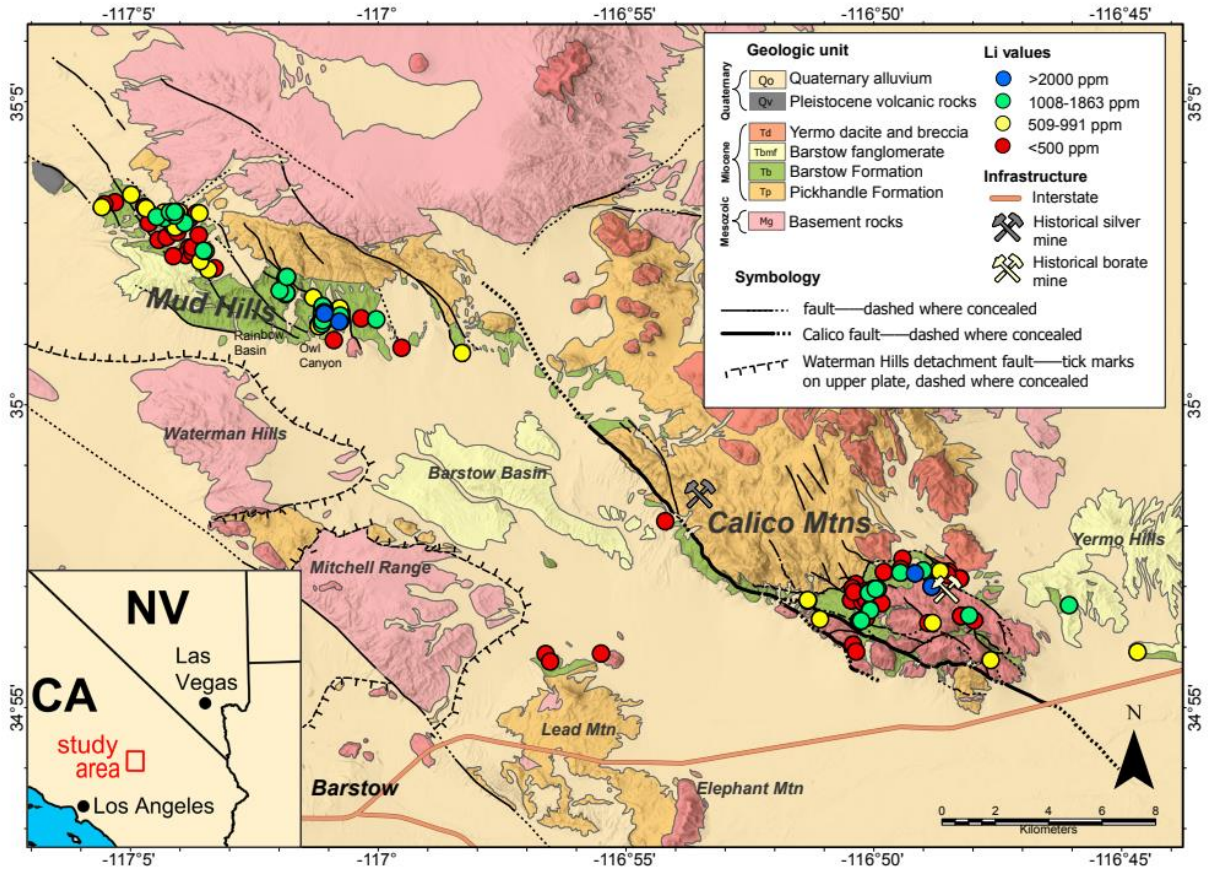

Figure 1. Geologic map of the study area. The Barstow Formation is exposed in the Mud Hills and Calico Mountain regions where mudstones were sampled. Assay data are labeled by circles and colored based on bulk Li concentrations. Sample locations are generalized to protect proprietary company data (Lithium Americas Corp.). Abbreviations: CA = California, NV = Nevada.

Tectonic Setting of the Barstow Formation

Since the Oligocene, the western margin of the United States has been undergoing a transition from Andean-style convergent tectonics to an extensional-transform regime (Atwater, 1970; Faulds et al., 2008). Prior to the deposition of the Barstow Formation, the area experienced Basin and Range crustal extension from 26-19 Ma, related bimodal volcanism, and low-angle detachment faulting (Fillmore et al., 1996; Glazner et al., 2002). Major extension on the Waterman Hills detachment fault (Fig 1), which underlies the Barstow Formation, occurred from 24 Ma to ca. 19 Ma (Singelton and Gans, 2007). The BF was then deposited from 19.4 Ma to 13.0 Ma in a non-tectonic NW-SE trending elongate basin.

The shearing related to North America- Pacific relative plate motion led to the establishment of the San Andreas fault system and ECSZ (Dokka and Travis, 1990; Schermer et al., 1996; Bennett et al., 2016, Nuriel et al., 2019; Dorsey et al., 2021). The ECSZ is defined by the San Andreas fault zone to the west, Transverse Mountains to the southwest, Garlock Fault to the north, and Death Valley and Granite Mountain faults to the east (MacFadden et al., 1990; Faulds et al., 2008). The ECSZ accommodates ~25% of Pacific- North America plate motion, leading to abundant NW-trending right-lateral faults (Dokka and Travis, 1990) and zones of transpression (Dibblee Jr, 1994) within the Barstow area. However, dextral transpression in the central Mojave did not begin till 12 Ma, meaning that the folding, contraction, and exhumation of the BF, especially in the Calico Mountains, occurred after deposition. These right-lateral faults are in some cases reactivated northwest-striking normal faults initiated during early Miocene extension prior to the deposition of the Barstow Formation (Singleton and Gans, 2008).

A major active right-lateral fault bisecting the Barstow basin is the Calico fault. The Calico fault forms a restraining bend 10 km in length within the Calico Mountains (Fig. 1). Around the

restraining bend and north of the Calico fault are extensive upright east-west trending anticlines and synclines (Singleton and Gans, 2008). The timing of slip on the Calico fault is not well constrained but inferred to be post-10 Ma by Dokka (1983) based on fault-opal ages in the central Mojave region (Nuriel et al., 2019).

Regional Geology

Basement lithologies of the central Mojave consists of the Precambrian Waterman Gneiss, Paleozoic Coyote Group, and late Mesozoic volcanic rocks (Jessey, 2010). The Waterman Gneiss is found within the Waterman Hills, Mitchel Range, and Hinkley Hills (Fig. 1) and includes dioritic gneiss and impure marble, quartzite, and various types of mylonite. The Coyote Group consists of marble, schist, conglomerate, quartzite, hornfels, and metamorphosed andesite and basalt. It is truncated at the top and bottom by Mesozoic intrusive rocks. The middle-late Mesozoic plutonic intrusions consist of quartz diorite and quartz monzonite. The Waterman Hills detachment fault (ca. 25-19 Ma; Singleton and Gans, 2008) separates the basement units from the overlying Cenozoic volcanic and sedimentary rocks.

Overlying Cenozoic lithologies consist of the Jackhammer Formation and Pickhandle Formations (25.6- ca. 19 Ma) (Burke et al., 1982; Dokka, 1989; Glazner et al., 2002; Singleton and Gans, 2008), and the Li-enriched Barstow Formation (BF; 19.4-13.0 Ma; Singleton and Gans, 2008; Eden et al., in review). The Jackhammer Formation consists of tuff, tuff breccia, volcanogenic sedimentary rock, arkosic conglomerate, and basalt (McCulloh, 1952; Jessey, 2010). The Pickhandle Formation is described as pyroclastic rocks and dacitic to rhyodacitic lavas. Volcaniclastic sedimentary units become more prevalent in the uppermost portions of the Pickhandle Formation underneath the overlying BF.

Barstow Formation

The BF contains many lateral and vertical facies changes across the Barstow region, which make it difficult to generalize stratigraphic units. Type sections for the BF are exposed in the Mud Hills and Calico Mountains. In the Mud Hills, unambiguous exposures of typical BF fluvio-lacustrine rocks have recently been constrained to between 16.4 and 13.0 Ma based on U-Pb dating of zircons in key ash marker beds (Eden et al., in review), which post-date the lacustrine units of the Calico Mountains area (19.5-16.9 Ma; Singleton and Gans, 2008). Restoring as little as 3 km of dextral slip along the Calico fault (Singleton and Gans, 2008) or up to 9.6 km (Dokka, 1983) would bring the two sub-basins adjacent to each other. Regional reconnaissance exploration efforts by Lithium Americas Corp. (Benson, 2023) ascertained that while many of the sediments mapped as BF contain Li above the average sedimentary rock (100-1000 ppm); the most Li-rich and economic locations (>1,000 ppm Li) in the BF occur in the Mud Hills and Calico Mountains north of the town of Barstow (Fig. 1; this study). The age constraints and similar geochemistry suggest the Mud Hills and Calico Mountains rocks record sedimentation within the same ancient basin. We therefore divide the BF into two members—the Mud Hills member (Fig. 2a) and the Calico member (Fig. 2b). We summarize the Mud Hills and Calico members based on field observations and previously established stratigraphic relationships outlined in Loughney and Badgley (2020; 2017) and Singleton and Gans (2008) respectively.

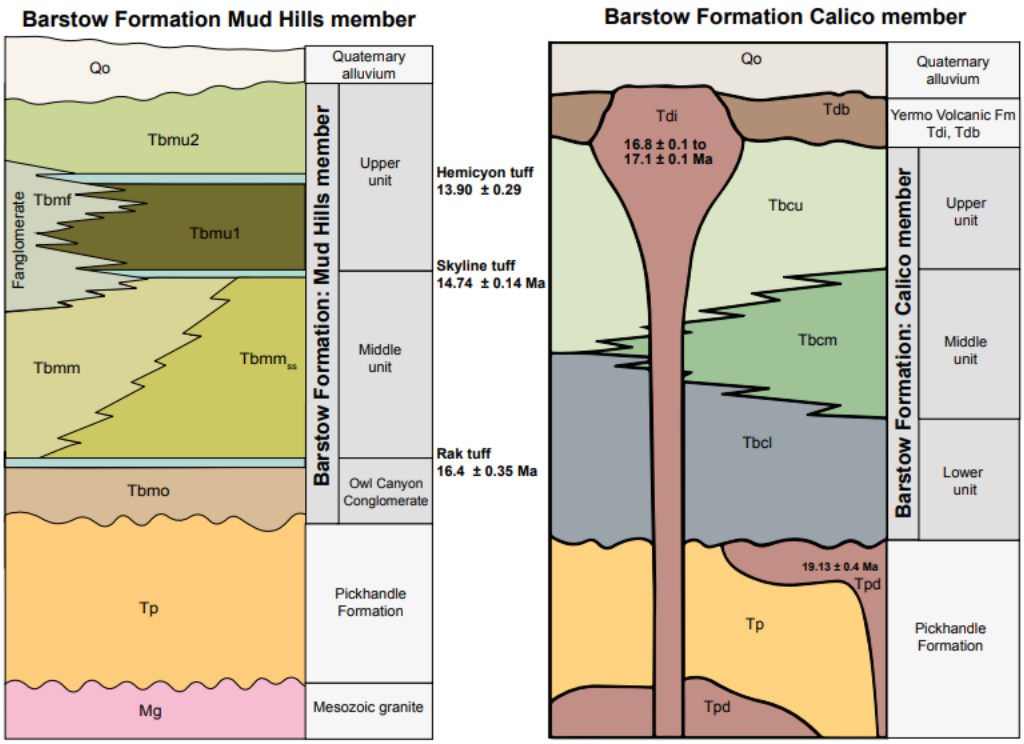

Figure 2. Schematic diagrams of stratigraphic units within Barstow Formation type section of the Mud Hills region (left; 16.4– 13.0 Ma; R. Eden, unpub. data, 2025) adapted from Loughney and Badgley (2017, 2020) and the Calico Member of the Barstow Formation (right; 19–17 Ma) adapted from Singleton and Gans (2008).

The Calico member

The Calico member (Fig. 2b) generalizes the stratigraphy of several sampling localities in and around the Calico Mountains area north of the Calico Fault (Singleton and Gans, 2008) (Fig. 1). The section consists of a Li-rich Lower, Middle, and Upper unit unconformably overlaying the Li-poor Pickhandle Formation. The Lower unit (Tbcl) consists of calcareous sandstones, siltstones, and carbonates. The Middle unit (Tbcm) contains fine-grained sandstones and mudstones with the rare calcareous sandstone. The Upper unit (Tbcu) contains mudstones, interbedded carbonates, siltstones, and evaporite beds. The Upper unit is capped unconformably by the Yermo Volcanic Formation (16.8-17.1 Ma; Singleton and Gans, 2008). Sporadic middle Miocene dacite intrusions

crosscut these units in various locations around the Calico Mountains area, especially along their northeast margins (Miller et al., 2022). The middle Miocene intrusions of dacite ca.16.8-17.1 Ma (Miller et al., 2022) have been linked to the formation of boron deposits north of the Calico fault (Carpenter and Reynolds, 2004). Similarly, andesitic intrusions west of Barstow are thought to be the cause for boron mineralization in the Rio Tinto Borax mine in Boron, California (Gans, 2023). In addition to boron, localized epithermal silver deposits exist within the Barstow Formation on the western side of the Calico Mountains, Mitchell Range, and Waterman Hills (Jessey, 2010).

Mud Hills member

The Mud Hills section (Fig. 2a) generalizes the stratigraphy of several sampling localities in the Mud Hills area including the BF type-section, which is widely known for its abundant Hemingfordian and Barstovian fossil assemblages (Woodburne et al., 1990; Park and Downing, 2001; Pagnac, 2009; Loughney and Badgley, 2017; Loughney et al., 2020; Loughney and Badgley, 2020; Loughney et al., 2023). The section contains three major lithologic sub-units: the Owl Conglomerate, Middle unit, and Upper unit (Lindsay, 1972; Woodburne et al., 1990; Dibblee Jr, 1994).

The Owl Conglomerate (Tbmc) of the Mud Hills member is made up of reddish conglomerates interbedded with sparse very fine to medium-grained sandstone, mudstone, and claystone units that unconformably overly the Pickhandle Formation. Its thickness ranges from 40-200 m (Woodburne et al., 1990). Tbmc contains trough cross-stratification and channel scours. Claystone interbeds are 30-40 cm thick and contain pedogenic structures, phytoliths (Loughney and Smith, 2015) root traces, and evidence of insect burrows (Loughney and Badgley, 2017). Tbmc is capped by 3m-thick tufa with mud cracks and stromatolitic layers.

The Middle unit of the Mud Hills member is composed of Tbmm (lacustrine) and $Tbmm_{ss}$ (sandstone) and is 470-570 m thick. It contains green-gray sandstones, siltstones, claystones, marl, some beds of tuff, and becomes finer grained eastward, northward, and northeastward. Sedimentary structures in this unit include burrows and mud cracks, redoximorphic concretions, algal laminae, root traces, stromatolites (Loughney and Badgley, 2017) and turbidite-like beds. Unit Tbmfg, which interfingers with the Middle member, is made up of coarse fanglomerate deposits as well as massively bedded sandy siltstones, and clayey siltstones interbedded with carbonate nodules. Tbmfg is exposed 4 km through the central Mud Hills (Woodburne et al., 1990).

The Skyline Tuff delineates the Middle member from the Upper member of the Mud Hills unit (Woodburne et al., 1990) and has a new age of 14.74 ± 0.14 Ma based on U-Pb zircon geochronology (Eden et al., in review). The Upper unit is at least 159 m-thick and consists of arkosic sandstone, as well as minor beds of limestone, tuff, and conglomerate. The Hemicyon Tuff (13.90 ± 0.29 Ma; Eden et al., in review) divides the Upper unit into two sub-units. The older strata (Tbmu1) also contain silty greenish-gray to brown claystones, often massively bedded while the younger strata (Tbmu2) contain grayish green, mud-cracked claystones and sandy siltstones. Other sedimentary structures include root casts, burrows, and weakly developed pedogenic features.

Detailed interpretations of the BF depositional setting from Loughney and Badgley (2017) depict an often-heterogeneous landscape with frequent hydrologic changes. To summarize, the Owl Conglomerate was likely deposited within a dynamic landscape of bedload-dominated stream channels and fine-grained interfluves on an alluvial fan. The depositional environment for the Middle unit of the Mud Hill member likely fluctuated between fluvial and lacustrine settings. The algal limestone and turbidite-like beds among alternating sandstones, and siltstones, and claystones particularly support the interpretation that the area was episodically inundated by a closed-basin

lake. The lacustrine units extend into the upper unit of the Mud Hills member of the Barstow Formation but become less frequent as the landscape transitions to more of a floodplain and ponded mudflat environment.

Materials and Methods

Lithologic samples were gathered from outcrops of the BF in the Mud Hills and Calico Mountains areas (Fig. 1). Sampling was focused on calcareous mudstones, as finer grain sizes tend to concentrate Li (Hampton and Benson, *This Volume*). Samples were classified based on the member from which they were collected (Fig. 2). While the generalized members provide a first-order constraint on the relative age and stratigraphic relation of samples, lateral changes in sedimentology across the large sampling region add some uncertainty to our classifications. Samples with ambiguous stratigraphic relationships are placed within undifferentiated sub-units (e.g., Tbm*; Fig. 2).

Trace Elemental Analysis

Trace element compositions for 174 outcrop whole-rock samples were measured at the Lithium Americas Li Technical Development Center (LiTDC) in Reno, Nevada. Samples were prepared using a two-step microwave-assisted acid digestion procedure and subsequently measured by inductively coupled plasma optical emission spectroscopy (ICP-OES). Dried bulk sample was weighed and dissolved with concentrated hydrochloric acid, nitric acid, and 50% hydrofluoric acid. The mixture was left to pre-digest for 10 min at room temperature before digestion within a CEM MARS6 Xpress microwave digestion oven. Next, boric acid was added prior to a second microwave digestion to dissolve fluorides. The resulting digestate was diluted to 50 mL prior to analysis.

The ICP-OES was calibrated from 0.1-40 ppm using 100 ppm analyte standard mix and an additional internal standard. The typical standard mix is a 100 ppm solution of Al, As, B, Be, Bi, Ca, Cd, Co, Cr, Cs, Cu, Fe, K, Li, Mg, Mn, Mo, Na, P, Rb, S, Sb, Se, Si, Sr, Ti, U, V, and Zn in 7% HNO_3. A blank solution and calibration verification was performed every 10-12 samples. Samples were volumetrically diluted as necessary to match the analyte concentration to the calibrated range.

Carbonate Oxygen and Carbon Isotopes ($\delta^{18}O$ and $\delta^{13}C$)

Bulk rock samples were first homogenized via ceramic mortar and pestle. For each sample, 500-2000 μg aliquots were weighed out and reacted with 70 °C phosphoric acid using a Kiel IV carbonate device. The evolved CO_2 was measured on a Thermo Finnigan MAT 253+. External precision (1σ) of oxygen and carbon isotope data was <0.1‰, based upon repeated measurements of two internal laboratory marble standards, BYM63150 and Carrara63150, calibrated against NBS 18, NBS 19, NBS 20, IAEA 603, ETH2 and ETH4 (Gagnon et al., 2023; Kaushik et al., 2023).

Clay Mineral Separations

Clay (<0.5 micrometer fraction) separations were performed on a subset of 12 bulk samples chosen to span a wide range of carbonate $\delta^{18}O$ and Li concentration values. This range was chosen to investigate Li enrichment under potentially different evaporative lake conditions. Bulk samples were first ground with a ceramic mortar and pestle and then reacted with a pH 5 potassium acetate buffer to remove all carbonates. We chose this reagent over HCl to avoid the potential dissolution of clay (Hu et al., 2022). The samples were then disaggregated with an ultrasonic probe for 1 minute before separating via centrifugation for 2 min at 2400 rpm. The resulting supernatant was transferred to a new vial and centrifuged for 30 min at 2400 rpm, decanted, then freeze dried for

48 hours. Centrifuge speeds and times were based on the centrifuge specifications and Stokes Law optimized for a <0.5 micrometer fraction (Poppe et al., 2001).

Clay Mineral X-ray Diffractometry

Clay mineral assemblages were determined via powder X-ray diffraction by matching measured peaks to reference patterns. Claystones were first crushed using an agate mortar and pestle using an up and down motion to minimize structural damage to the clays. Sample powders were mixed with DI water and pipetted onto inverted zero background mounts and then dried overnight on a hot plate at 50°C to make *{00l}* oriented mounts.

Samples were measured on a Bruker D2 phaser instrument equipped with a Cu Kα X-ray source, a 0.6 mm diffraction grating, 0.1mm anti-scatter shield for low angle measurements, 2° soller slits, Ni K-β filter, and a Lynxeye detector. Dried samples were measured from 3-50° 2θ, with a 0.02° 2θ step size and an integration time of 3 s/step. Following the DI water dried measurements, samples were kept overnight in a beaker with ethylene glycol to force the swelling clays to expand and then re-measured on the XRD under the same experimental conditions.

Qualitative clay mineral identifications were performed using the Diffrac.EVA software package from Bruker by matching patterns from the International Centre for Diffraction Data database. Quantitative clay fraction mineral percentages were calculated based on a linear counting rate following the calculations of Shofner (2006) after Hughes et al. (1994). The counts per second (cps) values for the 12.6-17.7 Å major smectite reflection, 6.9 Å kaolinite reflection, 7.2 Å chlorite reflection, and 10 Å illite reflection were used to calculate the percentage of smectite, illite, kaolinite and chlorite.

Carbonate Clumped Isotopes (Δ_{47})

Carbonate formation temperatures were determined using carbonate clumped isotope thermometry. Clumped values (Δ_{47}) were obtained from 6-8 mg of carbonate per replicate using an IBEX device (John and Davis, 2015; Davies et al., 2021). The IBEX first reacts the carbonate sample in a common acid bath using 90 °C phosphoric acid. After reacting for 10 minutes, the evolved CO_2 was purified and subsequently introduced and measured on the same Thermo Finnigan MAT 253+ in dual inlet mode at 17 V. Values for Δ_{47} were corrected using a standard reference frame, the Δ_{47} CDES scale, via measurement of international standards ETH1, ETH2, and ETH3 (Bernasconi et al., 2018; Bernasconi et al., 2021). Measurements at Brown University are made following the procedures outlined in Huntington et al., (2009), Dennis et al., (2011), and Davies et al., (2021) using the ^{17}O corrections outlined in Brand et al. (2021) and with a background correction based on mass scans using the mass 47.5 cup (Fiebig et al., 2019). Data reduction was conducted using the Easotope software (John and Bowen, 2016) including a non-linearity correction and empirical transfer function via the ETH standards to the Δ_{47} CDES reference frame to account for the working gas composition and scale compression (Bernasconi et al., 2021). Temperatures are calculated using the multi-lab consensus calibration of Anderson et al. (2021). Secondary standards ETH4, BYM63150 and Carrara63150 indicate Δ_{47} precision of 0.024 (1 S.D.) over the course of the four sessions. ETH4 Δ_{47} CDES values indicated an accuracy within ±0.02‰. Samples for this study were measured from July 2023 to January 2024.

Clay Oxygen Isotopes ($\delta^{18}O$)

Oxygen isotope composition of clays pellets were determined via dual inlet measurements on a Thermo Finnigan MAT 253+ mass spectrometer at 5 V following sample gas generation on a laser fluorination line. Briefly, clay separates were first mixed in a 1:1 ratio with LiF and pressed into pellets to prevent dispersion during lasing (Mix and Chamberlain, 2014; Mix et al., 2016).

Samples were then placed under vacuum in the laser chamber overnight. At the beginning of each analysis day, the samples were exposed to three 180 second preflourinations under vacuum with BrF_5 to liberate impurities from the samples and fluorination line. The O_2 gas was liberated from the samples by reaction with BrF_5 using a laser ablation system as described in (Ibarra et al., 2022; 2023). The O_2 gas was passed through a liquid N_2 trap, a KBr trap, a second liquid N_2 trap, and then sorbed on to a zeolite trap at liquid N_2 temperature. After evacuating remaining non-condensables, the O_2 gas was then passed through a molecular sieve gas chromatography column to another chilled zeolite using a He carrier gas before being introduced to the sample side bellow of the mass spectrometer. Daily drift corrections for oxygen isotope ratios were applied to the samples using the kaolinite reference standard Kga-1b (Mix et al., 2016; Gao et al., 2021; Kukla et al., 2022). All clay isotopic ratios are reported with respect to Vienna standard mean ocean water (VSMOW).

Clay Hydrogen Isotopes (δD)

A KCl cation exchange was first performed on separated clay samples to reduce the interlayer water content (Kanik et al., 2022). A total of 5mg of sample was mixed with 2mL of 1M KCl and heated for 24 hours at 60°C. Samples were rinsed three times, freeze dried, and weighed before being placed into silver capsules. The capsules were heated under vacuum at 250°C for 12 hours. Samples were loaded directly from the oven into an autosampler and pyrolyzed using a High Temperature Flash Elemental Analyzer (EA) in a ceramic reactor filled with glassy carbon at 1250 °C (Sharp et al., 2001). The EA was interfaced in continuous flow mode to a Delta V Isotope Ratio Mass Spectrometer (IRMS). Daily drift corrections for the hydrogen isotope ratios were applied to the samples using the mica standards USGS-58 and USGS-62 (Qi et al., 2017). Standard error is reported using KGa-1b as a secondary standard.

Calculation of Smectite Formation Temperatures and Water Composition ($\delta^{18}O_w$)

Formation temperatures were estimated for the smectite-rich samples in three different methods. Method 1 utilizes the measured hydrogen and oxygen isotopic composition for a given sample combined with known temperature dependent fractionation factor equations and the relationship between δD and $\delta^{18}O$ in meteoric waters:

$$3.54 * 10^6 T^{-2} = \delta\,^{18}O_{smectite} - 0.125\,\delta D_{smectite} + 8.95 \quad (0\text{-}150^oC)$$

(Delgado and Reyes, 1996)

The other two methods involve solving for the smectite formation temperature and $\delta^{18}O_w$ needed to explain the measured difference between $\delta^{18}O_{carb}$ and $\delta^{18}O_{clay}$ pairs. Utilizing the $\delta^{18}O_{carb}$ provides additional constraints on formation conditions and can be used to corroborate the results from Method 1. Methods 2 and 3 are based on intrinsic differences between the fractionation factor for the calcite-water system ($\alpha_{calcite\text{-}water}$) (Kim and O'Neil, 1997) and smectite-water system ($\alpha_{smectite\text{-}water}$) (Sheppard and Gilg, 1996) which, when combined, yield a predictable offset in $\delta^{18}O$ values for calcite and smectite ($\Delta\delta\,^{18}O_{smectite\text{-}calcite}$) formed from the same water. For minerals forming at a given temperature from the same water, this relationship depends on the measured $\delta^{18}O_{calcite}$, measured $\delta^{18}O_{smectite}$, and temperature.

$$\Delta\delta\,^{18}O_{smectite\text{-}calcite} = 2.55\,(10^6 T^{-2}) - 18.03(10^3 T^{-1}) + 28.37$$

(Kukla et al., 2022)

Based on this equation, the expected $\delta^{18}O$ offset between coeval calcite and clay would be approximately 3.5 ‰ between 0 and 30ºC (Kukla et al, 2022). The relationship is further complicated when each mineral phase forms at a different temperature and/or from a different formation water composition. In this case, an equation with one unknown becomes an equation with three or more unknowns. Adding constraints, however, is more insightful in cases where each mineral is forming under slightly different conditions, which leads us to Methods 2 and 3.

Method 2 for determining the smectite-specific formation temperatures and formation water compositions uses the measured $\delta^{18}O_{carb}$-$\delta^{18}O_{clay}$ offset combined with measured clumped isotope constraints of carbonate formation temperature and water composition. First, we used the measured $\delta^{18}O_{carb}$ and the measured carbonate $\delta^{18}O_{water}$ to calculate the $\alpha_{carb\text{-}water}$. We then used the $\alpha_{carb\text{-}water}$, $\delta^{18}O_{carb}$, and $\delta^{18}O_{clay}$ to calculate the $\alpha_{smectite\text{-}water}$. Using the smectite fractionation factor equation from Sheppard and Gilg (1996), we use the $\alpha_{smectite\text{-}water}$ to calculate the smectite formation temperature. We use the $\alpha_{smectite\text{-}water}$ and the measured $\delta^{18}O_{clay}$ to calculate the smectite $\delta^{18}O_{water}$ rearranging the equation based on the definition of the fractionation factor. This method assumes equilibrium formation conditions.

For method 3, we modeled the clay formation water composition and temperature combinations needed to satisfy the average observed $\delta^{18}O_{carb}$-$\delta^{18}O_{clay}$ offset in our the smectite-rich dominated samples, but this time varying the carbonate source water composition and carbonate formation temperature as well. This method avoids any potential error introduced from clumped isotope resetting during burial diagenesis (Passey and Henkes, 2012; Henkes et al., 2014; Stolper and Eiler, 2015). We calculated the $\delta^{18}O_{carb}$-$\delta^{18}O_{clay}$ offset using combinations of smectite formation temperatures (0-50 ℃), carbonate formation temperatures (0-50 ℃), clay $\delta^{18}O_w$ values (-20 to 10‰), and carbonate $\delta^{18}O_w$ values (-20 to 10‰). We kept only the results whose calculated

carbonate and clay $\delta^{18}O$ values were in the range of our measured datasets. We also filtered the results using conditions that would be reasonable for a lake system. The offset in the carbonate and clay formation $\delta^{18}O_w$ were filtered to be >0 and <5 ‰ to reflect a small and reasonable change in the $\delta^{18}O$-depth profile of the lake. Differences of a few per mil between surface waters and bottom waters are reasonable for arid-zone ephemeral lake or wetland systems (Costelloe et al., 2009). Similarly, the formation temperature offset between the carbonate and clay was filtered to be >0 and <15 °C to reflect a reasonable lake thermal gradient based on a database of modern long-term summertime vertical temperature profiles in 153 lakes (Pilla et al., 2021).

Results

Elemental concentrations

Bulk elemental concentrations measured on all collected samples are summarized in Appendix Table A1. Bulk Li concentrations range from 24 to 2496 ppm. Elevated Li also corresponds to magnesium-rich samples (Fig. 3), suggesting that the bulk of the Li is held within Mg-rich clays rather than other mineral phases, like carbonates or oxides. When regressed against Li/Mg, silicon, iron, aluminum, and potassium show no correlation (Fig. 4). We also observe no clear relationship between the abundance of Li and the abundance of arsenic, rubidium, molybdenum, or sulfur.

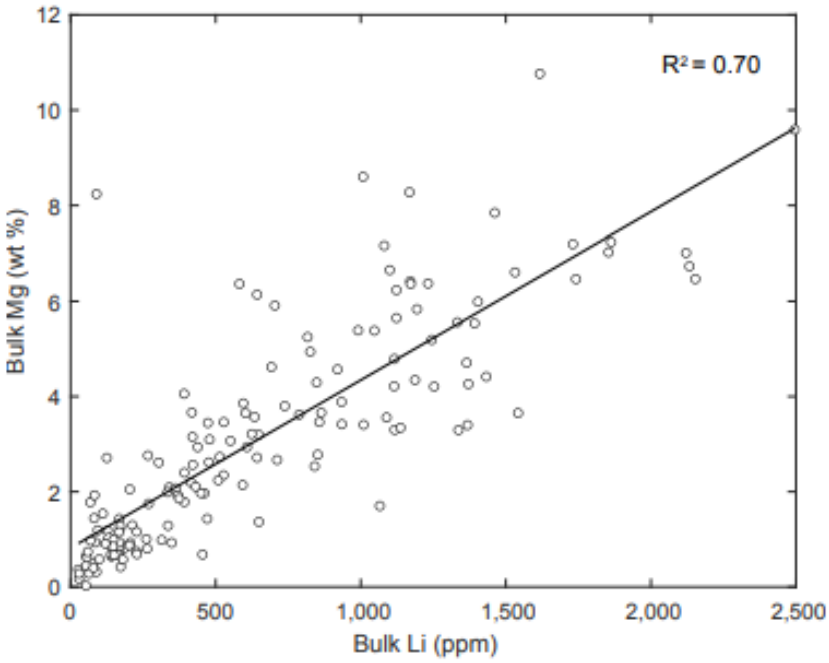

Figure 3. Lithium versus magnesium abundance in bulk outcrop samples from this study. Covariance suggests that Li is held mainly within the Mg-rich clay fraction of the bulk material.

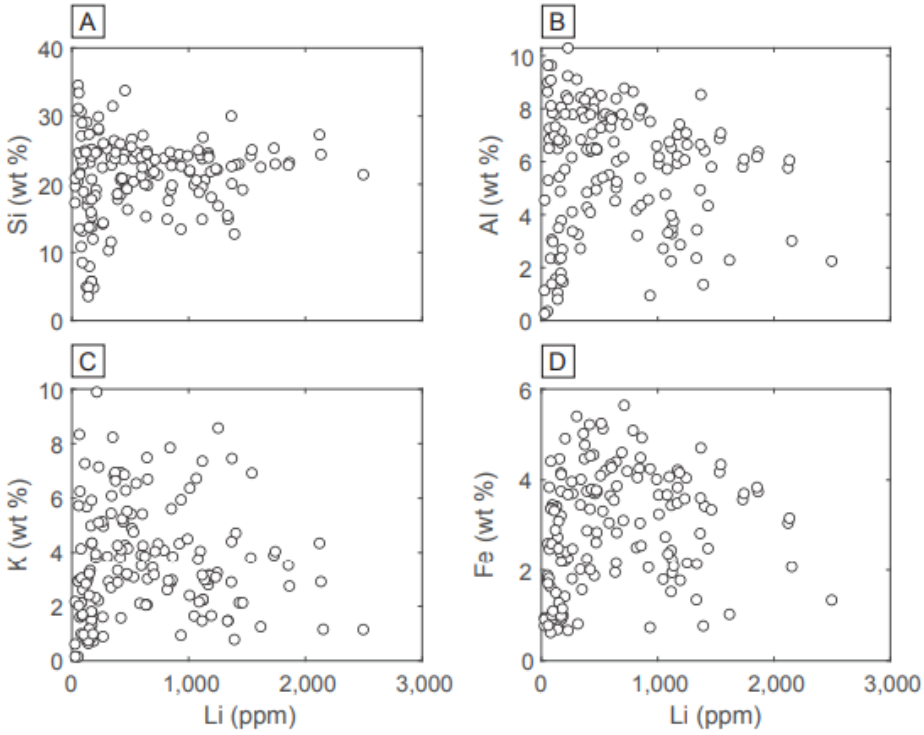

Fig. 4. Bulk elemental Si (A), Al (B), K (C), and Fe (D) versus bulk Li ppm.

Mineralogy

A subset of five Mud Hills samples and seven Calico Mountain samples were chosen for further XRD, clay isotope analysis, and carbonate clumped analysis. Samples were chosen for their high carbonate content, high clay content, and wide range of Li concentrations and isotope values. The bulk and clay separate mineralogy of these twelve samples are summarized in Table 1. Common phases in the bulk samples include calcite, dolomite, or both; quartz; Na-zeolite; and a variety of sodium and potassium-rich feldspars.

With respect to the clay separates, seven samples exhibited peak shifts after glycolation, indicating a smectite component (Fig. 5). The XRD spectra of four samples were unchanged after glycolation, demonstrating the absence of a mixed-layer or smectite component (Table 2; Fig. 5). The XRD result therefore shows the characteristic double reflections associated with the I(001)/S(002) and I(002)/S(003) peaks, which is an important identifier of mixed layer clays (Moore and Reynolds Jr., 1989; Mills et al., 2023). Clay fraction mineral percentages show that Li concentrations covary with percent smectitic clay (Table 2, Fig. 5-6). Conversely, some of the most Li-poor samples have a higher percentage of illitic clay (Fig. 5-6). In addition to smectite, illite, and some kaolinte, the clay separates often contained Na-zeolites and felspar phases. There appears to be a negative correlation with % K, Fe, and Al in samples >40% smectite. Samples <40% smectite have more variable chemistry and correspond with some of both the highest and lowest K, Fe, Al, and Si concentrations.

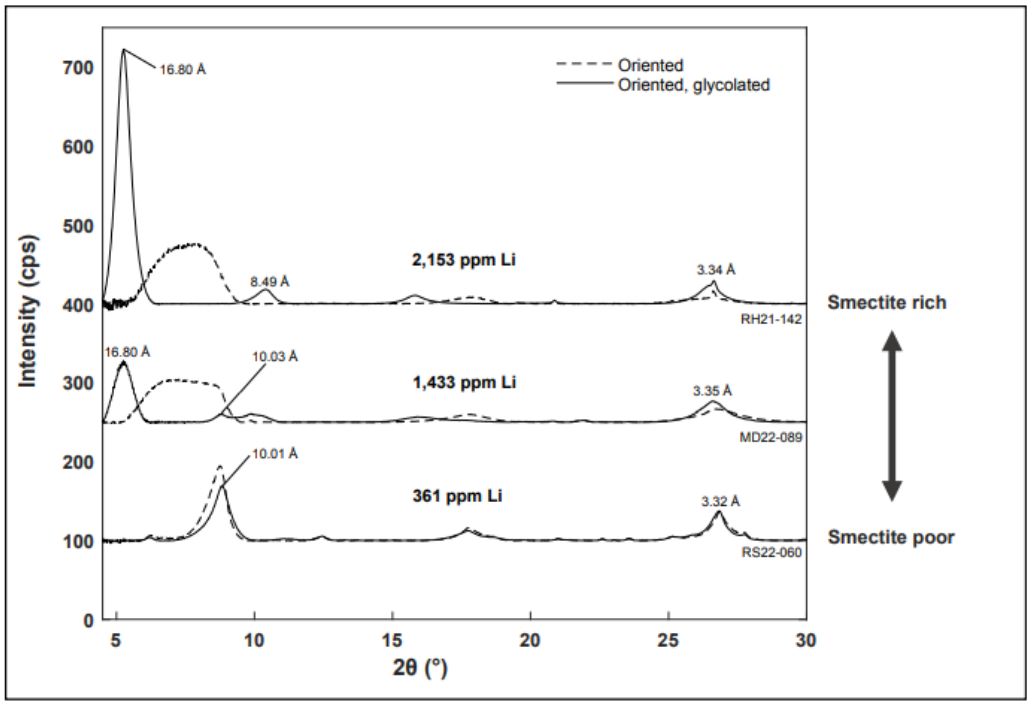

Figure 5. Representative peak intensities for oriented clay separates before (dotted line) and after (solid line) glycolation. Samples with a high percentage of smectite are generally associated with higher bulk Li concentrations.

Table 1. Summary of Barstow mineralogy

Location	Sample ID	Clay separates	Bulk sample
Calico Mountains	RS22-081	Illite and smectite	Calcite, dolomite, albite, illite, sicherite, sanadine, quartz, clinoptilolite
	RS22-072	Minor smectite, illite, lots of quartz, potassium feldspar, possible chlorite (peak at 6-2theta)	Calcite, sanadine cristobalite, quartz, montmorillonite, illite, kaolinite, albite, natrolite, bassanite, brucite
	RS22-060	Illite, clinochlore, zeolite, diopside/anorthite	Calcite, albiite, dolomite, clinochlore, muscovite, sanadine, orthoclase
	RH21-142	Almost pure smectite	Ankerite, quartz, calcite, montmorillonite, gypsum, analcime, magnetite, hematite
	WJ22-069	Smectite, illite, kaolinite, fair amount of calcite	Calcite, bassanite, quartz, illite, montmorillonite, albite, ankerite, magnesite
	WJ22-068	Poor sample yield; not measured	Calcite, ankerite, quartz, calcium sulfate, illite, kaolinite, albite, orthoclase
	MD22-089	Smectite, illite, clinoptilolite, cristobalite	Calcite, clinoptilolite, quartz, illite, montmorillonite, cristobalite, ankerite, titanite, sanadine, albite
Mud Hills	OC23-024	Illite, sanidine, analcime, kaolinite	Calcite, albite, sanadine, analcime, illite
	OC23-027	Smectite, illite, kaolinite, analcime, diopside	Calcite, illite, montmorillonite, cristobalite, diopside, sanadine, analcime
	OC23-022	Illite, kaolinite, analcime, sanidine	Calcite, sanadine, analcime, illite, cristobalite, natrolite, ankerite
	OC23-021	Illite, kaolinite, diopside, sanidine	Calcite, orthoclase, illite, analcime, cristobalite, albite
	OC23-028[1]	Smectite, illite, analcime, kaolinite, sanidine	Calcite, dolomite, illite, sanadine, analcime

[1]Bulk carbonate values are from sandy-siltstone interbed, rather than the mudstone matrix

Table 2. Peak location and heights of clay phases and their calculated percentages

			Smectite			Illite		Chlorite and kaolinite		
Location	Sample ID	Li (ppm)	Peak location	Max intensity (cps)	% of clay	Max intensity (cps)	% of clay	Peak location	Max cps	% of clay
Calico Mountains	MD22-089	1,433	5.130	77.715	71	10.824	28	12.392	0.280	0.33
	RH21-142	2,153	5.148	322.017	96	3.774	3	12.392	1.943	0.74
	RS22-060	361	5.272	1.837	1	69.660	96	12.331	5.454	3.37
	RS22-072	168	5.251	1.375	6	5.116	62	12.230	5.946	32.34
	RS22-081	643	5.089	147.804	82	11.159	18	12.392	0.505	0.36
	WJ22-069	1,392	5.150	166.071	96	2.281	4	12.412	0.646	0.48
Mud Hills	OC23-021	841	5.251	1.375	1	52.892	99	12.392	0.544	0.46
	OC23-022	1,371	5.332	0.948	1	51.500	99	12.412	0.375	0.32
	OC23-024	935	5.373	1.450	1	41.426	98	12.412	0.972	1.03
	OC23-027	2,133	5.150	4.762	7	23.469	93	12.392	0.380	0.68
	OC23-028	1,863	5.150	54.248	47	21.476	53	12.392	0.383	0.42

Note: Peak locations reflect 2Θ values after anchoring illite peak to 8.7

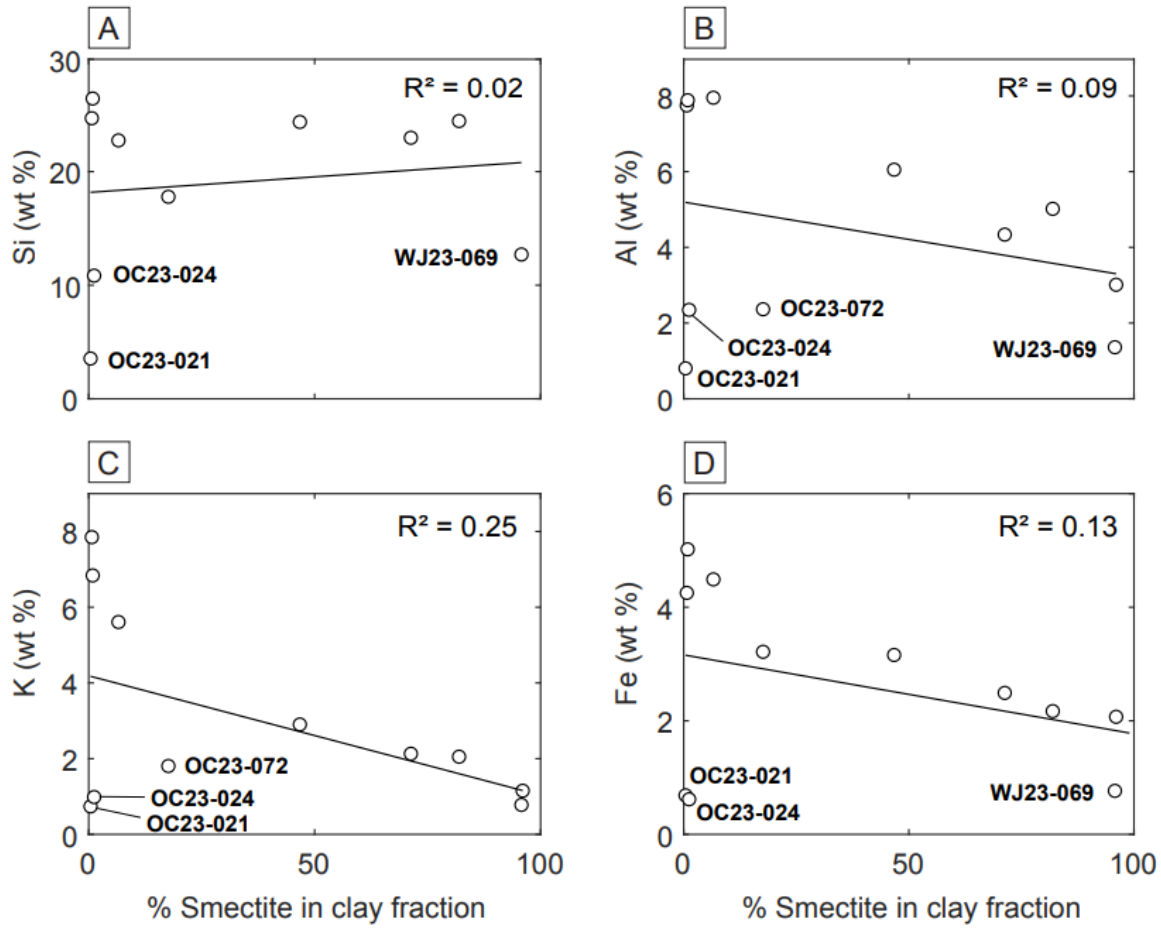

Figure 6. Bulk elemental Si (A), Al (B), K (C), and Fe (D) versus relative percent smectite within the clay fraction.

Carbonate stable isotopes

All samples were analyzed for bulk inorganic $\delta^{18}O$ and $\delta^{18}O$ (Table A2); however, we only report isotope values for samples with sufficient CO_2 yields (>5 % carbonate). In most cases, the carbonate minerals are calcite, dolomite, or a mixture of both (Table 1) finely mixed throughout the sample matrix and can only be identified in the field after applying a drop of 10% HCl. Rarely, mudstone samples contain fine carbonate laminations. Coarser-grained samples often contained carbonate in the form of fined-grained white cement or within yellow-orange stromatolitic layers. Carbonate $\delta^{18}O$ values range from -13.68‰ to 4.06‰ (VPDB) while $\delta^{13}C$ range from -16.09‰ to 5.57‰ (VPDB) (Fig. 7; Table A2). The oxygen isotope values of the Owl Canyon Conglomerate and the youngest Calico member samples are both on average higher than the samples from the Middle unit of the Mud Hills member. The samples from Tbu2 (<13.9 Ma) have lower than average values when compared to the rest of Mud Hills. We observe an overall slightly positive $\delta^{18}O$-$\delta^{13}C$ trend with a slightly variable slope and intercepts in each lithologic unit ($0.3 < R^2 < 0.8$; P-value <0.018). The $\delta^{13}C$ values generally decrease through time until the deposition of the Upper Mud Hills member when the average values increase slightly (Fig. 8). The lowest $\delta^{13}C$ values exist as outliers within the Middle Mud Hills unit, Tbmm (Fig. 7; Fig. 8).

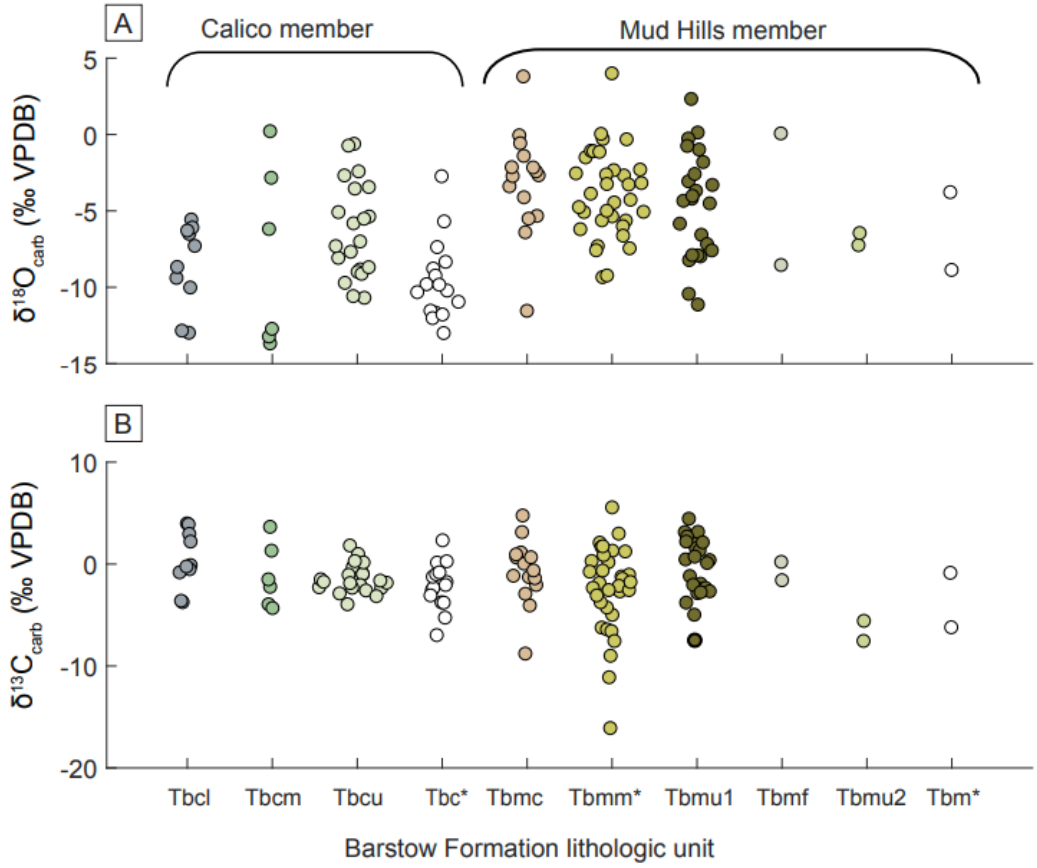

Figure 7. Carbonate δ18O values (A) and δ13C values (B) from mudstones within various members of the Barstow Formation. Lithologic symbols are described in Figure 2. Asterisks represent undifferentiated units. Abbreviation: VPDB = Vienna Pee Dee Belemnite.

Carbonate clumped values for Δ_{47} ranged from 0.50 to 0.63 (Table A3). The calculated carbonate clumped isotope mineral formation temperatures range from 15.0 +8.5/-9.3°C to 64.5+3.4/-3.5°C (Fig. 11; Table 4). The calculated formation waters compositions ranged from -4.60 +5.8/-8.9 to 7.92 +8.3/-9.2 VSMOW.

Table 3. Summary of carbonate clumped isotope temperatures

Location	Sample ID	Temperature calibration[1]	Δ_{47} (CDES)	Δ_{47} (CDES) SD	Δ_{47} (CDES) SE	Δ_{47} formation temp (°C)	Δ_{47} formation temp (°C) error	Δ_{47} formation water $\delta^{18}O$ (VSMOW)	Δ_{47} formation water $\delta^{18}O$ (VSMOW) error
Calico Mountains	RS22-081	Dolomite	0.580	0.011	0.008	31.8	+2.8/–2.9	–0.79	+5.8/–7.1
	RS22-072	Calcite	0.568	0.029	0.017	34.2	+6.1/–6.5	–4.60	+5.8/–8.9
	WJ22-068	Calcite	0.533	0.025	0.014	48.0	+5.8/–6.1	1.21	+8.5/–11.3
	WJ22-069	Calcite	0.497	0.013	0.007	64.5	+3.4/–3.5	6.05	+11.8/–13.5
	MD22-089	Calcite	0.597	0.015	0.007	23.9	+2.3/–2.4	–2.93	+4.7/–5.9
	RH21-142	Dolomite	0.587	0.018	0.010	29.3	+3.4/–3.5	2.26	+5.2/–6.9
Mud Hills	OC23-23	Calcite	0.625	0.041	0.029	15.0	+8.5/–9.3	–2.94	+1.4/5.7
	OC23-028	Dolomite	0.549	0.008	0.005	43.4	+2.0/–2.0	7.92	+8.3/–9.2

Standard ID	*n* replicates	Δ_{47} (CDES) Average	Δ_{47} (CDES) SD	Δ_{47} (CDES) SE	Known Δ_{47} (Bersaconi et al., 2021)
Primary standards					
ETH1	23	0.2067	0.0261	0.0054	0.2052
ETH2	25	0.2068	0.0278	0.0056	0.2085
ETH3	35	0.6124	0.0164	0.0028	0.6132
Secondary standards					
BYM	8	0.3305	0.0244	0.0086	
Cararra	14	0.3100	0.0323	0.0086	
ETH4	7	0.4337	0.0152	0.0058	0.4505

Clay stable isotopes

The twelve clay separates were analyzed for their δD_{clay} and $\delta^{18}O_{clay}$. The $\delta^{18}O_{clay}$ values range from 7.3 to 19.3‰ VSMOW, while the δD_{clay} values range from -106.6 to -139.3‰ VSMOW (Table 3). Clay $\delta^{18}O$ and δD values plot in a distribution subparallel to the stable isotopic global meteoric water line with a shallower slope (Fig. 9). When considering only smectite-rich samples, the distribution has a steeper slope due to lower δD in the smectites. The clay formation temperatures range from 14.1 +6.7/-6.2°C to 51.2 +7.1/-6.7°C (Fig. 11; Table 3).

Table 4. Clay oxygen and hydrogen isotope values

	Sample ID	Pellet $\delta^{18}O$ (VSMOW)	Pellet replicates	$\delta^{18}O$ SD	$\delta^{18}O$ SE	δD (VSMOW)	δD replicates	δD corrected SD	δD Corrected SE	Formation temperature (°C)	Clay temp positive error (°C)	Clay temp negative error (°C)
Calico Mountains	MD22-089	19.35	2	1.28	0.91	–116.93	2	11.50	8.13	14.06	6.66	6.22
	RH21-142	15.41	3	1.74	1.01	–130.18	3	2.43	1.40	22.00	4.39	4.20
	RS22-060	12.03	3	0.55	0.32	–107.26	2	0.96	0.68	47.72	1.90	1.87
	RS22-072	11.43	2	1.10	0.78	–109.84	2	3.06	2.17	49.01	5.06	4.83
	RS22-081	17.38	1	1.34	0.37	–125.73	2	5.35	3.78	17.00	2.96	2.87
	WJ22-068	7.29	2	1.96	1.39		1		0.43	51.16	7.16	6.72
	WJ22-069	12.38	2	2.71	1.92	–130.33	2	1.15	0.81	33.61	8.59	7.92
Mud Hills	OC23-021	18.14	1	1.34	0.37	–117.61	2	5.70	4.03	17.90	3.09	3.00
	OC23-022	16.89	1	1.34	0.37	–114.11	2	5.76	4.07	23.94	3.31	3.21
	OC23-024	14.67	2	2.74	1.94	–114.76	2	7.93	5.61	32.20	11.21	10.10
	OC23-027	17.97	1	1.34	0.37	–122.46	2	1.98	1.40	16.39	1.89	1.85
	OC23-028[1]	13.80	3	1.75	1.01	–122.24	2	3.87	2.73	31.96	5.57	5.28

Standard ID	$\delta^{18}O$ drift corrected average	$\delta^{18}O$ replicates	$\delta^{18}O$ drift corrected SD	$\delta^{18}O$ drift corrected SE	δD (VSMOW) average	δD replicates	δD corrected SD	δD corrected SE
Kga-1b	21.23	32	0.68	0.12	–55.5917204	3	0.53	0.31
SKFS	32.94	10	1.24	0.39				
SHCa-1	20.59	7	1.05	0.40				
SCO_3	6.63	2	1.27	0.90				
Brazil Quartz	17.55	2	1.19	0.84				
C-6	13.70	13	1.34	0.37				
USGS-57					–30.2183327	6	0.60	0.25
USGS-58					–30.2183327	5	0.60	0.27

Abbreviation: SD = dstandard deviation, SE = standard error, VSMOW = Vienna standard mean ocean water
[1]Bulk carbonate values are from sandy-siltstone interbed, rather than the mudstone matrix

Table 5. Summary of paired clay and carbonate isotope measurements

Table 5. Summary of Paired Clay and Carbonate Isotope Measurements

Location	Sample ID	$\delta^{18}O_{carb}$ (VSMOW)	$\delta^{18}O_{clay}$ (VSMOW)	δD_{clay} (VSMOW)	$\Delta^{18}O_{carb\text{-}clay}$
Calico Mountains	MD22-089	25.66	19.35	–108.80	6.32
	RH21-142	30.29	15.41	–128.37	14.88
	RS22-060	24.55	12.03	–106.58	12.52
	RS22-072	21.88	11.43	–112.01	10.45
	RS22-081	26.66	17.38	–121.94	9.27
	WJ22-068	25.24	7.29	–139.31	17.95
	WJ22-069	27.38	12.38	–129.52	15.00
Mud Hills					
	OC23-021	29.79	18.14	–113.58	11.65
	OC23-022	26.02	16.89	–110.03	9.13
	OC23-024	29.75	14.67	–109.15	15.08
	OC23-027	30.59	17.97	–121.06	12.62
	OC23-028[1]	33.32	13.80	–119.51	19.53

Abbreviation: VSMOW = Vienna standard mean ocean water
[1]Bulk carbonate values are from sandy-siltstone interbed, rather than the mudstone matrix

Discussion

Carbonate Formation Conditions

The covariation in $\delta^{18}O$ and $\delta^{13}C$ values of BF carbonates indicate that the carbonate minerals formed in a range of evaporatively evolved lake or pore water conditions associated with an underfilled lake discharge basin to a balance-filled lake basin (Fig. 8). Generally, a strong covariance ($R^2 > 0.7$) indicates considerable long-term stability in the hydrological characteristics of a lake, and is indicative of a underfilled discharge basin, such as CV, with characteristics that include intermittent surficial water influx, persistently closed surficial outflow, and persistent groundwater inflow with no groundwater outflow (Li and Ku, 1997; Gagnon et al., 2023; Benavente and Bohacs, 2024, and references therein). Common features of this basin type include ephemeral to intermittent ponds and sparsely developed wetlands. Balance filled systems have surface and groundwater hydrology that is open on various timescales and consequently have a range of water residence times and lake $\delta^{18}O$ and $\delta^{13}C$ compositions impacting the expression of the covariant trend through time. Generally, underfilled basins have a minor to moderate carbonate $\delta^{18}O$ and $\delta^{13}C$ covariation, and more common ponds and wetlands than underfilled systems. Open systems have no $\delta^{18}O$ and $\delta^{13}C$ covariation but contain abundant ponds, wetland/ fluvial systems (Benavente and Bohacs, 2024, and references therein).

During the deposition of Tbcm (Early Miocene), Barstow carbonates indicate an underfilled lake discharge basin ($R^2 > 0.8$). Additional evidence to support this interpretation includes the presence of dark green mudstones and gypsum laminae, and sub cm scale bedding. During the deposition of Tbcl and Tbcu (Early Miocene) and Tbmc, Tbmm, and Tbmu (Middle Miocene), Barstow carbonates had a low to moderate covariation in $\delta^{18}O$ and $\delta^{13}C$ ($0.3<R^2<0.7$), indicative of a balance-filled lake basin that was periodically open (Fig 8). Our interpretations for

the Barstow basin type are consistent with the range of depositional environments expressed throughout the Mud Hills region (Loughney and Badgely, 2020).

Changes in lake basin morphology likely impact the carbonate $\delta^{18}O$-$\delta^{13}C$ trend through time (Fig. 8). The slope of the $\delta^{18}O$ and $\delta^{13}C$ trend is directly related to their area-to-depth ratio, such that wide and shallow (narrow and deep) water bodies have a shallower (steeper) slope (Talbot, 1990). Changes in the intercept may be due to changes in the slope, or when the slope is constant, changes to the $\delta^{18}O$ and $\delta^{13}C$ of source waters to the lake basin (Benavente and Bohacs, 2024, and references therein). For example, an increase in primary production, fermentation, or non-equilibrium CO_2 outgassing could impact the covariant trend by driving lake $\delta^{13}C$ values are anomalously high. Generally, lower $\delta^{13}C$ values may be the result of an increase in hydrothermal waters feeding the lake, the presence of methanogens, or an increase in vegetation cover on the landscape.

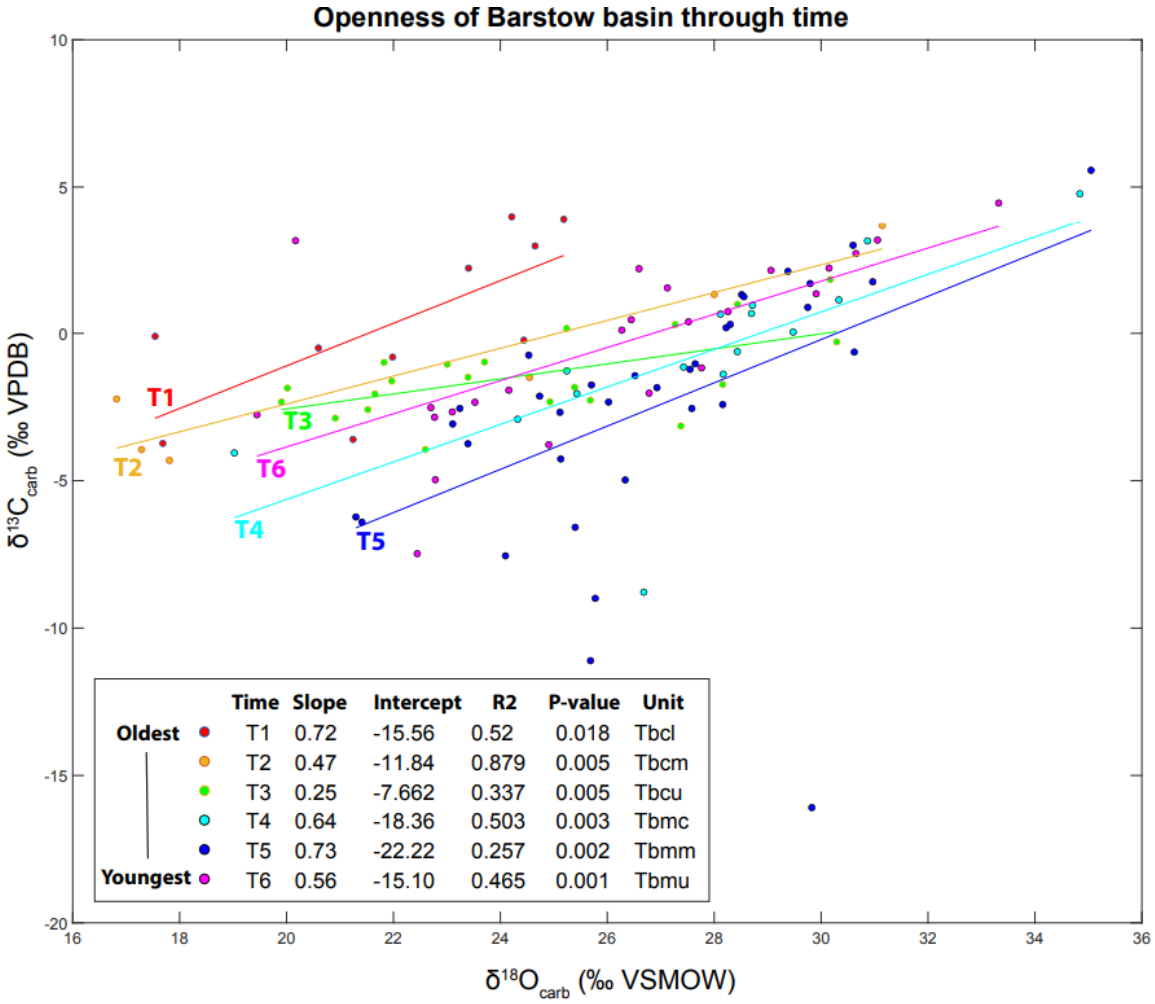

Figure 8. Changes in the covariant trend in Barstow carbonate δ18O-δ13C through time based on stratigraphic order of lithologic units from Figure 2 with n > 3. Carbonates show a moderate to strong correlation between δ18O versus δ13C, with minimal changes in the slope and intercept of the covariant trend. Abbreviations: VPDB = Vienna Pee Dee Belemnite, VSMOW = Vienna standard mean ocean water.

The Barstow Formation experienced a shallowing of its $\delta^{18}O$-$\delta^{13}C$ slope during the depositional interval spanning the Calico member. This indicates the basin was shallowing and widening through the middle Miocene. There is a decrease in the y-intercept ($\delta^{13}C$ values) between the lower unit and middle unit of the Calico member, which may indicate an increase in hydrothermal fluids entering the catchment after the deposition of Tbcl. We prefer this interpretation based on the existence of coeval felsic magmatism in the Calico Mountain area, and

the additional observation that generally higher Li concentrations are observed within the younger units of the Calico member. The $\delta^{18}O$-$\delta^{13}C$ slope steepened slightly between the deposition of the upper Calico member and lower Mud Hills member, then remained strikingly consistent through the end of the BF. The y-intercept continues to decrease through deposition of the Mud Hills member, then increases during the deposition of the Upper unit (Tbmu). Changes to this uppermost unit may be the result of coeval changes related to the C4 grass expansion, cooling, and drying of the landscape (Laughney and Badgley, 2023). We observe negative $\delta^{13}C$ outliers in some Mud Hills samples from the Mud Hills (Fig. 7B; Fig. 8), and therefore argue that the lake was at least occasionally fed by hydrothermal waters. The existence of hot springs is evident from the presence of tufa in the Mud Hills combined with elevated clumped isotope formation temperatures (Horton et al., 2016).

The clumped isotope results provide further insight into carbonate mineralization conditions. The clumped values for temperature and $\delta^{18}O_{water}$ reflect the lake or pore water conditions at the time of authigenic carbonate mineralization, burial diagenesis, or hydrothermal fluid conditions during re-crystallization. Despite some elevated temperatures, we rule out hydrothermal formation waters for two reasons. (1) Calcite forming from hydrothermal fluids would lead to an inverse or absence of correlation between bulk Li and $\delta^{18}O_{carb}$ which is the opposite of what we observe (Fig. 8B). Although hydrothermal fluid alteration can increase the concentration of Li within the bulk sediments, isotopic exchange of oxygen with hydrothermal fluids would drive the neoformed carbonates toward lower $\delta^{18}O$ values. The positive correlation between Li and $\delta^{18}O_{carb}$ instead suggests that the carbonates formed under evaporative conditions, as recently hypothesized for CV (Fig. 12; Gagnon et al., 2023). (2) Additionally, the wide range of $\delta^{13}C$ and its covariance with $\delta^{18}O_{carb}$ are more characteristic of low temperature surface

environments. In contrast, hydrothermally altered sediments of the TP deposit contain carbonates with a narrow range of enriched, magmatic $\delta^{13}C$ values and no correlation between $\delta^{18}O$ and $\delta^{13}C$ (Emproto et al., *This Volume*). Alternatively, the elevated carbonate formation temperatures could reflect carbonate clumped reordering during diagenesis. This may be the case for at least some Calico Mountains region samples north of the Calico fault where there may have been high heat flow due to Miocene dacite intrusions and/or dissolution-reprecipitation reactions related to post-depositional deformation from dextral transpression. Future in-depth mineralogical and petrological analyses of the carbonate minerals may clarify the role of diagenesis in the high temperature carbonate clumped samples.

We interpret the carbonate clumped isotope values as primary ephemeral lake or pore water temperatures during calcite and/or dolomite mineralization in hyperalkaline ephemeral wetland environment. Although ancient lacustrine carbonate Δ_{47} temperatures upwards of 30 °C to 40 °C are often interpreted to represent early diagenesis, a few modern hypersaline lakes have regularly reported temperatures of near 40 °C and have high salt concentrations and chemical precipitates like gypsum and halite (Hren and Sheldon, 2012). We note evidence of gypsum within several hand samples including one of the three samples with Δ_{47} temperatures >40 °C (64.5 °C, WJ22-069).

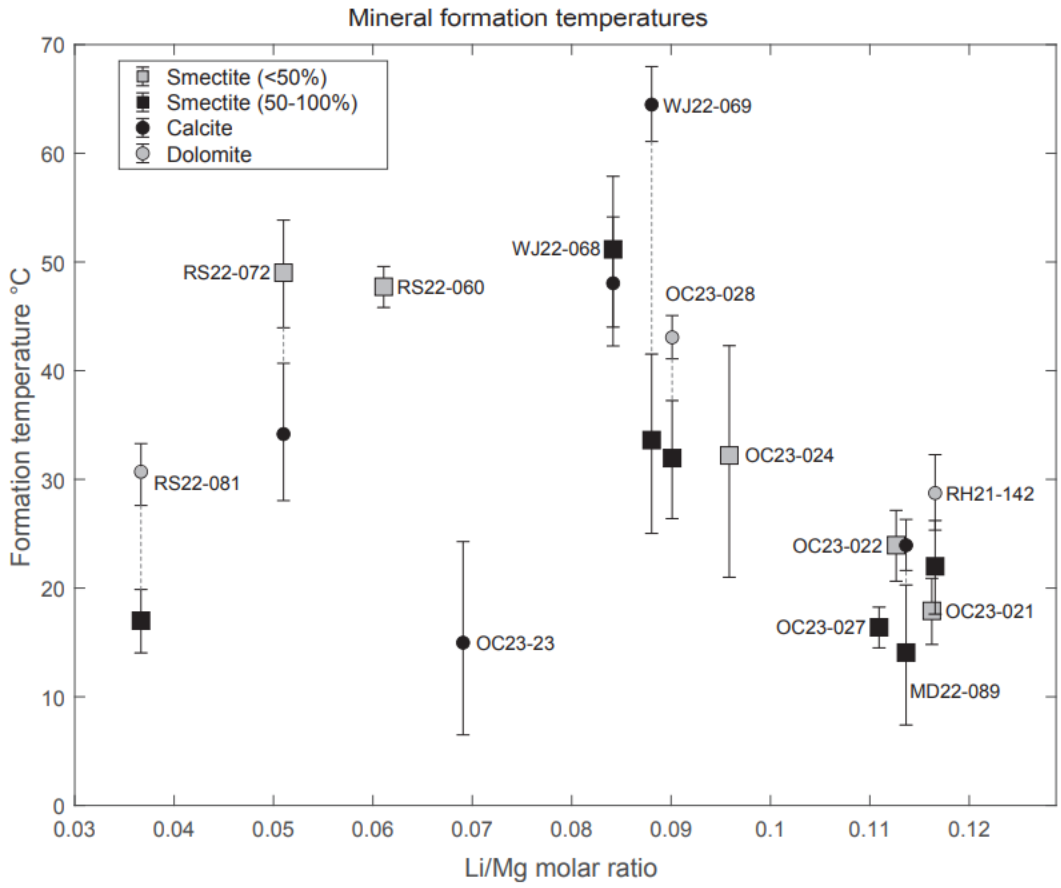

Figure 9. Calculated smectite, calcite, and dolomite formation temperatures. Smectite formation temperatures were calculated using the relationship between δD and $\delta^{18}O$ in meteoric waters after Delgado and Reyes (1996). Calcite formation temperatures were calculated from clumped isotope values using the composite Δ_{47} temperature regression from Anderson et al. (2021). Dolomite temperatures were calculated from the composite Δ_{47} temperature regression from Anderson et al. (2024).

We suspect the wide range in Δ_{47} temperatures and $\delta^{18}O_{water}$ values to be a result of large diurnal and sub-annual water temperature fluctuations. Ephemeral wetlands have been shown to have diurnal to multi-annual scale changes in water chemistry, due to their generally shallow nature and fluctuating water level (Boeckman, 2007; Black, 1976; Serrano, 1995). A study of small ponds in Oklahoma documented a range of surface water temperatures from 0.5 °C to 39.4 °C over the course of 2 years, which covers most of the range of our Δ_{47} temperatures (Black, 1976).

The high carbonate clumped $\delta^{18}O_{water}$ values provide additional evidence that the carbonates were forming in an environment with precipitation fluxes outpacing evaporation. The carbonate $\delta^{18}O_{water}$ values, which we think reflect ancient $\delta^{18}O_{lake}$ values, are much higher (Fig.3) (-4.60 ‰ to 8.27 ‰) than modern meteoric water for the southern Great Basin region ($\delta^{18}O_{meteoric}$, -15 to -10 ‰) (Coplen and Kendall, 2000; Friedman, 2000; Friedman et al., 2002; Henderson and Shuman, 2009). In modern waters of western North America, there is an average offset of $\delta^{18}O_{lake}$ and $\delta^{18}O_{meteoric}$ of +4.6‰ with a maximum of +23.5‰ (Horton et al., 2016); the difference is greater in regions with lower humidity.

In summary, the carbonate stable isotope results suggest that the carbonate minerals within the fine-grained (and Li-rich) facies are mostly forming from evaporatively evolved shallow lake to ephemeral wetland waters with some potential influence from hydrothermal input to the surface watershed.

Clay Formation Conditions

Our bulk geochemical data indicate that the BF Li-clays from both the Mud Hills and Calico Mts. are primarily Mg-smectites. In addition to high concentrations of Mg, samples generally display a high abundance of smectite and a correlation between Mg and Li (Fig. 3). Previously reported sedimentological observations are consistent with variable underfilled ephemeral lake and wet playa environments, which are known to support the formation of authigenic magnesian clays (Warren, 2016; Pozo and Calvo, 2018). Clay formation temperatures gleaned from the stable isotopes are also consistent with a near-surface formation environment (Fig.11). These smectite formation temperatures derived from the paired $\delta^{18}O$ and δD measurements (Fig. 9) are likely a maximum due to evaporative effects (Chamberlain et al., 2012; Mix et al., 2016; Ibarra and Evaristo, 2024). Additionally, the shallow slopes of the hydrogen and

oxygen isotope values when compared to the global meteoric water line are indicative of evaporative modification of waters around the time of smectite formation in the Barstow basin (Fig. 9). These hydrogen and oxygen isotope results are consistent with $\delta^{18}O$ and δD values of previously sampled smectites from Rainbow Basin in the Mud Hills (Horton and Chamberlain, 2006). The slightly shallower $\delta^{18}O$ vs δD slope in the BF smectites reflects a regional climate that is slightly drier than the conditions observed in the Late Miocene El Paso Basin (13.5 Ma – 7 Ma) just north of the Mojave block to the east of the southern Sierra Nevada (Horton and Chamberlain, 2006). Both the ancient Barstow and El Paso basins have more evaporative slopes than the modern southern Great Basin today (Fig 9; Putman et al., 2019).

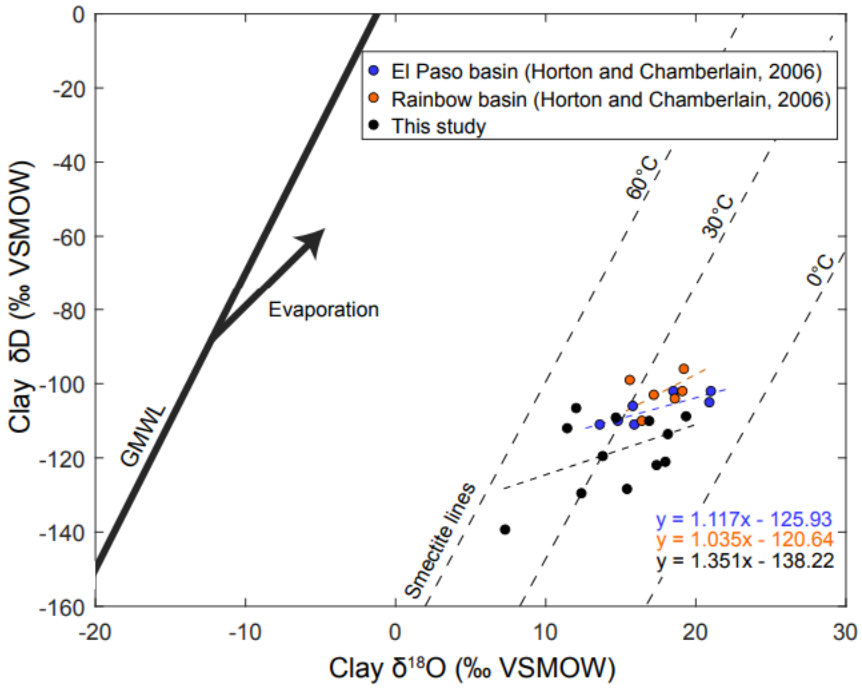

Figure 10. Mixed clay δD versus $\delta^{18}O$ values from this study compared with previously measured smectites from Rainbow basin, California (orange) and El Paso basin, California (blue). Abbreviations: GMWL = global meteoric water line, VSMOW = Vienna standard mean ocean water. Smectite lines represent the expected fractionation from the GMWL at various temperatures.

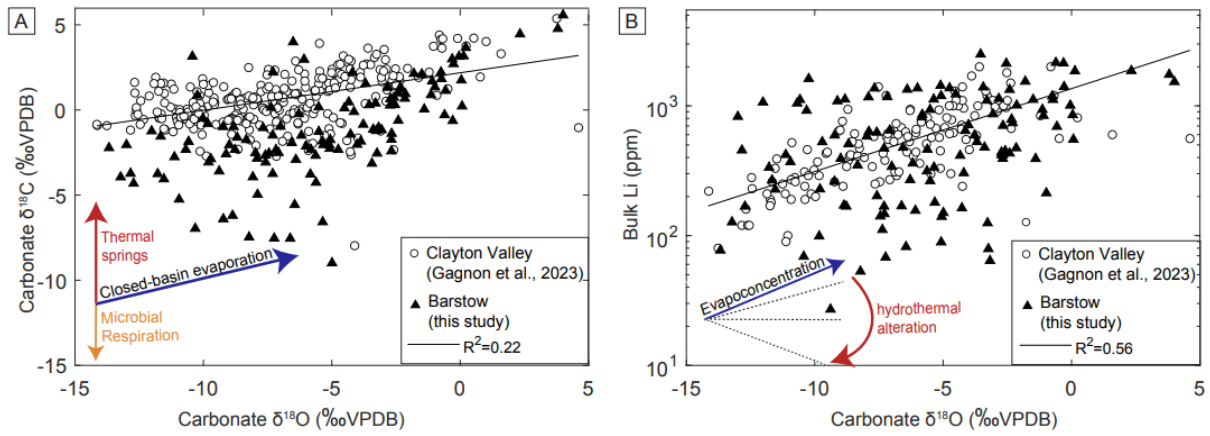

Figure 11. Clayton Valley and Barstow carbonate $\delta^{18}O$ versus $\delta^{13}C$ (A) and carbonate $\delta^{18}O$ versus bulk Li (B) from Gagnon et al. (2023). Barstow shows a correlation between $\delta^{18}O$ versus $\delta^{13}C$, suggesting kinetic effects due to evapoconcentration. Clayton Valley, like Barstow Formation, shows a correlation between $\delta^{18}O$ versus $\delta^{13}C$, suggesting kinetic effects due to evapoconcentration. Mechanisms for potential deviations in this slope are annotated. Abbreviation: VPDB = Vienna Pee Dee Belemnite.

Samples used for the twelve paired clay and carbonate measurements were selected in a way to avoid ambiguous clay and carbonate facies relationships. Each measurement pair comes from a mudstone with fine matrix carbonate, except for OC23-028 which consists of measurements made separately on a mudstone and carbonate interbed. Trends between the carbonate and clay $\delta^{18}O$ values suggest that Li-rich clays of the BF are most likely authigenic and formed from evaporatively evolved lake waters like the carbonate minerals. However, the offset in $\delta^{18}O$ (12.5‰) is too large to conclude that both were forming at the same temperature and from the same source water (Fig. 10). The average offset we observe for $\delta^{18}O_{clay}$ and $\delta^{18}O_{carb}$ is 12.5‰. The expected offset for smectite and calcite is ca. 3.5 ‰ (e.g. Kukla et al, 2022) for these two phases mineralizing in equilibrium out of lake water. Assuming that the minerals are forming under equilibrium conditions, there are three explanations for the large offset in the $\delta^{18}O_{clay}$ and $\delta^{18}O_{carb}$. Either (1) the clay and carbonate minerals formed from separate water reservoirs, (2) each mineral

formed from the same evolving reservoir, but at slightly different temperatures and/or from different water compositions, (3) detrital phases are contributing to the offset via mixing.

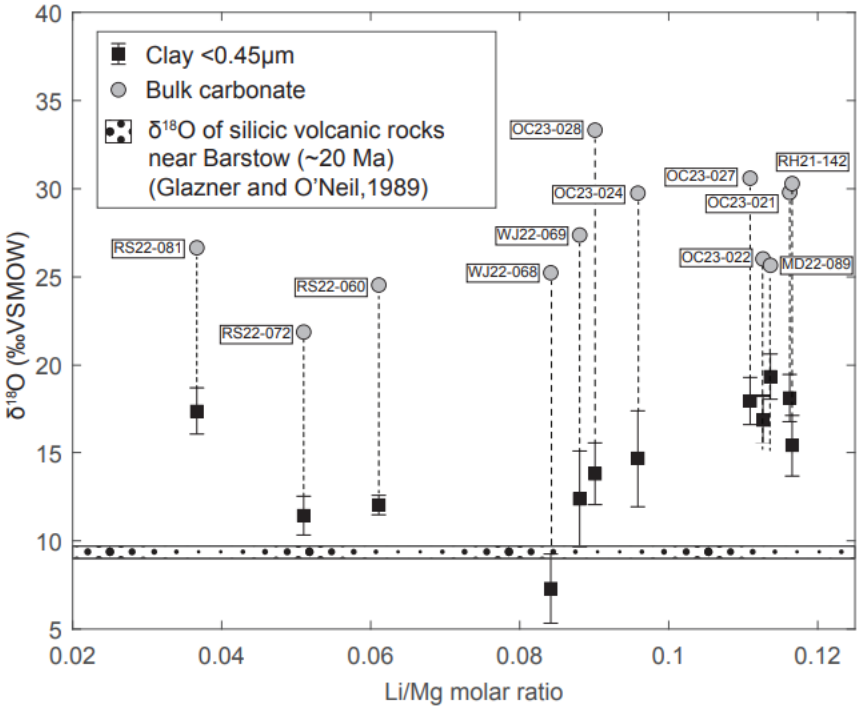

Figure 12. Paired carbonate (circles) and clay δ18O (squares) values for Barstow Formation mudstones spanning different degrees of Li enrichment. Crosshatched region marks the range of δ18O values for Miocene silicic volcanic rocks near Barstow reported by Glazner and O'Neil (1989). To distinguish between enrichment versus a larger abundance of Li clays in the bulk sample, the bulk Li concentrations for each sample are normalized by the bulk Mg concentrations and plotted on the horizontal axis.

Case 1 would describe a situation where authigenic carbonate is produced from the lake, but the smectite is weathered and carried into the lake by a stream and deposited with the carbonate. In this case, the carbonate formation water temperatures and $\delta^{18}O_{water}$ values could be more elevated than the smectite formation water temperatures and $\delta^{18}O_{water}$ values. While possible, case 1 does not explain why the $\delta^{18}O_{clay}$ and $\delta^{18}O_{carb}$ trends are strikingly similar.

Case 2 may describe a situation where carbonate minerals form authigenically in the surface waters and authigenic clays may be crystallizing near the sediment-water interface or shallowly buried pore spaces where pre-cursor Mg-silicate gels have been shown to persist (Tosca and Wright, 2018a). In a stratified lake, the bottom waters/pore waters of a lake are typically cooler and isotopically more negative with respect to oxygen than surface waters. Carbonates may form in relatively warm surface waters where evaporation driven enrichment drives an increase in the $\delta^{18}O_{water}$values. Together, the differences in formation temperature and water isotopic composition while still being within the same evolving water reservoir through the Miocene could potentially explain both the large offset and similar trend within the $\delta^{18}O_{clay}$ and $\delta^{18}O_{carb}$ datasets. Ephemeral wetlands may be stratified in temperature across shallow depths (16 °C in 30 cm depth; 10.3°C in 18cm depth; 15°C in 40 cm), though the stability of that stratification is very low, since water depth and chemical parameters fluctuate seasonally and, in some cases, diurnally (Eriksen 1966; Black, 1976; Serrano 1994; Boeckman, 2007). We suspect the formation and deposition of authigenic clay and carbonate minerals may be biased towards stratified conditions in the late summer, near the end of a hydroperiod (Boeckman, 2007). However, as ephemeral wetlands change shape and size in three dimensions, stratification would likely not be maintained over meaningful geologic timescales. What more, if the carbonates were forming in the surface waters and the clays near the sediment-water interface, the difference between clay and carbonate formation water compositions would then represent the range of $\delta^{18}O_{lake}$ values within the vertical lake profile. When considering clumped isotope constraints (described earlier as Method 2), we calculated a maximum difference of 17.6‰ in $\delta^{18}O_{lake}$ values which is an order of magnitude too large compared to modern day vertical lake profile observations. Lakes only change by a few per mil with depth in modern volcanic and rift lake vertical profiles (Tongwa et al., 2015).

Case 2 may also reflect sequential mineralization from wetland pore waters. This is the proposed mechanism for Li-smectite authigenesis in the northern McDermitt Caldera (Putzolu et al., this issue). In this scenario, we suggest carbonate precipitates in shallow pore spaces first, then Li and Mg-smectites form alongside sodium-rich zeolites, like analcime. The remaining pore fluids become enriched with potassium, and consequently precipitate authigenic feldspar. As sequential mineral formation progresses, the pore water $\delta^{18}O$ becomes increasingly negative, driving the authigenic feldspar values to be significantly more negative compared to the carbonate and clay minerals. The resulting measured clay $\delta^{18}O$ may then be forming from more fractionated waters and represent a mixture between clay minerals and small amounts of analcime, and authigenic feldspar.

Alternatively, as case 3 states additional offset may be due to the presence of detrital grains with low endmember $\delta^{18}O$ values like Miocene silicic volcanic rocks near Barstow (Fig. 9; ~ 9‰; Glazner & O'Neil, 1989). Most clay separates clay separates contain illite, chlorite, and feldspar phases, especially those with low Li concentration, which could be detrital. The idea that detrital material dilutes Li concentrations in claystones has been called upon in other nearby ancient lake basins, such as Owens Valley, where illite and chlorite are thought to have been mechanically weathered and recycled from surrounding metasedimentary rocks (Menking et al., 1993). The low $\delta^{18}O_{clay}$ values in samples lacking common detrital phases is evidence to support the burial, dissolution, and reprecipitation pathway for clay authigenesis (Tosca and Wright, 2018). The measured $\delta^{18}O_{clay}$ would therefore reflect a mixture of pore water and parent clay mineral oxygen isotope compositions. However, the preservation of the evaporative fingerprint in the hydrogen and oxygen isotope values (Fig. 9) indicates a significant proportion of the parent material is still lake derived.

It is important to note that crystallization of authigenic Mg-silicates first requires nucleation. Nucleation can be either homogeneous (from solution) or heterogeneous (via substrate). Homogeneous nucleation is highly dependent on dissolved Mg^{2+}, SiO_2, pH, and salinity, and must meet threshold conditions to occur, which include higher concentrations of $SiO_{2(aq)}$, lower Mg, and/or pH (Tosca, 2014; Tosca and Wright, 2018). This does not immediately lead to crystallization, but rather produces a Mg-silicate "gel" (Tosca and Masterson, 2014) which persists in the sediment water interface and subsurface (Tosca and Wright, 2018). As such, crystallization occurs upon dehydration during wet-dry cycles, prolonged saline conditions, or shallow burial and heating of the Mg-silicate gel (Tosca and Wright, 2018). It is unclear whether Li smectite forms directly from homogenous nucleation or heterogeneous nucleation. The presence of dolomite, magnetite, iron oxides, and stromatolites in some clay rich samples suggest a potential role of microbial activity in nucleation (Dong et al., 2022). Microbially mediated formation of Mg-calcites/dolomites and Mg-clays occurs in modern ephemeral systems today (Sanz-Montero et al., 2023; Hobbs et al., 2024). Further mineral characterization, imaging, and trace element mapping of geological samples will clarify the nature of crystal nucleation and growth.

Based on our isotopic constraints and the similar mineral assemblages observed in other basins, Mg-silicates nucleated from evaporatively evolved waters of shallow or ephemeral lake, mudflat, or wet playa pore waters. Crystallization of carbonates and clays most likely occurred in sequence near the sediment-water interface upon burial in the shallow subsurface pore waters, where temperatures were <50°C. Overall, low formation temperatures, preservation of an evaporative signal in both the clay and carbonate isotope results, and low concentration of Li in illite-rich samples rule out formation from hydrothermal fluids as a widespread Li-clay formation mechanism at Barstow.

Comparing Conditions of the Mud Hills and Calico Mountains Regions

Between the extensive post-depositional deformation proximal to the Calico Fault and the many syn-depositional dacite intrusions (~17 Ma) highly localized to the Calico Mountains area (Miller et al., 2022) it is possible the Calico Mountains experienced more alteration than the Mud Hills region (Burke et al., 1982; Singleton and Gans, 2008). We therefore expect to see trends in the mineralogy and isotope geochemistry that could potentially reflect different ore formation conditions, despite having broadly similar sedimentology. Specifically, we hypothesized that the Mud Hills region would represent a low temperature, lake evapoconcentration Li enrichment mechanism while the Calico Mountains region would potentially represent hydrothermal alteration Li enrichment at high temperature.

The data show no clear difference in the Li concentrations between the Calico Mountains and the Mud Hills regions. Both areas were found to contain mudstones >2000 ppm Li. The sample with the highest concentration of Li, RH21-142, came from the Calico Mountains close to the old borate mine. It is a waxy, chocolate brown-red mudstone with finely laminated stromatolites. The sample's clay mineral assemblage is nearly 100% smectite, with quartz, calcite, ankerite, analcime, ferrihydrite present in the bulk sample (Table A1). The formation temperatures of the calcite and smectite are 27 ℃ and >23 ℃, respectively. The sample also has an extremely high $\delta^{18}O_{carb}$ value compared to the other samples, which suggests that the mineralization waters were evaporatively evolved. The sample with the highest Li concentration in the Mud Hills region, OC23-027, was found near eastern Owl Canyon. It is a massive buff-tan mudstone with popcorn weathering features that contains some evaporite minerals. The sample consists of mixed illite-smectite with some kaolinite, analcime, and diopside (Table 1). The clay formation temperature (assuming all clay is smectite) was calculated to be approximately >17 ℃. The sample also had a

moderately high $\delta^{18}O_{carb}$ value, suggesting mineralization waters were evaporatively evolved. It is significant that both highest concentration samples have relatively cold clay formation temperatures and a high $\delta^{18}O_{carb}$ value, suggesting authigenic processes dominate Li enrichment in these clays.

The clay mineral assemblages in the Calico Mountains region tend to contain more smectite, whereas the Mud Hills samples typically contain a higher abundance of illite and zeolites. Unlike Thacker Pass (e.g., Castor and Henry, 2020; Benson et al., 2023; Emproto et al., *This Volume*), the presence of illite within the Barstow Formation does not appear to correspond to lithium enrichment. An increase in the illite content in each sample may instead represent an increase in detrital sediments to the depositional environment and subsequent dilution of bulk Li. The Al/Mg content in these illite rich samples is generally higher than the smectite rich samples as well. Higher Al/Mg is expected for detrital clays (Bentz and Peterson, 2020). If this is indeed the case, then it appears that over the period of deposition the Mud Hills region experienced a higher influx of detrital material compared to the Calico Mountains. It is also possible that high Al/Mg whole-rock values correspond to higher abundances of aluminosilicates like feldspar, which could have crystallized authigenically after Li smectite mineralization during closed system diagenesis (Casor and Henry, 2020; Putzolu et al., *This Volume*).

The sample with the lowest formation temperature comes from the eastern Mud Hills region, while the sample with the hottest temperature comes from the Calico Mountains region. The minimal abundance of illite and the fact that both regions yielded cool formation temperatures rules out illitization as a likely mechanism for lithium enrichment. Due to our small sample size and high variance among samples, we cannot be confident in any major conclusion regarding regional differences in clay and carbonate formation temperatures between the Mud Hills and

Calico Mountains. Restoring as little as 3 km of dextral slip along the Calico fault (Singleton and Gans, 2008) or up to 9.6 km (Dokka, 1983) would bring the two sub-basins adjacent to each other. It may be that sediments from both sub-basins preserve the original depositional conditions, which were actually very similar.

Barstow Li Deposit Model

New geochemical and mineralogical data allows us to develop a conceptual model for Li-rich sediments of the BF and similar smectite-dominated volcano-sedimentary Li deposits globally (Fig. 13; Putzolu et al., *This Volume*). In the following we walk through the steps leading to Li enrichment and variability observed in the Barstow Basin.

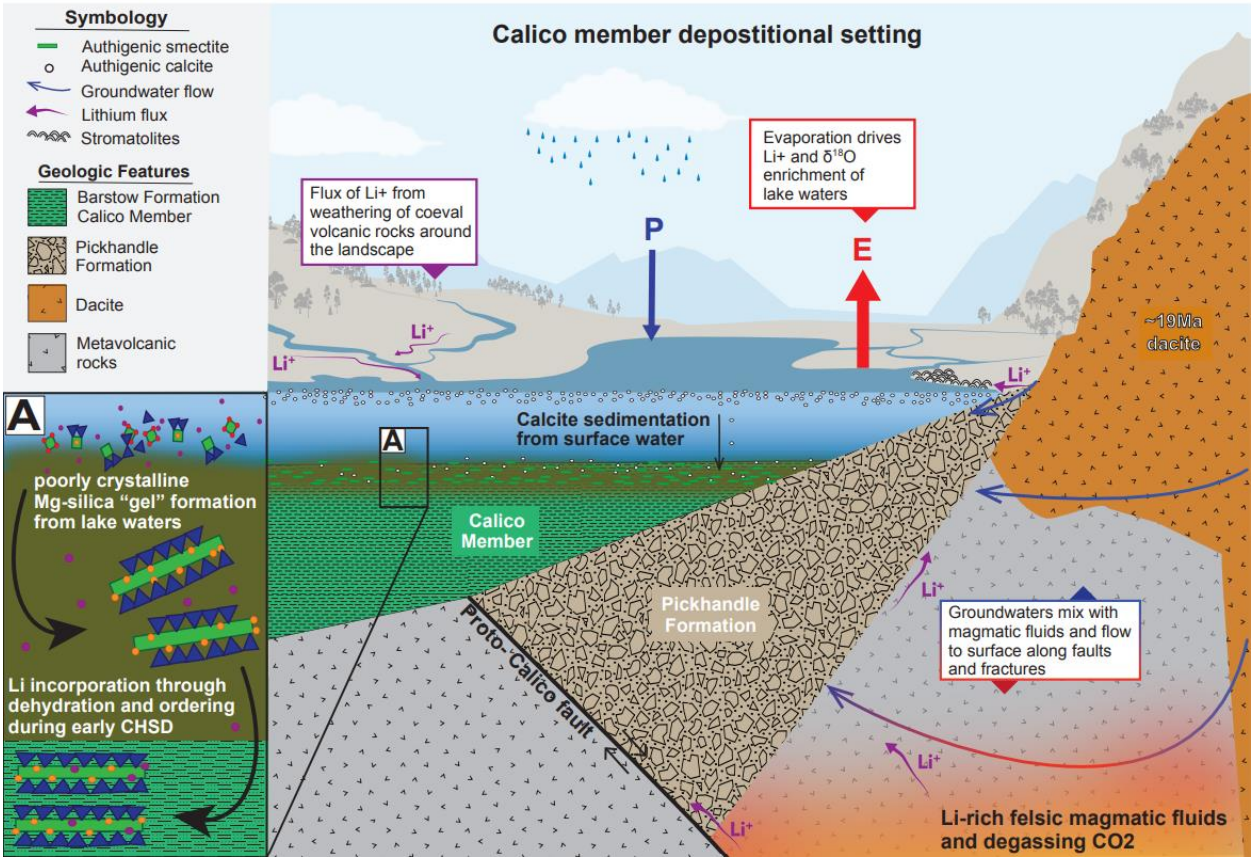

Figure 13. Barstow lithium deposit conceptual model showing lithium flux to a lacustrine depositional system with precipitation (P), evaporation (E), Mg silica gel formation, closed

hydrologic system diagenesis (CHSD), and magmatic fluids associated with intrusion possibly playing a key role in deposit formation and enrichment.

First, dissolved Li^+ accumulates in the shallow to ephemeral waters from weathered coeval ashes and glasses deposited in the basin (Ellis et al., 2022). Although there are several <1m ashes that fell directly in ephemeral waters, these ashes had a likely, at a maximum, ~200 ppm in primary Li content, which could not be a sufficient source of Li to produce 100s of meters of ~1,000 ppm Li claystone. Additional dissolved Li^+ from weathered sources around the basin was likely transported into the shallow-ephemeral lake through surface tributaries and groundwaters. Localized hydrothermal fluids related to coeval silicic volcanism may have delivered additional Li to surface waters around the basin, though the evidence for this is minor and restricted to the Calico Mountains and one sample locality in the Mud Hills. The magmatic volatile phases associated with dacite intrusions may have provided Li mass to the hydrologic system, as is shown in magmatic systems adjacent to active brine deposits in South America (Cortes-Calderon et al., *This Volume*). The relative proportion of hydrothermal Li inputs to the watershed from these localized areas remains unclear, however our generally low mineralization temperatures and evaporative isotope signatures suggest the input may be minor.

Secondly, evaporation modulates the concentration of Li^+ in the lake or pore waters in conjunction with changes in the hydrologic cycle. During times when precipitation outpaces evaporation in an underfilled to balance-filled setting (Carroll and Bohacs, 1999; Benavente and Bohacs, 2024), the waters become depleted in Li, ^{18}O and ^{13}C and the relative amount of detrital material delivered to the lake increases. During particularly warm and wet climate stages, enhanced weathering reactions may consequently increase the Li flux to the lake. When

evaporation outpaces precipitation in an underfilled setting (e.g., Carroll and Bohacs, 1999; Benavente and Bohacs, 2024), the waters become enriched in dissolved Li, ^{18}O, and ^{13}C.

Finally, when the saturation of dissolved inorganic carbon is high due to evaporation calcite mineralizes in stratified surface waters or wetland pore waters enriched in ^{18}O. We hypothesize that poorly crystalline Mg-silicates subsequently form in similar concentrated alkaline lake or pore waters and mineralize in the presence of high dissolved Li^+ in pore spaces of shallowly buried sediments. During authigenic smectite mineralization, the smectite incorporates the dissolved Li into its interlayer proportional to the concentration of Li preserved within the lake or wetland pore waters, and into the octahedral sheet based upon the chemical availability of charge-balancing elements (Decarreau et al., 2012; Emproto et al, *This Volume*). We assume the pore waters are derived from the same waters as the carbonates because of their similar isotope trends, but they are cooler and relatively depleted in ^{18}O compared to the surface waters where prior calcite mineralization takes place.

Comparison to Other Volcano-Sedimentary Li Deposits

The enrichment of Li in the BF and compositionally similar CV claystones is a result of paleoclimate and basin evolution. The calcareous mudstones where the Li is most concentrated and from which our data are gathered bear resemblance to the evaporative isotopic trends observed in the calcareous mudstones of the hydrologically closed CV basin (Coffey et al., 2021; Gagnon et al., 2023). It is possible that Li-enriched units represent points in time where the Barstow basin was behaving as a hydrologically closed system, like CV. Broadly, the two authigenic deposits formed during a warm and wet climate interval within an underfilled to balance-filled setting (Pound et al., 2012; Kasbohm and Schoene, 2018; Steinthorsdottir et al., 2021; Kukla et al., 2022). The Barstow deposit formed under warm and wet mid-Miocene playa lake conditions, which

transitioned over millions of years into floodplains and wetlands, and then arid wooded grasslands (Loughney and Badgley, 2020; Loughney et al., 2023). We observe gypsum in several areas and consider the ancient Barstow Basin to have fluctuated between a balance-filled basin and an underfilled basin setting, like CV. The CV deposit also initiated under the warm and wet conditions, but in the late Pliocene, which transitioned to more arid and colder conditions through the Pleistocene (Ibarra et al., 2018; Menemenlis et al., 2022; Gagnon et al., 2023; Bhattacharya et al., 2024). CV sustained a longer-lived and deeper lake than Barstow, however the lake-balance was still evaporatively concentrated and extremely saline as evident from evaporite sequences (Coffey et al., 2021; Gagnon et al., 2023).

Enhanced weathering of coeval volcanic rocks and ashes around the watershed during warm wet periods, punctuated by increasingly more frequent times of aridity, likely provided the ideal conditions for deposit enrichment in both locations. Although hydrothermal Li isotope signatures have been measured in CV playa sediments (Araoka et al., 2014), there is otherwise minimal evidence to support hydrothermal Li^+ contributions to each basin. These surface dominated formation conditions lead to Barstow and CV deposits being very similar mineralogically and geochemically. Both host authigenic mudstones with mixed I-S clays and bulk Li concentrations of up to 2,500 ppm. Some of the most Li-enriched samples in the Calico Mountains are almost purely Mg-rich smectite. At CV, samples have been shown to contain a more consistent presence of illite (35-50%) and an overall higher abundance of aluminum (Morissette, 2012; Coffey et al., 2021; Gagnon et al., 2023).

The Li deposit in McDermitt caldera starkly contrasts to that of the CV and Barstow. McDermitt caldera lake sediments are characterized by ubiquitous Li-rich Mg-smectites throughout the whole caldera lake with whole-rock grades up to ~4,000 ppm and localized illite-

rich sediments with bulk ore up to 1 wt. % Li only in the TP area (Benson et al., 2023). The initial hypothesis for deposit formation proposed by Castor and Henry (2020) involves closed hydrologic system diagenesis of tuffaceous sediments. This source model cannot resolve the Li budget and requires additional Li sources such as magma-derived hydrothermal fluids proposed by Benson et al. (2017). The origin of the primary Li-rich smectite at TP may involve early closed-lake balance processes like the CV and Barstow deposits (Benson et al., 2023; Emproto et al., *This Volume*). The Li-illite at TP formed from the hydrothermal illitization of pre-existing authigenic Mg-smectite at high temperature around the caldera resurgent dome (Benson et al., 2023). The TP high-grade illitic ore is significantly more enriched in Li compared to other sedimentary deposits; however, the high-grade ore is localized around faults related to the resurgent dome in the southern part of the McDermitt caldera (Benson et al., 2023).

The BF deposit model slightly contrasts other known occurrences of Li-bearing clays in the Mojave Desert. The Hector deposit 60 km east of Barstow contains the eponymous Li-Mg smectite, hectorite, which likely formed within a hot spring lagoon based on the high abundance of fluorine and lithium (Ames et al., 1958a; Morissette, 2012). Recent drilling in the land surrounding the Hector mine by 5E Advanced Materials (formerly American Pacific Borates) indicates the presence of other discontinuous pod-like occurrences of hectorite and borates (American Pacific Borates Ltd., 2021). This points to a more localized hot-spring-type mineralization for the Hector-area Li clay occurrences, like the hectorite observed farther east in the Mojave Desert at Franklin Wells, CA (Wilkerson et al., 2001). West of the BF, the Kramer-Borax mine in Boron, CA, contains borate ore and interstitial Li-bearing clays are believed to have formed when basaltic sills intruded into wet sediments at ~19.5 Ma directly below the mined orebody, leading to a hydrothermal origin of the deposit (Rio Tinto, 2021; Gans, 2023).

Interestingly, the age of the sediments at Kramer-Borax (~21-19 Ma) and the Calico Mountains (~19-17 Ma) overlap, and both locations contain spatially associated borate mineralization despite having differing postulated formation mechanisms. Application of the stable isotopic methods used in this study at the Kramer-Borax deposit would inform if the deposit formed authigenically like the coeval Li-B sediments at Calico Mountains, or at higher or associated with a hydrothermal origin like the Hector and Franklin Wells deposits. (Gans, 2023) Regardless, the presence of borate minerals at some of the Li-clay occurrences in the Mojave is striking, and similar correlations have been noted at other volcano-sedimentary Li deposits (Darin et al., *This Volume*; Putzolu et al., *This Volume* and references therein). Borate minerals, though not ubiquitous at Li deposits in the Mojave (e.g., Mud Hills and Franklin Wells), may therefore be a useful exploration tool to vector towards other Li-clay deposits in the region and globally.

Conclusions

Formation of Authigenic Volcano-Sedimentary Li Deposits

Authigenic, lacustrine volcano-sedimentary Li deposits are widespread, and are largely shaped by past hydroclimate, basin geology, and often hydrothermal input. Endorheic basins, such as the underfilled to balance-filled Miocene Barstow basin, provide space for the accumulation of Li in basin waters and sediments. In the ancient Barstow basin, dissolved Li sources from weathered coeval volcanic rocks and additional hydrothermally derived Li sources from coeval felsic volcanism enter the surface watershed, accumulating in ephemeral lake and wetland environments. The Li enrichment of the ancient Barstow basin waters and authigenic sediments was disproportionately controlled by environmental conditions, such as evapoconcentration and depositional environment. Enhanced weathering during warm wet periods, followed by punctuated

and increasingly more frequent times of aridity through the Miocene likely provided the ideal conditions for concentrating Li in ephemeral waters.

Although the nature of silicate clay nucleation remains elusive for the Barstow system, we suspect microbially mediated substrates in shallow ephemeral systems played a role in driving Mg-smectite nucleation, as evidenced by abundant stromatolites in many of the lithium-rich intervals, which consequently provided a sink for Li out of solution. Alternatively, Mg-silicate "gels" form in ephemeral lake waters through homogeneous nucleation, and upon shallow burial or desiccation, the amorphous clays crystalize. During crystallization, Li from lake-derived pore waters is incorporated into the octahedral layer of the clay mineral, where most of the Li is held within sedimentary ore (Coffey et al., 2021). The resulting concentration of the Li bearing smectite is a function of the formation water Li/Mg concentration, temperature, and time (Decarreau et al., 2012). The implication of this, is that during times of desiccation or extreme aridity, evaporatively enriched waters are likely generating clays with higher concentrations of Li. This evaporative enrichment leads to an observable positive correlation between bulk rock Li concentrations and oxygen isotope ratios of authigenic sedimentary Li deposits (Li et al., 2004; Gagnon et al., 2023). Hydrothermal spring waters from around the catchment may also increase Li inputs to the lake prior to carbonate and clay mineralization. However, the generally high carbon isotope values of the BF suggest hydrothermal fluid contributions to the basin catchment are minor and/or highly localized. Lithium isotope measurements may further clarify the origin of Li (e.g. hot springs vs. river weathering products) to the ancient hydrologic budget in Barstow.

The nature and extent of subsequent alteration within the Barstow Deposit remains unclear. Under the right conditions, a given authigenic deposit may transform, and their chemistry no longer reflects that of its initial formation environment. For example, at TP, subsequent high

temperature alteration in the presence of Li-rich fluids led to the illitization and enhanced Li enrichment of the primary sediments. Although our mineral formation temperatures are not hot enough to have led to illitization, we speculate that early post-depositional alteration may still explain some compositional differences between the MH and CM samples. In the CM, coeval felsic intrusions are documented nearby. Similar intrusions near at the Kramer-Borax mine have been linked to borate mineralization in coeval sediments (Rio Tinto, 2021; Gans, 2023). Additional mineral imaging characterization techniques will elucidate the diagenetic history of the Barstow mudstones.

Implications for Smectite-Dominated Volcano-Sedimentary Deposits

The Barstow conceptual model presented herein describes the archetypal formation environment for the rather widespread smectite-dominated volcano-sedimentary deposits. It demonstrates that low temperature, near-surface processes can be the dominant mechanism for the inception of volcano-sedimentary Li-deposits. While hydrothermal inputs might still be a requirement to maintain a long-lived Li-rich surface environment (e.g., Cortes-Calderon et al., *This Volume*), direct alteration of sediments via hydrothermal fluids is not necessary in a closed basin environment with sufficient evapoconcentration in a warm-wet climate.

Future nearby exploration should therefore be focused on mapping out the extent of lithologic units beneath alluvial cover and to project the structures or surface exposures of the BF at depth. Since the Barstow deposit is shaped by processes largely linked to regional hydroclimate, occurrences of this nature are likely more laterally continuous and only restricted by changes in the depositional facies and basin geometry. Additionally, local exploration efforts may target areas of potential hydrothermal influence, such as areas that contain borates and other ore deposits juxtaposed to sedimentary units. Alteration of sediments via hydrothermal fluids would lead to

highly localized ore sources, restricted to basin bounding faults and other conduits for Li-rich fluids to intrude into sediments, in a fashion like what is observed at TP (e.g., Emproto et al., *This Volume*).

Global exploration efforts should carefully consider locations where the paleoenvironmental conditions were conducive to the formation of Li-smectite. These key ancient conditions include: (1) a warm, semi-arid climate; (2) a hydrologically underfilled to balance-filled basins; (3) basin volcanic material rich in Li and/or Li rich hydrothermal springs. In some cases, like CV (3.1 Ma-0.04 Ma), the ancient lake basin architecture is somewhat preserved on the modern landscape. In contrast, the BF (19.4-13.0 Ma) rocks are visible in high-relief areas on the landscape where the ancient lake basin hypsometry is not well represented. Sedimentary units targeted for exploration should consist of calcareous lacustrine mudstones with occasional evaporite minerals. Depositional facies should range from ponded mudflats to shallow lakes. Additional indicators include anomalously high boron, fluorine, or clinoptilolite content, which is associated with hydrothermal input.

Local hydroclimate undoubtedly plays a large role in the development of smectite-dominated volcano-sedimentary Li deposits. Warmer, wetter climates drive more enhanced weathering and Li delivery, whereas drier climates allow for the precipitation of authigenic smectite. Regional and local climate change events may be more important in targeting Li rich intervals than large-scale climate events, since large scale climate events lead to asynchronous facies changes between basins (Ibarra et al., 2014; Knott et al., 2019). For example, larger and deeper lakes may buffer regional hydrologic changes, like drought, better than smaller, shallower lake systems. Individual basin-scale exploration is therefore important for targeting Li rich facies in sedimentary deposits. Ongoing exploration, including the application of stable isotope

geochemistry in conjunction with mineralogy and whole rock analyses, will likely clarify the role of climate in other volcano-sedimentary Li deposits.

Acknowledgements

We thank Rachel Hampton, Stephen Pearcey, and Lithium Americas Corporation for access to samples, field notes, funding, and analyses. Matthew Dietel, William Jarvis, Dave Miller, Eytan Orent, Ryan Silver, Mebrahtu Weldeghebriel are thanked for their assistance in the field. We thank Marcelo Alexandre, Brooke Wagenheim, Shaw Miller, Theodore Bobik, and Steve Clemens for their assistance processing and measuring samples for isotopic analysis. We extend our gratitude to reviewers Mike Darin and Lisa Thompson for thoughtful and detailed feedback.

References

Ames, L.L., Sand, L.B., and Goldich, S.S., 1958, A contribution on the Hector, California bentonite deposit: Economic Geology, v. 53, no. 1, p. 22–37.

Anderson, N. T., Bonifacie, M., Jost, A. B., Siebert, J., Bontognali, T., Horita, J., ... & Bergmann, K. D. (2024). Re-Assessing the Need for Apatite-and Dolomite-Specific Calibrations of the Carbonate Clumped Isotope Thermometer. Geochemistry, Geophysics, Geosystems, 25(1), e2023GC011049.

Anderson, N.T., Kelson, J.R., Kele, S., Daëron, M., Bonifacie, M., Horita, J., Mackey, T.J., John, C.M., Kluge, T., Petschnig, P., Jost, A.B., Huntington, K.W., Bernasconi, S.M., and Bergmann, K.D., 2021, A Unified Clumped Isotope Thermometer Calibration (0.5–1,100°C) Using Carbonate-Based Standardization: Geophysical Research Letters, v. 48, no. 7, p.1-11. e2020GL092069.

Araoka, D., Kawahata, H., Takagi, T., Watanabe, Y., Nishimura, K., and Nishio, Y., 2014, Lithium and strontium isotopic systematics in playas in Nevada, USA: constraints on the origin of lithium: Mineralium Deposita, v. 49, no. 3, p. 371–379.

Asher-Bolinder, S., 1991, Descriptive model of lithium in smectites of closed basins: Some Industrial Mineral Deposit Models: Descriptive Deposit Models, USGS Open File Report, p. 11-12.

Bartley, J.M., Fletcher, J.M., and Glazner, A.F., 1990, Tertiary extension and contraction of lower-plate rocks in the central Mojave metamorphic core complex, southern California: Tectonics, v. 9, no. 3, p. 521–534.

Benavente, C. A., & Bohacs, K. M. (2024). Advances in Limnogeology: The lake-basin-type model revisited 25 years after… anomalies, conundrums and upgrades: The Depositional Record, 44 p.

Benson, T.R., Coble, M.A., and Dilles, J.H., 2024, Hydrothermal enrichment of lithium in intracaldera illite-bearing claystones: Science Advances, v. 9, no. 35, p. 1-10. eadh8183.

Bentz, J.L., and Peterson, R.C., 2020, The formation of clay minerals in the mudflats of Bolivian salars: Clays and Clay Minerals, v. 68, no. 2, p. 115–134.

Bernasconi, S.M., Müller, I.A., Bergmann, K.D., Breitenbach, S.F.M., Fernandez, A., Hodell, D.A., Jaggi, M., Meckler, A.N., Millan, I., and Ziegler, M., 2018, Reducing uncertainties in carbonate clumped isotope analysis through consistent carbonate-based standardization: Geochemistry, Geophysics, Geosystems, v. 19, no. 9, p. 2895–2914.

Bernasconi, S.M., Daëron, M., Bergmann, K.D., Bonifacie, M., Meckler, A.N., Affek, H.P., Anderson, N., Bajnai, D., Barkan, E., and Beverly, E., 2021, InterCarb: A community effort to improve interlaboratory standardization of the carbonate clumped isotope thermometer using carbonate standards: Geochemistry, Geophysics, Geosystems, v. 22, no. 5, p. 1-25. e2020GC009588.

Black JH. 1976. Environmental fluctuations in central Oklahoma temporary ponds: Proceedings of the Oklahoma Academy of Science, v. 56, p 1-8.

Boeckman, C. J..2007, Spatial and seasonal variability in the water quality characteristics of an ephemeral wetland. In Proceedings of the Oklahoma Academy of Science, p. 45-54.

Bogdanov, D., Farfan, J., Sadovskaia, K., Aghahosseini, A., Child, M., Gulagi, A., Oyewo, A.S., de Souza Noel Simas Barbosa, L., and Breyer, C., 2019, Radical transformation pathway towards sustainable electricity via evolutionary steps: Nature communications, v. 10, no. 1, p. 1–16.

Brand, W. A., Assonov, S. S., & Coplen, T. B. , 2010, Correction for the 17O interference in δ (13C) measurements when analyzing CO2 with stable isotope mass spectrometry (IUPAC Technical Report): Pure and Applied Chemistry, v. 82, no. 8, p. 1719-1733.

Brenner-Tourtelot, E.F., and Glanzman, R.K., 1978, Lithium-bearing rocks of the horse spring formation, Clark County, Nevada, in Lithium Needs and Resources: Elsevier, p. 255–262.

Breyer, C., Bogdanov, D., Aghahosseini, A., Gulagi, A., Child, M., Oyewo, A.S., Farfan, J., Sadovskaia, K., and Vainikka, P., 2018, Solar photovoltaics demand for the global energy transition in the power sector: Progress in Photovoltaics: Research and Applications, v. 26, no. 8, p. 505–523.

Burke, D.B., Hillhouse, J.W., McKee, E.H., Miller, S.T., and Morton, J.L., 1982, Cenozoic rocks in the Barstow basin area of southern California: Stratigraphic relations, radiometric ages, and paleomagnetism: Geological Survey Bulletin 1529-E. US Geological Survey. .

Bussar, C., Stöcker, P., Cai, Z., Moraes Jr, L., Magnor, D., Wiernes, P., van Bracht, N., Moser, A., and Sauer, D.U., 2016, Large-scale integration of renewable energies and impact on storage demand in a European renewable power system of 2050—Sensitivity study: Journal of Energy Storage, v. 6, p. 1–10.

Byers Jr, F.M., 1960, Geology of the Alvord Mountain quadrangle, San Bernardino County, California. Geological Survey Bulletin 1089-A. US Geological Survey. p. 1-71.

Carpenter, S.B., and Reynolds, J.T., 2004, Borates in Western North America, in Betting on Industrial Minerals. Proceedings of the 39th Forum on the Geology of Industrial Minerals: Nev. Bur. Mines Geol. Special Publication Reno, Nevada, p. 51–56.

Carroll, A.R., and Bohacs, K.M., 1999, Stratigraphic classification of ancient lakes: Balancing tectonic and climatic controls: Geology, v. 27, no. 2, p. 99–102.

Castor, S.B., and Henry, C.D., 2020, Lithium-rich claystone in the McDermitt Caldera, Nevada, USA: Geologic, mineralogical, and geochemical characteristics and possible origin: Minerals, v. 10, no. 1, p. 68.

Chafetz, D.A., 2023, Mineralogy and Geochemistry of a Lithium and Boron Enriched Stratiform Ore Zone in the Cave Spring Formation, Rhyolite Ridge, NV, USA (MSc dissertation): University of Nevada, Reno, 619 gil

1685 https://scholarworks.unr.edu/handle/11714/10868.

Chamberlain, C.P., Mix, H.T., Mulch, A., Hren, M.T., Kent-Corson, M.L., Davis, S.J., Horton, T.W., and Graham, S.A., 2012, The Cenozoic climatic and topographic evolution of the western North American Cordillera: American Journal of Science, v. 312, no. 2, p. 213–262.

Coffey, D.M., Munk, L.A., Ibarra, D.E., Butler, K.L., Boutt, D.F., and Jenckes, J., 2021, Lithium storage and release from lacustrine sediments: Implications for lithium enrichment and sustainability in continental brines: Geochemistry, Geophysics, Geosystems, v. 22, no. 12, p.1-22. p. e2021GC009916.

Connolly, D., Lund, H., and Mathiesen, B.V., 2016, Smart Energy Europe: The technical and economic impact of one potential 100% renewable energy scenario for the European Union: Renewable and Sustainable Energy Reviews, v. 60, p. 1634–1653.

Coplen, T.B., and Kendall, C., 2000, Stable hydrogen and oxygen isotope ratios for selected sites of the US Geological Survey's NASQAN and benchmark surface-water networks: US Department of the Interior, US Geological Survey, Open-File Report 00-160, p. 424.

Costelloe, J.F., Irvine, E.C., Western, A.W., and Herczeg, A.L., 2009, Groundwater recharge and discharge dynamics in an arid-zone ephemeral lake system, Australia: Limnology and Oceanography, v. 54, no. 1, p. 86–100.

Davies, A.J., Davis, S., and John, C.M., 2021, Evidence of taxonomic non-equilibrium effects in the clumped isotope composition of modern cephalopod carbonate: Chemical Geology, v. 578, p. 120317.

Decarreau, A., Vigier, N., Pálková, H., Petit, S., Vieillard, P., and Fontaine, C., 2012, Partitioning of lithium between smectite and solution: An experimental approach: Geochimica et Cosmochimica Acta, v. 85, p. 314–325.

Delgado, A., and Reyes, E., 1996, Oxygen and hydrogen isotope compositions in clay minerals: a potential single-mineral geothermometer: Geochimica et cosmochimica acta, v. 60, no. 21, p. 4285–4289.

Dennis, K.J., Affek, H.P., Passey, B.H., Schrag, D.P., and Eiler, J.M., 2011, Defining an absolute reference frame for 'clumped'isotope studies of CO2: Geochimica et Cosmochimica Acta, v. 75, no. 22, p. 7117–7131.

Dibblee Jr, T.W., 1994, Pre-Cenozoic rock units of the Mojave Desert, in Mojave Desert: v.22, p. 100–127.

Dokka, R.K., 1983, Displacement on late Cenozoic strike-slip faults of the central Mojave Desert, California: Geology, v. 11, no. 5, p. 305–308

Dokka, R.K., 1989, The Mojave Extensional Belt of southern California: Tectonics, v. 8, no. 2, p. 363–390.

Dokka, R.K., and Travis, C.J., 1990, Late Cenozoic strike-slip faulting in the Mojave Desert, California: Tectonics, v. 9, no. 2, p. 311–340.

Dong H, Huang L, Zhao L, Zeng Q, Liu X, Sheng Y, Shi L, Wu G, Jiang H, Li F, Zhang L, Guo D, Li G, Hou W, Chen H. A critical review of mineral-microbe interaction and co-evolution: mechanisms and applications: National Science Review. v. 9, no.10, p.nwac128.

Eden, R., Gans, P., and Cottle, J. New insights into basin development of the middle Miocene Barstow Fm. through U-(Th-)Pb Tephrochronology (in review)

Ellis, B.S., Szymanowski, D., Harris, C., Tollan, P.M.E., Neukampf, J., Guillong, M., Cortes-Calderon, E.A., and Bachmann, O., 2022, Evaluating the potential of rhyolitic glass as a lithium source for brine deposits: Economic Geology, v. 117, no. 1, p. 91–105.

Eriksen CH. 1966. Diurnal limnology of two highly turbid puddles. Proceedings of the International Association of Theoretical and Applied Limnology 16:507-514.

Faulds, J.E., Henry, C.D., Spencer, J.E., and Titley, S.R., 2008, Tectonic influences on the spatial and temporal evolution of the Walker Lane: An incipient transform fault along the evolving Pacific–North American plate boundary: Ores and orogenesis: Circum-Pacific tectonics, geologic evolution, and ore deposits: Arizona Geological Society Digest, v. 22, p. 437–470.

Fiebig, J., Bajnai, D., Löffler, N., Methner, K., Krsnik, E., Mulch, A., and Hofmann, S., 2019, Combined high-precision Δ48 and Δ47 analysis of carbonates: Chemical Geology, v. 522, p. 186–191.

Fillmore, R.P., Walker, J.D., and Beratan, K.K., 1996, Evolution of a supradetachment extensional basin: The lower Miocene Pickhandle basin, central Mojave Desert, California: Special Papers-Geological Society of America, p. 107–126.

Foshag, W.F., and Woodford, A.O., 1936, Bentonitic magnesian clay mineral from California: American Mineralogist: Journal of Earth and Planetary Materials, v. 21, no. 4, p. 238–244.

Friedman, I., 2000, data-base of surface and ground water samples analyzed for deuterium and oxygen-18 from the western states of Arizona, California, Colorado, Idaho, Montana, Nevada, New Mexico, Oregon, Utah, Washington, and Wyoming. (No. 2000-388). US Dept. of the Interior, US Geological Survey.

Friedman, I., Smith, G.I., Johnson, C.A., and Moscati, R.J., 2002, Stable isotope compositions of waters in the Great Basin, United States 2. Modern precipitation: Journal of Geophysical Research: Atmospheres, v. 107, no. D19, p. ACL-15.

Gagnon, C.A., Butler, K.L., Gaviria, E., Terrazas, A., Gao, A., Bhattacharya, T., Boutt, D.F., Munk, L.A., and Ibarra, D.E., 2023, Paleoclimate controls on lithium enrichment in Great Basin Pliocene− Pleistocene lacustrine clays: Geological Society of America Bulletin. v. 135, no. 11-12, p. 3201-3212.

Gans, P.B., 2023, Geologic framework of the Rio Tinto boron deposit, Mojave Desert, California, in Mines of the Mojave: 2023 Desert Symposium Field Guide and Proceedings:, p. 168–169.

Gao, Y., Gao, Y., Ibarra, D.E., Du, X., Dong, T., Liu, Z., and Wang, C., 2021, Clay mineralogical evidence for mid-latitude terrestrial climate change from the latest Cretaceous through the earliest Paleogene in the Songliao Basin, NE China: Cretaceous Research, v. 124, p. 104827.

Glazner, A.F., and O'Neil, J.R., 1989, Crustal structure of the Mojave Desert, California: Inferences from Sr and O Isotope studies of Miocene volcanic rocks: Journal of Geophysical Research: Solid Earth, v. 94, no. B6, p. 7861–7870.

Glazner, A.F., Walker, J.D., Bartley, J.M., and Fletcher, J.M., 2002, Cenozoic evolution of the Mojave block of southern California: Geological Society of America Memoirs, v. 195, p. 19–41.

Greim, P., Solomon, A.A., and Breyer, C., 2020, Assessment of lithium criticality in the global energy transition and addressing policy gaps in transportation: Nature communications, v. 11, no. 1, p. 4570.

Henderson, A.K., and Shuman, B.N., 2009, Hydrogen and oxygen isotopic compositions of lake water in the western United States: Geological Society of America Bulletin, v. 121, nos. 7–8, p. 1179–1189.

Henkes, G.A., Passey, B.H., Grossman, E.L., Shenton, B.J., Pérez-Huerta, A., and Yancey, T.E., 2014, Temperature limits for preservation of primary calcite clumped isotope paleotemperatures: Geochimica et cosmochimica acta, v. 139, p. 362–382.

Horton, T.W., and Chamberlain, C.P., 2006, Stable isotopic evidence for Neogene surface downdrop in the central Basin and Range Province: Geological Society of America Bulletin, v. 118, nos. 3–4, p. 475–490.

Horton, T.W., Defliese, W.F., Tripati, A.K., and Oze, C., 2016, Evaporation induced 18O and 13C enrichment in lake systems: A global perspective on hydrologic balance effects: Quaternary Science Reviews, v. 131, p. 365–379.

Hren, M. T., & Sheldon, N. D., 2012, Temporal variations in lake water temperature: Paleoenvironmental implications of lake carbonate δ18O and temperature records: Earth and Planetary Science Letters, v. 337, p. 77-84.

Hu, B., Zhang, C., and Zhang, X., 2022, The Effects of Hydrochloric Acid Pretreatment on Different Types of Clay Minerals: Minerals, v. 12, no. 9, p. 1167.

Hughes, R.E., Moore, D.M., and Glass, H.D., 1994, Qualitative and quantitative analysis of clay minerals in soils: Quantitative methods in soil mineralogy, p. 330–359.

Huntington, K.W., Eiler, J.M., Affek, H.P., Guo, W., Bonifacie, M., Yeung, L.Y., Thiagarajan, N., Passey, B., Tripati, A., and Daëron, M., 2009, Methods and limitations of 'clumped'CO2 isotope (Δ47) analysis by gas-source isotope ratio mass spectrometry: Journal of Mass Spectrometry, v. 44, no. 9, p. 1318–1329.

Ibarra, D.E., and Evaristo, J., 2024, Soil pore water evaporation and temperature influences on clay mineral paleothermometry: Communications Earth & Environment, v. 5, no. 1, p. 21.

Ibarra, D.E., Egger, A.E., Weaver, K.L., Harris, C.R., and Maher, K., 2014, Rise and fall of late Pleistocene pluvial lakes in response to reduced evaporation and precipitation: Evidence from Lake Surprise, California: Bulletin, v. 126, no. 11–12, p. 1387–1415.

Ibarra, D.E., Oster, J.L., Winnick, M.J., Caves Rugenstein, J.K., Byrne, M.P., and Chamberlain, C.P., 2018, Warm and cold wet states in the western United States during the Pliocene–Pleistocene: Geology, v. 46, no. 4, p. 355–358.

Ibarra, D.E., Yanchilina, A.G., Lloyd, M.K., Methner, K.A., Chamberlain, C.P., Yam, R., Shemesh, A., and Stolper, D.A., 2022, Triple oxygen isotope systematics of diagenetic recrystallization of diatom opal-A to opal-CT to microquartz in deep sea sediments: Geochimica et cosmochimica acta, v. 320, p. 304–323.

Ibarra, D.E., Dai, J., Gao, Y., Lang, X., Duan, P., Gao, Z., Chen, J., Methner, K., Sha, L., and Tong, H., 2023, High-elevation Tibetan Plateau before India–Eurasia collision recorded by triple oxygen isotopes: Nature Geoscience, v. 16, no. 9, p. 810–815.

IEA, 2021, The Role of Critical Minerals in Clean Energy Transitions, International Energy Agency, Paris. www.iea.org/reports/the-role-of-critical-minerals-in-clean-energy-transitions.

Jessey, D.R., 2010, Geology and Ore Genesis of Silver–Barite Mineralization in the Central Mojave Desert, CA, in CA: Abstracts of Proceedings: the 2010 Desert Symposium: California State University.

Jindalee Resources Limited,"Mineral Resource at McDermitt Increases to 21.5 Mt LCE, Now the Largest Lithium Deposit in the US", 2023, www.jindalee.net/site/pdf/a01eecf1-e9c2-45de-af32-c862da0f08ce/Resource-at-McDermitt-increases-to-215-Mt-LCE.pdf

John, C.M., and Bowen, D., 2016, Community software for challenging isotope analysis: First applications of 'Easotope'to clumped isotopes: Rapid Communications in Mass Spectrometry, v. 30, no. 21, p. 2285–2300.

John, C.M., and Davis, S., 2015, A Review of the Performance of the "Imperial Batch EXtraction"(IBEX) Device for Clumped Isotope Analysis:

Kanik, N.J., Longstaffe, F.J., Kuligiewicz, A., and Derkowski, A., 2022, Systematics of smectite hydrogen-isotope composition: Structural hydrogen versus adsorbed water: Applied Clay Science, v. 216, p. 106338.

Kasbohm, J., and Schoene, B., 2018, Rapid eruption of the Columbia River flood basalt and correlation with the mid-Miocene climate optimum: Science advances, v. 4, no. 9, p. eaat8223.

Kaushik, A., Gupta, A.K., Clemens, S.C., Kumar, P., Sanyal, P., Gupta, P., Jaiswal, M.K., Maurya, A.S., Sengupta, S., and Sharma, R., 2023, Paleoclimatic reconstruction of northwest Himalaya since CE 475 using lake sediments from Tadag Taal, Kumaun, India: Palaeogeography, Palaeoclimatology, Palaeoecology, v. 619, p. 111544.

Kim, S.-T., and O'Neil, J.R., 1997, Equilibrium and nonequilibrium oxygen isotope effects in synthetic carbonates: Geochimica et cosmochimica acta, v. 61, no. 16, p. 3461–3475.

Knott, J.R., Wan, E., Deino, A.L., Casteel, M., Reheis, M.C., Phillips, F.M., Walkup, L., McCarty, K., Manoukian, D.N., and Nunez, E., 2019, Lake Andrei: A Pliocene pluvial lake in Eureka Valley, eastern California, in Starratt, S., and Rosen, M.R., eds., From Saline to Freshwater: The Diversity of Western Lakes in Space and Time: Geological Society of America Special Paper 536, p. 125–142.

Kukla, T., Rugenstein, J.K.C., Ibarra, D.E., Winnick, M.J., Strömberg, C.A.E., and Chamberlain, C.P., 2022, Drier winters drove Cenozoic open habitat expansion in North America: AGU Advances, v. 3, no. 2, p. e2021AV000566.

Li, H.-C., and Ku, T.-L., 1997, δ13C–δ18C covariance as a paleohydrological indicator for closed-basin lakes: Palaeogeography, Palaeoclimatology, Palaeoecology, v. 133, nos. 1–2, p. 69–80.

Lindsay, E.H., 1972, Small mammal fossils from the Barstow Formation, California:

Loughney, K.M., and Badgley, C., 2017, Facies, environments, and fossil preservation in the Barstow Formation, Mojave Desert, California: Palaios, v. 32, no. 6, p. 396–412.

Loughney, K.M., and Badgley, C., 2020, The influence of depositional environment and basin history on the taphonomy of mammalian assemblages from the Barstow Formation (Middle Miocene), California: Palaios, v. 35, no. 4, p. 175–190.

Loughney, K.M., and Smith, S.Y., 2015, Phytoliths of the Barstow Formation through the Middle Miocene Climatic Optimum: preliminary findings. 2015 Desert Symposium.

Loughney, K.M., Hren, M.T., Smith, S.Y., and Pappas, J.L., 2020, Vegetation and habitat change in southern California through the Middle Miocene Climatic Optimum: paleoenvironmental records from the Barstow Formation, Mojave Desert, USA: GSA Bulletin, v. 132, nos. 1–2, p. 113–129.

Loughney, K.M., Harkness, A., and Badgley, C., 2023, Middle Miocene fire activity and C4 vegetation expansion in the Barstow Formation, California, USA: Geology, v. 51, no. 8, p. 763-767.

MacFadden, B.J., Swisher III, C.C., Opdyke, N.D., and Woodburne, M.O., 1990, Paleomagnetism, geochronology, and possible tectonic rotation of the middle Miocene Barstow Formation, Mojave Desert, southern California: Geological Society of America Bulletin, v. 102, no. 4, p. 478–493.

McCulloh, T.H., 1952, Geology of the southern half of the Lane Mountain quadrangle, California: Los Angeles, University of California: Los Angeles, University of California: 1–139 p.

Menemenlis, S., White, S.M., Ibarra, D.E., and Lora, J.M., 2022, A proxy-model comparison for mid-Pliocene warm period hydroclimate in the Southwestern US: Earth and Planetary Science Letters, v. 596, p. 117803.

Menking, K.M., Musler, H.M., Fitts, J.P., and Code, S., 1993, Clay mineralogical analyses of the Owens Lake core: Core OL-92 From Owens Lake, Southeast California, v. 93, no. 683, p. 73.

Miller, D.M., Gans, P.B., Felger, T.J., and Vazquez, J.A., 2022, Post-Early Miocene silicic volcanism in the northern Mojave Desert, California: 2022 Desert symposium field guide and proceedings, p. 124-141

Mills, M.M., Sanchez, A.C., Boisvert, L., Payne, C.B., Ho, T.A., and Wang, Y., 2023, Understanding smectite to illite transformation at elevated (> 100° C) temperature: Effects of liquid/solid ratio, interlayer cation, solution chemistry and reaction time: Chemical Geology, v. 615, p. 121214.

Mix, H.T., and Chamberlain, C.P., 2014, Stable isotope records of hydrologic change and paleotemperature from smectite in Cenozoic western North America: Geochimica et Cosmochimica Acta, v. 141, p. 532–546.

Mix, H.T., Ibarra, D.E., Mulch, A., Graham, S.A., and Chamberlain, C.P., 2016, A hot and high Eocene Sierra Nevada: Bulletin, v. 128, nos. 3–4, p. 531–542.

Moore, D.M., and Reynolds Jr, R.C., 1989, X-ray Diffraction and the Identification and Analysis of Clay Minerals.: Oxford University Press (OUP).

Morissette, C.L., 2012, The impact of geological environment on the lithium concentration and structural composition of hectorite clays: M.Sc. thesis Reno, NV, University of Nevada, Reno, p. 243.

Nuriel, P., Miller, D. M., Schmidt, K. M., Coble, M. A., & Maher, K., 2019. Ten-million years of activity within the Eastern California Shear Zone from U–Pb dating of fault-zone opal. Earth and Planetary Science Letters, 521, 37-45.

Ogilvie, I.A., 2023, Structure, stratigraphy, and source of sediment-hosted lithium deposits at Rhyolite Ridge, Silver Peak Range, western Nevada: M.Sc. thesis, Reno, NV, University of Nevada-Reno, 153 p.

Orris, G.J., and Bliss, J.D., 1991, Some industrial mineral deposit models: descriptive deposit models: Citeseer.

Pagnac, D., 2009, Revised large mammal biostratigraphy and biochronology of the Barstow Formation (Middle Miocene), California: PaleoBios, v. 29, no. 2, p. 48-59.

Park, L.E., and Downing, K.F., 2001, Paleoecology of an exceptionally preserved arthropod fauna from lake deposits of the Miocene Barstow Formation, Southern California, USA: Palaios, v. 16, no. 2, p. 175–184.

Passey, B.H., and Henkes, G.A., 2012, Carbonate clumped isotope bond reordering and geospeedometry: Earth and Planetary Science Letters, v. 351, p. 223–236.

Pilla, R.M., Mette, E.M., Williamson, C.E., Adamovich, B. V, Adrian, R., Anneville, O., Balseiro, E., Ban, S., Chandra, S., and Colom-Montero, W., 2021, Global data set of long-term summertime vertical temperature profiles in 153 lakes: Scientific data, v. 8, no. 1, p. 200.

Poppe, L.J., Paskevich, V.F., Hathaway, J.C., and Blackwood, D.S., 2001, A laboratory manual for X-ray powder diffraction: US Geological Survey open-file report, v. 1, no. 041, p. 1–88.

Pound, M.J., Haywood, A.M., Salzmann, U., and Riding, J.B., 2012, Global vegetation dynamics and latitudinal temperature gradients during the Mid to Late Miocene (15.97–5.33 Ma): Earth-Science Reviews, v. 112, nos. 1–2, p. 1–22.

Pozo, M., and Calvo, J.P., 2018, An overview of authigenic magnesian clays: Minerals, v. 8, no. 11, p. 520.

Putman, A. L., and Bowen, G. J., 2019, A global database of the stable isotopic ratios of meteoric and terrestrial waters: Hydrology and Earth System Sciences, v. 23, no. 10, p. 4389-4396.

Qi, H., Coplen, T.B., Gehre, M., Vennemann, T.W., Brand, W.A., Geilmann, H., Olack, G., Bindeman, I.N., Palandri, J., and Huang, L., 2017, New biotite and muscovite isotopic reference materials, USGS57 and USGS58, for δ2H measurements–A replacement for NBS 30: Chemical Geology, v. 467, p. 89–99.

Reynolds, J.T., and Chafetz, D.A., 2020, Geology of the Lithium-Boron Rhyolite Ridge Project, Silver Peak Range, Esmeralda County, Nevada: Geological Society of Nevada Symposium Reno, p. 435-450.

Serrano L., 1994, Daily variations in two ponds with different mixing dynamics in the Donana National Park (SW Spain): Proceedings of the International Association of Theoretical and Applied Limnology, v 25, p. 1345-1349.

Sharp, Z.D., Atudorei, V., and Durakiewicz, T., 2001, A rapid method for determination of hydrogen and oxygen isotope ratios from water and hydrous minerals: Chemical geology, v. 178, nos. 1–4, p. 197–210.

Sheppard, S.M.F., and Gilg, H.A., 1996, Stable isotope geochemistry of clay minerals:“The story of sloppy, sticky, lumpy and tough” Cairns-Smith (1971): Clay minerals, v. 31, no. 1, p. 1–24.

Shofner, G.A., 2006, The Quaternary geology of the Ames 7.5-minute quadrangle, Monroe and Randolph counties, Illinois: Southern Illinois University at Carbondale.

Singleton, J.S., and Gans, P.B., 2008, Structural and stratigraphic evolution of the Calico Mountains: Implications for early Miocene extension and Neogene transpression in the central Mojave Desert, California: Geosphere, v. 4, no. 3, p. 459–479.

Steinthorsdottir, M., Coxall, H.K., De Boer, A.M., Huber, M., Barbolini, N., Bradshaw, C.D., Burls, N.J., Feakins, S.J., Gasson, E., and Henderiks, J., 2021, The Miocene: The future of the past: Paleoceanography and Paleoclimatology, v. 36, no. 4, p. e2020PA004037.

Stolper, D.A., and Eiler, J.M., 2015, The kinetics of solid-state isotope-exchange reactions for clumped isotopes: A study of inorganic calcites and apatites from natural and experimental samples: American Journal of Science, v. 315, no. 5, p. 363–411.

Talbot, M.R., 1990, A review of the palaeohydrological interpretation of carbon and oxygen isotopic ratios in primary lacustrine carbonates: Chemical Geology: Isotope Geoscience Section, v. 80, no. 4, p. 261–279.

Tongwa, F.A., Mouliom, A.G., Rouwet, D., Fantong, W.Y., Tchamabé, B.C., Ohba, T., Yoshida, Y., Sighomnou, D., Sigha, N., and Kusakabe, M., 2015, δ18O and δD variations in some volcanic lakes on the Cameroon Volcanic Line (West-Africa): generating isotopic baseline data for volcano monitoring and surveillance in Cameroon: Journal of Limnology, v. 74, no. 1.

Tosca, N., 2014, Geochemical pathways to Mg-clay formation, in Magnesian clays: Characterization, origin and applications: AIPEA Special Publication: AIPEA, p. 1–52.

Tosca, N.J., and Masterson, A.L., 2014, Chemical controls on incipient Mg-silicate crystallization at 25 C: Implications for early and late diagenesis: Clay Minerals, v. 49, no. 2, p. 165–194.

Tosca, N.J., and Wright, V.P., 2018a, Diagenetic pathways linked to labile Mg-clays in lacustrine carbonate reservoirs: a model for the origin of secondary porosity in the Cretaceous pre-salt Barra Velha Formation, offshore Brazil: Geological Society, London, Special Publications, v. 435, no. 1, p. 33–46.

U.S. Geological Survey, 2024, Mineral commodity summaries 2024. https://pubs.usgs.gov/periodicals/mcs2024/mcs2024.pdf

Warren, J.K., 2016, Evaporites: A geological compendium: Springer.

Woodburne, M.O., Tedford, R.H., and SWISHER III, C.C., 1990, Lithostratigraphy, biostratigraphy, and geochronology of the Barstow Formation, Mojave Desert, southern California: Geological Society of America Bulletin, v. 102, no. 4, p. 459–477.

CHAPTER 5

Characterization of lithium clays and their favorability for Li release during acid leaching reactions

Catherine Gagnon[1,2], Mike Whittaker[1]

1. Lawrence Berkeley National Laboratory

1 Cyclotron Road

Berkeley, CA

2. Department of Earth, Environmental, and Planetary Sciences

Institute at Brown for Environment and Society

Brown University

Providence, RI

Abstract

Lithium-bearing clay deposits, an emerging type of lithium resource, can be highly heterogeneous in their mineralogical and chemical compositions, which can lead to variability in extraction behavior and production yields during ore processing. Optimizing ore processing therefore requires detailed, deposit-specific characterization coupled with a mechanistic understanding of the leaching reaction chemistry that governs lithium release from the clay structure. This study details the bulk element chemistry and mineralogy of lithium-rich clays from the northern McDermitt Caldera, NV-OR using XRD and SEM-EDS paired with principal component analysis (PCA). Further, we present isothermal titration calorimetry (ITC) data for clay–acid reactions of suspended hectorite and sulfuric or citric acid. X-ray diffraction and SEM-EDS analyses confirm that the mudstones are dominated by hectorite-group smectites with variable calcite, feldspar, and Fe-oxide contents. Principal component and cluster analyses of assay and EDS data reveal systematic elemental associations, particularly between Li, Mg, Ca, and Sr, that reflect co-variation of clay and carbonate phases and other groupings related to the presence of feldspar and sulfides. ITC experiments performed with sulfuric and citric acids at varying concentrations yield direct measurements of enthalpy (ΔH), Gibbs free energy (ΔG), and entropy (ΔS) for clay–acid reactions. Sulfuric acid titrations exhibit consistent, moderately exothermic enthalpies (−18.7 to −29.5 kJ/mol) and small stoichiometries corresponding to cation-exchange capacities of 60–110 meq/100 g, consistent with available literature values for Li-hectorite. These reactions are reproducible and strongly favorable ($\Delta G \approx -22$ to −35 kJ/mol), reflecting rapid, stoichiometric proton exchange. In contrast, citric acid titrations produce variable and sometimes extreme heats (−1.6 to −29.5 kJ/mol) and poorly constrained stoichiometries, indicating a mix of heat contributions from protonation, dissolution, and cation complexation. The associated ΔS values suggest greater structural disorder

during citrate reactions relative to sulfate. Together, these results demonstrate that while sulfuric acid promotes efficient ion-exchange reactions with predictable energetics, citric acid induces additional pathways that potentially destabilize the clay structure. Understanding these thermodynamic differences provides a mechanistic foundation for optimizing leaching protocols, balancing extraction efficiency with environmental and reagent costs in the processing of lithium-bearing clays.

1. Introduction

The demand for lithium as a critical component in rechargeable batteries has intensified the search for efficient and sustainable methods to extract lithium from unconventional sedimentary deposits such as lithium-bearing clays (IEA, 2024; Vega-Muratalla et al., 2024; Wu et al, 2025). In contrast to spodumene and salar brine deposits, where lithium is extracted through high-temperature roasting or solar evaporation (e.g., Nandihalli et al., 2024; Zhao, 2023), lithium-bearing clays–predominantly smectite and illite—must be chemically leached to release lithium from their structurally bound sites within the silicate framework (Zhao, 2023; Liu, 2024). The most widely used approaches are roasting (Crocker and Lien, 1987) and acid leaching (Lithium Americas, 2022), both of which aim to convert clay lattice bound lithium into soluble lithium salts which can be recovered from solution. During roasting, clays are mixed with limestone and gypsum and pelletized prior to roasting at 900 °C. Upon roasting, lithium is converted to lithium sulfate and leached using water (Crocker and Lien, 1987; Roy et al., 2024). During the acid leaching procedure, clays are reacted with sulfuric acid to produce lithium sulfate, the solution of which is then neutralized and precipitated as lithium carbonate using soda ash (Lithium Americas, 2022; Roy et al., 2024).

The efficiency, recovery, and environmental impacts of different extraction methods vary significantly depending on the clay's mineralogy, reaction conditions, and the type of acid used (e.g., Xie et al., 2024). Life cycle assessments comparing the environmental impacts of each extraction method reveal that acid leaching is currently around 5 times more energy efficient than roasting methods and when compared to spodumene mining showed reductions in impacts like carbon dioxide emissions, freshwater water contamination and ecotoxicity, and air pollution (Roy et al., 2024). Acid leaching, however, involves significantly more water consumption than other methods, which is problematic in water stressed regions of the United States where these deposits tend to occur (Putzolu et al., 2025).

Although lithium-bearing clays represent one of the most abundant potential sources of lithium, the mechanisms controlling lithium release during acid leaching remain poorly quantified at the molecular scale. Understanding the reaction chemistry from a kinetic and thermodynamic standpoint may assist in the optimization of acid leaching protocols for Li-bearing clays (Zhao et al., 2023; Zhong et al., 2024; Dong et al., submitted). Identifying which acid yields more favorable energetics (e.g., citric acid's complexation vs. sulfuric acid's simple protonation) informs reagent selection while quantifying reaction enthalpy and apparent stoichiometry (n) constrains acid demand and reaction completeness, which are key to minimizing environmental impacts of ore processing.

Previous studies have modeled lithium–clay equilibria by updating thermodynamic databases (e.g., Bethke, et al., 2022) to produce self-consistent thermodynamic properties of formation for many different clay types including hectorite and Li-illite (Boschetti & Awolayo, 2025). Here, we directly measure the enthalpy (ΔH), Gibbs free energy (ΔG), and entropy (ΔS) of protonation and ion exchange reactions during clay leaching of hectorite using isothermal titration

calorimetry (ITC) — an approach that provides quantitative, mechanistic energetics at the site level (e.g., Bastos et al., 2023). We use purified hectorite suspensions from natural samples, varying acid type and concentration to isolate individual protonation/ion-exchange events during clay leaching. Before conducting the calorimetric experiments on the hectorite, we performed a detailed mineralogical and elemental characterization of the lithium-bearing claystones from the sample region to provide a compositional basis for interpreting the reaction energetics.

2. Materials and Methods

2.1. Samples and datasets

Drill core assay data and lithium mudstone core samples analyzed in this study are from the northern Mcdermitt Caldera, NV-OR and were made accessible by Jindalee Lithium. The mudstone samples analyzed via XRD and SEM-EDS were collected from multiple Jindalee drill cores over the course of three field and core-sampling campaigns in 2024 and 2025. The three samples used in the isothermal titration calorimetry experiments include SHCa-1, a Clay Mineral Society hectorite standard (Chipera et al., 2001) which was size separated by Dong et al., (submitted); JMf0, a fluorohectorite sample from the McDermitt deposit size separated and characterized by Dong et al. (in preparation); and MDD-006 #8, a similar lithium rich hectorite from the same locality. MDD-006 #8 was separated and characterized for this work.

2.2. Clay separations

Samples that were used in the calorimetry experiments were first separated following the procedure outlined by Dong et al., (submitted). Clay samples were dispersed in Milli-Q water in a concentration of 50 $g \cdot L^{-1}$ and ultrasonicated to ensure complete disaggregation. The resulting slurry was separated into 3-5 primary size classes by wet sieving. The <63 μm fraction left over from sieving was further subdivided into finer fractions by centrifugation, using settling times

calculated from Stokes' law to control sedimentation velocity (Allen, 1997; Guy 1969; Poppe et al., 2001). The finest colloidal fraction was vacuum dried down to a gel-like consistency, then purified via dialysis using a cellulose ester membrane with a molecular weight cut-off of 3,500 Da (Spectra/Por Float-A-Lyzer) against Milli-Q water (18.2 MΩ·cm) (Dong et al., submitted).

2.3. X-ray diffractometry

The mineralogical compositions of powdered bulk mudstone samples were analyzed by X-ray diffraction (XRD) using a Rigaku SmartLab® diffractometer (Dong et al., submitted; Dong et al., 2020). The diffractometer was equipped with a theta-theta goniometer and a rotating sample holder using Cu (λkα1 = 1.5406 Å and λkα2 = 1.5444 Å) cathode. The data were collected from 2° to 90° of 2θ with a 0.02 °2θ step-size and speed duration time of 0.5 using a Kα radiation tube (40 kV, 40 mA). The diffraction patterns were analyzed using the software Sieve+ extended which made use of the PDF-4 mineral database (International Centre for Diffraction Data, 2025).

2.4. Scanning electron microscopy and energy dispersive spectroscopy (SEM-EDS)

Bulk powdered samples were mounted onto SEM sample holders using carbon tape, and analyzed for their relative elemental abundances and spatial distributions using EDS.

2.5. Principal component analysis

Whole-rock assay data and associated metadata on drill cores from the northern McDermitt were compiled to perform an initial characterization of the deposit using principal component analysis in R. All geochemical variables were standardized to z-scores to place them on a comparable scale. Principal component analysis (PCA) was then performed using the *FactoMineR* package (Lê et al., 2008) in R, retaining 5 components to capture the main patterns of elemental variation after Jolliffe and Cadima (2016).

After the PCA, we examined the eigenvalue plot to assess how much variance each principal component explains and used loadings plots to evaluate each element's contribution. The loadings show which elements are driving the differences along each PC. High positive or negative loadings on the same PC indicate elements that change together, which inform what geochemical trends each axis represents.

Gaussian mixture modeling (GMM) was applied to the PCA scores from 5 principal components using the *mclust* package (Scrucca et al., 2016) in R to classify samples into statistically distinct geochemical groups, with the optimal number of clusters selected by the Bayesian Information Criterion (BIC; Schwarz, 1978). To group elements by similarity, hierarchical clustering was performed on the loading vectors using cosine distance and Ward's method (Ward 1963), producing dendrograms that reveal key associations among elements.

2.6. Isothermal Titration Calorimetry

Isothermal titration calorimetry (ITC) experiments were performed using a TA Instruments Affinity micro-ITC equipped with a 0.182 mL reaction cell. Either sulfuric acid (0.01 M or 0.0025 M) or citric acid (0.1 M or 0.001 M) was incrementally titrated into the cell in 1–2 μL injections, with a total of 25–50 injections per run. The cell contained dilute (1.6 mM) suspensions of purified clay samples (~100 nm diameter). Injections were spaced by 120–300 s to allow the system to return to baseline between titrations. All experiments were conducted at a constant temperature of 25 °C and a fixed stirring rate across all runs.

Integrated heat data from the ITC experiments were background corrected using the NanoAnalyze Software by subtracting heats from blank titrations in which acid of the same concentration and injection schedule was added to Milli-Q water. The corrected heats (μJ per injection) were then modeled using theWiseman one-site isotherm (Wiseman et al., 1989) and,

when appropriate, a two-site model to capture additional heat not explained by a single equilibrium site. The one-site model fits the heat evolved on each injection using the following equation 1 (Wiseman et al., 1989):

$$q_i = \Delta H\ \Delta C_i \times 10^6 + q_0$$

where q_i is the incremental heat, ΔH the molar enthalpy of titrant binding or proton exchange (J mol^{-1}), ΔC_i the change in complex concentration between injections, and q_0 a constant baseline. Parameters estimated by nonlinear least-squares fitting (Python/SciPy) included the apparent stoichiometry (n), dissociation constant (K_d), ΔH, and q_0. The cell volume (182 µL) and actual titrant and suspension concentrations were used to account for dilution after each injection.

A value for the cation exchange capacity (CEC) was calculated from the fitted stoichiometry n using the following equation 2:

$$CEC = n \times v \times 100{,}000 MW$$

where ν is the number of protons per titrant molecule (2 for H_2SO_4, 3 for citric acid) and MW is the molar mass of the clay. The JMf0 hectorite formula used was determined by Dong et al. (in preparation) using a combination of ICP-MS and ion chromatography to be $Na_{0.01}Ca_{0.12}(Li_{0.35}Mg_{2.65})(Si_{3.71}Al_{0.09}Fe_{0.13}Mn_{0.07})O_{10}(OH)_1F_1$. Since the exact molecular formula is unknown for SHCa-1 and MDD-006-8, we used the same molecular weight as an estimate.

For citric acid titrations, a single-site Wiseman model often left structure in the residuals, indicating that heat was being generated by additional processes beyond simple proton exchange. To better capture this behavior, we also tested a two-site fit in which the total heat is modeled as the sum of two independent site classes with their own stoichiometry, affinity, and enthalpy (Freyer & Lewis, 2008). Because citrate can simultaneously donate protons and strongly complex released

cations, the second “site” is used to lump slower, structural dissolution, metal chelation, and baseline drift together. To avoid parameter overfitting, we also evaluated a constrained version of the model, fixing the well-defined fast proton exchange parameters based on those obtained from the sulfuric acid runs. This constrained fit was used to check whether the extra heat could consistently be captured without inflating stoichiometry or producing spurious results.

3. Results

3.1. Mineralogy and Elemental Analyses

Bulk mudstones measured by XRD (10 samples) showed a large, broad smectite peak consistent with hectorite, stevensite, or nontronite (Figure 1). Clay peak positions were surprisingly consistent considering all samples were only air dried and not glycolated. Other detected minerals included calcite, quartz, orthoclase, sanidine, fluorapatite, and magnesian iron oxide. SEM–EDS analyses (30 samples) reported in atomic percent of powdered lithium mudstones reveal a dominantly silicate framework with high oxygen (58–67 %) and silicon (11–21 %). Magnesium (7–10 %) and calcium (up to 11 %) are common with minor but variable aluminum and iron (≤4 %). Trace sodium, potassium, and phosphorus occur in most samples, while redox-sensitive and transition elements (Mn, Ti, Mo) appear in some samples at very low levels (<1%).

Table 1. Elemental composition (atomic %) of northern McDermitt mudstones by EDS

Core	Top Depth (m)	Bottom Depth (m)	O	Si	Mg	Ca	F	Al	Fe	Na	K	P	S	Mn	Ti	Mo
MDD025	201.03	201.06	64.7	13.9	9.5	7.3	2.7	0.6	0.6	0.4	0.1	0				
MDD025	200.56	200.58	66.7	10.9	7.3	10.9	2.9	0.4	0.5	0.4	0.1	0				
MDD025	196.87	196.9	63.7	14.7	9.8	6.6	4.2	0.3	0.1	0.4	0.1	0				
MDD025	190.89	190.87	60	20.3	8.9	1.6	4.1	2	0.6	0.5	1.7	0	0.3	0.1		
MDD025	175.289	175.409	57.9	20.6	9	0.5	5.6	1.9	1	0.8	2.1	0	0.4	0		
MDD025	175.98	176.38	58.8	18.9	8.1	2.1	5.5	2	1.2	0.7	2.1	0	0.6	0		
MDD011	164.489	164.549	62.1	17.6	2.9	4.6	1.9	4.1	1.4	0.2	4.3	0	0.6	0	0.2	
MDD011	164.259	164.259	60.4	20	6.4	1.8	3.4	3.1	1	0.3	2.9	0	0.3	0	0.2	
MDD025	175.98	176.38	58.8	18.9	8.1	2.1	5.5	2.1	1.2	0.7	2.1	0	0.6	0		
MDD025	175.289	175.409	57.9	20.6	9	0.5	5.6	1.9	1	0.8	2.1	0	0.4	0		
MDD025	190.89	190.87	60	20.3	8.9	1.6	4.1	2	0.6	0.5	1.7	0	0.3	0.1		
MDD025	196.87	196.9	63.7	14.7	9.8	6.6	4.2	0.3	0.1	0.4	0.1	0				
MDD025	200.56	200.58	66.7	10.9	7.3	10.9	2.9	0.4	0.5	0.4	0.1	0				
MDD025	201.03	201.06	64.7	13.9	9.5	7.3	2.7	0.6	0.6	0.4	0.1	0				0.2
MDD011	159.346	159.366	61.8	16	7.9	5.1	4.5	1.6	0.8	0.6	1.5	0	0.1	0.1	0.1	
MDD011	156.242	156.262	59.4	19.8	8.2	1.6	5	2.3	0.8	0.4	2.2	0	0.1	0	0.2	
MDD011	155.43	155.46	64.1	13.4	5.9	8.7	3.9	1.5	0.5	0.3	1.4	0	0.3	0		
MDD011	152.01	152.04	59.2	20.8	9.3	2.3	5.8	0.9	0.4	0.4	0.9	0				
MDD011	149.36	149.41														
MDD011	147.48	147.52	60.1	18.2	10.2	3	5.8	0.8	0.4	0.6	0.7	0	0.1			
MDD011	142.56	142.6	59.8	19.6	8.8	1.5	4.1	2.2	0.9	0.7	2	0	0.3	0		
MDD011	141.81	141.85	58.5	20	12.4	0.9	5.8	0.7	0.3	0.7	0.5	0	0.1	0		
MDD011	137.11	137.15	60.9	18.1	11.3	0.8	5.6	1.2	0.5	0.8	0.5	0	0.2	0		
MDD011	133.66	133.7	61.8	16	7.9	5.1	4.5	1.6	0.8	0.6	1.5	0	0.1	0.1	0.1	
MDD011	128.31	128.35	59	21.3	6.9	0.8	4.2	3.2	0.6	0.5	3.2	0	0.1		0.1	
MDD011	123.59	123.62	61.6	20.1	4.6	1.9	2.1	4.1	1	1.5	3.1	0				
MDD011	119.86	119.89	61.9	21.3	4.3	0.5		4.7	1.6	0.4	4.8	0	0.2	0.1	0.2	
MDD011	113.12	113.15	61.5	21.6	8.5	0.7	2.1	2.2	1.4	0.5	1.5	0				
MDD011	111.45	111.454	61.1	20.5	70	0.5	1.7	3.8	1.5	1.1	2.4	0	0.2		0.3	
MDD011	108.7	108.75	59.1	20.5	10.2	0.8	3.7	1.7	1.4	0.6	1.3	0	0.1	0.1	0.5	

Table 2. Mineralogy of northern McDermitt mudstones

Core	Top Depth (m)	Bottom Depth (m)	Mineralogy
MDD025	190.89	190.87	calcite, hectorite, celsian, stevensite, sanadine, nontronite, montmorillonite, quartz
MDD011	159.346	159.366	quartz, sanadine, calcite, orthoclase, stevensite
MDD011	149.36	149.41	calcite, stevensite, orthoclase, quartz
MDD011	147.48	147.52	calcite, quartz, stevensite, nontronite, sanadine
MDD011	141.81	141.85	stevensite, quartz, calcite, orthoclase, nontronite
MDD011	161.205	161.233	quartz, sanadine, nontronite, calcite, magnesium iron oxide
MDD021	37.49	37.56	quartz, calcite, stevensite, sanadine
MDD006	128.09	128.14	quartz, calcite, stevensite, sanadine
MDD006 #8	119.78	122.53	stevensite, quartz, calcite, saponite, nontronite, orthoclase

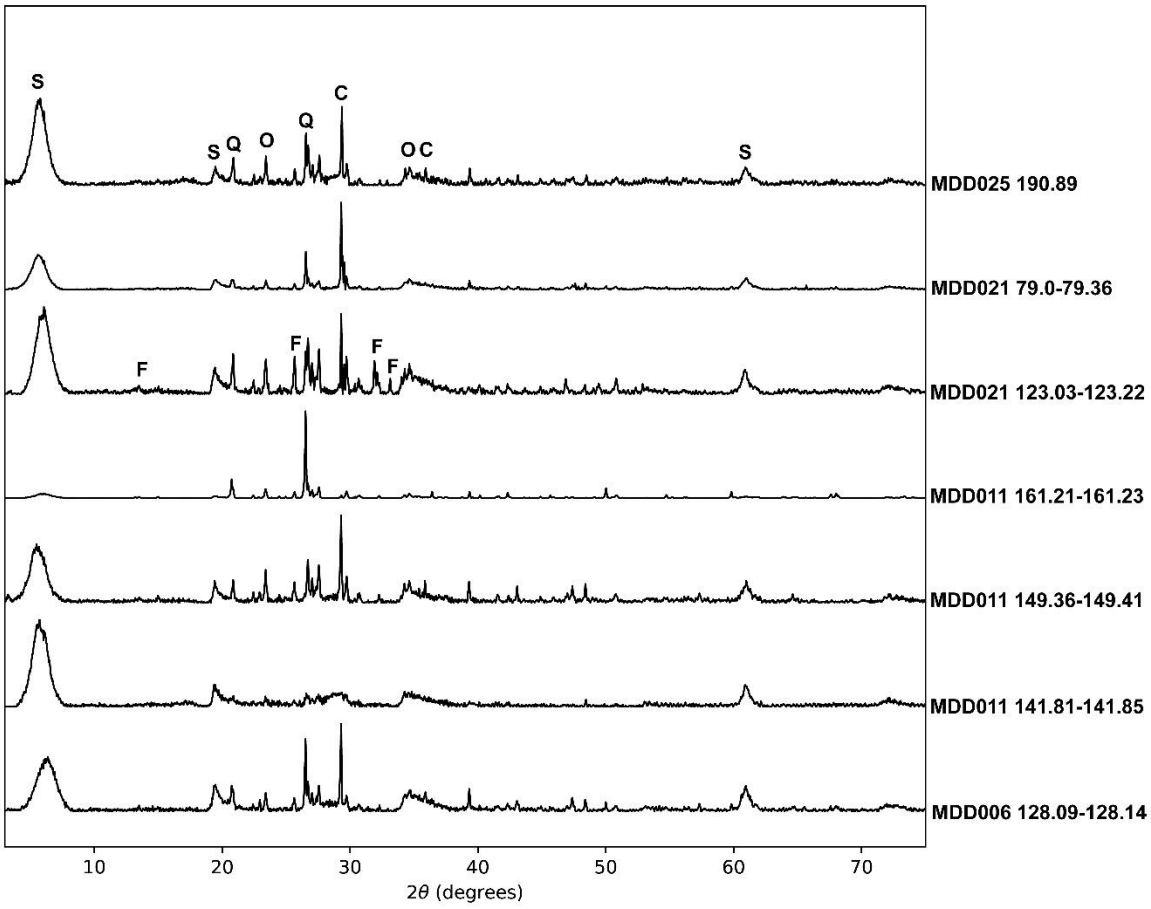

Figure 1. Intensity normalized XRD scans for several example Li mudstone samples from the northern McDermitt deposit with major peaks mineralogies labeled for smectite (S), quartz (Q), orthoclase (O), calcite (C), and fluorapatite (F).

3.1.1. Principal Component Analysis of Assay Data

Results from the principal component analysis on the Jindalee elemental assay data across 62 drill core holes (5491 samples) are summarized in figure 1. The PCA biplot (Fig 2A) shows that the first two principal components explain about 33% of the total variance in the dataset (PC1 = 22.8%, PC2 = 10%). Variables with long arrows and similar directions are positively correlated, while those pointing in opposite directions are negatively correlated. Elements such as Al, Ga, Zn,

Y, Hf, Ta, and Ce have strong positive loadings on PC1, indicating that they vary together. In contrast, Li, Mg, Ca, and Sr load strongly negative on PC1, forming a separate geochemical association that probably reflects carbonate or clay-rich phases. PC2 captures variation among Fe, Mn, Ti, and P, which cluster upward on the plot and may represent redox-sensitive or oxide-associated processes.

Figure 2B shows the hierarchical clustering dendrogram of elemental loadings, which groups elements based on the similarity of their multivariate behavior across the principal components. The analysis identifies nine distinct clusters, each represented by a unique color. The first cluster (red) contains Ag, Co, Cu, Ni, Sn, and W, a compact group of transition metals with very similar loading patterns. The second cluster (blue) includes Cr and V and shares a branch with the third cluster (green) Li, Mg, Ca, Sr. The fourth cluster (purple) is composed of Y, Na, Al, Ga, Zn, Ge,In, Pb, Zr ,Cs, Hf, Nb, Ta, Ce, and La. The fifth cluster (orange) consists of Cd, K, Rb, a tightly grouped set characterized by highly consistent loadings. The sixth cluster (brown) contains As, Sb, Tl, Bi, Te, and S. The seventh cluster (pink) contains Re, Mo, and Se. The eight cluster (grey) encompasses U and Be. The ninth cluster (teal) shares a branch with the eighth cluster and includes Ba, Fe, Ti, P, Sc, Mn, and Th.

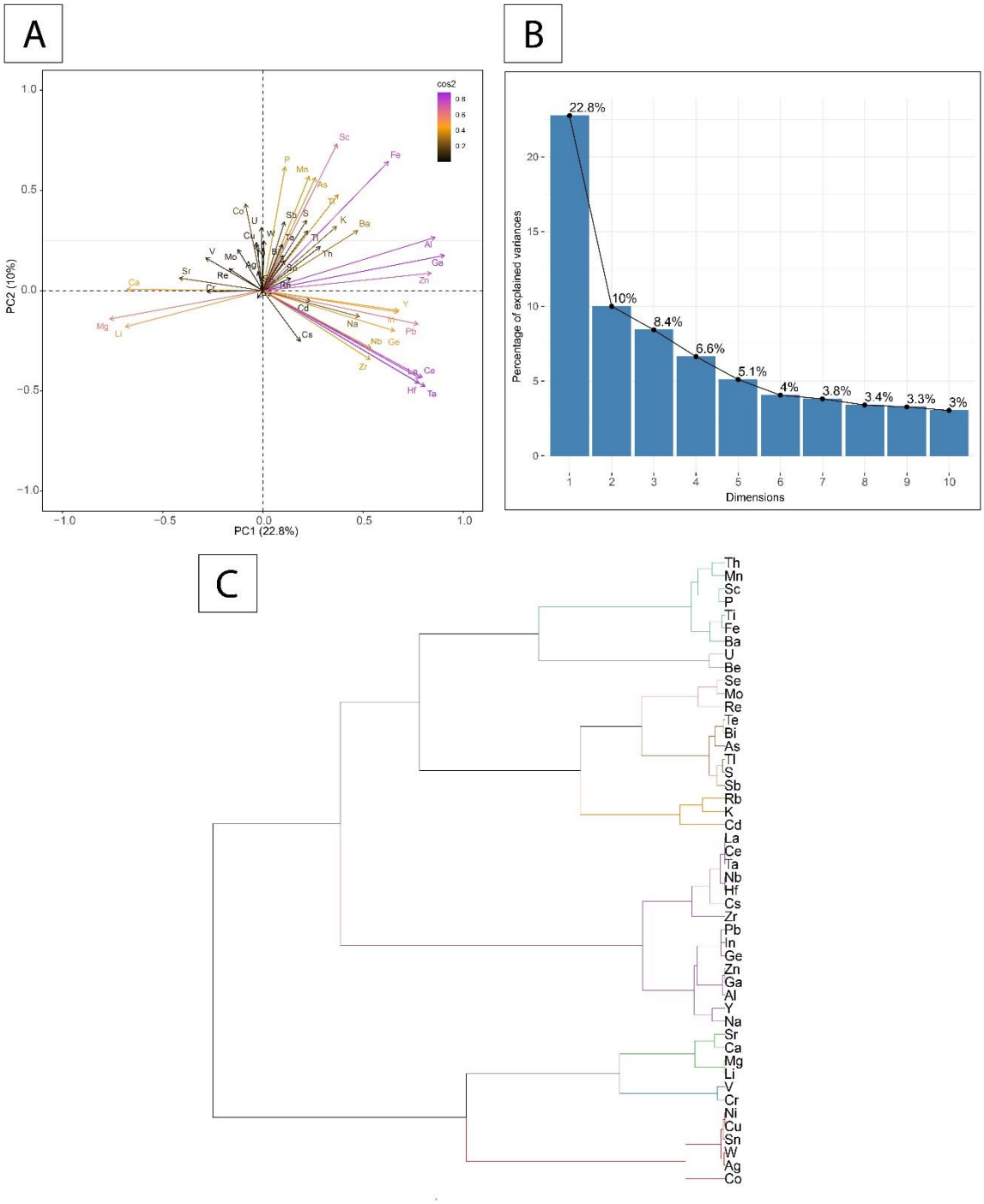

Figure 2. PCA and cluster analysis of Jindalee elemental assay data from multiple drill holes showing elemental covariance. (A) Biplot in PC1 versus PC2 space contoured by cosine squared values. (B) Scree plot showing he percent of variance explained for the first ten principal components. (C) Hierarchical element clusters based on loadings from PC1-PC5 and calculated cosine similarity indices. Colors represent distinct clusters.

3.1.2. Principal Component Analysis of SEM-EDS Data

Principal component analysis of elemental maps obtained from EDS (30 samples) reveal elemental spatial covariations, further contextualizing the co-occurrence results from assay data. The analysis was conducted on each individual sample EDS map and included PC1-PC5. To better assess which PCs may represent elemental pairings, a cluster analysis was performed on the loadings for each of the five PCs (Figure 3). Across most samples, one of the PCs was typically influenced almost entirely by Fe and S (i.e. trace pyrite) while another was influenced almost entirely by Ca and C (i.e. carbonate). This can be seen in Figure 3 where the Fe-S cluster's loading distribution is narrow and strongly positive on PC3 when compared to other clusters and the Ca-C cluster's loading distribution is narrow and strongly positive on PC2 compared to other element clusters (Figure 3). We therefore conclude that in this sample, PC3 and PC5 represent the pyrite and calcite respectively, and map these based on pixel PC scores in Figure 4. Other clusters contain wider distributions, which reflect variable loading contributions from each of those clusters' elements on a given PC. This suggests that the variance is not explained by one dominant mineralogy for those elements. Oxygen for example, is colocalized with many numerous elements found in carbonates, clays, feldspar, and oxides. Si may be associated with quartz, or feldspars and clays of different compositions. For some samples, Si was clustered with Mg and O, which is consistent with magnesian clays. In the example shown in figures 3 and 4, Si is most strongly associated with K and Al, which suggests that PC1 may capture variance due to the presence of feldspar.

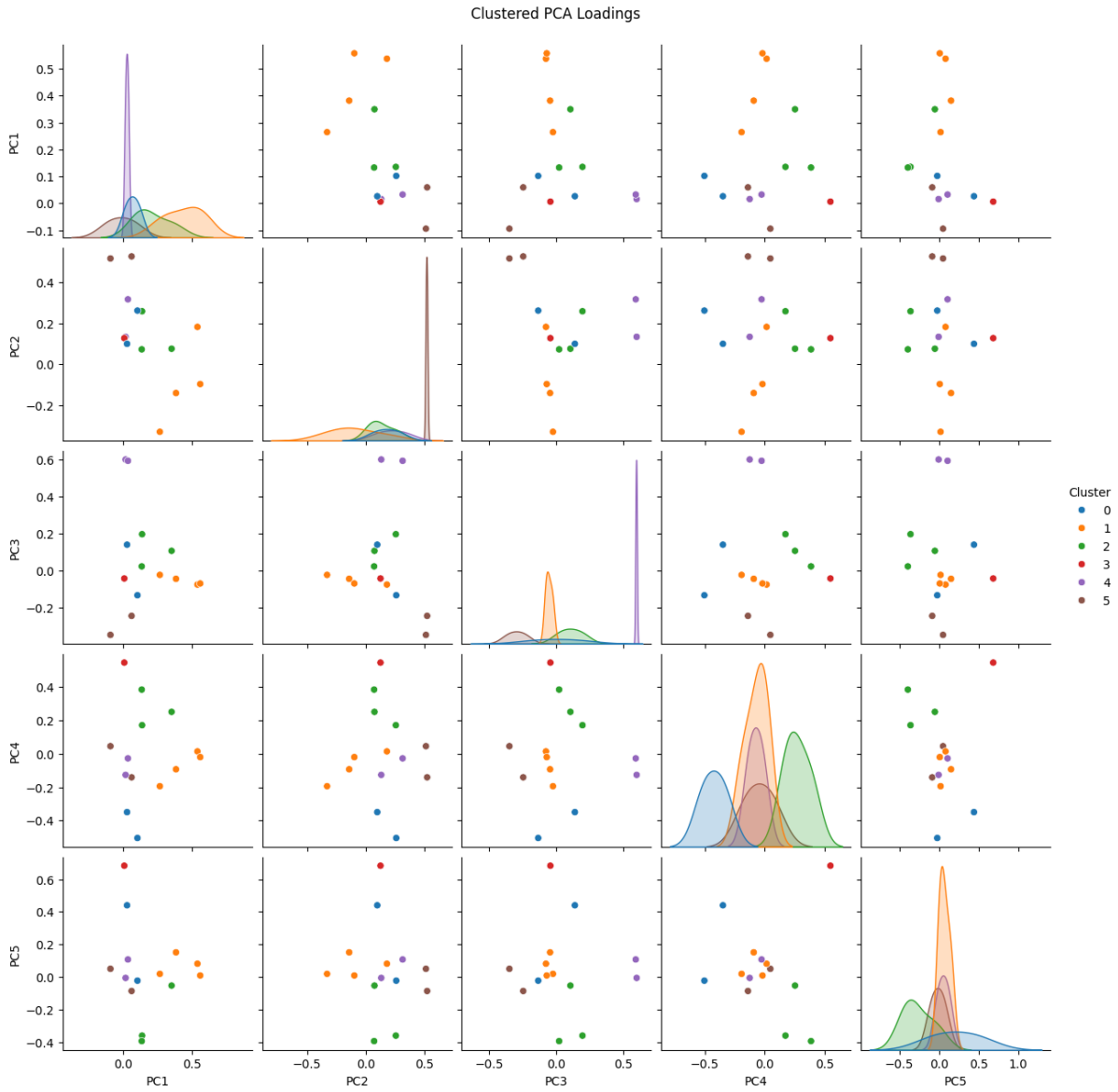

Figure 3. Biplots of the first 5 principal components for sample MDD-025 175.98- 176.38 with loading distributions plotted on the diagonal. Colors represent clusters of covarying elements Ti and P (0); Al, K,O, Si (1); Mg, F, Na (2); Mn (3); Fe and S (4); Ca and C (5).

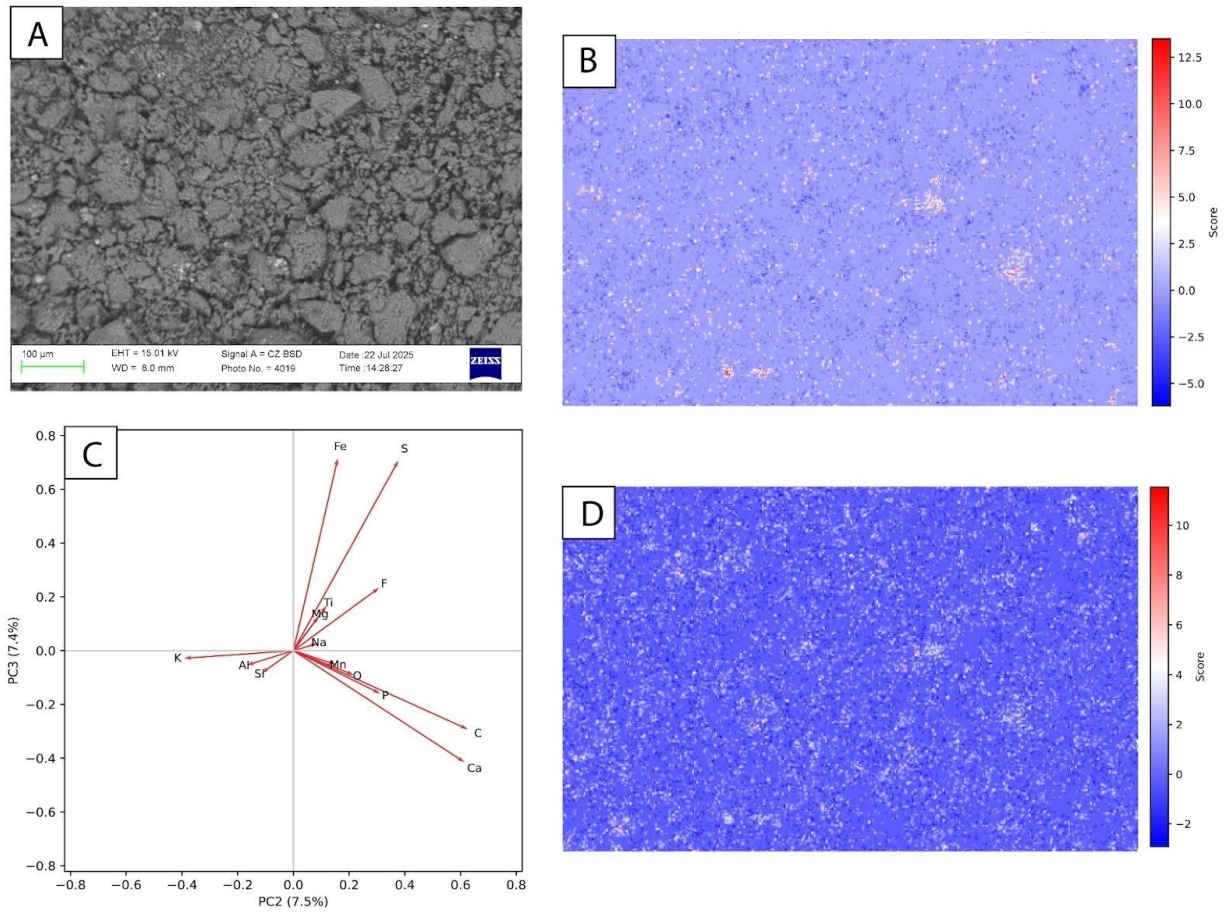

Figure 4. Results of principal component analysis on individual sample MDD-025 175.98-176.38 EDS data. (A) SEM back scatter image of sample. (C) Loading vector plot of PC2 and PC3 for elements in the same sample. (B) Mapped PC3 scores highlighting areas of strong Fe and S association (red) and (D) mapped PC2 scores highlighting areas of strong Ca and C association (red).

3.2. Isothermal titration calorimetry

We chose two representative mudstone samples from the McDermitt deposit for the titration calorimetry experiments based on their high smectite and Li content. We included a well characterized hectorite standard from the Clay Minerals Society source clay repository, SHCa-1, for comparison. Example heat flow curves and modeled fits are shown for sample JMf0 in Figure 5.

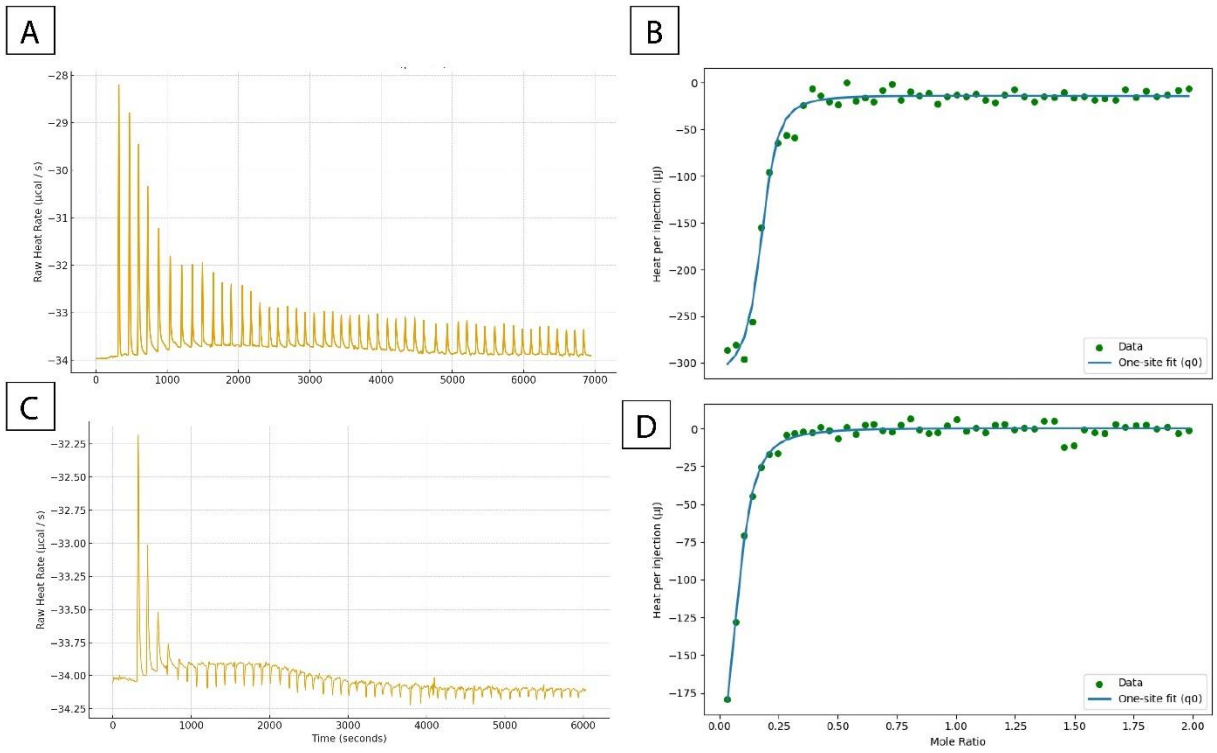

Figure 5. Background corrected heat curves (A, C) and one-site model fits to corrected heat injections (B, D) for 1uL injections of 0.01M sulfuric acid (A,B) and 0.01M citric acid (C, D) into 1.6 mM JMF0 hectorite clay suspension.

3.2.1. Sample JMf0

The sulfuric acid ΔH is consistently ~ −23 to −29 kJ/mol at both 0.01 M and 0.0025 M indicating a slight exothermic, stoichiometric process. The values are consistent across acid concentrations and injection volume, reflecting a true protonation/ion-exchange process. If instead the signal were dominated by dilution heat or ionic strength jumps, then the apparent ΔH would scale with concentration, and there would be different values at 0.01 M versus 0.0025 M. The n value is small at 0.13–0.22 which would equate to a 67-114 meq/100 g CEC. This value is similar to other reported CEC values for Li-hectorite and montmorillonite of ~70-120 meq/100 g (Jordaan, 2007). The K_d values fall within a tight window of 10^{-6}–10^{-5} M, which implies strong binding for

ions onto exchangeable sites. The q_0 values are negative, but reproducible with values of ~ −17 to −24 μJ.

The citric acid ΔH, n, K_d values and associated errors were highly variable under the one site model. This was attributed to the poorly constrained n combined with different experimental conditions (# of injections and volume of acid added). In order to minimize error and extraneous values, the n parameter was restricted to ranges consistent with known CEC values for sample SHCa-1 and CEC ranges determined by the sulfuric acid runs for samples JMf0 and MDD-006 #8. The ΔH values ranged from −6.1 to −29.5 kJ/mol, with higher values corresponding to experimental setups with larger injection volumes. The variable ΔH at different concentrations likely reflects dissolution or coupled chelation effects of citrate complexing Mg^{2+} and Al^{3+} released from the clay. The inconsistency suggests the one-site model is over-simplifying the reaction. The n values vary between samples and acid concentrations with the 0.1M citric acid JMf0 experiments. They range from 0.1630 to 0.4321. K_d varies widely from 10^{-4} to 10^{-6} M. The inconsistency in the results and difficulty constraining n suggest the citric acid data may require a two-site or sequential binding model rather than the one-site model.

3.2.2. *Sample SHCa-1*

The ΔH for the sulfuric acid experiments are consistently ~ −18 to −19 kJ/mol at 0.0025 M and −19 to −25 kJ/mol at 0.01 M. This narrow range of values, like sample JMf0 indicates a slight exothermic, stoichiometric process in each of the reactions. The n value for the sulfuric acid experiments ranges from 0.08 to 0.12 and therefore its CEC is calculated to be 46-67 meq/ 100 g. This CEC value is very close to the accepted value for SHCa-1 CEC which is 66.4meq/100 g (Borden and Giese, 2001). The K_d values fall within a tight window of $7.7x10^{-7}$ $-1.6x10^{-6}$ M, which implies strong binding for protons onto exchangeable sites.

The citric acid ΔH is variable under the one-site model depending on acid concentration, with 0.01M fits showing values of -6.1 to -10.2 kJ/mol, while the 0.1M fits yield extreme values of -1.6 to -3.0 kJ/mol. The n values are consistent between the 0.01M fits (0.25167) and the 0.1M fits (0.25165). The K_d values for the 0.01M experiments ranged narrowly from $8.7x10^{-5}$ M to $1.0x10^{-4}$ while the 0.1M experiments yielded a slightly larger range of $6.5x10^{-5}$ M to $2.4 x10^{-4}$.

3.2.3. Sample MDD-006 #8

The six sulfuric acid experiments for sample MDD-006 #8 consistently yielded ΔH values of -18.7 to 21.5 kJ/mol. They all produced n values between 0.08 and 0.14. Although the chemical formula and molecular weight of MDD-006 #8 are unknown, since they are from the same locality as JMF0, we used the MW from JMf0 to estimate the CEC. The n values equate to a CEC of 43 to 67 meq/100 g. The K_d values ranged narrowly from $1.4 x10^{-6}$ to $7.6 x10^{-6}$ M.

Of the two citric acid concentrations, only the 0.01 M experiments were conducted on sample MDD-006 #8. The ΔH values varied moderately from -13.6 to -25 kJ/mol. The n values were fit to be 0.16297. The K_d values were within error to be $2.6x10^{-5}$ to $2.9x10^{-5}$ M.

*3.2.4. Thermodynamic parameters (*ΔG, ΔS)

Using the model fit parameters, values for Gibbs free energy (ΔG) and entropy (ΔS) were calculated for each of the experiments (Figure 6, Table 3). The ΔG for all experiments stayed within a range of -21.4 to -37.9 kJ/mol with more negative values being attributed to more concentrated sulfuric acid conditions. SHCa-1 yielded consistently more negative values when compared to other samples under the same acid conditions. The ΔG value for JMf0 and MDD-006 #8 were within error of each other at higher sulfuric acid concentrations, however MDD-006 #8 was slightly more negative than JMf0 during lower sulfuric acid conditions. The ΔS value ranged from -26.9 to 78.5 J/mol/K across all experiments and varied widely even between replicates. The

ΔS values were more positive in citric acid experiments at high concentrations, and these values became more negative at weaker concentrations of citric acid. The sulfuric acid ΔS values sustained a slightly narrower range of positive values than the sulfuric acid experiments.

Table 3. Calculated thermodynamic parameters from one-site Wiseman model fits

	sample	Injection volume (uL)	# injections	ΔH (kJ/mol)	n	Kd (M)	q0 (uJ)	ΔG (kJ/mol)	ΔG err	ΔS (J/mol/K)	ΔS err	TΔS (kJ/mol)	ΔH per H+
0.01 M citric acid													
	JMf0	2	25	-23.082 ± 9.254	0.2539 ± 0.0670	7.441e-5 ± 9.679e-5	-9.04 ∓ 1.50	-23.563	3.224	1.615	10.815	0.481	-7.69
	JMf0	1	50	-6.132 ± 4.526	0.2539 ± 0.1215	1.058e-4 ± 2.071e-4	-5.68 ∓ 0.94	-22.691	4.852	55.539	16.274	16.559	-2.04
	JMf0	1	50	-10.157 ± 6.204	0.2539 ± 0.1014	8.916e-5 ± 1.598e-4	-6.87 ∓ 1.33	-23.115	4.443	43.462	14.901	12.958	-3.39
	SHCa-1	1	50	-9.047 ± 4.914	0.25167 ± 0.0898	8.378e-5 ± 1.376e-4	-2.07 ∓ 0.73	-23.269	4.071	47.702	13.655	14.222	-3.02
	SHCa-1	1	50	-6.152 ± 4.480	0.25166 ± 0.1191	1.036e-4 ± 2.01e-4	-0.75 ∓ 1.15	-22.743	4.809	55.647	16.130	16.591	-2.05
	SHCa-1	1	50	-10.196 ± 6.136	0.25166 ± 0.0993	8.726e-5 ± 1.551e-4	-3.57 ∓ 0.73	-23.169	4.406	43.510	14.778	12.973	-3.40
	MDD-006 #8	1	50	-13.659 ± 3.384	0.16297 ± 0.0185	2.930e-5 ± 1.966e-5	-1.88 ∓ 0.60	-25.874	1.663	40.968	5.579	12.215	-4.55
	MDD-006 #8	1	50	-25.650 ± 3.291	0.16297 ± 0.0149	2.939e-5 ± 1.589e-5	-6.87 ∓ 0.87	-25.866	1.340	0.725	4.495	0.216	-8.55
	MDD-006 #8	1	50	-19.613 ± 2.994	0.16297 ± 0.0178	2.632e-5 ± 1.795e-5	-2.89 ∓ 0.68	-26.140	1.691	21.890	5.670	6.527	-6.54
0.1M citric acid													
	JMf0	2	25	-6.299 ± 3.038	0.4321 ± 0.1967	8.808e-5 ± 6.464e-5	-6.18 ∓ 0.59	-23.145	1.819	56.503	6.101	16.846	-2.10
	JMf0	1	50	-6.996 ± 0.577	0.3430 ± 0.0241	2.191e-5 ± 9.519e-6	-8.20 ∓ 0.48	-26.594	1.077	65.733	3.612	19.598	-2.33
	JMf0	1	50	-9.059 ± 0.372	0.3805 ± 0.0132	2.948e-6 ± 3.267e-6	-14.16 ∓1.29	-31.566	2.747	75.490	9.214	22.507	-3.02
	SHCa-1	1	50	-2.236 ± 2.267	0.25165 ± 0.2321	6.498e-5 ± 1.163e-4	-3.40 ∓ 0.88	-23.899	4.437	72.659	14.880	21.663	-0.75
	SHCa-1	1	50	-3.089 ± 6.108	0.25165 ± 0.4712	2.286e-5 ± 1.074e-4	-0.62 ∓ 1.49	-26.489	11.646	78.484	39.061	23.400	-1.03
	SHCa-1	1	50	-1.634 ± 2.530	0.25165 ± 0.3473	2.396e-4 ± 3.629e-4	-0.62 ∓ 1.50	-20.665	3.754	63.830	12.592	19.031	-0.54
0.0025 M sulfuric acid													
	JMf0	1	40	-25.854 ± 1.633	0.1852 ± 0.0064	7.871e-6 ± 3.254e-6	-13.07 ∓ 2.13	-29.132	1.025	10.994	3.437	3.278	-12.93
	JMf0	1	50	-23.882 ± 1.725	0.1506 ± 0.0067	5.267e-6 ± 3.099e-6	-9.12 ∓ 1.66	-30.128	1.458	20.948	4.892	6.246	-11.94
	JMf0	1	50	-23.920 ± 1.620	0.1425 ± 0.005	3.093e-6 ± 2.031e-6	-8.45 ∓ 1.63	-31.447	1.628	25.246	5.459	7.527	-11.96
	SHCa-1	1	50	-18.999 ± 1.375	0.0898 ± 0.0035	5.786e-7 ± 6.507e-7	-4.00 ∓ 1.25	-35.602	2.788	55.688	9.350	16.603	-9.50
	SHCa-1	1	50	-18.160 ± 1.092	0.0912 ± 0.0031	7.668e-7 ± 6.555e-7	-3.04 ∓ 0.98	-34.904	2.119	56.161	7.107	16.744	-9.08
	SHCa-1	1	50	-19.094 ± 1.357	0.1162 ± 0.0048	1.607e-6 ± 1.329e-6	-3.27 ∓ 1.30	-33.070	2.050	46.877	6.876	13.976	-9.55
	MDD-006 #8	1	50	-18.740 ± 1.483	0.1357 ± 0.0062	1.923e-6 ± 1.714e-6	-7.18 ∓ 1.54	-32.625	2.209	46.571	7.410	13.885	-9.37
	MDD-006 #8	1	50	-20.142 ± 1.287	0.1308 ± 0.0047	1.609e-6 ± 1.221e-6	-6.92 ∓ 1.33	-33.067	1.881	43.351	6.309	12.925	-10.07
	MDD-006 #8	1	50	-20.568 ± 0.875	0.1351 ± 0.0032	1.458e-6 ± 7.641e-7	-6.06 ∓ 0.94	-33.311	1.299	42.742	4.357	12.743	-10.28
0.01 M sulfuric acid													
	JMf0	1	50	-29.459 ± 0.915	0.1694 ± 0.0038	1.070e-5 ± 2.337e-6	-20.42 ∓ 1.46	-28.371	0.541	-3.650	1.816	-1.088	-14.73
	JMf0	1	50	-22.868 ±1.256	0.2164 ± 0.0081	7.117e-6 ± 3.561e-6	-24.39 ∓ 2.75	-29.382	1.240	21.846	4.160	6.514	-11.43
	JMf0	1	50	-22.877 ± 0.702	0.1289 ± 0.0022	8.100e-6 ± 1.358e-6	-17.20 ∓ 0.96	-29.061	0.416	20.741	1.394	6.184	-11.44
	JMf0	1	50	-26.972 ± 1.128	0.1251 ± 0.0035	3.045e-6 ± 1.432e-6	-17.80 ∓ 1.94	-31.486	1.166	15.140	3.910	4.514	-13.49
	SHCa-1	1	50	-24.297 ± 0.808	0.1112 ± 0.0023	3.767e-7 ± 3.742e-7	-14.91 ∓ 1.48	-36.666	2.462	41.487	8.259	12.369	-12.15
	SHCa-1	1	50	-25.000 ± 1.624	0.0830 ± 0.0018	2.283e-7 ± 7.7e-7	-14.33 ∓ 1.13	-37.908	8.360	43.292	28.041	12.908	-12.50
	MDD-006 #8	1	50	-21.516 ± 0.976	0.0895 ± 0.0029	7.665e-6 ± 2.19e-6	-11.89 ∓ 0.95	-29.198	0.708	25.764	2.375	7.682	-10.76
	MDD-006 #8	1	50	-19.528 ± 0.746	0.0969 ± 0.0027	3.468e-6 ± 0.0027e-6	-0.75 ∓ 1.15	-31.164	0.002	39.026	0.007	11.636	-9.76
	MDD-006 #8	1	50	-20.607 ± 0.812	0.1253 ± 0.0034	3.606e-6 ± 0.0034e-6	-9.34 ∓ 1.35	-31.067	0.002	35.082	0.008	10.460	-10.30

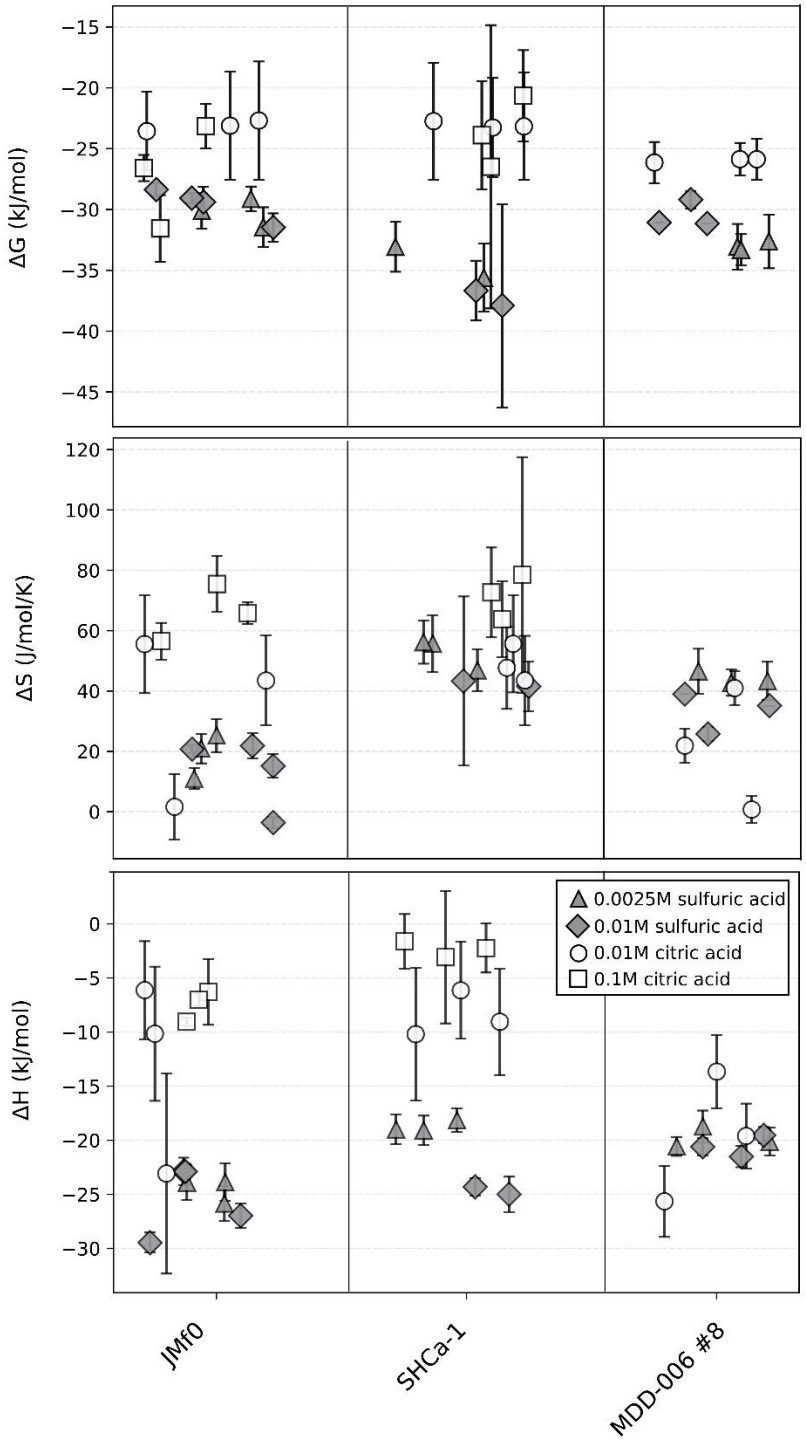

Figure 6. Calculated thermodynamic values for (a) gibbs free energy (b) entropy and (c) enthalpy of each replicate for samples JMf0, SHCa-1, and MDD-006 #8 colored by acid conditions. Outliers from poor Wiseman fits.

4. Discussion

4.1. Reaction favorability by clay and acid type

Across all samples, sulfuric acid experiments yield more negative ΔG values than citric acid experiments under similar proton conditions, indicating that acid dissolution is more favorable in sulfuric acid than citric acid. Sulfuric acid is a strong acid that deprotonates almost completely, and sulfate, its conjugate base, interacts weakly with dissolved cation (Faure, 1998). Consistency between the modeled stoichiometric coefficient (*n*) and the cation exchange capacity (CEC), is a strong indication that the measured free energies correspond to the exchange of surface-bound cations with protons (section 3.2.1). In contrast, the ΔG values for citric acid reactions are less negative and more scattered, reflecting variable contributions from secondary processes such as partial dissolution of the structural layers and ion chelation. Citric acid is a weak acid, and its conjugate base, citrate, is known to complex with divalent cations such as Mg^{2+}, Mn^{2+}, and Fe^{2+} that are released as clay dissolves. Thus, dissolution is likely to be a competition of two simultaneous process that may exhibit different, and concentration-dependent, rates.

Entropy values span a broad range and show no consistent ordering by sample type. However, the largest positive ΔS values are associated with the 0.1M citric acid experiments. This may be consistent with strong chelation of cations Mg, Mn and Fe by citrate that drives the deprotonation of citric acid. Under these conditions, citric acid dissolution more closely resembles the ion-exchange driven dissolution in sulfuric acid. More negative ΔS values in lower concentration citric acid experiments may represent a situation where there is less dissolution, because the relatively smaller amount of divalent cations released by the smaller quantity of acid does not drive further deprotonation of citric acid to citrate, freeing protons to bind to and dissolve the clay. There is unresolved uncertainty whether clay-citrate colloidal interactions are responsible

for *n* values dropping below the threshold for a simple proton exchange reaction. The variation in entropy for 0.01 M citric acid conditions is due to entropy strongly depending on the n value. Overall, the results suggest that although sulfate drives strongly favorable cation-exchange reactions, citric acid-clay solutions adopt a more complex configuration space.

4.2. Experimental reaction sequence during ITC

The reaction sequence for the acid digestion of clays involves (1) fast layer exchange (Ca^{2+} is released into solution) and (2) edge protonation and partial framework attack (Fe/Mn release with Si in the tetrahedral sheets) and (3) brucite-like octahedral layer breakdown enabling Mg and Li release into solution (Dong et al., submitted). Based on existing kinetic models for JMF0 (Dong et al., submitted), the pH range and reaction times were likely insufficient for capturing step 3. The one site model fit for sulfuric acid reactions likely captures the entire first step of clay digestion.

Each experimental run was converted to ΔH per mole H^+ by dividing by the number of acidic protons (ν=2 for H_2SO_4, ν=3 for citric acid) and the citric versus sulfuric reactions were compared at matched proton equivalents to isolate protonation versus citrate-specific processes. Even when normalized to H^+, citrate runs are not systematically less exothermic per proton than the sulfuric acid runs, and in one replicate are more exothermic than sulfate. This additional heat in the citric acid runs capture the chelation of Mg^{2+}, Fe^{2+}/Fe^{3+}, Mn^{2+} and Ca^{2+} after proton exchange, which consequently promotes the breakdown of the octahedral or brucite-like layers, letting Li, Mg, Fe go into solution and a higher ΔS value. By comparison, the sulfuric acid runs were clean, reproducible exchanges which likely do not progress beyond the $H^+ \leftrightarrow$ Na/Ca exchange step. The implications of this are that citric acid may dissolve the hectorite more by complexing the cations and promoting more effective structural breakdown, making it a more effective acid for clay digestion under these experimental conditions.

5. Conclusion

Understanding deposit chemistry and the thermodynamic differences during acid leaching provides a mechanistic foundation for optimizing leaching protocols, balancing extraction efficiency with environmental and reagent costs in the processing of lithium-bearing clays. We characterized the elemental and mineralogical composition of Li mudstones from the northern McDermitt deposit and quantified the thermodynamics of acid-clay reactions of 2 representative hectorite samples and a standard. We summarize our findings in the following points:

SEM–EDS mapping confirms a silicate-dominated matrix (Si, O, Mg, Ca) with minor Al and Fe, Na, K, and P.

1. XRD analyses show that the mudstones are dominated by Li-rich hectorite-group smectites, with variable amounts of calcite, feldspar, quartz, fluorapatite, and Fe-oxides.
2. Principal component and cluster analyses of assay data identify nine element groups, with Li, Mg, Ca, and Sr forming a distinct association that reflects clay and carbonate-bearing phases.
3. Sulfuric acid promotes reproducible, stoichiometric proton-exchange reactions, whereas citric acid induces additional dissolution and metal-chelation processes that generate more variable heats.
4. Sulfate reactions are consistently exothermic ($\Delta H \approx -18$ to -29 kJ/mol) and strongly favorable ($\Delta G \approx -22$ to -35 kJ/mol), while citrate reactions show broader, less predictable energetics.
5. Positive ΔS values in citric acid systems indicate greater disorder, suggesting partial disruption of the clay lattice.

Although the assay/EDS correlation analysis and the calorimetry experiments operate at different scales, they are linked through a common control: the mineralogical and compositional factors that govern the abundance and reactivity of surface/interlayer sites. Comparing ITC parameters to sample PC scores could test whether variations in calorimetric response are consistent with compositional variance. The PCA/clustering of elemental data provides a compact description of compositional endmembers including a clay component, carbonate/buffering component, and an Fe-Mn/oxide or trace metal component, which could be treated as predictors of reactivity with enough ongoing calorimetry experiments on a larger variety of clay samples. Calorimetry integrates multiple coupled reactions, so agreement (or lack thereof) with elemental PCs constrains when bulk composition is sufficient to predict leaching energetics and when mineral-specific site chemistry or texture must dominate. Future work may involve expanding the dataset to include clays from samples with distinct chemistries/PC scores to test this hypothesis. Further, if the underlying drivers for downcore PC scores could be tied with proxies to environmental conditions (redox conditions, diagenesis, fluid chemistry, etc.), the geochemical conditions most favorable for lithium clay genesis could perhaps be elucidated.

Acknowledgements

This project was made possible with funding from the Department of Energy SCGSR program office in collaboration with the Lawrence Berkeley National Laboratory. We thank Wenming Dong and John Christensen for their assistance with fieldwork, analytical support, and ongoing collaborations related to this work. We would like to thank Jindalee Lithium for access to assay data and core materials. Additionally, we also thank collaborators from OSU, NETL, DOGAMI, and University of Nevada, Reno for invaluable discussions surrounding Li mudstone processing.

References

Allen, T. *Particle Size Measurement* Chapman & Hall, 1997.

Bastos M, Abian O, Johnson CM, Ferreira-da-Silva F, Vega S, Jimenez-Alesanco A, Ortega-Alarcon D, Velazquez-Campoy A. Isothermal titration calorimetry. Nature Reviews Methods Primers. 2023 Mar 9;3(1):17.

Boschetti, T. and Awolayo, A.N., 2025. Constraining lithium-clay equilibria in sedimentary environments using a new thermodynamic dataset. *Journal of Geochemical Exploration*, p.107920.

Bethke, C.M. and Yeakel, S., 2014. The Geochemist's Workbench Release 10.0: GWB Essentials Guide. *Aqueous Solutions, LLC, Champagin, IL, 149p*.

Borden, D. and Giese, R.F., 2001. Baseline studies of the clay minerals society source clays: cation exchange capacity measurements by the ammonia-electrode method. *Clays and Clay Minerals*, *49*(5), pp.444-445.

Chipera, S.J. and Bish, D.L., 2001. Baseline studies of the clay minerals society source clays: powder X-ray diffraction analyses. *Clays and Clay Minerals*, *49*(5), pp.398-409. https://doi.org/10.1346/CCMN.2001.0490507.

Crocker, L. and Lien, R.H., 1988. Lithium and its recovery from low-grade Nevada clays, United States Bureau of Mines (1987)

Dong, W., Yan, R., Gagnon, C. A., Khaladj D. A., Getenet, M., Whittaker, M. L. (submitted), Multistep incongruent dissolution controls lithium extraction from hectorite.

Dong, W., Bhattacharyya, A., Fox, P.M., Bill, M., Dwivedi, D., Carrero, S., Conrad, M. and Nico, P.S., 2020. Geochemical controls on release and speciation of Fe (II) and Mn (II) from hyporheic sediments of East River, Colorado. *Frontiers in Water*, *2*, p.562298.

Faure, G. (1998). *Principles and Applications of Geochemistry* (2nd ed.). Upper Saddle River, New Jersey: Prentice Hall.

Freyer, M. W., & Lewis, E. A. (2008). Isothermal titration calorimetry: experimental design, data analysis, and probing macromolecule/ligand binding and kinetic interactions. *Methods in cell biology*, *84*, 79-113.

Guy, H. P., 1969. Laboratory theory and methods for sediment analysis. US Geological Survey Techniques of Water Resources Investigation. Book 5, chapt. Cl.

International Centre for Diffraction Data (ICDD). (2025). *PDF-4: Powder Diffraction File, Mineral Database* [Database]. International Centre for Diffraction Data. https://www.icdd.com

International Energy Agency. *Lithium – Analysis*. Paris: IEA, 2024.

Jolliffe, I. T., & Cadima, J. (2016). Principal component analysis: A review and recent developments. *Philosophical Transactions of the Royal Society A*, 374(2065), 20150202.

Jordaan, W.J., 2007. Meaningful CEC values of clay minerals from heavy mineral deposits. In *The 6th International Heavy Minerals Conference 'Back to Basics', the Southern African Institute of Mining and Metallurgy* (pp. 163-166).

Lê, S., Josse, J., & Husson, F. (2008). FactoMineR: An R package for multivariate analysis. *Journal of Statistical Software*, 25(1), 1–18.

Lithium Americas, 2022, Feasibility Study National Instrument 43-101 Technical Report. Humboldt County, Nevada, USA

Liu, J., Xu, R., Sun, W., Wang, L. and Zhang, Y., 2024. Lithium extraction from lithium-bearing clay minerals by calcination-leaching method. *Minerals*, *14*(3), p.248.

Nandihalli, N., Chouhan, R.K., Kuchi, R. and Hlova, I.Z., 2024. Aspects of spodumene lithium extraction techniques. *Sustainability*, *16*(19), p.8513.

Poppe, L.J., Paskevich, V.F., Hathaway, J.C. and Blackwood, D.S., 2001. US geological survey open-file report 01–041. A Laboratory Manual for X-Ray Powder Diffraction. *US Geological Survey, Coastal and Marine Geology Program, Wood Hole Field Centre, Woods Hole, Massachusetts, USA*.

Putzolu, F., Armstrong, R.N., Benson, T.R., Boutt, D.F., Butler, K.L., Dolgopolova, A., Herrington, R.J., Ibarra, D.E. and Munk, L.A., 2025. Volcano-sedimentary deposits: Overview of an emerging type of lithium resource. Economic Geology, 120(3), pp.541-573.

Roy, V., Paranthaman, M.P. and Zhao, F., 2024. Lithium from clay: Assessing the environmental impacts of extraction. *Sustainable Production and Consumption*, *52*, pp.324-332.

Schwarz, G. (1978). Estimating the dimension of a model. *The Annals of Statistics*, 6(2), 461–464.

Scrucca, L., Fop, M., Murphy, T. B., & Raftery, A. E. (2016). mclust 5: Clustering, classification and density estimation using Gaussian finite mixture models. *The R Journal*, 8(1), 289–317.

Vega-Muratalla, V.O., Ramírez-Márquez, C., Lira-Barragán, L.F. and Ponce-Ortega, J.M., 2024. Review of lithium as a strategic resource for electric vehicle battery production: Availability, extraction, and future prospects. *Resources*, *13*(11), p.148.

Ward, J. H. Jr. (1963). Hierarchical grouping to optimize an objective function. *Journal of the American Statistical Association*, 58(301), 236–244.

Wiseman, T., Williston, S., Brandts, J. F., & Lin, L. N. (1989). Rapid measurement of binding constants and heats of binding using a new titration calorimeter. *Analytical Biochemistry*, 179(1), 131–137. https://doi.org/10.1016/0003-2697(89)90213-5

Wu, F., Shivakumar, K.R., Konhauser, K.O. and Alessi, D.S., 2025. Lithium resources and novel strategies for their extraction and purification. *npj Materials Sustainability*, *3*(1), p.30.

Xie, R., Zhao, Z., Tong, X., Xie, X., Song, Q. and Fan, P., 2024. Review of the research on the development and utilization of clay-type lithium resources. *Particuology*, *87*, pp.46-53.

Zhao, H., Wang, Y. and Cheng, H., 2023. Recent advances in lithium extraction from lithium-bearing clay minerals. *Hydrometallurgy*, *217*, p.106025.

Zhong, W., Yang, L., Rao, F., Tong, L. and Feng, H., 2024. Efficient extraction of lithium from calcined kaolin lithium clay with dilute sulfuric acid. *Minerals*, *14*(4), p.359.